Habilitation à diriger des recherches
UPMC Univ Paris 6

présentée par

David LACOSTE

De la matière molle aux milieux biologiques : quelques applications en Physique Statistique

soutenue publiquement le 9 octobre 2009
devant un jury composé de

M. Luca Peliti, rapporteur
M. E. Trizac, rapporteur
M. J-F. Joanny, examinateur
M. A. Ajdari, invité
M. S. Turner, examinateur
R. Golestanian, rapporteur

Remerciements

Ce mémoire est une synthèse de mes travaux de recherche afin d'obtenir l'Habilitation à diriger des recherches de l'Université Pierre et Marie Curie. Je remercie vivement tous les membres du jury pour leur participation, et tout particulièrement L. Peliti, R. Golestanian et E. Trizac pour avoir accepté d'examiner ce travail.

Après mon doctorat, mon séjour postdoctoral à l'Université de Pennsylvanie fut très instructif et me permis d'acquérir nombre de compétences dans le domaine de la matière molle, bien au delà de ce que je pouvais imaginer à l'époque. Nombre de sujets de recherches présentés dans ce mémoire, sont directement liés à cette période. Je remercie chaleureusement T. Lubensky pour m'avoir accueilli et formé dans son laboratoire.

Évidemment l'activité d'un chercheur ne peut s'épanouir que dans un environnement stimulant. Je remercie les directeurs successifs du Laboratoire Physico-Chimie Théorique, A. Ajdari, T. Maggs et E. Raphaël pour m'avoir permis de rejoindre leur groupe à l'ESPCI. Je suis très reconnaissant à J. B. Fournier, pour m'avoir initié à la Physique des membranes biologiques à mon arrivée au laboratoire de Physico-Chimie Théorique, et pour m'avoir transmis l'envie de poursuivre dans cette voie. Même si je n'ai jamais collaboré avec Armand, j'ai beaucoup apprécié nos discussions, qui ont eu un rôle déterminant pour plusieurs sujets de recherche présentés ici. Je le remercie d'avoir accepté de compléter ce jury.

Ces dernières années, mon activité de recherche doit beaucoup à mes collègues de l'Institut Curie (l'équipe de P. Bassereau, JF. Joanny et J. Prost) ainsi qu'à K. Mallick du Service de Physique Théorique de Saclay, qui ont directement contribué à mener à bien beaucoup de travaux présentés dans ce mémoire. Je les remercie vivement, pour leur grande disponibilité, pour leur patience, leur gentillesse, et pour leurs nombreux conseils.

Je tiens enfin à remercier notre secrétaire Mme Fridelance ainsi que tous les autres membres du laboratoire de Physico-Chimie Théorique, dont les suggestions et les conseils m'ont aidé : Florent, Pierre, Michael, Ken, Hélène, Falko, Serge, et bien sûr l'ensemble des membres de Gulliver pour leur présence chaleureuse au quotidien.

Avant propos

Ce mémoire présente une synthèse de mes travaux de recherche depuis mon doctorat. J'ai d'abord mené des recherches sur le transport de la lumière dans des milieux complexes. Puis, j'ai abordé des thématiques nouvelles, comme celle liée à l'autoassemblage de particules colloïdales. Je me suis également intéressé à des questions inspirées par les systèmes vivants. Une de ces questions concerne par exemple la description des fluctuations hors d'équilibre qui se produisent dans certains systèmes biologiques (comme des moteurs moléculaires, des biofilaments ou des membranes contenant des canaux à ions).

Ce mémoire retrace cette évolution qui est à la fois thématique et chronologique. Par delà la diversité thématique, certaines questions sont demeurées centrales. Comment décrire théoriquement des systèmes physiques dans lesquels les fluctuations thermiques sont importantes ? Quel lien s'opère entre les échelles microscopiques et macroscopiques d'un tel système ? Dans les systèmes biologiques typiquement hors d'équilibre, comment distinguer les fluctuations d'équilibre (comme celles associées au mouvement brownien par exemple) des fluctuations hors d'équilibre (comme celles associées au mouvement d'une bactérie par exemple) ?

Transport de la polarisation de la lumière dans un milieu diffusant

Ce premier chapitre traite d'un domaine assez différent des deux suivants puisqu'il s'agit des propriétés de transport de la lumière polarisée dans un milieu complexe fortement anisotrope comme des tissus biologiques ou des cristaux liquides. Ce sujet est issu de mes travaux de thèse et a été poursuivi pendant mon séjour postdoctoral. A cette occasion, j'ai développé une approche théorique pour décrire le transport de la lumière dans un milieu diffusant et fortement anisotrope comme des cristaux liquides chiraux. De retour en France, j'ai poursuivi la thématique du transport de la lumière dans un milieu diffusant quelconque (pas nécessairement des cristaux liquides). Je me suis intéressé aux motifs formés par la lumière rétrodiffusée dans un milieu diffusant. J'ai également obtenu une détermination de la longueur caractéristique associée au transport de la polarisation en diffusion multiple (l'analogue de ℓ^* pour la polarisation) à partir de mesures de fonctions de corrélation de l'intensité diffusée.

Auto-assemblage de colloïdes magnétiques et cristaux liquides

Dans ce second chapitre, il est question de l'auto-organisation de colloïdes magnétiques de type ferrofluide purs ou mélangés à des colloïdes non-magnétiques en présence de champ magnétique. On traite également d'un modèle théorique pour les gels nématiques, qui sont des gels de polymères réticulés contenant des particules colloïdales (non-magnétiques) en forme de bâtonnets. Les recherches présentées dans ce chapitre visent à concevoir de nouvelles classes de matériaux "activables" par une force ou un agent extérieur, qui sont, dans les colloïdes magnétiques, le champ magnétique et, dans les gels nématiques, la pression osmotique.

Applications de la Physique Statistique à des systèmes biologiques

Enfin, le dernier chapitre est consacré à la physique du cytosquelette, qui est un élément essentiel d'une cellule biologique. Les membranes lipidiques sont un constituant majeur des cellules biologiques, et elles jouent un rôle essentiel dans le transport intracellulaire. Les propriétés à l'équilibre des membranes lipidiques sont décrites par l'hamiltonien de Helfrich qui rend correctement compte de la phénoménologie des formes de membranes observées. Cependant les membranes lipidiques des cellules biologiques sont des systèmes hors d'équilibre plus complexes à étudier. Pour cette raison, on a souvent recours à des systèmes biomimétiques comme des vésicules lipidiques géantes. J'ai développé plusieurs modèles théoriques pour décrire les propriétés hors d'équilibre de systèmes biomimétiques à base de membranes lipidiques : par exemple, la membrane lipidique peut être couplée à un cytosquelette dans un modèle simple de cellule biologique, ou bien la membrane peut contenir des canaux à ions activables par la lumière dans le cas des membranes dites actives, ou bien la membrane peut être soumise à un champ électrique qui génère des courants ioniques et des écoulements électrocinétiques.

Dans une cellule biologique, des protéines très particulières, les moteurs moléculaires réalisent une transformation d'énergie chimique, provenant de l'hydrolyse de l'ATP, en énergie mécanique. Grâce à un modèle simple, j'ai étudié les contraintes thermodynamiques que doivent vérifier de façon générale les modèles théoriques de moteurs moléculaires. Cette analyse thermodynamique s'appuie sur une vérification de la symétrie du théorème de fluctuations (relation de Gallavotti-Cohen en particulier), qui est une manifestation macroscopique de la symétrie de renversement du temps valable à l'échelle microscopique. J'ai pu par la suite appliquer certaines techniques de Physique Statistique à d'autres systèmes biologiques également capables de réaliser une conversion d'énergie chimique en énergie mécanique comme certains biopolymères comme l'actine ou les microtubules.

Table des matières

CURRICULUM VITAE

État civil

né le 22 décembre 1971 à Montpellier (France),
nationalité française, marié avec deux enfants.
Mail : david@turner.pct.espci.fr, **Tel** : 33-1-40-79-51-40,
Fax : 33-1-40-79-47-31,
Web : http ://www.pct.espci.fr/∼david/

Formation

1996 Doctorat de Physique de l'Université Joseph Fourier, Grenoble,
intitulé *Diffusion de la lumière dans des milieux magnéto-optiques ou chiraux.*
1995 Agrégation de Physique
1994 Ecole Normale Supérieure, DEA de Physique Quantique
1992 Scolarité à l'Ecole Normale Supérieure, Paris

Recherche

depuis juin 2005 CNRS, Chargé de Recherches CR1
Janv 2002 – juin 2005 CNRS, Chargé de Recherches CR2
Janv 2000 – janv 2002 Stage postdoctoral à l'Université de Pennsylvanie, Philadelphie, sous la direction de T. Lubensky.

Enseignement

depuis 2008 Travaux dirigés en M2 pour le parcours Physique des Liquides. Sujet : Physique Statistique des fluides classiques.
depuis 2002 Préceptorat en 3ème année à l'ESCPI. Le sujet de cet enseignement concerne les transitions de phase et les lois d'échelle.
2005 Cours en M2 pour le parcours Physique des Liquides. Sujet : Biophysique
1996 – 1999 Allocataire moniteur de l'Université Joseph Fourier. Emploi : Préparation de l'agrégation de Physique

Encadrement

A partir de septembre 2009 3 chercheurs postdoctoraux : deux sont localisés à l'Institut Curie, Luis Dinis et Kostas Tsekouras et sont partagés avec JF. Joanny, le dernier est F. Ziebert et travaille à l'ESPCI. Enfin Gatien Verley a commencé sa thèse sous ma direction depuis septembre 2009
2007 – 2009 chercheur postdoctoral : Ranjith Padinhateeri (80%, avec J. F. Joanny)
2007 Encadrement du stage de M2 de Julien Deseigne
2004 – 2008 thèse de Faris El-Alaoui (20%, avec P. Bassereau)
2004 – 2005 chercheur postdoctoral : Marco Lagomarsino (80%, avec J. F. Joanny)
2004 Encadrement du stage de M2 de Navid Némati
Depuis 2002 Encadrement de 5 ou 6 stagiaires de 3ème année de l'ESPCI (un par an environ).

Projets de recherche financés

- Participant à un contrat du Centre Franco-indien pour la Promotion de la Recherche Avancée (CEFIPRA) n° 3504-2, *Mécanique de la matière vivante 2006-2009* ;
- Participant à une ANR Blanche : ARTIF NEURON, *Potentiel d'action dans un nanotube lipidique : système minimal de signalisation neuronale 2008-2011* ;
- Participant à une ANR du Programme interdisciplinaire de recherches sur les systèmes moléculaires et cellulaires, et d'innovation biomédicale (PIRIbio) : ACTIMAG, *Force associée à la polymérisation de l'actine. Aspects biochimiques et mécaniques* 2009-2012.

Activités d'intérêt collectif

- Membre de la commission de spécialistes (CS 29), de l'Université d'Orsay depuis 2007, ainsi de la commission de spécialistes (CS 30), de l'Université Pierre et Marie Curie (l'intitulé de la CS 30 est "milieux dilués et optique") depuis 2008 ;

- Activité de referee pour les revues Physical Review Letters, Physical Review E, Europhysics Letters, European Physical Journal E, Langmuir, Physica D, et Physical Biology ;

- Organisation de conférences :
  Dec 2004 Organisation d'un workshop sur "Les ondes dans les milieux complexes : propagation dans la matière molle et dans les milieux granulaires à l'ESPCI".
  Juin 2004 ESPCI, Organisation d'un workshop intitulé "Biophysique Théorique sur la montagne St-Geneviève" à Université de Jussieu.

Conférences invitées, communications orales dans des congrès ou symposiums

- "Fluctuations de longueur d'un filament d'actine/microtubule couplé à l'hydrolyse de l'ATP", GdR Phénix, Lyon, novembre 2009.
- "Electrokinetic effects near a membrane" and "Non-equilibrium self-assembly of a filament coupled to ATP hydrolysis", APS March Meeting, Pittsburgh, Pennsylvania 2009.
- "Non-equilibrium fluctuations in models of molecular motors and active filaments", Conference on Active Matter, Institut Henry Poincaré, 2009.
- "Fluctuation Theorem and large deviation function for a solvable model of a molecular motor", Workshop Collective Effects in Cell Biophysics, Les Houches 2008.
- "Non-equilibrium fluctuations and mechanochemical couplings of a molecular motor", Focus meeting on Non-equilibrium steady states, Institut Henry Pointcaré 2008.
- "Non-equilibrium fluctuations and mechanochemical couplings of a molecular motor", Conference Traffic and Granular flow, Orsay 2007.
- "Fluctuations hors d'équilibre dans les systèmes biologiques : membranes actives et moteurs moléculaires", Jounéees Chimie Physique des Milieux Complexes 2007.
- "Depolarization of backscattered light", Workshop Waves in complex media 2004.

Bibliographie

[1] Sonoluminescence from Single Bubbles in Nonaqueaous Liquids : New Parameter Space for Sonochemistry, K. Weninger, R. Hiller, BP. Barber, D. Lacoste and S. Putterman, J. Phys. Chem. **99**, No. 39, 14195-7 (1995).

[2] Optics of a Faraday Mie sphere, D. Lacoste, B. van Tiggelen, G. Rikken and A. Sparenberg, J. Opt. Soc. Am. A, **15**(6), 1632-42 (1998).

[3] Transport Mean Free Path for Magneto-Transverse Light Diffusion, D. Lacoste and B. van Tiggelen, Europhys. Lett., **45**(6), 721-725 (1999).

[4] Magneto-Optics with diffuse light, D. Lacoste, B. van Tiggelen and G. Rikken, Physica B, **279**, 13-16, (2000).

[5] Photonic Hall effect in ferrofluids : theory and experiments, D. Lacoste, F. Donatini, S. Neveu, S. Serughettti and B. van Tiggelen, Phys. Rev. E, **62**(3), 3934-43 (2000).

[6] The Photonic Hall Effect in absorbing media, S. Wiebel, A. Sparenberg, G. Rikken, D. Lacoste and B. van Tiggelen, Phys. Rev. E, **62**(6), 8636-9 (2000).

[7] Coherent Backscattering of light in a magnetic field, D. Lacoste and B. van Tiggelen, Phys. Rev. E, **61**(4), 4556-65 (2000).

[8] Transport theory for magneto-transverse light diffusion, D. Lacoste, Waves in Random Media, **10**(3), 367-372 (2000).

[9] Phase transitions in a ferrofluid at magnetic field induced microphase separation, D. Lacoste and T. Lubensky, Phys. Rev. E, **64**, 041506 (2001).

[10] Effective index of refraction, optical rotation, and circular dichroism in isotropic liquid crystals, D. Lacoste, P. Collings and T. Lubensky, Phys. Rev. E, **65**, 031717 (2002).

[11] Phase transitions in lyotropic nematic gels, D. Lacoste, A. Lau and T. Lubensky Eur. Phys. J. E **8**, 403 (2002).

[12] Field-induced structures in miscible ferrofluid suspensions with and without latex spheres, M. Islam, K. Lin, D. Lacoste, T. Lubensky and A. Yodh, Phys. Rev. E, **67**, 021402 (2003).

[13] Depolarization of backscattered linearly polarized light, L-F. Rochas Ochoa, D. Lacoste, R. Lenke, P. Schurtenberger and F. Scheffold, J. Opt. Soc. Am. A, **21**(9), 1799-1804 (2004).

[14] Geometric depolarization in patterns formed by backscattered light, D. Lacoste, V. Rossetto, F. Jaillon and H. Saint-Jalmes, Optics Letters, **29**(17), 2040-2 (2004).

[15] Fluctuation spectrum of fluid membranes coupled to an elastic meshwork : jump of the effective surface tension at the mesh size J.-B. Fournier, D. Lacoste, E. Raphaël, Phys. Rev. Lett. **92**, 018102 (2004).

[16] Dynamics of active membrane with internal noise, D. Lacoste and A. Lau, Europhys. Lett., **70** (3), 418 (2005).

[17] Fluctuations of a driven membrane in an electrolyte, D. Lacoste, M. Cosentino Lagomarsino, and JF. Joanny, Europhys. Lett., **77**, 18006 (2007).

[18] Non-equilibrium fluctuations and mechanochemical couplings of a molecular motor, A. W. C. Lau, D. Lacoste, and K. Mallick, Phys. Rev. Lett., **99**, 158102 (2007).

[19] Fluctuation Theorem and large deviation function for a solvable model of a molecular motor, D. Lacoste, A. W. C. Lau, and K. Mallick, Phys. Rev. E, **78**, 011915 (2008).

[20] Membrane tension lowering induced by protein activity, M. D. El Alaoui, D. Lacoste, J. Pécréaux, JF. Joanny, J. Prost, and P. Bassereau, Phys. Rev. Lett., **102**, 038102 (2009).

[21] Electrostatic and electrokinetic contributions to the elastic moduli of a driven membrane, D. Lacoste, G. I. Menon, M. Z. Bazant and J.-F. Joanny, Eur. Phys. J. E, **28**, 243 (2009).

[22] Non-equilibrum self-assembly of a filament coupled to ATP/GTP hydrolysis, P. Ranjith, D. Lacoste, K. Mallick and JF. Joanny, Biophys. J., **96**, 2146 (2009).

[23] Measuring colloidal forces with the magnetic chaining technique, R. Dreyfus, D. Lacoste, J. Bibette, J. Baudry, Eur. Phys. J. E, **28**, 113 (2009).

[24] Stochastic model for nucleosome sliding in the presence of DNA ligands, L. Mollazadeh-Beidokhi, J. Deseigne, D. Lacoste, F. Mohammad-Raffie and H. Schiessel, Phys. Rev. E, **79**, 031922 (2009).

[25] Thermal expansion within a chain of magnetic colloidal particles, D. Lacoste, C. Brangbour, J. Bibette and J. Baudry, Phys. Rev. E, **80**, 011401 (2009).

[26] Fluctuation Theorem for the flashing ratchet model of molecular motors, D. Lacoste, K. Mallick, Phys. Rev. E, **80**, 021923 (2009).

Articles acceptés

[27] Role of ATP-hydrolysis in the dynamics of a single actin filament, P. Ranjith, K. Mallick, JF. Joanny, D. Lacoste, accepté à Biophys. J, disponible sur http ://arxiv.org/abs/0908.0657.

[28] Effective zero-thickness model for a conductive membrane driven by an electric field, F. Ziebert, M. Z. Bazant, D. Lacoste, accepté à Phys. Rev. E, disponible sur http ://arxiv.org/abs/0911.1034.

Articles soumis

[29] Fluctuation Relations for Molecular Motors, D. Lacoste, K. Mallick, soumis à la revue Séminaires Poincaré 2009.

Actes de colloques à comité de lecture

[30] Growth and Collapse of Bubbles in Superfluid 4He, P. Roche, H. Lambare, E. Rolley, D. Lacoste, S. Balibar, C. Guthmann and HJ. Maris, Proceedings of the 21st International Conference on Low Temperature Physics, Suppl S1, Czech. J. Phys., **46**, 381-2 (1996).

[31] Stokes parameters for light scattering from a Faraday-active sphere, B. van Tiggelen and D. Lacoste, Journal of Quantitative Spectroscopy and Radiative Transfer, **63**, 305-19,(1999).

[32] Recent trends in the theory of magneto-scattering of light in Recent Trends in Theory of Physical Phenomena in High Magnetic Fields, B. A. van Tiggelen, G. Rikken, F. Pinheiro and D. Lacoste (edited by I.D. Vagner et al, Kluwer Academic (2003), pp 323-331).

Chapitre 1

Transport de la polarisation de la lumière dans un milieu diffusant

> « Le vent était tombé, il bruinait, et la lueur des réverbères n'était qu'un halo dans le brouillard. »
>
> Roger Martin du Gard, *Les Thibault.*

Comment peut on décrire le transport de la lumière dans un milieu fortement diffusant ? Quelle sont les longueurs caractéristiques associées au transport de l'intensité et de la polarisation de la lumière dans le régime de diffusion multiple ? Que deviennent ces longueurs dans des milieux fortement anisotropes comme les cristaux liquides ou encore les tissus biologiques ? Toutes ces questions et d'autres ont motivé les travaux suivants.

1.1 Diffusion de la lumière dans les cristaux liquides chiraux

Au cours de mon séjour postdoctoral, je me suis intéressé à la diffusion de la lumière par des cristaux liquides particuliers, à la fois chiraux et isotropes, appelés phases bleues. Les phases bleues sont des cristaux liquides chiraux, qui doivent leur appellation au fait que deux phases de cette famille (BP I) et (BP II) sont des phases ordonnées qui diffractent la lumière par diffraction de Bragg dans le domaine visible [1]. La structure de la phase (BP III) appelée aussi "blue fog" est restée longtemps mystérieuse car elle n'a pas à la différence de BP I et BP II d'ordre à longue portée. Le mystérieux "blue fog" s'est en quelque sorte dissipé, lorsqu'on a pu démontrer expérimentalement [2] et expliquer théoriquement [3] l'existence d'une transition continue entre la phase BP III et la phase isotrope, avec un point critique terminant la ligne de coexistence entre ces deux phases. Ma contribution à l'étude des milieux chiraux isotropes de ce type (phase BP III ou phase isotrope chirale)

a été d'établir une théorie pour l'indice de réfraction effectif d'un tel milieu [4]. Cet indice effectif permet de décrire le pouvoir rotatoire, le dichroïsme circulaire ou encore les corrections à l'indice moyen dues aux fluctuations de la constante dielectrique. J'ai obtenu en particulier des expressions générales (indépendantes de la valeur du rapport longueur d'onde sur le pas du cholestérique) pour la dépendance en longueur d'onde du pouvoir rotatoire, expressions que l'on a pu comparer de façon très satisfaisante à des expériences réalisées par P. Collings du Swarthmore College en Pennsylvanie comme illustré sur la figure Fig. 1.1.

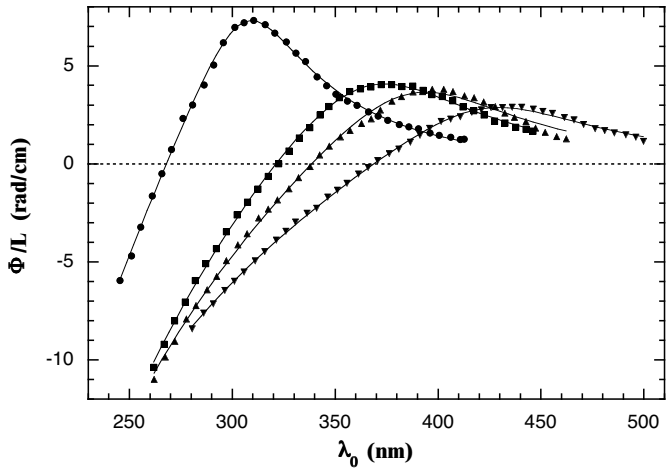

FIGURE 1.1 – Comparaison entre les mesures de pouvoir rotatoire (points) réalisées dans la phase bleue BP III en fonction de la longueur d'onde dans le vide λ_0, avec un fit obtenu à partir du modèle développé dans Ref. [4] (courbe continue). Les spectres correspondent pour les symboles circulaires à du cholesteryl myristate (CM) pur, à du cholesteryl nonanoate (CN) pur pour les carrés, et à un mélange de CN avec 5 et 10 mol% de cholesteryl chloride (CC) pour les symboles triangulaires (supérieurs et inférieurs respectivement).

1.2 Longueur caractéristique associée au transport de la polarisation

Après mon arrivée au laboratoire de Physico-Chimie Théorique, j'ai poursuivi la thématique de la diffusion de la lumière dans des milieux complexes mais cette fois sous un angle différent, qui soit plus général et non particulier aux cristaux liquides. Je me suis intéressé à une formulation théorique du transport de la polarisation de la lumière dans des milieux diffusants, comme par exemple des tissus biologiques. Dans de tels milieux, la lumière est diffusée de nombreuses fois avant d'être absorbée. Cette propriété est mise à profit dans diverses techniques d'imagerie utilisant des photons dans le domaine optique. L'avantage d'utiliser des photons dans le domaine optique, est de rendre cette technique d'imagerie parfaitement non-invasive, ce qui est essentiel pour les applications en imagerie médicale (pour le dépistage du cancer

en particulier). A cause de la diffusion multiple de la lumière, ce transport de la lumière s'effectue de façon diffuse sur une échelle de longueur appelée longueur de parcours moyen de transport ℓ^*. En général, la polarisation, par exemple linéaire de la lumière, disparaît dans un milieu diffusant sur une échelle de longueur $\ell_\perp$ différente mais comparable au libre parcours moyen de transport ℓ^* [5]. Un des objectifs de mes recherches a été de déterminer théoriquement cette longueur caractéristique $\ell_\perp$. Comprendre les propriétés de transport de la lumière liées à la polarisation n'est pas qu'une question académique, car la polarisation contient une information précieuse pour l'imagerie, et cette information n'est le plus souvent pas utilisée dans les techniques usuelles d'imagerie des tissus, lesquelles reposent sur l'information contenue dans l'intensité de la lumière plutôt que sur celle contenue dans la polarisation.

Ma contribution à ce sujet porte sur une analyse quantitative des motifs formés par de la lumière polarisée qui a été diffusée dans la direction arrière après avoir traversé un milieu diffusant [6]. Un exemple d'un tel motif est illustré sur la figure 1.2. Dans cette étude, le transport de la lumière est décrit au moyen de simulations

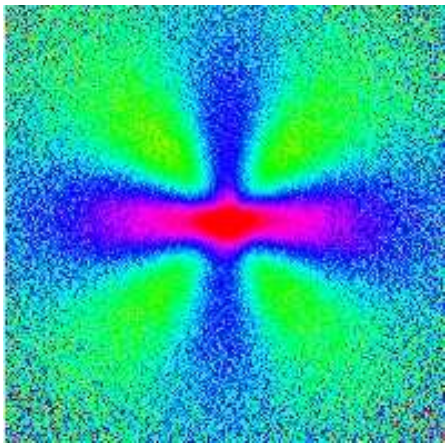

FIGURE 1.2 – *Motifs en forme de croix obtenus avec de la lumière polarisée linéairement en rétrodiffusion sur un milieu diffusant [6]. Image obtenue par S. Jaillon.*

de Monte Carlo, qui reposent sur une analogie entre la trajectoire suivie par un photon de lumière polarisée dans un milieu diffusant et un polymère semi-flexible contenant des degrés de liberté de torsion. Dans cette analogie, formulée par A. Maggs et V. Rossetto [7], la longueur de persistence du polymère correspond à $\ell_\perp$, et les degrés de liberté de torsion du polymère correspondent aux degrés de liberté associés à la polarisation. Grâce à ces degrés de liberté, on peut définir une vrille géométrique pour les polymères qui est reliée à la phase de Berry [8]. Par ailleurs, la phase de Berry se manifeste par une rotation du plan de polarisation de la lumière lorsque la lumière se propage dans une fibre optique non-biréfringente et vrillée. Cet effet a été mis en évidence expérimentalement en enroulant la fibre optique sur un cylindre de rayon variable de façon à créer une "torsion" contrôlée de la trajectoire [9]. Tout cela suggère donc une analogie entre la vrille géométrique des polymères et la phase associée au transport de la polarisation de la lumière. En fait, l'analogie dont il est question ici concerne un régime de la diffusion multiple de la lumière dans

lequel la lumière est diffusée dans toutes les directions mais de façon très anisotrope. En effet, une diffusion très anisotrope implique de faibles changements de direction de la lumière, ce qui permet de justifier l'hypothèse d'adiabaticité qui est nécessaire pour pouvoir définir la phase de Berry. Afin de déterminer si cette analogie pouvait conduire à des prédictions quantitatives, qu'on puisse tester expérimentalement, je me suis intéressé à une expérience simple à réaliser. Cette expérience consiste à focaliser la lumière d'un laser sur un point d'une surface diffusante (par exemple un liquide contenant des particules colloïdales en suspension) et à regarder la lumière rétrodiffusée à travers un polariseur. Cette lumière rétrodiffusée forme des motifs, qui ont une forme de croix si la polarisation incidente est linéaire. Ces motifs sont représentés sur la figure 1.2.

A chaque trajectoire suivie par un photon, on peut associer une phase géométrique, et l'intensité diffusée résultante est une moyenne de contributions associées à chaque chemin lumineux avec un poids qui dépend de la phase géométrique sur le chemin considéré. Par cette approche, on obtient que l'intensité a une modulation en $\cos(4\phi)$ où ϕ est l'angle azimuthal défini par rapport à la direction de la lumière incidente, ce qui explique la forme des motifs en croix. Le préfacteur dans l'expression de l'intensité diffusée permet de rendre compte de la taille des motifs d'ordre $\ell_\perp$ [6].

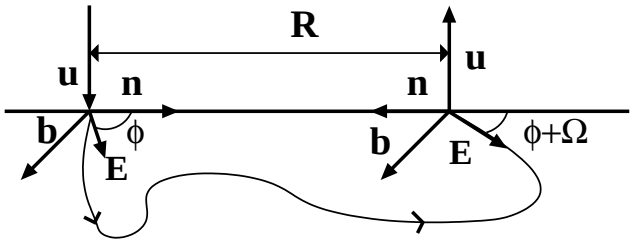

FIGURE 1.3 – *Réprésentation d'un chemin lumineux dans un milieu semi-infini diffusant en rétrodiffusion (la direction incidente est opposée à la direction émergente et séparée par une distance R). Les vecteurs* **u**, **n** *et* **b** *définissent le repère de Frenet, ϕ est l'angle azimuthal défini par rapport à la direction de la lumière incidente et Ω est la phase géométrique [6].*

On peut donc utiliser cette expérience pour mesurer $\ell_\perp$, cependant cette détermination de $\ell_\perp$ n'est pas très précise. Pour améliorer la mesure, une technique résolue en temps est bien plus avantageuse. Cela est possible grâce à la DWS (diffuse wave scattering c'est à dire spectroscopie d'ondes diffuses [10, 11]), qui généralise la technique de diffusion dynamique de la lumière (ou Dynamic Light Scattering DLS) au régime de diffusion multiple. Dans la spectroscopie d'ondes diffuses, l'information contenue dans les fonctions de corrélations de l'intensité de la lumière diffusée est utilisée pour caractériser un milieu diffusant (en termes de la taille des particules qu'il contient, concentration en particules diffusantes, coefficient de diffusion..). Comme la diffusion multiple implique de nombreuses diffusions qui changent la direction des photons, la DWS est une technique sensible à des déplacements de

très petite amplitude des diffuseurs (qui sont le plus souvent des particules sondes ajoutées au milieu que l'on cherche à caractériser) et permet également de mesurer ℓ^* ou d'accéder à une information rhéologique sur le milieu étudié [12]. Le plus souvent, la DWS est utilisée avec de la lumière non-polarisée mais dans la Ref. [13] on s'intéresse précisément à la dépendance des fonctions de corrélation de l'intensité mesurée en DWS avec la polarisation. Une analyse de ces fonctions de corrélation permet de déterminer précisément $\ell_\perp$, et cela a été fait dans des suspensions colloïdales contenant des particules de forme et de taille différentes. Les fonctions de corrélations correspondant à cette expérience sont représentées à la figure 1.4 pour les deux configurations qui sont possibles avec de la lumière polarisée linéairement.

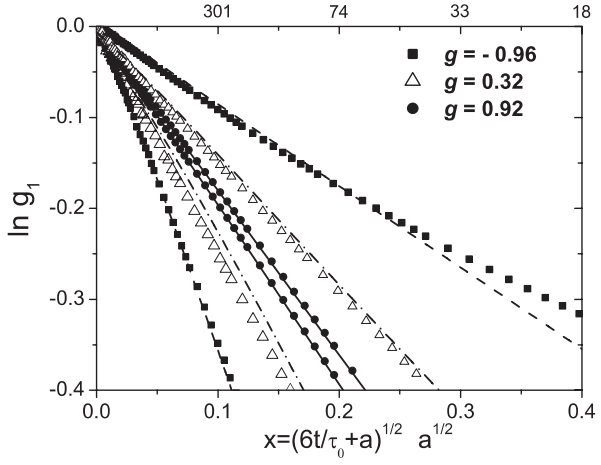

FIGURE 1.4 – *Fonction de corrélation temporelle de l'intensité $g_1(t)$ mesurée dans une expérience de DWS avec des suspensions colloïdales contenant des particules différentes caractérisées par leur paramètre d'anisotropie de diffusion g. Pour chaque série de symboles, la ligne du haut correspond à des polarisations parallèles pour la lumière incidente et émergente, et la ligne du bas correspond à des polarisations croisées dans les mêmes conditions [13].*

Bibliographie

[1] P. G. de Gennes and J. Prost. *The Physics of Liquid Crystals*. Oxford Science Publications, Oxford, 1993.

[2] Z. Kutnjak, C. W. Garland, J. L. Passmore, and P. J. Collings. Supercritical conversion of the third blue phase to the isotropic phase in a highly chiral liquid crystal. *Phys. Rev. Lett.*, 74(24) :4859, 1995.

[3] TC Lubensky and H Stark. Theory of a critical point in the blue-phase-iii-isotropic phase diagram. *Phys. Rev. E*, 53(1, Part A) :714–720, 1996.

[4] D. Lacoste, P. J. Collings, and T. C. Lubensky. Effective index of refraction, optical rotation, and circular dichroism in isotropic chiral liquid crystals. *Phys. Rev. E*, 65(3) :031717, 2002.

[5] F. C. MacKintosh, J. X. Zhu, D. J. Pine, and D. A. Weitz. Polarization memory of multiply scattered light. *Phys. Rev. B*, 40 :9342, 1989.

[6] D. Lacoste, V. Rossetto, F. Jaillon, and H. Saint-Jalmes. Geometric depolarization in patterns formed by backscattered light. *Optics Letters*, 29(17) :2040, 2004.

[7] V. Rossetto and A. C. Maggs. Writhing geometry of stiff polymers and scattered light. *Eur. Phys. J. B.*, 29 :323, 2002.

[8] M. V. Berry. Interpreting the anholonomy of coiled light. *Nature*, 326 :277, 1987.

[9] A. Tomita and R. Y. Chiao. Observation of Berry's topological phase by use of an optical fiber. *Phys. Rev. Lett.*, 57 :937, 1986.

[10] D. J. Pine, D. A. Weitz, P. M. Chaikin, and E. Herbolzheimer. Diffusing wave spectroscopy. *Phys. Rev. Lett.*, 60(12) :1134, 1988.

[11] G. Maret and P. E. Wolf. Multiple light scattering from disordered media. the effect of brownian motion of scatterers. *Z. Phys. B.*, 65 :409, 1987.

[12] F. Morin, R. Borrega, M. Cloitre, and D. Durian. Static and dynamic properties of highly turbid media determined by spatially resolved diffusive-wave spectroscopy. *Applied Optics*, 41(34) :7294, 2002.

[13] L-F. Rochas Ochoa, D. Lacoste, R. Lenke, P. Schurtenberger, and F. Scheffold. Depolarization of backscattered linearly polarized light. *J. Opt. Soc. Am. A*, 21(9) :1799, 2004.

Chapitre 2

Structures auto-assemblées à base de colloïdes

Après 2004, mes recherches sur la diffusion multiple de la lumière ont laissé place à d'autres sujets. Un de ces sujets concerne l'auto-assemblage de particules colloïdales qui est un moyen de concevoir une nouvelle classe de matériaux "activables" par une force ou agent extérieur (lumière, champ magnétique ou électrique, température, contraintes...). Un premier exemple de telles structures concerne les suspensions de particules colloïdales magnétiques appelées ferrofluides, qui sont activables par l'application d'un champ magnétique. Un autre exemple concerne les structures formées par auto-assemblage de particules colloïdales en forme de bâtonnets au sein d'un gel. Ces structures sont activables dans le sens où il est possible d'induire une transition isotrope-nématique dans ces gels soit en faisant varier la température (pour les gels thermotropes), soit en faisant varier la concentration des bâtonnets ou la qualité du solvant (pour les gels lyotropes).

2.1 Structures auto-assemblées à base de colloïdes magnétiques

2.1.1 Diagramme de phase d'un ferrofluide sous champ magnétique

Lorsqu'un champ magnétique est appliqué perpendiculairement à une mince couche de ferrofluide, des structures modulées spatialement apparaissent au dessus d'un certain champ critique. La longueur caractéristique de ces structures résulte d'une compétition entre l'interaction dipolaire attractive, et à longue portée, et une interaction répulsive et de courte portée d'origine entropique s'opposant aux variations de densité [1]. Cette compétition conduit à une "micro-phase separation" marquée par l'apparition de phases ordonnées modulées spatialement, comme une phase hexagonale ou une phase lamellaire [2, 3]. Cette "micro-phase separation" apparaît au dessus d'un certain champ magnétique critique, en dessous, le système reste dans une phase de liquide isotrope, comme représenté sur la figure 2.1. On

peut remarquer qu'un diagramme de phase très similaire existe dans les films de Langmuir [4], les couches minces magnétiques [5], les bloc-copolymères [6] ou encore les supraconducteurs de type I. Les mêmes phases modulées sont observées dans tous ces divers systèmes car la compétition mentionnée plus haut entre des interactions à courte portée et répulsives et des interactions attractives et à longue portée est à chaque fois présente.

Le modèle développé en Ref. [7] pour les ferrofluides repose sur une approche de champ moyen, qui inclut deux paramètres d'ordre scalaires : la composante de l'aimantation perpendiculaire à la couche et la densité locale du ferrofluide. La partie non-magnétique de l'interaction entre particules du fluide est décrite au moyen soit d'un modèle de type gaz sur réseau soit un modèle de Carnahan-Starling comme indiqué sur la figure 2.1. Par la suite, nous avons étendu l'approche théorique développée pour les ferrofluides purs au cas plus complexe où le ferrofluide est mélangé avec une autre suspension colloïdale non-magnétique. Expérimentalement, on observe une très grande richesse de phases dans de tels mélanges, avec par exemple des phases de type oignons [8] (il s'agit ici d'oignons à symétrie cylindrique d'axe parallèle au champ magnétique appliqué et formés par une alternance de couches de ferrofluide et de suspension colloïdale non-magnétique).

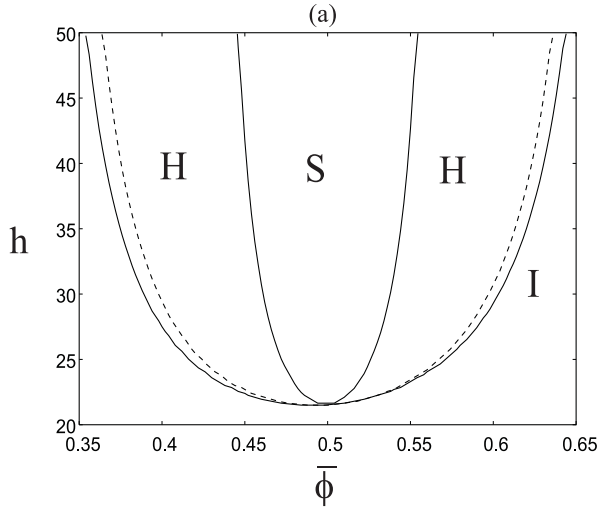

FIGURE 2.1 – *Diagramme de phases dans les coordonnées (h, f) où h est le champ magnétique adimensionné et ϕ est la fraction volumique moyenne de ferrofluide. S désigne la phase lamellaire, H la phase hexagonale, et I la phase isotrope. Les lignes continues représentent des lignes de coexistence et la ligne pointillée est la spinodale. Ce diagramme a été obtenu avec le modèle de gas sur réseau, un diagramme du même type a été réalisé pour un fluide obéissant à l'équation de Carnahan-Starling [7].*

Après ces travaux sur les diagramme de phases des colloïdes magnétiques réalisés pendant mon postdoctorat, j'ai poursuivi au laboratoire PCT l'étude des colloïdes

magnétiques mais avec des matériaux assez différents. L'étude précédente portait sur les ferrofluides classiques, qui sont des nanoparticules solides en suspension dans un solvant, qui peut être soit aqueux soit huileux (non-polaire). A présent, on va s'intéresser à des particules plus grandes constituées d'émulsions de ferrofluide huileux dans l'eau, de 100nm à 500nm de rayon, fabriquées selon un procédé mis au point par J. Bibette du laboratoire de Colloïdes et Matériaux Divisés de l'ESPCI. Lorsqu'un champ magnétique est appliqué, ces particules colloïdales s'auto-organisent sous la forme de chaînes et de façon réversible dans la direction du champ appliqué. La distance entre particules colloïdales au sein de la chaîne résulte d'une compétition entre les interactions dipolaires magnétiques qui sont attractives et à longue portée et les interactions électrostatiques dues aux charges portées par les particules colloïdales qui sont à courte portée et répulsives [9].

Les chaînes formées par ces particules colloïdales forment un réseau unidimensionnel qui diffracte la lumière par diffraction de Bragg. La mesure de la longueur d'onde associée au pic de Bragg, donne accès à la distance interparticule [10]. Comme on connaît par ailleurs le champ appliqué, on peut calculer la force magnétique qui s'exerce entre les billes et donc obtenir la relation force-distance. Ces relations force-distance caractérisent la stabilité de la suspension colloïdale.

2.1.2 Expansion thermique dans une chaîne de particules colloïdales

En collaboration avec J. Baudry de ce même laboratoire, nous avons étudié les fluctuations thermiques des particules colloïdales magnétiques au sein d'une chaîne formée par ces particules [11]. L'importance relative des interactions dipolaires par rapport aux fluctuations thermiques est mesurée par le paramètre sans dimension λ, de sorte que dans l'expérience le paramètre $1/\lambda$ joue le rôle d'une température effective pour ces colloïdes. Un avantage des systèmes colloïdaux est de permettre de changer directement les interactions entre particules, et de permettre une observation directe de chaque particule par vidéomicroscopie. Un autre intérêt est que ces chaînes sont des systèmes quasi-unidimensionnels. Ce type d'expériences serait très difficile à réaliser avec les systèmes condensés unidimensionnels classiquement étudiés en physique des solides (comme les sels de mercure [12] ou les nanotubes de carbone par exemple), à cause des difficultés à contrôler les interactions et à observer chaque particule au sein de ces structures.

Nous avons formulé une analogie entre l'expansion de la chaîne de colloïdes magnétiques et l'expansion thermique présente classiquement dans un solide ordinaire. Dans un solide ordinaire, l'expansion thermique résulte de l'anharmonicité des interactions entre particules au sein du solide [13]. Dans la chaîne de particules colloïdales magnétiques, l'anharmonicité des interactions entre particules voisines conduit également à une expansion, qui se manifeste par une différence entre la position correspondant au minimum du potentiel et celle correspondant à la position moyenne (cf. figure 2.2). On peut voir aussi cet effet comme un mode de fluctuations de la chaîne dans lequel la distance entre particules voisines varie de la même façon pour toutes les particules de la chaîne. Comme la mesure de force repose sur une mesure

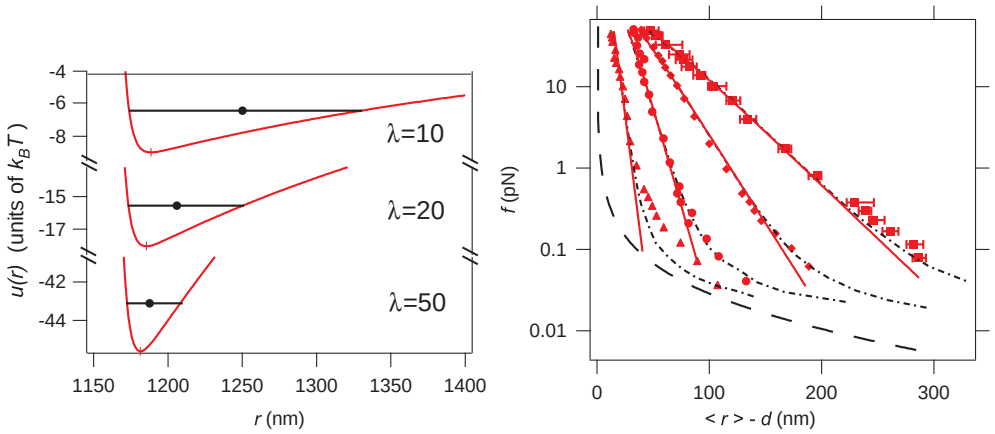

FIGURE 2.2 – *A gauche : Potentiel d'interaction de paire $u(r)$ en unités de k_BT en fonction de la distance r entre les centres de particules colloïdales voisines pour différentes valeurs de $\lambda = 10$, 20 ou 50. Les points noirs représentent la position moyenne, qui diffère de la position du minimum du potentiel. A droite : Force agissant entre particules colloïdales en fonction de la distance moyenne entre les surfaces des particules colloïdales pour différentes valeurs de la force ionique de la solution. Les différents types de symboles représentent des expériences, qui ont été réalisées de gauche à droite pour des forces ioniques décroissantes. Les lignes rouges en trait continu représentent la partie électrostatique de la force, les courbes en pointillés noirs représentent les simulations de Monte Carlo, et la courbe en tirets noirs la plus à gauche représente le cas d'un potentiel de sphère dure.*

de distance relative entre particules voisines, cet effet a des conséquences directes sur les mesures de force par cette technique. Nous avons pu montrer que les fluctuations thermiques introduisent dans les mesures de force une déviation (par rapport au cas limite où le champ magnétique est très fort et où les fluctuations thermiques sont négligeables) dans les courbes force-distance lorsque le champ magnétique est faible (ou, ce qui revient au même, lorsque la distance entre particules voisines devient assez grande). Grâce à des simulations de Monte Carlo, nous sommes parvenus à quantifier cet effet et rendre compte de la déviation observée expérimentalement [11]. Lorsque le champ magnétique est abaissé, la chaîne se dilate et commence à fluctuer jusqu'a se briser, comme un cristal qui d'abord se dilate lorsqu'il est chauffé puis finit par fondre.

Avec le temps, des applications insoupçonnées de l'expérience originale conçue par J. Bibette ont été développées. Par exemple, il est apparu assez vite qu'on pouvait utiliser cette expérience pour appliquer des forces de façon contrôlée sur des biomolécules greffées sur les particules colloïdales magnétiques. Cela a permis d'étudier certaines propriétés élastiques de l'ADN [14] ou de l'actine, d'une façon complémentaire par rapport à ce que l'on sait faire avec des pinces optiques par exemple. On a aussi utilisé cette expérience pour étudier des cinétiques de reconnaissance entre biomolécules liées par des liens polymériques aux colloïdes magnétiques [15], ce qui a conduit au développement d'une application pour le diagnostic médical. Dans une

direction tout à fait différente, R. Dreyfus et ses collaborateurs ont conçu à partir de cette expérience un nageur artificiel en appliquant un champ magnétique alternatif sur la chaîne de particules colloïdales, ce qui a pour effet lorsque la chaîne est asymétrique de créer des ondulations et un mouvement de liquide qui propulse le nageur. Ce nageur colloïdal magnétique [16] a suscité beaucoup d'intérêt de la part des théoriciens et des expérimentateurs intéressés par les applications des colloïdes actifs, capables de s'auto-propulser [17].

2.2 Structures auto-assemblées à base de bâtonnets colloïdaux

Un second exemple de structures formées par auto-assemblage est un gel nématique [18], qui est un gel contenant des particules colloïdales en forme de bâtonnets. Lorsque le gel est assez dense, les bâtonnets peuvent s'orienter et former une phase nématique. Sur la figure 2.3, sont représentées deux types de gels et leurs diagrammes de phase correspondant. Dans les deux cas, des bâtonnets sont inclus dans un réseau de polymères réticulé. Dans le modèle 1 (figure 2.3a), les bâtonnets font partie du réseau qui est constitué de chaînes formées par des bâtonnets rigides reliés entre eux par des chaînes flexibles de polymères. Dans le modèle 2 (figure 2.3b), des bâtonnets rigides et indépendants sont dispersés dans les interstices d'un réseau de polymères flexibles réticulé.

Depuis les travaux de Tanaka [19], on sait expliquer théoriquement l'effondrement d'un gel induit par le changement de qualité du solvant, en utilisant la théorie de Flory pour les gels [20]. Warner et Wang [21] ont étendu ces idées au cas des gels anisotropes en introduisant l'élasticité des élastomères anisotropes. Notre approche a suivi ce traitement de l'élasticité des gels, mais a utilisé la théorie de Onsager [22] pour la transition isotrope-nématique d'un ensemble de bâtonnets. Dans la figure 2.4, est représenté les diagrammes de phase pour les modèles 1 et 2 dans les coordonnées fraction volumique du gel ϕ en fonction de χ, le paramètre caractérisant la qualité du solvant. Les courbes continues en gras représentent les isobares à la pression osmotique Π, qui présentent une discontinuité pour une valeur particulière de χ. L'isobare $\Pi = 0$ joue un rôle particulier puisque c'est lui qui définit la stabilité du gel en l'absence de contraintes mécaniques appliquées au gel. Le collapse du gel dans ce modèle est différent du scénario classique de Tanaka [19], car ici c'est la transition isotrope-nématique qui induit le collapse. Il est intéressant de remarquer que le diagramme de phase présente des analogies avec le diagramme de phase d'un système de bâtonnets avec des interactions attractives (induites par des interactions de déplétion par exemple). Le modèle 2 présente en outre deux caractéristiques nouvelles que sont la possibilité d'une coexistence entre deux phases isotropes ou deux phases nématiques.

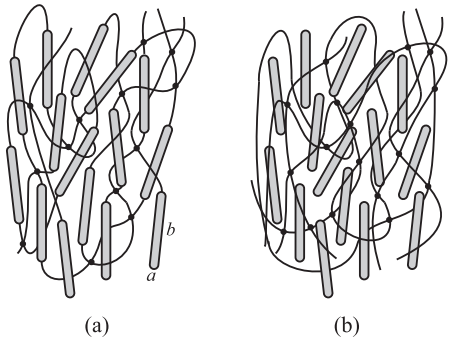

FIGURE 2.3 – *Représentation des gels nématiques pour les modèles 1 pour la figure a et modèle 2 pour la figure b [18].*

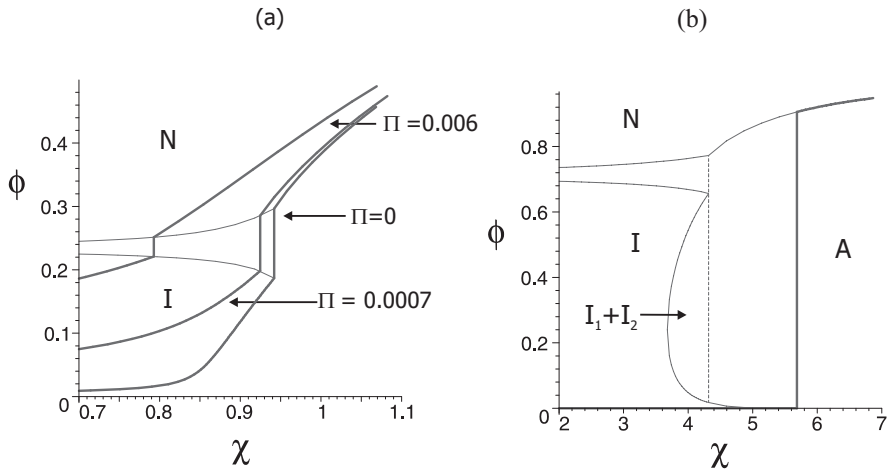

FIGURE 2.4 – *(a) : diagramme de phase du modèle 1 en fonction de la fraction volumique du réseau de polymères ϕ et du paramètre de Flory-Huggins χ. (b) : diagramme de phase pour le modèle 2, qui montre la coexistence entre deux phases isotropes I_1 et I_2.*

Bibliographie

[1] M. J. Stevens and G. S. Grest. Evolution of disorder in magnetic stripe domains. Transverse instabilities and disclination unbinding in lamellar structures. *Phys. Rev. A*, 72(23) :3686–9, 1992.

[2] M. Doi and S. F. Edwards. *The Theory of Polymer Dynamics*. Oxford University Press, London, 1979.

[3] A. Cebers. Transformation of the concentration domain structures of liquid magnetics in plane layers. *Magnetohydrodynamics*, 31(1,2) :58–72, 1995.

[4] D. Andelman, F. Brochard, and J-F. Joanny. Phase transitions in Langmuir monolayers of polar molecules. *J. Chem. Phys.*, 86(6) :3673–81, 1987.

[5] T. Garel and S. Doniach. Phase transitions with spontaneous modulation - the dipolar Ising ferromagnet. *Phys. Rev. B*, 26(1) :325–9, 1982.

[6] L. Leibler. Theory of Microphase separation in block copolymers. *Macromolecules*, 13 :1602, 1980.

[7] D. Lacoste and T. C. Lubensky. Phase transitions in a ferrofluid at magnetic-field-induced microphase separation. *Phys. Rev. E*, 64(4) :041506, 2001.

[8] M. F. Islam, K. H. Lin, D. Lacoste, T. C. Lubensky, and A. G. Yodh. Field-induced structures in miscible ferrofluid suspensions with and without latex spheres. *Phys. Rev. E*, 67(2) :021402, 2003.

[9] F. Leal Calderon, T. Stora, O. Mondain Monval, P. Poulin, and J. Bibette. Direct measurement of colloidal forces. *Phys. Rev. Lett.*, 72(18) :2959–2962, 1994.

[10] R. Dreyfus, D. Lacoste, J. Bibette, and J. Baudry. Measuring colloidal forces with the magnetic chaining technique. *Eur. Phys. J. E*, 28(2) :113–123, 2009.

[11] D. Lacoste, C. Brangbour, J. Bibette, and J. Baudry. Thermal expansion within a chain of magnetic colloidal particles. *Phys. Rev. E*, 80 :011401, 2009.

[12] P. M. Chaikin and T. Lubensky. *Principles of condensed matter physics*. Cambridge University Press, 1995.

[13] P. M. Ma. *Statistical Physics*. Cambridge University Press, 1995.

[14] A. Koenig, P. Hebraud, C. Gosse, R. Dreyfus, J. Baudry, E. Bertrand, and J. Bibette. Magnetic force probe for nanoscale biomolecules. *Phys. Rev. Lett.*, 95(12), 2005.

[15] L. Cohen-Tannoudji, E. Bertrand, J Baudry, C. Robic, C. Goubault, M. Pellissier, A. Johner, F. Thalmann, N. K Lee, C. M. Marques, and J. Bibette. Measuring the kinetics of biomolecular recognition with magnetic colloids. *Phys. Rev. Lett.*, 100(10) :108301, 2008.

[16] R. Dreyfus, J. Baudry, M. L. Roper, M. Fermigier, and H. A. Stone. Microscopic artificial swimmers. *Nature*, 437 :862, 2005.

[17] Jonathan R. Howse, Richard A. L. Jones, Anthony J. Ryan, Tim Gough, Reza Vafabakhsh, and Ramin Golestanian. Self-motile colloidal particles : From directed propulsion to random walk. *Physical Review Letters*, 99(4) :048102, 2007.

[18] D. Lacoste, A.W.C. Lau, and T.C. Lubensky. Phase transitions in lyotropic nematic gels. *Eur. Phys. J. E*, 8(4) :403–411, 2002.

[19] T. Tanaka. Collapse of gels and the critical endpoint. *Phys. Rev. Lett.*, 40(12) :820, 1978.

[20] P. J. Flory. *Principles of Polymer Chemistry*. Cornell University Press, London, 1953.

[21] M. Warner and X. J. Wang. Phase-equilibria of swollen nematic elastomers. *Macromolecules*, 25 :445, 1992.

[22] L. Onsager. The effects of shape on the interaction of colloidal particles. *Ann. N. Y. Acad. Sci.*, 51 :627, 1949.

Chapitre 3

Applications de la physique statistique à des systèmes biologiques

> « Un système vivant est un système ouvert et pourtant stable. On peut le comparer à une flamme. »
>
> L. Brillouin, *Vie, matière et observation.*

> « What I wish to make clear in this last chapter is, in short, from all we have learnt about the structure of living matter, we must be prepared to find it working in a manner that cannot be reduced to the ordinary laws of physics. And that not on the ground that there is any 'new force' or what not, directing the behavior of the single atoms within a living organism, but because the construction is different from anything we have yet tested in the physical laboratory. »
>
> E. Schrödinger, *What is life.*

Une cellule biologique est un système ouvert intrinsèquement hors d'équilibre, puisque cette cellule ne se maintient en vie que précisément que par des réactions chimiques qui impliquent des flux de matière (acides aminés, ATP, eau, ions..) entre l'intérieur de la cellule et le milieu extérieur. A cause de ces échanges, une cellule vivante peut être décrite en première approximation comme étant dans un état stationnaire hors d'équilibre, typiquement loin de l'équilibre thermodynamique. Dans la suite, on présente trois classes de systèmes : (i) des systèmes biomimétiques à base de membranes lipidiques, (ii) des moteurs moléculaires, et (iii) des filaments d'actine ou de microtubules, qui illustrent chacun d'une façon différente certaines propriétés hors d'équilibre associés aux systèmes vivants.

3.1 Systèmes biomimétiques à base de membranes lipidiques

3.1.1 Membrane lipidique couplée à un cytosquelette

Depuis quelques décennies, les membranes lipidiques, artificielles ou biologiques ont suscité beaucoup d'intérêt. Depuis les travaux d'Helfrich, il est bien connu que les fluctuations de ces membranes sont dominées par le module de courbure κ, ce qui conduit à un spectre de fluctuations pour ces membranes proportionnel à $(\kappa q^4 + \sigma q^2)^{-1}$, où σ désigne la tension de surface. Lorsque la membrane interagit avec d'autres systèmes (par exemple un substrat rigide, une autre membrane, un réseau de polymères ou de filaments, ou contient des inclusions comme des protéines), le spectre est modifié et la situation est plus complexe à analyser.

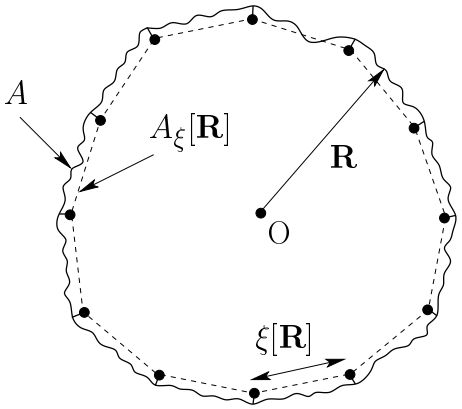

FIGURE 3.1 – Section d'une vésicule fluctuante (trait plein) à laquelle est attaché un réseau de ressorts (lignes pointillées), dont la taille de la maille est ξ. L'aire de la membrane est A, l'aire du réseau est A_ξ [1].

On rappelle que le cytosquelette est un réseau de polymères réticulé qui donne à une cellule biologique sa rigidité. Dans la Ref. [1], un modèle simple de membrane lipidique couplée à un cytosquelette est présenté et étudié. Dans ce modèle, le cytosquelette est décrit comme un réseau régulier hexagonal de ressorts entropiques connectés en certains points à la membrane comme indiqué sur la figure 3.1. Dans les globules rouges, ce réseau est constitué de polymères flexibles appelés spectrine. Nous avons utilisé ce modèle pour analyser des mesures du spectre de fluctuations des membranes de globules rouges par Reflexion Interference Contrast Microscopy (RICM) réalisées par le groupe de E. Sackmann en 1987. En dépit du bruit qui est important dans ces mesures, l'allure de ces spectres suggère l'existence d'un saut de tension à un vecteur d'onde correspondant à la maille du réseau de spectrine en bon accord avec le modèle théorique.

Il est important de rappeler que dans le modèle théorique justement, la membrane est traitée comme une membrane à l'équilibre, alors que dans les systèmes réels comme une cellule biologique ce n'est certainement pas le cas, puisque le cy-

tosquelette introduit de nombreux effets hors d'équilibre dans ce système, dont nous allons reparler dans ce chapitre. De plus, le réseau de filaments de spectrine qui couvre la surface des globules rouges contient de nombreux défauts et on peut se demander quels effets ont ces défauts sur le spectre de fluctuations de la membrane. Ces deux questions ont été abordées dans la thèse de C. Dubus encadrée par JB. Fournier [2].

3.1.2 Dynamique des fluctuations de membranes actives

Les membranes actives sont des membranes lipidiques contenant des inclusions, en général des protéines comme des canaux à ions ou des pompes qui produisent des forces sur la membrane et modifient les fluctuations de la surface de la membrane. Sur le plan théorique, il y a deux approches principales pour décrire ces membranes actives : le modèle de Prost-Bruinsma (PB) [3] introduit des forces hors d'équilibre sous la forme d'un bruit actif, qui inclut la diffusion et la nature stochastique (bruit de shot-noise) des pompes mais ne tient pas compte du couplage entre les pompes et la courbure de la membrane. Un autre modèle proposé par Ramaswamy, Toner et Prost (RTP) [4] incorpore ce couplage mais ignore la nature stochastique du fonctionnement des pompes. Pour des mesures stationnaires, comme celles réalisées dans les expériences de micropipettes, le modèle RTP décrit très bien les expériences. Dans la Ref. [5], certaines propriétés dynamiques du modèle RTP sont analysées, et il est montré qu'il est important d'inclure le shot noise pour les mesures dynamiques. Deux variantes du modèle RTP sont développées qui incluent le shot noise et les effets de couplage à la courbure. Dans le premier modèle, qui est un modèle pour les pompes du type bactériorhodopsine, les forces actives fluctuent sur une échelle de temps plus courte que le temps caractéristique des fluctuations de la membrane. Dans le second modèle, qui est un modèle à deux états pour les canaux à ions, les transitions entre états on et off se produisent sur une échelle de temps longue par rapport au temps caractéristique des fluctuations de la membrane. Ces deux variantes sont deux extensions naturelles du modèle RTP et elles ont des comportements dynamiques distincts. Dans le modèle à deux états, le déplacement quadratique moyen d'un point situé sur la membrane suit une loi de superdiffusion en $t^{5/3}$ à temps courts alors que le modèle RTP prédirait un comportement sous-diffusif dans les mêmes conditions.

Au moment où l'étude [5] a été réalisée, il n'existait pas d'expériences permettant de mesurer des quantités dynamiques liées aux fluctuations des membranes actives (comme les fonctions de corrélation temporelles de la hauteur de la membrane), c'était donc un travail à caractère complètement prédictif. A présent, des expériences sont en cours de réalisation à l'Institut Curie par T. Betz du groupe de C. Sykes. Ces expériences permettent de mesurer ces fonctions de corrélation temporelles pour des globules rouges ou pour des membranes actives artificielles et devraient donc conduire à des comparaisons intéressantes avec les modèles théoriques.

3.1.3 Membrane lipidique traversée par des courants ioniques

Pour décrire théoriquement les membranes actives, le point de départ de nombreuses études est un modèle de membrane à l'équilibre auquel on ajoute des forces actives hors d'équilibre, dont la forme est dictée par des considérations de symétrie [4, 6, 7]. Une limitation de ce type d'approche est que ces forces actives contiennent typiquement des coefficients phénoménologiques, qui ne sont pas a priori connus et qui peuvent s'avérer difficiles à mesurer. Une autre limitation tient à ce que ces forces actives ne sont pas dérivées d'une approche incorporant les effets électrostatiques ou électrocinétiques présents dans le problème. Ces effets sont impliqués dans les changements de conformation des protéines et dans le transport d'ions à travers la membrane, et devraient donc être pris en compte dans une approche plus complète du fonctionnement des pompes ou canaux à ions. Pour tenter de surmonter ces limitations, nous nous sommes intéressés à des modèles de type Poisson-Nernst-Planck qui permettent de prendre en compte au moyen d'équations électrocinétiques les flux et les concentrations des ions dans tout le système. Cette approche permet d'éviter l'introduction de termes phénoménologiques pour décrire les forces actives qui résultent du transport des ions [4, 6, 7].

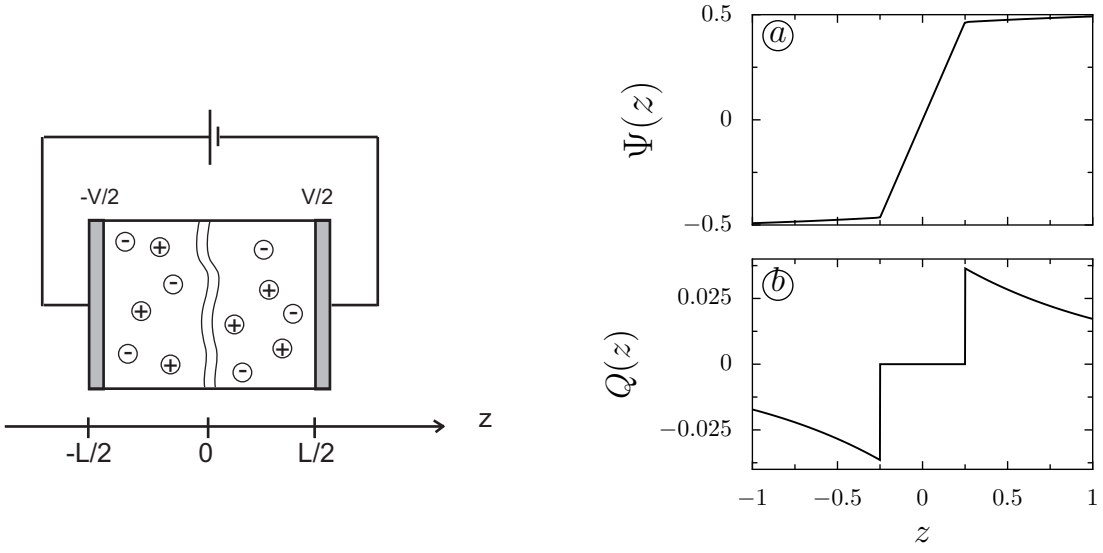

FIGURE 3.2 – A gauche : Schéma représentant une membrane lipidique quasi-plane placée dans un electrolyte. La bicouche (membrane) est représentée par les deux lignes fluctuantes situées près du plan $z = 0$. Un potentiel V est appliqué sur les électrodes situées de part et d'autre de la membrane, et séparées par une distance L. A droite : (a) potentiel électrostatique en fonction de z (la distance z est exprimée en unités de la longueur de Debye, qui est ici de 2.4 nm), et (b) distribution de charges associée (également adimensionnée). On note que l'essentiel de la différence de potentiel se produit aux bornes de la membrane, et que la charge est nulle à l'intérieur de la membrane.

Dans les Refs. [8, 9, 10], nous avons considéré théoriquement une membrane électriquement neutre contenant une distribution homogène de canaux à ions dans

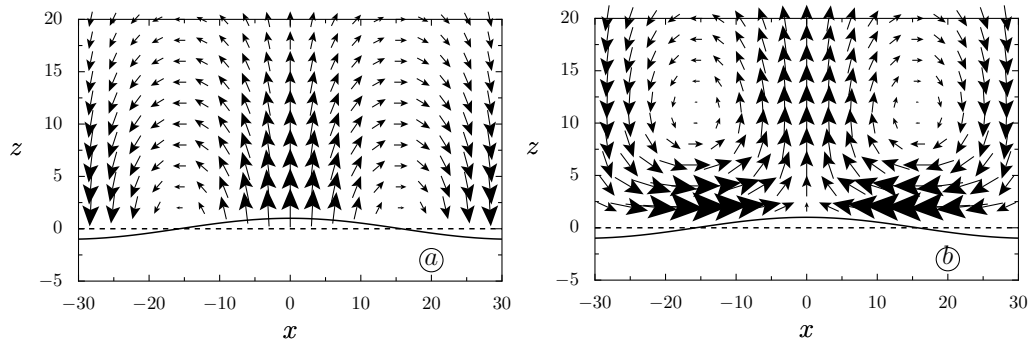

FIGURE 3.3 – Écoulement de fluide autour d'une membrane dans le plan (z, x). (a) Mode de courbure d'une membrane avec l'écoulement de fluide correspondant, en l'absence de champ électrique appliqué. Dans ce cas, c'est la déformation de la membrane qui crée l'écoulement de fluide. (b) Membrane et écoulement correspondant lorsqu'un champ électrique normal à la membrane est appliqué. L'écoulement résulte de l'application du champ électrique sur les charges induites accumulées au voisinage de la membrane (electro-osmose de charges induites ou ICEO). Contrairement au cas (a), ici c'est l'écoulement qui est responsable de la déformation de la membrane. Dans les deux figures, l'unité de longueur est la longueur de Debye.

une solution d'electrolyte (cf. schéma 3.2). Un courant constant traverse cette membrane, que l'on suppose, pour un type d'ion donné, proportionnel à la différence de potentiel chimique de l'ion considéré entre les deux cotés de la membrane. Dans cette géométrie plane, on peut résoudre analytiquement à la fois les équations électrocinétiques linéarisées dans l'approximation de Debye-Hückel et les équations de Stokes caractérisant l'hydrodynamique du fluide environnant à bas nombre de Reynolds. A partir de là, une méthode de perturbations permet de calculer les fluctuations de la membrane par rapport à un état de référence plan. Cette méthode est appliquée au cas d'une membrane d'épaisseur et de constante dielectrique nulle puis au cas plus réaliste d'une membrane d'épaisseur et de constante dielectrique finies. En fait, seul ce dernier cas rend compte du signe correct de la distribution de charge au voisinage de la membrane et des effets capacitifs qu'on souhaite décrire. De plus, nous avons montré que le modèle d'épaisseur finie fournit une estimation correcte des corrections électrocinétiques aux modules élastiques de la membrane et est compatible avec le spectre de fluctuations des membranes actives de la figure 3.4.

Les équations électrocinétiques permettent également d'obtenir le profil de l'écoulement de fluide autour de la membrane, qui est représenté sur la figure 3.3. Cette figure montre que dans certaines conditions, un écoulement significatif peut être généré sur une épaisseur de l'ordre de la longueur de Debye au voisinage de la membrane. Cette vitesse de glissement du fluide par rapport à la membrane, est due à la composante parallèle au plan de la membrane du champ électrique, agissant sur les charges présentes dans les couches de Debye. Cette vitesse de glissement peut se calculer par la relation de Smoluchowski. Cet effet électro-osmotique est similaire à celui qui existe de façon générale au voisinage d'une surface polarisable lorsqu'un

champ électrique alternatif ou continu est appliqué. Comme le champ électrique agit sur des charges induites par ce même champ électrique, l'effet est quadratique donc non-linéaire dans le champ appliqué. Les écoulements électro-osmotiques de charges induites (ICEO) sont le sujet d'études poussées dans le contexte d'applications en microfluidique [11, 12].

Les équations électrocinétiques dans le cas d'une membrane d'épaisseur et de constant dielectrique finies sont assez complexes et doivent être résolues numériquement. Toutefois, nous avons montré très récemment [10], qu'il est possible de modifier les conditions aux limites pour le potentiel électrostatique sur la membrane, d'une façon qui permet de décrire très correctement et analytiquement, la densité de charge et les corrections électrocinétiques aux modules élastiques de la membrane. Cette approche a l'avantage de permettre de conserver la simplicité de l'approximation d'épaisseur nulle pour la membrane, sur laquelle repose l'essentiel des travaux théoriques sur les membranes fluides. Cette méthode est suffisamment simple à mettre en oeuvre pour servir de point de départ à d'autres généralisations, qui pourraient inclure par exemple divers effets non-linéaires. Les effets non-linéaires intéressants dans ce contexte sont les effets élastiques non-linéaires de la membrane, la réponse non-linéaire courant-tension des canaux à ions inclus dans la membrane, et les effets électrostatiques non-linéaires associés à la présence d'une charge ou d'un potentiel élevée au voisinage de la membrane.

3.1.4 Spectre de fluctuations de membranes actives

Des expériences de diffusion de la lumière par les bords des membranes de globules rouges indiquent que ces fluctuations ne peuvent être décrites uniquement par des fluctuations thermiques. Il y a donc en plus de la contribution thermique dite passive, une autre contribution active/hors d'équilibre due au cytosquelette. Pour mettre en évidence ces différentes contributions dans les fluctuations, l'idéal serait de disposer d'un système permettant d'annuler ou de maintenir l'activité des pompes de façon à comparer directement le système actif avec le système passif pour une même cellule dans les mêmes conditions. On peut en fait réaliser ce type d'expériences avec des membranes actives, étudiées expérimentalement par le groupe de P. Bassereau depuis 1995 environ à l'Institut Curie. Ces membranes actives sont des membranes lipidiques unilamellaires géantes contenant des protéines activables, comme la bactériorhodopsine (BR). Cette protéine subit des changements de conformation lorsqu'elle éclairée avec une longueur d'onde appropriée, ce qui se traduit par le transport d'un proton entre l'intérieur et l'extérieur de la membrane, d'où le terme de pompe à protons. La BR n'utilise pas l'hydrolyse de l'ATP à la différence d'autres pompes, comme la Ca^{2+}-ATPase dont l'activité résulte de l'énergie libérée par la réaction d'hydrolyse de l'ATP, et qui transfère des ions Ca^{2+} à la place des protons.

Le groupe de P. Bassereau a d'abord étudié ces membranes actives au moyen de la technique de micropipettes [13], et ce n'est que très récemment que les premières mesures directes du spectre de fluctuations de vésicules géantes contenant de la bactériorhodopsine (BR) ont été réalisées par la technique de video-microscopie

[14]. Les deux types de mesures sont complémentaires. Lorsque les pompes sont activées par une lumière de longueur d'onde appropriée, on observe globalement une diminution significative du spectre de fluctuations, ce qui indique que l'activité des pompes augmente les fluctuations de la vésicule. D'autre part, on observe que l'effet est maximum dans une région de petit vecteur d'onde (cf. figure 3.4), ce que nous interprétons comme une diminution de la tension de membrane due à l'activité des pompes. Cette correction de tension liée à l'activité des pompes à ions n'aurait pas pu être mesurée par la technique de micropipettes, car dans cette technique la tension est fixée par l'expérimentateur. Au contraire dans les mesures par vidéomicroscopie, la mesure ne correspond pas au même ensemble thermodynamique et on peut définir dans ce cas une correction de tension. Nous présentons dans la Ref. [14] une approche commune pour décrire l'activité des pompes, qui permet de rendre compte à la fois des mesures de micropipettes et des mesures de vidéo-microscopie. Nous proposons que la diminution de la tension de membrane due aux processus actifs est provoquée par les contraintes de Maxwell associée aux charges présentes dans les couches de Debye. Ces charges s'accumulent à cet endroit par un effet électrocinétique, similaire à celui décrit dans la sous-section précédente [9].

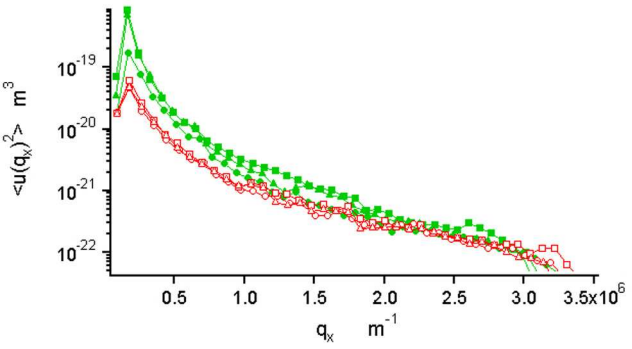

FIGURE 3.4 – Spectre de fluctuations d'une vésicule géante unilamellaire (GUV) contenant de la bactériorhodopsine. Les symboles vides en rouges correspondent à trois spectres passifs enregistrés consécutivement et les symboles pleins en vert correspondent à trois spectres consécutifs actifs [14].

3.2 Modèles stochastiques de moteurs moléculaires

Les moteurs moléculaires sont des enzymes capables de transformer l'énergie chimique issue de la réaction d'hydrolyse de l'ATP en énergie mécanique. Il existe une grande diversité de moteurs moléculaires regroupés au sein de différentes familles. Les principales familles sont les moteurs linéaires comme la kinésine, la myosine ou la RNA polymérase, et les moteurs rotatifs comme le moteur F_0/F_1. Les recherches dans ce domaine ne visent pas seulement à mieux comprendre le fonctionnement de ces moteurs pour des applications en biologie, il s'agit aussi par ces études de

préparer le développement de nanomachines artificielles capables de remplir des fonctions similaires.

Sur le plan théorique, les moteurs moléculaires ont été décrits principalement par des modèles de type ratchet [15, 16] ou par des approches fondées sur des équations maîtresses dans un espace discret [17, 18]. Nous avons utilisé ces deux approches, la seconde dans les Refs. [19, 20], puis la première dans la Ref. [21]. L'ensemble de ce travail a fait l'objet d'un article de revue soumis très récemment à la revue Séminaires Poincaré [22]. Dans ce qui suit, nous présentons d'abord le modèle de flashing ratchet [15, 23, 24], car ce modèle contient en fait une infinité de modèles discrets du type de ceux de [21].

Dans le modèle de flashing ratchet, le moteur a deux états internes $i = 1, 2$, décrits par deux potentiels indépendants du temps $U_i(x)$, périodiques de période a, comme représenté à la figure 3.5. La probabilité que le moteur soit à la position x au temps t et dans l'état i est $P_i(x,t)$. La dynamique du modèle est décrite par

$$\begin{aligned} \frac{\partial P_1}{\partial t} + \frac{\partial J_1}{\partial x} &= -\omega_1(x)P_1 + \omega_2(x)P_2 \\ \frac{\partial P_2}{\partial t} + \frac{\partial J_2}{\partial x} &= \omega_1(x)P_1 - \omega_2(x)P_2\,, \end{aligned} \tag{3.1}$$

où les taux $\omega_1(x)$ et $\omega_2(x)$ sont des taux de transitions dépendant de l'espace, et les courants locaux J_i sont définis par :

$$J_i = -D_0 \left(\frac{\partial P_i}{\partial x} + \frac{1}{k_B T} \left(\frac{\partial U_i}{\partial x} - F \right) P_i \right), \tag{3.2}$$

avec D_0 le coefficient de diffusion du moteur et F une force non-conservative agissant sur le moteur. Les taux de transitions peuvent être modélisés par les lois habituelles de la cinétique chimique appliquées à chaque chemin réactionnel [23] (pour une discussion plus précise de cette paramétrisation des taux de transitions voir l'article de revue de la Ref. [22]) :

$$\begin{aligned} \omega_1(x) &= [\omega(x) + \psi(x)e^{\Delta\mu}]e^{(U_1(x)-fx)/k_BT}, \\ \omega_2(x) &= [\omega(x) + \psi(x)]e^{(U_2(x)-fx)/k_BT}, \end{aligned} \tag{3.3}$$

où $\Delta\mu = \Delta\tilde{\mu}/k_BT$ est le potentiel chimique normalisé, $\Delta\tilde{\mu}$ le potentiel chimique associé à l'hydrolyse de l'ATP et $f = Fa/k_BT$ est la force normalisée. On distingue les termes proportionnels à $\omega(x)$ correspondant à des transitions thermiques, des termes proportionnels à $\psi(x)$ correspondant à des transitions induites par l'hydrolyse de l'ATP. Lorsque $F = 0$ et $\Delta\mu = 0$, le système est à l'équilibre car la relation de bilan détaillée est vérifiée

$$\frac{\omega_2(x)}{\omega_1(x)} = \exp\left(\frac{U_2 - U_1}{k_B T} \right). \tag{3.4}$$

Dans ce cas, les probabilités stationnaires P_1 et P_2 sont données par la distribution de Boltzmann, les courants J_1 et J_2 s'annulent et il n'y a pas de déplacement global

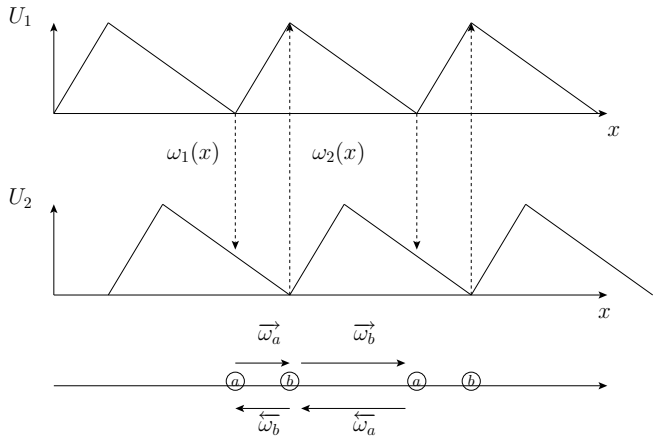

FIGURE 3.5 – Les deux courbes du haut représentent les deux potentiels $U_1(x)$ et $U_2(x)$ du modèle de flashing ratchet. Pour chaque position x, des transitions verticales sont possibles entre les deux états internes avec des taux $\omega_1(x)$ et $\omega_2(x)$. Le modèle discret correspondant est représenté au dessous. Il est obtenu en considérant les transitions effectives entre le minimum du potentiel 1 (état a) et celui du potentiel 2 (état b), caractérisées par les taux de transitions indiqués dans la figure du bas.

du moteur. Lorsque F et $\Delta\mu$ ne sont pas simultanément nuls, le système est hors d'équilibre et des courants sont présents.

A partir de ce modèle continu, on peut construire un modèle discret effectif [25], comme indiqué sur la figure 3.5. Dans chacun des potentiels, les transitions vers le minimum du potentiel sont supposées être instantanées, de sorte que le moteur a un temps de résidence nul dans tous les états qui ne sont pas des minima de $U_1(x)$ ou $U_2(x)$. Les transitions entre potentiels, représentées par des lignes pointillées, ont lieu avec des taux finis $\omega_1(x)$ et $\omega_2(x)$ mais seulement en des points qui sont à la même position x. Comme certaines transitions se produisent instantanément, des transitions ne se produisent de façon effective qu'entre le minimum de $U_1(x)$ et le minimum de $U_2(x)$, d'où la représentation par un modèle discret à 1D avec des transitions entre sites pairs et impairs notés a et b (correspondant aux minima de chaque potentiel) comme indiqué sur la figure. L'avantage de la formulation discrète est de permettre une description mathématique plus poussée tout en conservant l'essentiel du modèle original [17, 26, 18]. En ce sens, le modèle à deux états construit de cette façon est un modèle de ratchet *minimal*.

En dépit de sa simplicité, ce modèle permet de rendre compte de mesures de vitesses moyennes $\bar{v}$ d'une kinésine en fonction de la force ou de la concentration en ATP [27]. On peut aussi obtenir dans les mêmes conditions le taux moyen de consommation d'ATP, $\bar{r}$. A partir de ces grandeurs, nous avons réalisé un diagramme de fonctionnement, qui résume les différents régimes thermodynamiques possibles pour ce moteur [19]. C'est un diagramme qui est similaire à celui discuté dans la Ref. [15], mais qui est étendu au régime loin de l'équilibre. Ce diagramme montre que dans les conditions usuelles, la kinésine utilise l'énergie chimique issue de l'hydrolyse de l'ATP pour réaliser un travail mécanique, plutôt que de fonctionner dans l'autre

sens en synthétisant de l'ATP. Nous avons aussi analysé l'efficacité thermodynamique, définie comme le rapport entre le travail mécanique délivré sur l'énergie chimique consommée par le moteur. La kinésine opère de façon la plus efficace dans une échelle d'énergie correspondant à l'énergie libérée par la réaction d'hydrolyse de l'ATP (qui correspond dans les conditions physiologiques à $\Delta\mu \simeq 10 - 25$). Le maximum d'efficacité correspond à $40 - 60\%$, il est atteint autour d'un point isolé de coordonnées $(f, \Delta\mu)$, et la valeur de cette efficacité maximale est en accord avec des mesures récentes.

A ce point de l'analyse, on est en droit de se demander si un modèle aussi simple avec seulement deux états, peut réellement décrire toutes les propriétés dynamiques d'un moteur comme la kinésine. En fait, bien que le modèle à deux états suffise à décrire parfaitement les courbes de vitesse en fonction de la force et de la concentration en ATP, un modèle plus complet est nécessaire pour décrire les fluctuations de ce moteur [17]. Davantage d'états ou des ingrédients supplémentaires (comme l'effet des contraintes mécaniques sur les taux de transitions par exemple) sont également nécessaires pour décrire précisément la succession des changements de conformations du moteur, comme l'alternance des deux "têtes" du moteur dans sa marche sur le filament. Parmi les modèles plus complets de moteur moléculaire, on peut citer la Ref. [18] qui contient un modèle de la kinésine à 9 états, et la Ref. [28] qui contient un modèle très complet de la myosine V avec 7 états.

3.2.1 Moteurs moléculaires et relations de fluctuations

Les relations de Fluctuations quantifient les échanges d'énergie entre un système et son environnement, lorsque le système est dans un état hors d'équilibre [29, 30]. Ces relations s'appliquent arbitrairement loin de l'équilibre thermodynamique dans un régime, où les approches thermodynamiques usuelles, valables au voisinage de l'équilibre, ne s'appliquent pas. Depuis leur découverte il y a une dizaine d'années [31, 32, 33], ces relations ont suscité beaucoup d'intérêt pour comprendre et élucider leurs implications. Cet engouement a au moins le mérite de raviver de vieilles questions comme celles liées à l'origine de l'irréversibilité ou du second principe de la thermodynamique.

Pour des systèmes de petite taille (pour lesquels les fluctuations sont importantes, ce qui est le cas avec les moteurs moléculaires), ces relations imposent des contraintes particulières sur leur fonctionnement [34, 35], qu'on peut en principe tester expérimentalement. Sur le plan expérimental justement, des vérifications de ces relations ont été réalisées avec des biopolymères ou avec des particules colloïdales piégées avec des pinces optiques [36, 30]. Ces expériences ont montré par exemple qu'il est possible d'extraire des différences d'énergie libre à partir de processus irréversibles. Cependant, il est bon de noter que dans tous ces exemples, les expériences ont été conçues de façon à vérifier les relations de Fluctuations. Au contraire, le cas des moteurs moléculaires est particulièrement intéressant car c'est un système qui n'a pas été conçu dans ce but et qui est donc étudié dans ses conditions normales de fonctionnement.

La dynamique d'un moteur moléculaire viole le bilan détaillé, et conduit à un

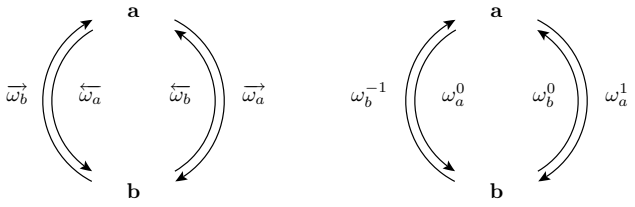

FIGURE 3.6 – Cycles associés avec l'évolution du moteur dans le modèle discret à deux états. A gauche est représenté le cycle pour la variable de position n ; cette longueur n parcourue par le moteur représente la moitié du nombre de tours parcourus le long du cycle (le facteur 1/2 vient de ce que la période du moteur représente deux fois l'unité du réseau sur lequel évolue le moteur). A droite est représenté le cycle pour la variable chimique y.

état stationnaire hors d'équilibre caractérisé par des courants non-nuls mais indépendants du temps. A chacun de ces courants, on peut associer un cycle (appelé aussi "boucle irreversible" par certains auteurs). La construction de ces cycles, et la manière d'associer des courants à ces cycles sont expliqués par une théorie générale des systèmes obéissant à une équation maîtresse [37, 38]. Un des résultats principaux de cette théorie est la relation suivante

$$\frac{\Pi^+(\mathcal{L})}{\Pi^-(\mathcal{L})} = \frac{J^+}{J^-} = e^{A/k_BT}, \tag{3.5}$$

où $\Pi^+(\mathcal{L})$ désigne le produit des constantes de réaction correspondant aux différentes transitions du cycle $\mathcal{L}$ parcouru dans le sens direct, et $\Pi^-(\mathcal{L})$ désigne le produit des constantes de réactions correspondant aux différentes transitions dans le sens opposé. On a noté J^+ le nombre de cycles parcourus par unité de temps dans le sens direct, et J^- le nombre de cycles parcourus par unité de temps dans le sens indirect, de sorte que le courant associé globalement au cycle est $J = J^+ - J^-$. La quantité A porte les noms d'affinité ou de force thermodynamique. Cette affinité est la dérivée du potentiel effectif, auquel doit être soumis un marcheur aléatoire satisfaisant le bilan détaillé de façon à retrouver la même dynamique [20]. Lorsque la relation de bilan détaillé est vérifiée, $\Pi^+(\mathcal{L}) = \Pi^-(\mathcal{L})$, le potentiel effectif est plat et $A = J = 0$. Dans le cas simple où le cycle considéré ne contient que deux états comme dans la figure 3.6, la relation 3.5 conduit à l'affinité suivante $A/k_BT = -2\Psi$ avec Ψ défini par

$$\Psi = \frac{1}{2}\ln\left(\frac{\overleftarrow{\omega}_a\overleftarrow{\omega}_b}{\overrightarrow{\omega}_a\overrightarrow{\omega}_b}\right), \tag{3.6}$$

et le courant associé J est ici la vitesse moyenne du moteur

$$\bar{v} = 2\frac{\overrightarrow{\omega}_a\overrightarrow{\omega}_b - \overleftarrow{\omega}_a\overleftarrow{\omega}_b}{\overrightarrow{\omega}_a + \overrightarrow{\omega}_b + \overleftarrow{\omega}_a + \overleftarrow{\omega}_b}. \tag{3.7}$$

Afin de décrire plus précisément la dynamique de ce système, considérons à présent $P_i(n,t)$, la probabilité que le moteur soit au temps t, au site i $(= a, b)$ et

à la position n (avec $x = nd$ où d est la distance entre les sites a et b). A cause de la périodicité du problème, on introduit les fonctions génératrices $F_i(\lambda, t) \equiv \sum_n e^{-\lambda n} P_i(n,t)$, qui évoluent selon : $\partial_t F_i = \mathcal{M}_{ij}\, F_j$, où $\mathcal{M}[\lambda]$ est une matrice 2×2 construite à partir de l'équation maîtresse satisfaite par $P_i(n,t)$:

$$\mathcal{M}[\lambda] = \begin{bmatrix} -\overrightarrow{\omega_a} - \overleftarrow{\omega_a} & e^{\lambda}\,\overleftarrow{\omega_b} + e^{-\lambda}\,\overrightarrow{\omega_b} \\ e^{\lambda}\,\overleftarrow{\omega_a} + e^{-\lambda}\,\overrightarrow{\omega_a} & -\overleftarrow{\omega_b} - \overrightarrow{\omega_b} \end{bmatrix}.$$

A temps long, les propriétés stationnaires du moteur peuvent être obtenues grâce à la plus grande valeur propre $\vartheta[\lambda]$ de cette matrice. En effet pour $t \to \infty$,

$$\left\langle\, e^{-\lambda n} \,\right\rangle = \sum_i F_i(\lambda, t) \sim \exp\left(\vartheta\, t\right). \tag{3.8}$$

La dérivée première de ϑ par rapport à λ donne la vitesse du moteur $\bar{v}$, la dérivée seconde donne le coefficient de diffusion du moteur.

A partir de l'expression explicite de cette valeur propre, on montre la propriété suivante

$$\vartheta(\lambda) = \vartheta(-\Psi - \lambda), \tag{3.9}$$

qui est une relation de Fluctuation (symétrie de Gallavotti-Cohen). D'autres formes équivalentes de cette relation peuvent être obtenues. L'une d'elle fait intervenir la fonction de grande déviation du courant v, $G(v)$ calculée explicitement pour ce modèle dans la Ref. [20]. Cette fonction a une forme analytique compliquée et non-linéaire, mais elle vérifie une relation étonnamment simple :

$$G(v) - G(-v) = \Psi v. \tag{3.10}$$

Cette relation implique que le rapport des probabilités pour observer une vitesse v ou $-v$ au bout d'un temps t doit satisfaire la relation :

$$\frac{\mathcal{P}(\frac{n}{t} = v)}{\mathcal{P}(\frac{n}{t} = -v)} = e^{-\Psi v t}. \tag{3.11}$$

En utilisant l'Eq. 3.10, et le fait que $G(v)$ et $\vartheta(\lambda)$ sont reliées par une transformée de Legendre, on retrouve bien la relation 3.9.

Nous avons jusqu'ici ignoré la dynamique des variables internes (ou chimiques) du moteur. Pour caractériser le courant chimique, r, qui représente le taux de consommation d'ATP par le moteur, il est nécessaire d'inclure dans la description de l'état du moteur, une variable chimique y associée au nombre moyen de molécules d'ATP consommées. En refaisant l'analyse précédente, on est amené à décomposer les taux de transitions en $\overleftarrow{\omega}_j^{\,l}$ et $\overrightarrow{\omega}_j^{\,l}$, correspondant aux taux de transitions pour quitter le site j vers un site voisin à gauche ou à droite respectivement, et ce avec $l\,(= -1, 0, 1)$ molecules d'ATP consommées. Avec les notations, $\omega_a^l = \overrightarrow{\omega}_a^{\,l} + \overleftarrow{\omega}_a^{\,l}$ et $\omega_a = \overrightarrow{\omega}_a + \overleftarrow{\omega}_a$ (et de même pour le site b), on obtient le courant chimique

$$r = \frac{\omega_a^1 \omega_b - \omega_b^{-1} \omega_a}{\omega_a + \omega_b}, \tag{3.12}$$

en accord avec la représentation en cycle de la figure 3.6.

Lorsqu'on écrit explicitement la forme de ces taux en fonction de la force normalisée appliquée sur le moteur f et du potentiel chimique normalisé $\Delta\mu$, on obtient une reformulation un peu plus précise de l'Eq. 3.5 :

$$k_B T \ln \frac{\overrightarrow{\omega_b}^{-l}\overrightarrow{\omega_a}^{l'}}{\overleftarrow{\omega_a}^{l}\overleftarrow{\omega_b}^{-l'}} = F_e(2d) - \Delta\tilde{\mu}\,(l - l')\,, \tag{3.13}$$

pour $l, l' = 0, 1$.

Cette équation peut se voir comme une expression du premier principe de la thermodynamique au niveau de transitions élémentaires. En effet, on peut associer le terme de gauche avec la chaleur libérée par le moteur dans son environnement (traité comme un réservoir à la même température) lors des transitions (l, l'). Le membre de droite s'interprète alors comme la différence entre le travail mécanique $-F_e(2d)$ et la variation d'énergie chimique $\Delta\tilde{\mu}\,(l - l')$ pour ces transitions. La variation d'énergie interne est nulle ici car on considère des transitions formant un cycle.

Cette idée importante, qu'il doit être possible de formuler le premier principe au niveau de transitions élémentaires, a d'abord été formulée par K. Sekimoto pour des trajectoires satisfaisant à l'équation de Langevin [39]. On comprend à présent que cette contrainte est plus générale, en particulier comme on le voit ici, elle est également présente dans des modèles discrets de moteurs moléculaires [18, 22]. Dans le modèle de flashing ratchet, c'est cette contrainte thermodynamique qui permet de justifier la paramétrisation des taux de transitions de l'Eq. 3.3. En fait, cette contrainte thermodynamique joue un rôle central dans le développement de la Thermodynamique Stochastique [40], dont l'essor récent est lié aux recherches autour des relations de fluctuation.

Ces équations conduisent à de nouvelles formulations des relations de Fluctuation, similaires à la relation 3.9 :

$$\vartheta(\lambda, \gamma) = \vartheta(-\tilde{\Psi} - \lambda, -\tilde{\chi} - \gamma), \tag{3.14}$$

avec de nouvelles affinités $-\tilde{\Psi}$ et $-\tilde{\chi}$ associées aux cycles mécaniques et chimiques. Ces affinités interviennent dans l'expression de la production d'entropie associée au fonctionnement du moteur [20], qui vérifie elle aussi une relation de Fluctuation différente mais reliée à celle vérifiée par les courants qui est discuté ici.

Dans la Ref. [21], nous avons généralisé l'étude au cas du modèle continu de flashing ratchet, en utilisant la méthode de déformation d'opérateurs introduite dans la Ref. [41]. Avec cette méthode, nous avons calculé numériquement la valeur propre associée à la matrice d'évolution des fonctions génératrices des courants, qui est représentée dans la figure 3.7. Nous avons montré que ce modèle satisfait toujours une relation de la forme 3.14, mais ne vérifie pas dans le cas général de relation de la forme 3.9-3.11 sauf dans le cas particulier où les taux de transitions entre les deux états satisfont au bilan détaillé.

En résumé, la dynamique d'un moteur moléculaire peut être assimilée à l'évolution d'un marcheur aléatoire dans un potentiel effectif $U_{eff}(x, y)$ où x est la variable mécanique et y la variable chimique. La périodicité du potentiel selon x et y implique que le potentiel a une forme en "egg-carton" (en forme de paquets d'oeufs).

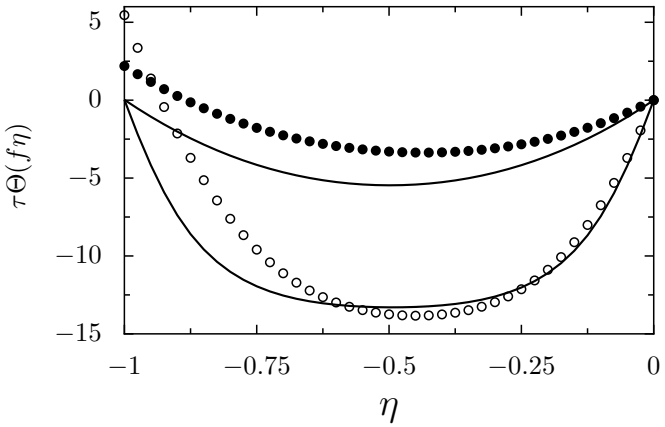

FIGURE 3.7 – Valeur propre normalisée $\tau\Theta(f\eta)$ du modèle de flashing ratchet en fonction de $\eta = \lambda/f$ avec τ le temps caractéristique a^2/D_0, pour une force normalisée $f = 5$ (pour les deux courbes du haut) et $f = 10$ (pour les deux courbes du bas). Les courbes continues correspondent au cas où les taux de transitions entre états internes satisfont au bilan détaillé, ce qui conduit à la symétrie de Gallavotti-Cohen, *i.e.* la symétrie par rapport à $\eta = -1/2$. Les courbes avec des ronds noirs ($f = 5$) et des ronds blancs ($f = 10$) correspondent aux cas où le bilan détaillé est violé avec des taux de transitions constants $\omega_1(x) = \omega_2(x) = 10\tau^{-1}$ et les mêmes potentiels.

La validité ou non des relations de Fluctuations dépend comme l'expression précise de la production d'entropie, du niveau de description qui est choisi. Cependant de nombreuses questions restent encore en suspens : dans le cas du modèle de flashing ratchet, où la relation de fluctuation pour la variable mécanique est violée en général, on peut la restorer en élargissant l'espace des phases et en modifiant la dynamique. On peut se demander si une telle procédure est toujours possible, en d'autres termes, est-il toujours possible de modifier la dynamique d'un système hors d'équilibre donné de façon à respecter une relation de Fluctuation par exemple pour les courants ou pour la production d'entropie ? Les relations de Fluctuations sont elles strictement vérifiées par les systèmes expérimentaux ou est-il possible de les briser même faiblement ?

3.3 Filaments actifs : actine et microtubule

Les filaments d'actine et de microtubules sont deux éléments structuraux essentiels des cellules, qui possèdent des propriétés dynamiques remarquables. Par exemple, les microtubules sont capables de transitions rapides entre un état de polymérisation (croissance) et un état de dépolymérisation rapide (catastrophe). Cette alternance conduit à de grandes fluctuations de longueur des microtubules et porte le nom d'instabilité dynamique. Les filaments d'actine dépolymérisent, en moyenne, à l'extrémité lente (le bout pointu) et polymérisent plutôt à l'extrémité rapide (le bout barbé), selon un processus appelé treadmilling. L'actine et les microtubules sont

impliqués dans de nombreux processus cellulaires : par exemple, le treadmilling des filaments d'actine joue un rôle essentiel dans la motilité cellulaire via la formation de structures sur le bord des cellules appelées filipodes et lamellipodes. Les fluctuations de longueurs des microtubules jouent un rôle essentiel dans le placement du fuseau mitotique lors de la division cellulaire.

La réaction d'hydrolyse de l'ATP/GTP n'est pas requise pour la polymérisation des filaments, mais elle joue un rôle essentiel dans leurs propriétés dynamiques. En effet, c'est le couplage de la polymérisation des filaments à la réaction d'hydrolyse de l'ATP/GTP qui est responsable des grandes fluctuations de longueur des filaments et donc de l'instabilité dynamique. L'instabilité dynamique des microtubules est à présent reconnue comme un ingrédient essentiel dans le contrôle de la génération de forces par les filaments d'actine ou les microtubules au niveau d'une cellule.

Nous avons développé un modèle pour décrire la dynamique d'un filament unique d'actine ou de microtubule [42]. Le modèle prend en compte les réactions élémentaires impliquées dans la cinétique de polymérisation (association ou dissociation d'un monomère à une extrémité du filament, hydrolyse des monomères liés à ATP..). Pour simplifier, on suppose que le filament est en contact avec un réservoir de monomères et que la polymérisation/dépolymérisation ne peut se produire qu'à partir d'une seule extrémité du filament (le bout barbé pour l'actine, l'extrémité plus pour un microtubule). A l'intérieur du filament, l'hydrolyse n'a lieu qu'à l'interface entre les monomères liés à l'ATP et ceux liés à l'ADP, c'est le modèle vectoriel. Dans un autre modèle discuté dans la littérature, le modèle aléatoire, un monomère donné lié à l'ATP peut être hydrolysé quelque soit l'état des monomères voisins [43]. Une spécificité de notre approche par rapport aux modèles théoriques bien établis pour décrire l'instabilité dynamique des microtubules [44], est de ne pas contenir de paramètres phénoménologiques (comme ceux associés aux transitions entre les deux états internes du filament), puisque notre modèle est formulé uniquement en terme de constantes cinétiques de réaction qui sont bien connues expérimentalement.

Dans le modèle vectoriel, l'état du filament ne dépend que de la longueur de la partie du filament contenant des monomères liés à l'ADP n et de la longueur de la partie du filament contenant des monomères liés à l'ATP (appelée cap) k (cf. schéma de la figure 3.8). L'évolution dynamique du filament est décrite par des équations maîtresses pour la probabilité de trouver le filament dans un état (n, k). Pour résoudre ces équations, nous avons formulé une analogie entre la dynamique du filament et celle d'un marcheur aléatoire dans un espace à deux dimensions défini par (n, k), comme indiqué à la figure 3.8.

Ce modèle contient trois états stationnaires possibles, correspondant à trois phases, qui sont illustrées à la figure Fig. 3.9. Il y a deux phases de croissance non-bornée, une phase dans laquelle le cap croît linéairement dans le temps et une autre dans laquelle la longueur du cap reste constante en fonction du temps. Il y a surtout une phase nouvelle qui n'avait pas été discutée auparavant pour ce modèle, qui est la phase de croissance bornée, dans laquelle la longueur du filament et du cap restent toutes deux constantes dans le temps. La caractérisation de cette phase est particulièrement importante car c'est la seule phase stationnaire qui demeure expérimentalement à temps long lorsqu'on prend en compte la contrainte de conser-

vation du nombre total de monomères : en effet les deux autres phases de croissance non-bornées mentionnées plus haut ne sont pas stationnaires dans ces conditions, puisqu'elles conduisent nécessairement à une déplétion des monomères libres de la solution. En pratique, on peut les observer mais de façon transitoire.

Nous avons analysé l'effet de l'hydrolyse de l'ATP/GTP sur les courbes force-vitesse, caractérisé les fluctuations de longueur du filament, et calculé les temps de premier passage associés à la disparition du cap ou du filament, qui caractérisent l'instabilité dynamique [42]. Les expressions analytiques obtenues pour toutes ces quantités sont en bon accord avec les résultats des simulations Monte Carlo.

A la suite de cette étude, nous avons développé plusieurs extensions de ce modèle dans la Ref. [45]. Une extension concerne la prise en compte de la dynamique des deux extrémités du filament (au lieu de ne considérer que l'extrémité rapide). Pour ce problème la, nous avons établi un diagramme de phase qui résume les principales phases dynamiques d'un filament d'actine ou de microtubule avec deux extrémités actives et un mécanisme d'hydrolyse vectoriel dans le filament. Nous avons également comparé les deux modèles pour décrire l'hydrolyse de l'ATP dans le filament (le modèle vectoriel et le modèle aléatoire). Des expressions exactes de la vitesse et du coefficient de diffusion caractérisant les fluctuations du filament avec deux extrémités actives, ont été obtenues pour le modèle vectoriel, et une très bonne approximation de la vitesse a été obtenue pour le modèle aléatoire grâce à une approche de champ moyen. Cette comparison dans le cas de l'actine indique que les mesures de vitesse de filaments réalisées classiquement par des techniques de fluorescence en "bulk", ainsi que les mesures du coefficient de diffusion associé aux fluctuations de longueur réalisées avec des filaments uniques, ne permettent pas de distinguer facilement les prédictions des deux modèles. Ceci est illustré pour la vitesse de croissance d'un filament d'actine à la figure 3.10, on voit que les prédictions des deux modèles sont superposés entre elles et superposés aux mesures expérimentales réalisées par MF. Carlier. En revanche, nous montrons au moyen de simulations, qu'il devrait être possible de distinguer les deux modèles par une étude plus précise de la dynamique de la longueur d'un filament en fonction du temps, même dans le cas où l'interface entre monomères hydrolysés et non-hydrolysés n'est pas détectable expérimentalement.

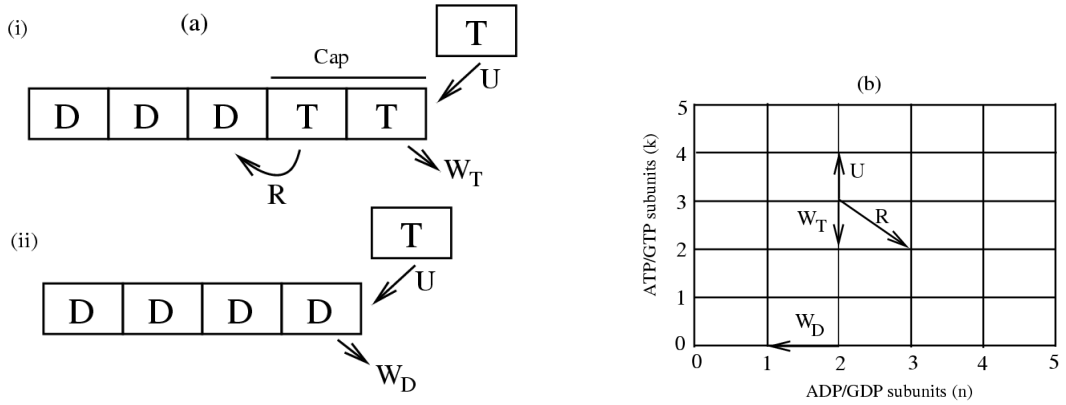

FIGURE 3.8 – (a) Représentation du filament, U est le taux d'ajout de monomères liés à l'ATP, W_T et W_D sont les taux de départ des monomères liés à l'ATP et à l'ADP : (i) pour le cas où la longueur du cap est non nulle et (ii) pour le cas où la longueur du cap est zero. T représente un monomère d'actine (tubuline) lié à l'ATP (ou GTP), D représente un monomère d'actine (tubuline) lié à l'ADP (ou GDP). A l'interface T-D représentée en (i), l'hydrolyse se produit avec un taux R (modèle vectoriel). (b) Représentation équivalente en terme d'une marche aléatoire dans le quart plan supérieur avec les mouvements suivants : U pour aller au nord, W_T pour aller au sud, R pour aller au sud-est et W_D pour aller à l'ouest. Ce dernier mouvement n'est possible que le long de la ligne $k = 0$ (bord sud).

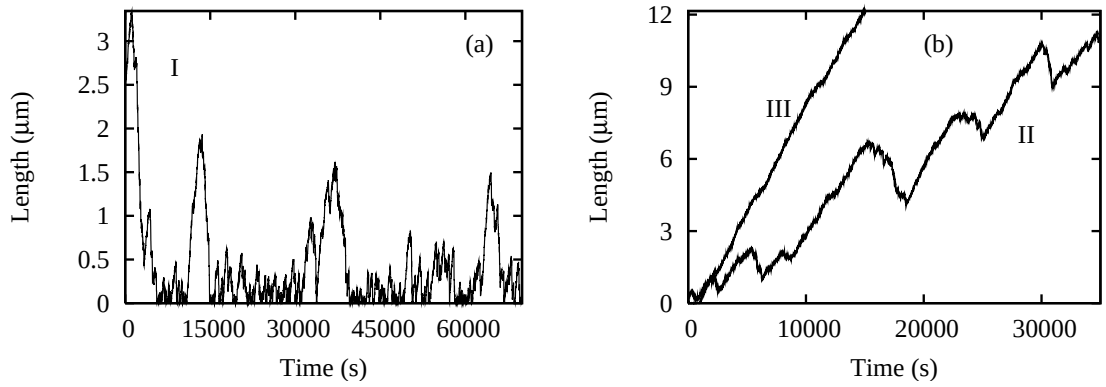

FIGURE 3.9 – *Longueur du filament en fonction du temps dans le modèle [42]. (a) : phase de croissance bornée, dans laquelle à la fois le filament et le cap restent bornés en fonction du temps. (b) : phases de croissance non-bornée. On distingue la phase III, dans laquelle à la fois le cap et le filament sont non-bornés, et la phase II, dans laquelle la longueur du filament est non-bornée mais la longueur du cap reste constante en fonction du temps.*

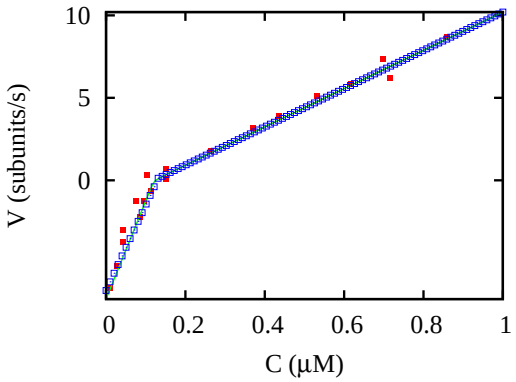

FIGURE 3.10 – *Vitesse d'un filament d'actine en fonction de la concentration en monomères libres. Les symboles carrés pleins représentent des données expérimentales tirées de la Ref. [46], la courbe continue est une approche de champ moyen pour le modèle aléatoire et les symboles carrés vides correspondent au modèle vectoriel, qui est essentiellement superposé au cas du modèle aléatoire [45].*

Bibliographie

[1] J.-B. Fournier, D. Lacoste, and E. Raphaël. Fluctuation spectrum of fluid membranes coupled to an elastic meshwork : jump of the effective surface tension at the mesh size. *Phys. Rev. Lett.*, 92 :018102, 2004.

[2] C. Dubus and J.-B. Fournier. A gaussian model for the membrane of red blood cells with cytoskeletal defects. *Eur. Phys. Lett.*, 75(1) :181, 2006.

[3] J. Prost and R. Bruinsma. Shape fluctuations of active membranes. *Eur. Phys. Lett.*, 33 :321, 1996.

[4] S. Ramaswamy, J. Toner, and J. Prost. Nonequilibrium fluctuations, traveling waves, and instabilities in active membranes. *Phys. Rev. Lett.*, 84 :3494, 2000.

[5] D. Lacoste and A. Lau. Dynamics of active membranes with internal noise. *Eur. Phys. Lett.*, 70 :418, 2005.

[6] N. Gov. Membrane undulations driven by force fluctuations of active proteins. *Phys. Rev. Lett.*, 93 :268104, 2004.

[7] S. Sankararaman, G. Menon, and P. B. S. Kumar. Two-component fluid membranes near repulsive walls : Linearized hydrodynamics of equilibrium and nonequilibrium states. *Phys. Rev. E*, 66 :031914, 2002.

[8] D. Lacoste, M. Cosentino Lagomarsino, and J-F. Joanny. Fluctuations of a driven membrane in an electrolyte. *Eur. Phys. Lett.*, 77 :18006, 2007.

[9] D. Lacoste, G. I. Menon, M. Z. Bazant, and J. F. Joanny. Electrostatic and electrokinetic contributions to the elastic moduli of a driven membrane. *Eur. Phys. J. E*, 28(3) :243–264, 2009.

[10] M. Z. Bazant F. Ziebert and D. Lacoste. Effective zero-thickness model for a conductive membrane driven by an electric field. *accepté pour Phys. Rev. E.*

[11] Armand Ajdari. Pumping liquids using asymmetric electrode arrays. *Phys. Rev. E*, 61(1) :R45–R48, 2000.

[12] Martin Z. Bazant and Todd M. Squires. Induced-charge electrokinetic phenomena : Theory and microfluidic applications. *Phys. Rev. Lett.*, 92(6) :066101, 2004.

[13] J. B. Manneville, P. Bassereau, S. Ramaswamy, and J. Prost. Active membrane fluctuations studied by micropipet aspiration. *Phys. Rev. E*, 64 :021908, 2001.

[14] M. D. El Alaoui Faris, D. Lacoste, J. Pécréaux, J.-F. Joanny, J. Prost, and P. Bassereau. Membrane tension lowering induced by protein activity. *Phys. Rev. Lett.*, 102(3) :038102, 2009.

[15] F. Jülicher et al. Modeling molecular motors. *Rev. Mod. Phys.*, 69 :1269, 1997.

[16] P. Reiman. Brownian motors : noisy transport far from equilibrium. *Phys. Rep.*, 361 :57, 2002.

[17] A. Kolomeisky and M.E. Fisher. Molecular Motors : A Theorist's Perspective. *Annu. Rev. Phys. Chem.*, 58 :675, 2007.

[18] R. Lipowsky and S. Liepelt. Chemomechanical coupling of molecular motors : Thermodynamics, network representations, and balance conditions. *J. Stat. Phys.*, 128 :77, 2008.

[19] A. W. C. Lau, D. Lacoste, and K. Mallick. Non-equilibrium fluctuations and mechanochemical couplings of a molecular motor. *Phys. Rev. Lett.*, 99 :158102, 2007.

[20] D. Lacoste, A. W. C. Lau, and K. Mallick. Fluctuation theorem and large deviation function for a solvable model of a molecular motor. *Phys. Rev. E*, 78 :011915, 2008.

[21] D. Lacoste and K. Mallick. Fluctuation theorem for the flashing ratchet model of molecular motors. *Phys. Rev. E*, 80 :021923, 2009.

[22] D. Lacoste and K. Mallick. Fluctuation relations for molecular motors. *submitted to Poincaré Séminar 2009*.

[23] A. Parmeggiani et al. Energy transduction of isothermal ratchets : Generic aspects and specific examples close to and far from equilibrium. *Phys. Rev. E*, 60 :2127, 1999.

[24] H. Wang, C. S. Peskin, and T. C. Elston. A robust numerical algorithm for studying biomolecular transport processes. *J. Theor. Biol.*, 221 :491, 2003.

[25] A. Kolomeisky and B. Widom. A simplified "ratchet" model of molecular motors. *J. Stat. Phys.*, 93 :633, 1998.

[26] Y. Kafri et al. Dynamics of molecular motors and polymer translocation with sequence heterogeneity. *Biophys. J.*, 86 :3373, 2004.

[27] M.J. Schnitzer and S.M. Block. Kinesin hydrolyses one ATP per 8-nm step. *Nature*, 388 :386, 1997. K. Visscher *et al.*, Nature **400**, 184 (1999).

[28] K. I. Skau, R. B. Hoyle, and M. S. Turner. A kinetic model describing the processivity of myosin-v. *Biophys. J.*, 91 :2475, 2006.

[29] J. Kurchan. Non-equilibrium work relations. *J. Stat. Mech.*, page P07005, 2007.

[30] F. Ritort. Nonequilibrium fluctuations in small systems : from physics to biology. *Adv. in Chem. Phys.*, 137 :31, 2008.

[31] G. E. Crooks. Path-ensemble averages in systems driven far from equilibrium. *Phys. Rev. E*, 61 :2361, 2000.

[32] G. Gallavotti and E. G. D. Cohen. Dynamical ensembles in nonequilibrium statistical mechanics. *Phys. Rev. Lett.*, 74(14) :2694–2697, 1995.

[33] C. Jarzynski. Nonequilibrium equality for free energy differences. *Phys. Rev. Lett.*, 78(14) :2690–2693, 1997.

[34] D. Andrieux and P. Gaspard. Fluctuation theorems and the nonequilibrium thermodynamics of molecular motors. *J. Chem. Phys.*, 120 :8898, 2004.

[35] U. Seifert. Fluctuation theorem for a single enzym or molecular motor. *Europhys. Lett.*, 70 :36, 2005.

[36] A. Imparato, L. Peliti, G. Pesce, G. Rusciano, and A. Sasso. Work and heat probability distribution of an optically driven brownian particle : Theory and experiments. *Phys. Rev. E*, 76(5) :050101, 2007.

[37] J. Schnakenberg. Network theory of microscopic and macroscopic behavior of master equation systems. *Rev. Mod. Phys.*, 48 :571, 1976.

[38] T. Hill. *Free Energy Transduction and Biochemical Cycle Kinetics.* Springer-Verlag, New York, 1989.

[39] K. Sekimoto. Langevin equation and thermodynamics. *Prog. of Theo. Phys.*, 130 :17, 1998.

[40] T. Schmiedl, T. Speck, and U. Seifert. Entropy production for mechanically or chemically driven biomolecules. *J. Stat. Phys.*, 128 :77, 2007.

[41] J. L. Lebowitz and H. Spohn. A Gallavotti-Cohen-Type symmetry in the large deviation functional for stochastic dynamics. *J. Stat. Phys.*, 95 :333, 1999.

[42] P. Ranjith, D. Lacoste, K. Mallick, and J-F. Joanny. Nonequilibrium Self-Assembly of a Filament Coupled to ATP/GTP Hydrolysis. *Biophys. J.*, 96 :2146–2159, 2009.

[43] T. Keiser, A. Schiller, and A. Wegner. Nonlinear increase of elongation rate of actin filaments with actin monomer concentration. *Biochem.*, 25(17) :4899–4906, 1986.

[44] H. Flyvbjerg, T. Holy, and S. Leibler. Microtubule dynamics : Caps, catastrophes, and coupled hydrolysis. *Phys. Rev. E*, 54(5) :5538–5560, Nov 1996.

[45] P. Ranjith, K. Mallick, J-F. Joanny, and D. Lacoste. Role of ATP-hydrolysis in the dynamics of a single actin filament. *accepted to Biophys. J.*, 2009.

[46] M.-F. Carlier, D. Pantaloni, and E. D . Korn. The Effects of Mg^{2+} at the high-affinity and low-affinity sites on the polymerization of actin and associated ATP Hydrolysis. *J. of Biol. Chem.*, 261 :10785–1079, 1986.

Chapitre 4

Conclusion et projets

4.1 Conclusion

Transport de la polarisation de la lumière dans un milieu diffusant

D'une part, nous avons caractérisé théoriquement le transport de la lumière dans un milieu diffusant et fortement anisotrope. D'autre part, nous avons vu quelques applications de ces idées à des problèmes concrets (analyse de motifs formés par la lumière rétrodiffusée) ou mesures de fonctions de corrélation de l'intensité en fonction de la polarisation (DWS). Ces recherches visent à mieux comprendre le transport de la lumière dans des milieux complexes comme des tissus biologiques.

Auto-assemblage de colloïdes magnétiques et cristaux liquides

D'une part, nous avons présenté des modèles pour décrire l'auto-organisation de colloïdes magnétiques de type ferrofluide mélangé ou non à des colloïdes non-magnétique en présence de champ magnétique. D'autre part, nous avons formulé un modèle pour décrire l'auto-organisation de particules colloïdales en forme de bâtonnets inclus dans un gel de polymères réticulé (gel nématique). Ces recherches visent à concevoir de nouvelles classes de matériaux "activables" par une force ou agent extérieur.

Applications de la Physique Statistique à des systèmes biologiques

Nous avons étudié un certain nombre de systèmes composites dans lesquels une membrane lipidique est couplée à un autre système extérieur (par exemple à un cytosquelette dans un modèle simple de cellule biologique) ou à un champ extérieur (comme un champ électrique qui génère des courants ioniques et des écoulements électrocinétiques au voisinage d'une membrane lipidique). Nous avons également étudié des systèmes actifs élémentaires, qui réalisent dans une cellule biologique la

transformation d'énergie chimique en énergie mécanique (comme des moteurs moléculaires ou des filaments d'actine). Dans le cas des moteurs moléculaires, nous avons développé une analyse thermodynamique, qui permet de rendre compte de cette transformation d'une forme d'énergie en l'autre. Cette analyse thermodynamique repose sur une vérification de la symétrie du théorème de fluctuations (relation de Gallavotti-Cohen en particulier), qui est une manifestation macroscopique de la symétrie de renversement du temps valable à l'échelle microscopique.

4.2 Projets

Dans les années qui viennent, je souhaite poursuivre de façon générale mon activité de recherche dans le domaine des applications de la physique statistique aux systèmes biologiques. Il y a deux projets principaux :

4.2.1 Effets des champs électriques sur les membranes lipidiques

Les effets électrostatiques et électrocinétiques jouent des rôles essentiels dans la matière molle et dans les milieux biologiques. Par exemple la réalisation de vésicules lipidiques repose sur l'électroformation, et l'ouverture de pores dans les membranes de façon contrôlée par l'application d'un champ électrique repose sur l'électroporation. Pour de nombreuses applications en biotechnologies, il serait utile de mieux comprendre ces effets, et plus généralement les modifications produites par l'application de champs électriques sur les membranes lipidiques.

De plus, ces questions concernent également de près l'électrophysiologie et la microfluidique. Des progrès technologiques récents permettent par exemple d'interfacer un système biologique comme un neurone avec un dispositif de microfluidique. Dans cette direction, nous envisageons une expérience permettant de recréer de façon contrôlée les conditions nécessaires à l'élaboration d'un potentiel d'action dans un tube de membrane lipidique contenant des canaux à ions, qui est un système modèle de neurone. Ce projet qui est très ambitieux expérimentalement contient aussi un volet important sur la modélisation de l'effets des champs électriques sur les membranes lipidiques et sur la propagation des potentiels d'action dans les cellules neuronales.

Participants : groupe expérimental de P. Bassereau, J. F. Joanny, J. Prost (ANR ARTIF NEURON)

4.2.2 Physique du cytosquelette

Dans ce deuxième projet, je propose de poursuivre les études engagées dans le domaine des moteurs moléculaires, des filaments comme l'actine et les microtubules et sur les structures complexes formées par leur association. Ces recherches visent

à mieux comprendre les propriétés physiques du cytosquelette, qui sont essentielles pour le fonctionnement des cellules biologiques. Deux grandes classes de systèmes biologiques élémentaires (moteurs ou biofilaments) réalisent une conversion d'énergie chimique en énergie mécanique, que l'on aimerait mieux comprendre. Les forces générées par les filaments d'actine ou par des moteurs moléculaires jouent un rôle essentiel dans de multiples aspects du fonctionnement des cellules. Si les mécanismes par lesquels ces forces sont générées sont de mieux en mieux compris à l'échelle d'un filament ou d'un moteur unique grâce au développement de techniques expérimentales (notamment optiques), il reste encore beaucoup à faire pour décrire les effets collectifs dans ces systèmes. Ces effets sont multiples, complexes et présents à différentes échelles. Un exemple d'un effet de ce type concerne le couplage entre plusieurs moteurs moléculaires entre eux, qui permet d'optimiser le transport d'une vésicule (cargo) d'un point à un autre d'une cellule par exemple. Un autre exemple concerne la recherche de modèles pour décrire la mobilité de cellules biologiques, laquelle repose sur la polymérisation de l'actine.

Sur le plan des idées théoriques, l'apport de la Physique Statistique hors d'équilibre est essentiel pour aborder ces questions. Il s'agit d'une physique statistique nouvelle et qui est encore sur bien des points à construire dans la mesure où l'on ne dispose pas encore à ce jour de théorie complètement satisfaisante pour décrire les systèmes hors d'équilibre. De ce fait, de nombreuses questions de nature thermodynamique portant sur des systèmes biologiques (même sur certains systèmes "élémentaires" comme des moteurs moléculaires uniques) nous échappent. L'enjeu des recherches dans ce domaine est donc de comprendre des questions fondamentales concernant la Physique Statistique des systèmes hors d'équilibre (comme celles touchant aux relations de fluctuations) tout en approfondissant notre compréhension encore limitée des systèmes vivants.

Participants théoriciens : J. F. Joanny de l'Institut Curie, K. Mallick du Service de Physique Théorique du CEA, Saclay.
Participants expérimentateurs : M. F. Carlier à Gif sur Yvette, J. Baudry, J. Bibette, J. Heuvingh, O. du Roure et M. Fermigier à ESPCI (ANR ACTIMAG).

4.3 Sélection d'articles

Fluctuation theorem and large deviation function for a solvable model of a molecular motor

D. Lacoste,[1] A. W.C. Lau,[2] and K. Mallick[3]
[1]*Laboratoire de Physico-Chimie Théorique, UMR 7083, ESPCI, 10 rue Vauquelin, 75231 Paris Cedex 05, France*
[2]*Department of Physics, Florida Atlantic University, 777 Glade Road, Boca Raton, Florida 33431, USA*
[3]*Institut de Physique Théorique, CEA Saclay, 91191 Gif, France*
(Received 25 January 2008; revised manuscript received 25 April 2008; published 22 July 2008)

We study a discrete stochastic model of a molecular motor. This discrete model can be viewed as a minimal ratchet model. We extend our previous work on this model, by further investigating the constraints imposed by the fluctuation theorem on the operation of a molecular motor far from equilibrium. In this work, we show the connections between different formulations of the fluctuation theorem. One formulation concerns the generating function of the currents while another one concerns the corresponding large deviation function, which we have calculated exactly for this model. A third formulation concerns the ratio of the probability of observing a velocity v to the same probability of observing a velocity $-v$. Finally, we show that all the formulations of the fluctuation theorem can be understood from the notion of entropy production.

DOI: 10.1103/PhysRevE.78.011915 PACS number(s): 87.15.−v, 87.16.Nn, 05.40.−a, 05.70.Ln

I. INTRODUCTION

The living cell has evolved a diverse array of proteins, which can perform a variety of chemical functions. These proteins catalyze chemical reactions, control key processes such as recognition or signaling, or act as molecular machines. Biological systems containing these elements are typically described as active because they are in a nonequilibrium state as opposed to nonactive systems which can be considered at thermal equilibrium. Recently there has been a lot of interest in the nonequilibrium properties of active biological systems, such as the hair bundle of the ear [1,2], active membranes [3], active gels [4], active networks [5], active lipid clusters [6], living cells [7], etc.

Clearly, one step toward understanding active biological systems starts with the understanding of single active proteins, such as, for instance, molecular motor proteins. These molecular motor are nanomachines that convert chemical energy derived from the hydrolysis of ATP into mechanical work and motion [8,9]. Important examples include kinesin, myosin, RNA polymerase, and the F_0/F_1 rotating motor. Mechanotransduction (i.e., the process of conversion of chemical energy into mechanical work) in motors has been described theoretically by ratchet models [10,11], which rely on the fruitful concept of broken symmetry. According to the Curie principle, directed motion requires to break the spatial symmetry and the time reversal symmetry associated with equilibrium (detailed balance). The spatial symmetry is broken by the asymmetric interaction between the motor and the filament, while the time reversal symmetry is broken by chemical transitions, which break locally the detailed balance condition. From the continuous ratchet models described by Langevin equations [10], it is possible to construct discrete stochastic models of molecular motors by considering only localized discrete transitions as explained in Ref. [12]. These discrete stochastic models are interesting because they are minimal, in the sense that they contain the main physical picture of ratchet models while being more amenable to precise mathematical analysis [13–16].

Recent advances in experimental techniques to probe the fluctuations of single motors provide ways to gain insight into their kinetic pathways [17–20]. However, a general description for fluctuations of systems driven out of equilibrium, and in particular of motors, is still lacking. Recently, the fluctuation theorem (FT) has emerged as a promising framework to characterize fluctuations in far-from-equilibrium regimes. This theorem is in fact a group of closely related results valid for a large class of nonequilibrium systems [21–25]. In a nutshell, FT states that the probability distribution for the entropy production rate obeys a symmetry relation. The theorem becomes particularly relevant for small systems in which fluctuations are large. For this reason, the FT has been verified in a number of beautiful experiments with small systems such as biopolymers and colloidal systems [26]. In the specific case of molecular motors, FT leads to constraints on the operation of molecular motors or nanomachines far from equilibrium in a regime where the usual thermodynamic laws do not apply [27–29].

In a recent work [30], we have extended a two-states discrete stochastic model introduced in Ref. [14] by including an important variable, namely, the number of ATP consumed. We have shown that this extended model satisfies FT, and we have constructed a thermodynamic framework allowing us to characterize quantities such as the average velocity, the average ATP consumption rate, and its thermodynamic efficiency. We have also analyzed the different thermodynamic modes of operation of the motor as functions of generalized forces arbitrarily far from equilibrium. Using FT, we have quantified the "violations" of Einstein and Onsager relations. The deviations from Einstein and Onsager relations can be studied by considering the linear response theory in the vicinity of a nonequilibrium steady state rather than near an equilibrium steady state. After determining the parameters of our model by a fit of single molecule experiments with kinesin [17], we have formulated a number of theoretical predictions for the "violations" of Einstein and Onsager relations for this motor.

In this paper, we further extend the analysis of this model. In particular, we provide a more detailed study of the modes of operation of the motor and its thermodynamic efficiency in relation with the experimental data of kinesin. This part contains important information which could not be presented

in Ref. [30] due to limited space. The rest of the paper is devoted to bringing together different formulations of FT, explaining their connections and their physical implications. One way to formulate FT involves the generating function of the currents. We show that this formulation leads to two versions of FT, a long time version of FT similar to the Gallavotti-Cohen relation which holds quite generally, and a finite time version which is analogous to the Crooks-Evans transient fluctuation theorem [24,25] which holds under restricted hypotheses for the initial state. Another formulation of FT takes the form of a property of the large deviation function of the current. There are very few nonequilibrium models for which the large deviation function of the current is known exactly. Our model is sufficiently simple for this analytical calculation to be possible, and by carrying it out we show that the large deviation function of the current indeed satisfies an FT relation. A by-product of this calculation is a third formulation of FT in terms of the ratio of probabilities for observing a velocity v to the same probability for observing a velocity $-v$. The prediction of this ratio of probabilities, which is obtained from the large deviation function of the current is one of the main results of this paper. We also study the connections between FT and the notion of entropy production. This entropy production can be explicitly calculated using the notion of affinities associated with a cyclic evolution of the mechanical and chemical variables, and the affinities precisely enter all the formulations of FT. We show that the entropy production can also be obtained from an evaluation of a quantity called the action functional [23]. The entropy production and therefore also FT depends on the coarse-graining of the description which we illustrate by considering three different levels of description: purely mechanical, purely chemical, and a combination of the two.

The paper is organized as follows. In Sec. II, we introduce the model, in Sec. III we consider the modes of operation of the motor, its thermodynamic efficiency, and the comparison of the model with experimental data for kinesin. Section IV is devoted to the formulation of FT in terms of generating functions, with its long time and its finite time versions, Sec. V discusses the formulation in terms of the large deviation function of the current and the significance of the third formulation of FT in terms of a ratio of probabilities, and the last section contains the discussion of the entropy production.

II. TWO-STATE MODEL FOR MOLECULAR MOTORS

A. Construction of the model

As a result of conformational changes powered by hydrolysis of ATP, a linear processive motor, such as kinesin, moves along a one-dimensional substrate (microtubule). The state of the molecular motor may be characterized by two variables: its position and the number of ATP consumed. To model the dynamics, we consider a linear discrete lattice, where the motor "hops" from one site to neighboring sites, either consuming or producing ATP (see Fig. 1). An alternate representation of the dynamics can be built in terms of cycles (see Fig. 2). The position is denoted by $x=nd$, where $2d \approx 8$ nm is the step size for kinesin. The even sites (denoted by a) are the low-energy state of the motor, whereas the odd sites (denoted by b) are its high-energy state; their energy difference is $\Delta E \equiv k_B T\epsilon$, where k_B is the Boltzmann constant and T is the temperature. This model is suitable to describe a two-headed kinesin walking on a microtubule, with the high-energy state corresponding to the state where a single head is bound to the filament, and the low-energy state corresponding to the two heads bound to it. Because of the periodicity of the filament, all the even (a) sites and all the odd (b) sites are equivalent.

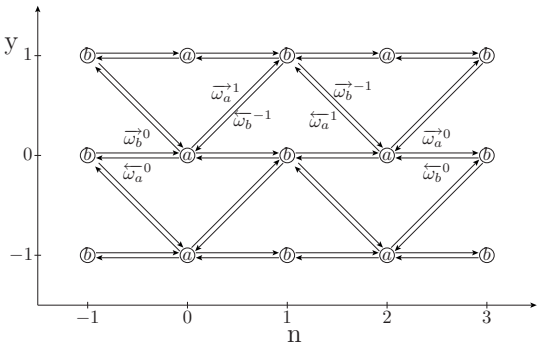

FIG. 1. A schematic of the rates for this two-state stochastic model of a single processive molecular motor. The position of the motor is n and y is the number of ATP consumed. The even and odd sites are denoted by a and b, respectively. In the case of two headed kinesin, site a represents a state where both heads are bound to the filament, whereas site b represents a state with only one head bound. Note that the lattice of a and b sites extend indefinitely in both directions along the n and y axis. All the possible transitions are represented with arrows on this particular section of the lattice.

The dynamics of the motor is governed by a master equation for the probability $P_i(n,y,t)$ that the motor, at time t, has consumed y units of ATP and is at site i $(=a,b)$ with position n:

$$\partial_t P_i(n,y,t) = -(\overleftarrow{\omega_i} + \overrightarrow{\omega_i})P_i(n,y,t) + \sum_{l=-1,0,1} [\overleftarrow{\omega}_j^l P_j(n+1,y-l,t) + \overrightarrow{\omega}_j^l P_j(n-1,y-l,t)], \quad (1)$$

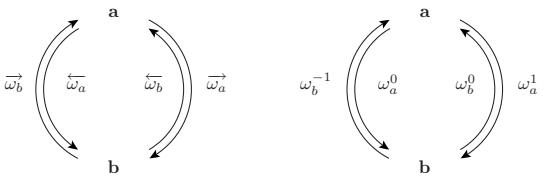

FIG. 2. Cycles associated with the evolution of the motor of Fig. 1. Left: cycle for the position variable n; the average length n undergone by the motor corresponds to half the number of full turns of the clock (the factor half is due to the period being equal to two lattice units) and with the rates as shown. Right: cycle for the chemical variable y, the average number of ATP units corresponds to the number of full turns with the rates shown. The affinities associated with these cycles are given by Eq. (11) for the mechanical variable and by Eq. (62) for the chemical variable.

with $i \neq j$, $\overleftarrow{\omega}_j \equiv \Sigma_l \overleftarrow{\omega}_j^l$, and $\overrightarrow{\omega}_j \equiv \Sigma_l \overrightarrow{\omega}_j^l$. We denote by $\overleftarrow{\omega}_j^l$ and $\overrightarrow{\omega}_j^l$ the transition rates from a site j to a neighboring site to the left or to the right, respectively, and with $l(=-1,0,1)$ ATP molecules consumed. Note that the index i is directly linked with the parity of n. We expect the rates $\overleftarrow{\omega}_j^l$ and $\overrightarrow{\omega}_j^l$ to be different even if no load is applied to the motor, because the interaction between the motor and the filament breaks the left-right (spatial) symmetry. This requirement is essential for generating directed motion.

Another essential requirement for generating directed motion is to break time-reversal symmetry. Such a symmetry is always present at equilibrium, where the detailed balance condition holds. Detailed balance is broken in molecular motors due to chemical transitions involved in the mechanotransduction process. To obtain a simple description of this process, we assume that transitions between the two states M_a and M_b of the motor [11] are possible via two different chemical pathways:

$$M_a + \mathrm{ATP} \underset{\alpha_b}{\overset{\alpha_a}{\rightleftharpoons}} M_b + \mathrm{ADP} + P \tag{2}$$

and

$$M_a \underset{\beta_b}{\overset{\beta_a}{\rightleftharpoons}} M_b, \tag{3}$$

where α_a (α_b) are forward (backward) rates. The first pathway (α) represents transitions of the motor accompanied by ATP hydrolysis, which we call "active," and the second pathway (β) represents transitions driven by thermal activation, which we call "passive." In the representation of Fig. 1, the α pathway represents oblique transitions which change both y and n whereas the β pathway is associated with horizontal transitions which change only n. It is straightforward to generalize the model with more chemical pathways, but here we focus only on these two [11]. In the absence of an external force, transition state theory of chemical reactions requires that [31,32]

$$\frac{\alpha_a}{\alpha_b} = e^{-\epsilon + \Delta\mu} \tag{4}$$

and

$$\frac{\beta_a}{\beta_b} = e^{-\epsilon}. \tag{5}$$

Taking $\alpha_a = \overrightarrow{\omega}_a^{\,1}, \alpha_b = \overleftarrow{\omega}_b^{\,-1}, \beta_a = \overrightarrow{\omega}_a^{\,0}, \beta_b = \overleftarrow{\omega}_b^{\,0}$ and $\alpha_a = \overleftarrow{\omega}_a^{\,1}, \alpha_b = \overrightarrow{\omega}_b^{\,-1}, \beta_a = \overleftarrow{\omega}_a^{\,0}, \beta_b = \overrightarrow{\omega}_b^{\,0}$, we construct the transition rates from only four unknown parameters α, α', ω, and ω' as follows:

$$\begin{aligned} &\overleftarrow{\omega}_b^{\,-1} = \alpha, \quad \overleftarrow{\omega}_b^{\,0} = \omega, \quad \overrightarrow{\omega}_a^{\,1} = \alpha\ e^{-\epsilon+\Delta\mu}, \quad \overrightarrow{\omega}_a^{\,0} = \omega\ e^{-\epsilon}, \\ &\overleftarrow{\omega}_a^{\,1} = \alpha'\ e^{-\epsilon+\Delta\mu}, \quad \overleftarrow{\omega}_a^{\,0} = \omega'\ e^{-\epsilon}, \quad \overrightarrow{\omega}_b^{\,-1} = \alpha', \\ &\overrightarrow{\omega}_b^{\,0} = \omega', \end{aligned} \tag{6}$$

and with $\overleftarrow{\omega}_b^{\,1} = \overrightarrow{\omega}_a^{\,-1} = \overleftarrow{\omega}_a^{\,-1} = \overrightarrow{\omega}_b^{\,1} = 0$. The only thermodynamic force driving the chemical cycle is the free energy of hydrolysis. This is quantified by the chemical potential $\Delta\tilde{\mu} \equiv k_B T \Delta\mu$, which is defined by the standard expression [33]

$$\Delta\tilde{\mu} = k_B T \ln\left(\frac{[\mathrm{ATP}][\mathrm{ADP}]_{\mathrm{eq}}[P]_{\mathrm{eq}}}{[\mathrm{ATP}]_{\mathrm{eq}}[\mathrm{ADP}][P]}\right), \tag{7}$$

where $[\cdots]$ denotes concentration under experimental conditions and $[\cdots]_{\mathrm{eq}}$ denotes equilibrium concentrations. The chemical potential of the hydrolysis reaction introduces a bias in the dynamics of the motor, which is responsible for breaking the time-reversal symmetry associated with the detailed balance condition (which holds at equilibrium).

Following Ref. [13], the transition rates can be generalized to include an external force F_e according to $\overleftarrow{\omega}_i^l(F_e) = \overleftarrow{\omega}_i^l(0) e^{-\theta_i^- f}$ and $\overrightarrow{\omega}_i^l(F_e) = \overrightarrow{\omega}_i^l(0) e^{+\theta_i^+ f}$, where $f \equiv F_e d/(k_B T)$ and $\theta_i^{\pm}$ are the load distribution factors. These load distribution factors take into account the fact that the external force may not distribute uniformly among different transitions [31]. Thus, we may write the nonzero rates in the presence of force as

$$\begin{aligned} &\overleftarrow{\omega}_b^{\,-1} = \alpha\ e^{-\theta_b^- f}, \quad \overleftarrow{\omega}_b^{\,0} = \omega\ e^{-\theta_b^- f}, \quad \overrightarrow{\omega}_a^{\,1} = \alpha\ e^{-\epsilon+\Delta\mu+\theta_a^+ f}, \\ &\overrightarrow{\omega}_a^{\,0} = \omega\ e^{-\epsilon+\theta_a^+ f}, \quad \overleftarrow{\omega}_a^{\,1} = \alpha'\ e^{-\epsilon+\Delta\mu-\theta_a^- f}, \\ &\overleftarrow{\omega}_a^{\,0} = \omega'\ e^{-\epsilon-\theta_a^- f}, \quad \overrightarrow{\omega}_b^{\,-1} = \alpha'\ e^{\theta_b^+ f}, \quad \overrightarrow{\omega}_b^{\,0} = \omega'\ e^{\theta_b^+ f}, \end{aligned} \tag{8}$$

In the above expressions, the values of the parameters $\theta_i^{\pm}$ are arbitrary except for the following constraint: After one period, the work done by F_e on the motor is $-F_e 2d$, implying that $\theta_a^+ + \theta_b^- + \theta_a^- + \theta_b^+ = 2$. Indeed, as shown in Fig. 4, the simplest model with all the $\theta_i^{\pm}$'s equal to 1/2, which was studied in Ref. [14], does not reproduce the experimental curves of velocity versus force for kinesin. The fact that the $\theta_i^{\pm}$'s are different from 1/2 agrees with standard models of kinesin, in which several chemical transitions are involved, and the force must be split unequally among the different transition rates [8]. We note that this splitting of the force (which involves the actual value of the $\theta_i^{\pm}$'s) is a matter of kinetics, whereas thermodynamics enforces only Eqs. (4) and (5). The expression of the rates given in Eqs. (6)–(8) is essential for the analysis which we develop below: we emphasize that these expressions are based on first principles. Once these rates are decomposed into an active and a passive part, the ratio of the passive transition rates in Eq. (5) follows from the condition of microreversibility (detailed balance), while the ratio of the active transition rates in Eq. (4) requires a more general principle for nonequilibrium chemical reactions. Such a principle is based on the notion of affinity, introduced by de Donder in Ref. [32] to characterize nonequilibrium chemical reactions. The de Donder equation relates the forward and the backward reactions rates $\vec{\alpha}$ and $\overleftarrow{\alpha}$ of an elementary step, as a consequence of transition state theory

$$\frac{\vec{\alpha}}{\overleftarrow{\alpha}} = e^{A/k_B T}, \tag{9}$$

where A is the affinity, defined as $-(\partial G/\partial\zeta)_{T,P}$ in terms of the Gibbs free energy G and ζ the extend of reaction. At equi-

librium, $A=0$ and Eq. (9) leads to $\vec{\alpha}=\overleftarrow{\alpha}$, which is the principle of microreversibility. Note that Eq. (4) is indeed of the form of Eq. (9), with the choice $\vec{\alpha}=\alpha_a$, $\overleftarrow{\alpha}=\alpha_b$, and $\Delta\mu=A/k_BT$ when $\epsilon=0$. Thus we can consider Eq. (4) as a De Donder relation, which generalizes the condition of microreversibility far from equilibrium [32]. Equivalently one can also interpret this equation as a particular case of generalized steady state balance conditions, we shall come back to this point in Sec. IV.

B. Effective description of the dynamics

Let us now further analyze the conditions for directed motion for this model, which as we mentioned earlier are required to break both the spatial symmetry and the symmetry associated with detailed balance. These conditions for directed motion can be derived by constructing an effective dynamics, which holds at long times and large length scales [14]. Let us first consider a coarse-grained description in which the position variable n is the only state variable. The chemical variable y may not be accessible or we simply do not wish to include it in this description. The dynamics of the motor is then described formally by a master equation, which can be obtained from Eq. (1) by integrating out over all possible values of y. We are then left with a coarse-grained master equation for $P_i(n,t)=\int dy P_i(n,y,t)$, which is

$$\partial_t P_i(n,t) = -(\overleftarrow{\omega}_i+\overrightarrow{\omega}_i)P_i(n,t) + [\overleftarrow{\omega}_j P_j(n+1,t)+\overrightarrow{\omega}_j P_j(n-1,t)], \quad (10)$$

with the same rates as before. Note that these rates may still depend on the ATP concentration. As shown in Ref. [14], an effective potential can be constructed for this problem by eliminating one of the sites (a or b) from the master equation (10), and describing the remaining dynamics in terms of an effective potential. This is the effective potential under which a random walker satisfying detailed balance would exhibit the same dynamics. Of course, the same effective evolution equation applies to occupation probabilities of site a or b. This reasoning [14] gives the effective energy difference $\Delta E=E(n+2)-E(n)$ between site n and site $n+2$, which we write as $\Delta E=2k_BT\Psi$ with

$$\Psi = \frac{1}{2}\ln\left(\frac{\overleftarrow{\omega}_a\overleftarrow{\omega}_b}{\overrightarrow{\omega}_a\overrightarrow{\omega}_b}\right). \quad (11)$$

When the rates of Eq. (8) are used, we find that

$$\Psi = \frac{1}{2}\ln\left(\frac{(\alpha+\omega)(\alpha' e^{\Delta\mu}+\omega')}{(\alpha e^{\Delta\mu}+\omega)(\alpha'+\omega')}\right) - f. \quad (12)$$

Note that the effective potential is independent of the load distribution factors $\theta_i^{\pm}$, and is identical to the expression obtained in Ref. [14] except for the change in the sign of the force [34]. A nice feature of Eq. (12) is that the conditions for directional motion can now be immediately obtained from it, in a way that is completely analogous to what is done for the ratchets models in Ref. [10]. Directed motion is only possible if the effective potential is tilted, i.e., $\Delta E\neq 0$. Thus directed motion requires (i) an asymmetric substrate which means either $\alpha\neq\alpha'$ or $\omega\neq\omega'$ and (ii) breaking of the detailed balance condition, so that either $\Delta\mu\neq 0$ or $f\neq 0$. When $\Delta\mu=f=0$ the system is in equilibrium, the effective potential is flat ($\Delta E=0$) and no directional motion is possible. A difference between this model and with the various ratchet models of Ref. [10], is that in ratchets the position of the motor is a continuous variable. In the classification of ratchet models given in Ref. [11], our model corresponds to a system of class A for which diffusion is not necessary for motion generation. In this class of models, the two ratchet potentials are identical and shifted with respect to each other in such a way that each chemical cycle generates with a high probability a step in the forward direction. As a consequence of this construction, one should expect (and indeed we will find) that in this model there is a strong coupling between the chemical and mechanical coordinates, and the motor has a strong directionality and a large thermodynamic efficiency.

III. MODES OF OPERATION OF THE MOLECULAR MOTOR, FIT OF EXPERIMENTAL CURVES AND THERMODYNAMIC EFFICIENCY

A. Description of the dynamics using generating functions

In this section, we analyze the long time behavior of our model using generating functions, which has the additional advantage of making the symmetry of the fluctuation theorem apparent as shown in the next section. Let us introduce the generating functions $F_i(\lambda,\gamma,t)\equiv\Sigma_y\Sigma_n e^{-\lambda n-\gamma y}P_i(n,y,t)$, whose time evolution is governed by $\partial_t F_i=\mathcal{M}_{ij}F_j$, where $\mathcal{M}[\lambda,\gamma]$ is the following 2×2 matrix which can be obtained from the master equation of Eq. (1):

$$\mathcal{M}[\lambda,\gamma] = \begin{bmatrix} -\overrightarrow{\omega}_a-\overleftarrow{\omega}_a & e^{\lambda}\overleftarrow{\rho}_b+e^{-\lambda}\overrightarrow{\rho}_b \\ e^{\lambda}\overleftarrow{\rho}_a+e^{-\lambda}\overrightarrow{\rho}_a & -\overleftarrow{\omega}_b-\overrightarrow{\omega}_b \end{bmatrix}, \quad (13)$$

with $\overrightarrow{\rho}_n(\gamma)\equiv\Sigma_l\overrightarrow{\omega}_n^l e^{-l\gamma}$ and $\overleftarrow{\rho}_n(\gamma)\equiv\Sigma_l\overleftarrow{\omega}_n^l e^{-l\gamma}$.

For $t\to\infty$, we find

$$\langle e^{-\lambda n-\gamma y}\rangle = \sum_i F_i(\lambda,\gamma,t)\sim\exp(\vartheta t), \quad (14)$$

where $\vartheta\equiv\vartheta[\lambda,\gamma]$ is the largest eigenvalue of $\mathcal{M}$. This eigenvalue, ϑ, contains all the steady-state properties of the motor and its exact expression is given by

$$\vartheta(\lambda) = \tfrac{1}{2}\{-\omega_a-\omega_b+[(\omega_a-\omega_b)^2 + 4(\overleftarrow{\rho}_b e^{\lambda}+\overrightarrow{\rho}_b e^{-\lambda})(\overleftarrow{\rho}_a e^{\lambda}+\overrightarrow{\rho}_a e^{-\lambda})]^{1/2}\}, \quad (15)$$

with the notations $\omega_a=\overrightarrow{\omega}_a+\overleftarrow{\omega}_a$ and $\omega_b=\overrightarrow{\omega}_b+\overleftarrow{\omega}_b$.

The average (normalized) velocity $\bar{v}$ is the current of the mechanical variable, which is given by

$$\bar{v} = \lim_{t\to\infty}\frac{\langle n(t)\rangle}{t} \quad (16)$$

and similarly the average ATP consumption rate r is the current of the chemical variable, which is given by

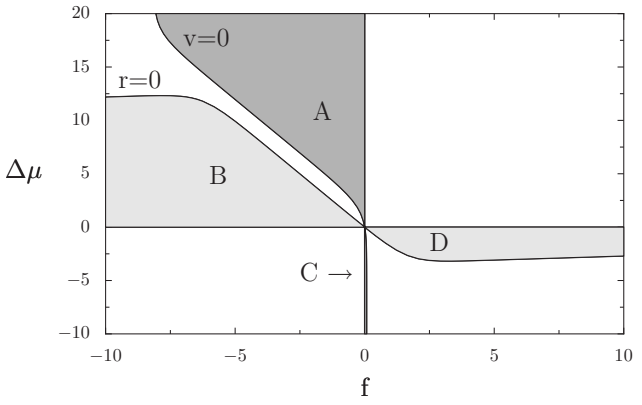

FIG. 3. Four modes of operation of a molecular motor, as delimited by $\bar{v}=0$ and $r=0$ [10]. The lines are generated with parameters that we have extracted by fitting the data for kinesin in Ref. [17] to our model, and this fit is shown in Fig. 4.

$$r = \lim_{t\to\infty} \frac{\langle y(t)\rangle}{t}. \tag{17}$$

From Eq. (14), we see that $\bar{v}=-\partial_\lambda \vartheta[0,0]$ and $r=-\partial_\gamma \vartheta[0,0]$ and from Eq. (15) we find explicitly that

$$\bar{v} = 2\frac{\vec{\omega}_a\vec{\omega}_b - \overleftarrow{\omega}_a\overleftarrow{\omega}_b}{\vec{\omega}_a + \vec{\omega}_b + \overleftarrow{\omega}_a + \overleftarrow{\omega}_b}, \tag{18}$$

$$r = \frac{(\overleftarrow{\omega}_a^{-1} + \vec{\omega}_a^{-1})(\vec{\omega}_b + \overleftarrow{\omega}_b) - (\overleftarrow{\omega}_b^{-1} + \vec{\omega}_b^{-1})(\vec{\omega}_a + \overleftarrow{\omega}_a)}{\vec{\omega}_a + \vec{\omega}_b + \overleftarrow{\omega}_a + \overleftarrow{\omega}_b}. \tag{19}$$

The method also gives access to higher moments of $n(t)$ and $y(t)$. The second moments for instance can be expressed in terms of the diffusion matrix

$$2D_{ij} = \frac{\partial^2 \vartheta}{\partial z_i \partial z_j}[0,0], \tag{20}$$

with the understanding that $z_1=\lambda$ and $z_2=\gamma$. These first and second moments can also be obtained by calculating the average of $n(t)$ and $y(t)$ directly from the master equation (1) [13,14,35].

B. Modes of operation of the motor

From the conditions of vanishing of the currents $\bar{v}=0$ and $r=0$, we can construct a full operation diagram of a motor, as shown in Fig. 3 for the case of kinesin. The curves $\bar{v}=0$ and $r=0$ define implicitly $f=f_{st}(\Delta\mu)$ (the stalling force) and $\Delta\mu=\Delta\mu_{st}(f)$, respectively. The stalling force is

$$f_{st}(\Delta\mu) = \frac{1}{2}\ln\left(\frac{(\alpha+\omega)(\alpha' e^{\Delta\mu}+\omega')}{(\alpha e^{\Delta\mu}+\omega)(\alpha'+\omega')}\right), \tag{21}$$

which means that for $f=f_{st}(\Delta\mu)$, $v=0$, and $\Psi=0$, where Ψ was defined in Eq. (12). At the stalling point, the mechanical variable is equilibrated but not the chemical variable. Therefore, in general, the motor consumes ATP, i.e., $r\neq 0$, even if it is stalled (in fact, it is only at equilibrium $f=\Delta\mu=0$ that both v and r vanish). Near stalling for $\Delta\mu\neq 0$, the motor evolves in a quasi-static manner but irreversibly. A similar phenomenon occurs in thermal ratchets [36,37].

Likewise, the condition $\Delta\mu=\Delta\mu_{st}(f)$ means that $r=0$. The explicit form of $\Delta\mu_{st}(f)$ is

$$\Delta\mu_{st}(f) = \ln\frac{(\alpha e^{-\theta_b^- f} + \alpha' e^{\theta_b^+ f})(\omega e^{\theta_a^+ f} + \omega' e^{-\theta_a^- f})}{(\alpha e^{\theta_a^+ f} + \alpha' e^{-\theta_a^- f})(\omega e^{-\theta_b^- f} + \omega' e^{-\theta_b^+ f})}. \tag{22}$$

The four different regimes of operation of the motor, discussed in Refs. [10,30] for ratchet models can be recovered here. In region A, where $r\Delta\mu>0$ and $f\bar{v}<0$, the motor uses chemical energy of ATP to perform mechanical work. This can be understood by considering a point on the y axis of Fig. 3 with $\Delta\mu>0$. There we expect that the motor drifts to the right with $\bar{v}>0$. Now in the presence of a small load $f<0$ on the motor, we expect that the motor is still going in the same direction although the drift is uphill and thus work is performed by the motor at a rate $\dot{W}=-f\bar{v}>0$. This holds as long as f is smaller than the stalling force, which defines the other boundary of region A. Similarly, in region B, where $r\Delta\mu<0$ and $f\bar{v}>0$, the motor produces ATP from mechanical work. In region C, where $r\Delta\mu>0$ and $f\bar{v}<0$, the motor uses ADP to perform mechanical work. In region D, where $r\Delta\mu<0$ and $f\bar{v}>0$, the motor produces ADP from mechanical work. It is interesting to note that the large asymmetry between regions A and C in Fig. 3 reflects the fact that kinesin is a unidirectional motor. Furthermore the regions A and B do not touch except at the origin. With kinesin operating in normal conditions in region A with $\Delta\mu\simeq 15$, the presence of a gap between regions A and B means that kinesin should not be able to switch into an ATP producing unit (region B), and indeed this has never been observed experimentally. Note that the explicit expressions for f_{st} and $\Delta\mu_{st}$ obtained in this model do not depend on the energy difference ϵ between the two states, due to a cancellation of the numerator and denominator in Eqs. (18) and (19). Thus the diagram of operation of the motor is valid for arbitrary value of ϵ.

C. Fit of experimental curves of velocity versus force for kinesin

We now discuss how the parameters of the model were determined using experimental data obtained for kinesin. In Fig. 4 (which is also Fig. 4 of Ref. [30]), we have fitted velocity vs. force curves for two values of ATP concentrations, and also several curves of velocity vs ATP concentration at different forces using the data of Ref. [17]. We have assumed that $e^{\Delta\mu}=k_0[\mathrm{ATP}]$, which is well verified at moderate or high levels of ATP. At low concentration of ATP, there is no such simple correspondence because it is no more legitimate to treat the ADP and P concentrations as constant. We think that this is probably the reason why the fit is not as good for the lowest ATP values (this concerns the first point in the curve at $F_e=-5.63$ pN and low ATP value in Fig. 4). Nevertheless, we can fit very well the majority of the experimental points with this model and we obtained the following values for the parameters: $\epsilon=10.81$, $k_0=1.4\times 10^5\ \mu\mathrm{M}^{-1}$, α

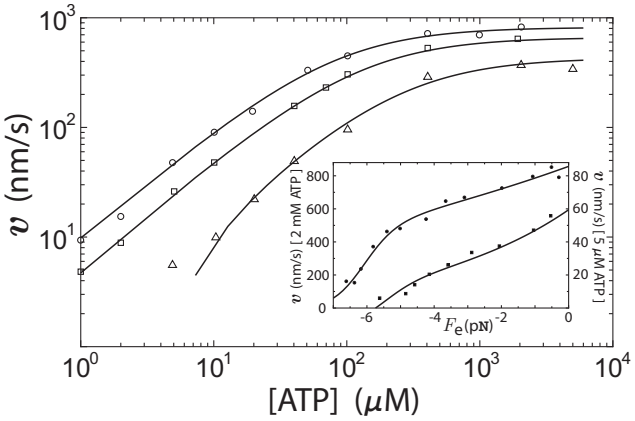

FIG. 4. Kinesin velocity vs ATP concentration under an external force [30]. The solid curves are the fits of our model to data from Ref. [17]. From the top down, the plots are for $F_e=-1.05,-3.59$ and -5.63 pN, respectively. Inset: Kinesin velocity vs force under a fixed ATP concentration. The solid curves are fits to the data of Ref. [17]. From the top down, the plots are for [ATP]=2 mM and 5 μM. From this fit, we obtained the following parameters for our model: $\epsilon=10.81$, $k_0=1.4\times10^5$ μM^{-1}, $\alpha=0.57$ s^{-1}, $\alpha'=1.3\times10^{-6}$ s^{-1}, $\omega=3.5$ s^{-1}, $\omega'=108.15$ s^{-1}, $\theta_a^+=0.25$, $\theta_a^-=1.83$, $\theta_b^+=0.08$, and $\theta_b^-=-0.16$.

$=0.57$ s^{-1}, $\alpha'=1.3\times10^{-6}$ s^{-1}, $\omega=3.5$ s^{-1}, $\omega'=108.15$ s^{-1}, $\theta_a^+=0.25$, $\theta_a^-=1.83$, $\theta_b^+=0.08$, and $\theta_b^-=-0.16$. These values are reasonable within the present accepted picture of the nano-operation of kinesin [8]. Indeed, ϵ and k_0^{-1} represent, respectively, the typical binding energy ($\sim 10k_BT$) of kinesin with microtubules and the ATP concentration at equilibrium ($\sim 10^{-5}$ μM). Moreover, $\theta_a^-=1.83$ indicates that the backsteps (transitions $a\to b$) of kinesin contain most of the force sensitivity [8]. Furthermore, our framework allows us to estimate a maximum stalling force of -7 pN.

A useful quantity to consider is the distance l, which is the motor walk using the hydrolysis of one ATP molecule, which is

$$l=\frac{\bar{v}}{r}. \tag{23}$$

We find for this model in agreement with Ref. [17]. that $l\simeq 0.97(2d)$ in the absence of load, which corresponds to one step (8 nm) per hydrolysis of one ATP molecule. Thus the coupling ratio of kinesin is indeed independent of ATP concentration and is 1:1 at negligible loads. We also find a global ATP consumption rate of $r\simeq 111$ s^{-1}, in excellent agreement with known values [8]. It should be remarked that the global ATP consumption rate measurements done in ATPase assays in the bulk are in agreement with the single molecule experiments, which are intrinsically very different experiments. Kinesin is well described by tightly coupled models which incorporate a single mechanically sensitive rate and this is consistent with our findings that there is only one transition (transitions $a\to b$) that has all the force sensitivity, i.e., the largest load distribution factor. In principle, by changing the parameters of the model, we could characterize motors which are less tightly coupled, but there will always be some coupling because, by construction, the mechanical steps are intrinsically linked with the chemical cycle.

We have compared our fit with that carried out by Fisher *et al.* in Ref. [13]. where the same data was fitted, and we observe that the outcome of both fits is comparable. In this comparison, there is an issue of complexity of the model under consideration to be taken into account. This is especially important in fitting experimental data of kinetics, which is typically hard to fit because one has many parameters to fit in an expression which is a sum of exponential functions. The model of Ref. [13] is of higher complexity because it involves four states instead of two states for our model, thus we might be tempted to say that our model does better in fitting the same data with less complexity. We believe that this is true when considering the data for the velocity only, but if we were to include also the data for the diffusion coefficient (which is related to the randomness parameter defined in Ref. [17]), we agree with Ref. [13] that a model with four states would then do better than a model with only two states.

D. Thermodynamic efficiency

Another important quantity that characterizes the working of a motor is its efficiency [10,36]. In region A, it is defined as the ratio of the work performed to the chemical energy

$$\eta=-\frac{f\bar{v}}{r\Delta\mu}=-\frac{fl}{\Delta\mu}. \tag{24}$$

By definition, η vanishes at $f=0$ and at the stalling force $f_{st}(\Delta\mu)$. Therefore, it has a local maximum $\eta_m(\Delta\mu)$ for some $f_m(\Delta\mu)$ between $f_{st}<f_m<0$. Near equilibrium, $\eta_m(\Delta\mu)$ has a constant value η_m^{eq} along a straight line $f_m(\Delta\mu)\propto\Delta\mu$ inside region A [10]. However, far from equilibrium, the picture is drastically different. We find that (i) $f_m(\Delta\mu)$ is no longer a straight line, (ii) $\eta_m-\eta_m^{eq}\propto\Delta\mu$ for small $\Delta\mu$, and (iii) $\eta_m\sim 1/\Delta\mu$ for large $\Delta\mu$. Therefore, η_m must have an absolute maximum at some $\Delta\mu>1$. One can also consider the curves of equal value of the efficiency within region A. In the particular case of the linear regime close to equilibrium, these curves are straight lines going through the origin [10], but in general far from equilibrium these curves are not straight lines as can be seen in Fig. 5, and the maximum efficiency is reached at a point within region A.

Note that η_m is substantially larger than η_m^{eq}. For instance with the parameters used in Fig. 5, the maximum efficiency is around 0.59 while $\eta_m^{eq}\simeq 0.03$ [see also Fig. 3(b) of Ref. [30] which contains a plot of η_m as a function of $\Delta\mu$ under the same conditions]. Hence, this motor achieves a higher efficiency in the far-from-equilibrium regime as was also found in other studies of molecular motors using continuous ratchet models (see, e.g., Ref. [11]). Under typical physiological conditions ($\Delta\tilde{\mu}\sim 10-25k_BT$), kinesin operates at an efficiency in the range of 40–60 %, in agreement with experiments [8]. It is interesting to note that kinesins operate most efficiently in an energy scale corresponding to the energy available from ATP hydrolysis.

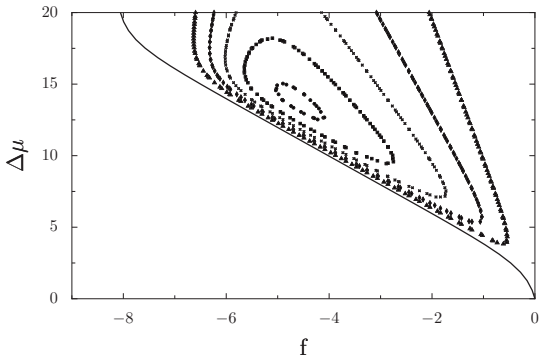

FIG. 5. Curves of equal efficiency η within region A (which is delimited by the solid line and by the y axis). The parameters are those used in Fig. 3 and obtained from the fit of Fig. 4. From the outside to the inside the curves correspond to $\eta=0.2$, $\eta=0.3$, $\eta=0.4$, $\eta=0.5$, and $\eta=0.58$. The absolute maximum efficiency for these parameters is about 59% and is located at $\Delta\mu\simeq 14$ and $f\simeq -4.9$.

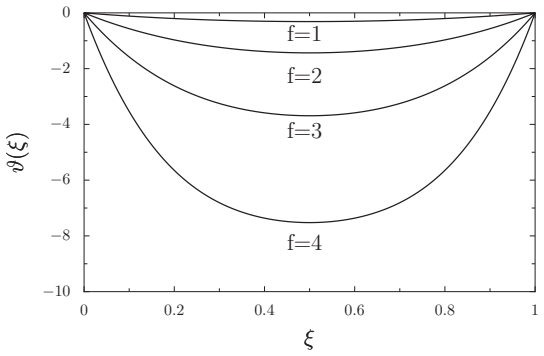

FIG. 6. Graphical illustration of the symmetry of the long-time fluctuation theorem (for simplicity a model without chemical variable has been used). The largest eigenvalue ϑ is shown as function of $\xi=\lambda/f$ for different values of the normalized force f. The symmetry of the long time fluctuation theorem corresponds to the symmetry of this curve with respect to $\xi=1/2$.

IV. FINITE TIME AND LONG TIME FLUCTUATION THEOREM

A. Long time FT

We note that the rates of Eq. (8) satisfy the following generalized detailed balance conditions:

$$\overrightarrow{\omega}_b^{-l} P_b^{\mathrm{eq}} = \overleftarrow{\omega}_a^{l} P_a^{\mathrm{eq}} e^{+(\theta_a^- + \theta_b^+)f - \Delta\mu l}, \tag{25}$$

$$\overleftarrow{\omega}_b^{-l} P_b^{\mathrm{eq}} = \overrightarrow{\omega}_a^{l} P_a^{\mathrm{eq}} e^{-(\theta_a^+ + \theta_b^-)f - \Delta\mu l}, \tag{26}$$

for $l=0,1$. Here, $P_a^{\mathrm{eq}}=1/(1+e^{-\epsilon})$ and $P_b^{\mathrm{eq}}=e^{-\epsilon}/(1+e^{-\epsilon})$ are the equilibrium probabilities corresponding to $f=0$ and $\Delta\mu=0$. We note that these relations (25) and (26), while valid arbitrarily far from equilibrium, still refer to the equilibrium state via the probabilities P_i^{eq}. Using the definition of the equilibrium probabilities, one can in fact rewrite Eqs. (25) and (26) as

$$\ln \frac{\overrightarrow{\omega}_b^{-l}}{\overleftarrow{\omega}_a^{l}} = \epsilon + (\theta_a^- + \theta_b^+)f - \Delta\mu l, \tag{27}$$

$$\ln \frac{\overleftarrow{\omega}_b^{-l'}}{\overrightarrow{\omega}_a^{l'}} = \epsilon - (\theta_a^+ + \theta_b^-)f - \Delta\mu l', \tag{28}$$

for $l,l'=0,1$. Note that these relations are analogous to the De Donder relation of Eq. (9) and to the transition state theory equations of Eqs. (4) and (5). Moreover, by combining these two equations, using the constraint that the sum of the load distribution factors is two and then multiplying the result by k_BT, one obtains

$$k_BT \ln \frac{\overrightarrow{\omega}_b^{-l}\overrightarrow{\omega}_a^{l'}}{\overleftarrow{\omega}_a^{l}\overleftarrow{\omega}_b^{-l'}} = F_e(2d) - \Delta\tilde{\mu}(l-l'), \tag{29}$$

which has the form of the steady state balance condition discussed in Refs. [38,39]. As pointed out in these references, by identifying the left hand side of Eq. (29) with the heat delivered to the medium, i.e., with the change of entropy of the medium, the right-hand side of Eq. (29) can be interpreted as the sum of the mechanical work $F_e(2d)$ and the chemical work $-\Delta\tilde{\mu}(l-l')$ on that particular set of cyclic transitions (l,l'). In that sense, Eqs. (27)–(29) can be understood as formulations of the first law at the level of elementary transitions. It is interesting to see that these steady state balance relations also lead to a FT as we now show below.

Using Eqs. (25) and (26), it can be shown that $\mathcal{M}$ and $\mathcal{M}^\dagger$, the adjoint of $\mathcal{M}$, are related by a similarity transformation

$$\mathcal{M}^\dagger[f-\lambda,\Delta\mu-\gamma] = \mathcal{Q}\mathcal{M}[\lambda,\gamma]\mathcal{Q}^{-1}, \tag{30}$$

where $\mathcal{Q}$ is the following diagonal matrix:

$$\mathcal{Q} = \begin{bmatrix} P_b^{\mathrm{eq}} e^{(\theta_a^+ + \theta_b^-)f/2} & 0 \\ 0 & P_a^{\mathrm{eq}} e^{(\theta_a^- + \theta_b^+)f/2} \end{bmatrix}. \tag{31}$$

This similarity relation implies that $\mathcal{M}[\lambda,\gamma]$ and $\mathcal{M}^\dagger[f-\lambda,\Delta\mu-\gamma]$ have the same spectra of eigenvalues and therefore

$$\vartheta[\lambda,\gamma] = \vartheta[f-\lambda,\Delta\mu-\gamma], \tag{32}$$

which is one form of FT. Since this relation holds at long times irrespective of the initial state, it is a Gallavotti-Cohen relation [32]. Such a symmetry is illustrated graphically on Fig. 6 for a simplified case where the chemical variable is absent.

B. Implications of FT in the linear regime

Here, we discuss the implications of FT in the linear regime, which leads to the Einstein and Onsager relations near equilibrium. Differentiating Eq. (32) with respect to λ and γ, we obtain

$$\bar{v} = -\frac{\partial\vartheta}{\partial\lambda}[0,0] = \frac{\partial\vartheta}{\partial\lambda}[f,\Delta\mu], \tag{33}$$

$$r = -\frac{\partial \vartheta}{\partial \gamma}[0,0] = \frac{\partial \vartheta}{\partial \gamma}[f,\Delta\mu]. \tag{34}$$

The response and fluctuations of a motor are quantified, respectively, by a response matrix λ_{ij} and by the diffusion matrix D_{ij} defined in Eq. (20). The physical meanings of λ_{ij} are as follows: $\lambda_{11} \equiv \partial \bar{v}/\partial f$ is the mobility, $\lambda_{22} \equiv \partial r/\partial \Delta\mu$ is the chemical admittance, and $\lambda_{12} \equiv \partial \bar{v}/\partial \Delta\mu$ and $\lambda_{21} \equiv \partial r/\partial f$ are the Onsager coefficients that quantify the mechanochemical couplings of the motor. Near equilibrium, where f and $\Delta\mu$ are small, a Taylor expansion of the right-hand sides of Eqs. (33) and (34) with respect to f and $\Delta\mu$ leads to

$$\left.\frac{\partial \vartheta}{\partial \lambda}\right|_{f,\Delta\mu} \simeq \left.\frac{\partial \vartheta}{\partial \lambda}\right|_{0,0} + f \left.\frac{\partial^2 \vartheta}{\partial^2 \lambda}\right|_{0,0} + \Delta\mu \left.\frac{\partial^2 \vartheta}{\partial \lambda\, \partial\, \gamma}\right|_{0,0}, \tag{35}$$

$$\left.\frac{\partial \vartheta}{\partial \gamma}\right|_{f,\Delta\mu} \simeq \left.\frac{\partial \vartheta}{\partial \gamma}\right|_{0,0} + f \left.\frac{\partial^2 \vartheta}{\partial \gamma\, \partial \lambda}\right|_{0,0} + \Delta\mu \left.\frac{\partial^2 \vartheta}{\partial^2 \gamma}\right|_{0,0}. \tag{36}$$

Using the definitions of $\bar{v}$ and r from Eqs. (33) and (34), one obtains directly

$$\bar{v} = \lambda_{11}^0 f + \lambda_{12}^0 \Delta\mu, \quad r = \lambda_{21}^0 f + \lambda_{22}^0 \Delta\mu, \tag{37}$$

with $\lambda_{ij}^0 = \partial_{z_i}\partial_{\tilde{z}_j}\vartheta[0,0]/2 \equiv D_{ij}$, which are the Einstein relations, and $\lambda_{12}^0 \equiv \partial_\gamma \partial_\lambda \vartheta[0,0]/2 = \partial_\lambda \partial_\gamma \vartheta[0,0]/2 \equiv \lambda_{21}^0$, which is the Onsager relation. Thus, FT describes the response and fluctuations near equilibrium [22,28].

It is interesting to investigate how Einstein or Onsager relations are broken in nonequilibrium situations. The "violations" of Einstein and Onsager relations when linear response theory is used in the vicinity of a nonequilibrium state rather than near an equilibrium state were studied in Ref. [30]. There, we quantified the violations of Einstein and Onsager relations, respectively, by four temperaturelike parameters T_{ij} and by the difference of the mechanochemical coupling coefficients $\Delta\lambda$. Of course, these effective temperatures are not thermodynamic temperatures: they are merely one of the ways to quantify deviations from Einstein relations; similarly our definition of $\Delta\lambda$ is just one of the possible ways to study the "violations" of Onsager relations: strictly speaking there are no real violations since Einstein and Onsager relations apply only to systems at equilibrium. We have shown in Ref. [30] some of the possible behaviors of T_{ij} and $\Delta\lambda$ for a kinesin motor using the parameters of the fit discussed above: in particular, we found that for kinesin the maximum value of $\Delta\lambda$ is $\Delta\lambda \sim 45$ pN^{-1} s^{-1}, and that at large $\Delta\mu$, $\Delta\lambda \sim -10$ pN^{-1} s^{-1}. We also found that (i) one of the Einstein relations holds near stalling [a point which we justify more precisely in the next section in Eq. (59)], (ii) the degree by which the Onsager symmetry is broken ($\Delta\lambda \neq 0$) is largely determined by the underlying asymmetry of the substrate, (iii) only two "effective" temperatures characterize the fluctuations of tightly coupled motors, (iv) kinesin's maximum efficiency and the maximum violation of Onsager symmetry occur roughly at the same energy scale, corresponding to that of ATP hydrolysis ($\sim 20 k_B T$) [30]. Experimental and theoretical violations of the fluctuation-dissipation relation have been observed and studied in many active biological systems [1,3–5,7], but to our knowledge no experiments testing the fluctuation-dissipation or the Onsager relations have been carried out at the single motor level.

C. Finite time FT

The similarity transformation (30) implies that all the eigenvalues of $\mathcal{M}[\lambda,\gamma]$ and $\mathcal{M}^\dagger[f-\lambda,\Delta\mu-\gamma]$ are identical, not just the largest one. This more general property allows us to prove a transient FT, because the dynamics of the model at finite time involves all the eigenvalues of $\mathcal{M}$ and not just the largest one. The price to pay to have a FT relation valid at finite time is that the initial state can no more be arbitrary. We show here that the relation still holds, in the particular case when the initial state is prepared to be in an equilibrium state (which corresponds to the condition $f=\Delta\mu=0$) and when, in addition, a specific condition on the load distribution factors is obeyed. To see how this comes about in this model, we assume that the motor at time $t=0$ is at the origin $n(0)=y(0)=0$ in an equilibrium state, and we calculate the values of the position $n(t)$ and of the chemical variable $y(t)$ at time t. We denote the initial state by the vector

$$|F_0\rangle = |F(t=0)\rangle = \begin{pmatrix} P_a^{\mathrm{eq}} \\ P_b^{\mathrm{eq}} \end{pmatrix}.$$

With $\langle 0| = (1,1)$, the initial state vector is normalized since $\langle 0|F_0\rangle = 1$. Let us introduce $\mathcal{U}(\lambda,\gamma,t) = e^{\mathcal{M}[\lambda,\gamma]t}$, the evolution operator for the generating functions F_i. By taking the exponential of Eq. (30), one finds that this operator also obeys an FT relation

$$\mathcal{U}^\dagger[f-\lambda,\Delta\mu-\gamma,t] = \mathcal{Q}\mathcal{U}[\lambda,\gamma,t]\mathcal{Q}^{-1}. \tag{38}$$

We calculate the following average, similar to Eq. (14):

$$\begin{aligned}
\langle e^{-(f-\lambda)n(t)-(\Delta\mu-\gamma)y(t)}\rangle &= \langle 0|\mathcal{U}(f-\lambda,\Delta\mu-\gamma,t)|F_0\rangle, \\
&= \langle F_0|\mathcal{U}^\dagger(f-\lambda,\Delta\mu-\gamma,t)|0\rangle, \\
&= \langle F_0|\mathcal{Q}\mathcal{U}(\lambda,\gamma,t)\mathcal{Q}^{-1}|0\rangle, \\
&= \langle 0|\mathcal{U}(f,\gamma,t)|F_0\rangle, \\
&= \langle e^{-\lambda n(t)-\gamma y(t)}\rangle.
\end{aligned} \tag{39}$$

We have used Eq. (38) to derive the third equality, and the final equation requires the condition $\langle F_0|\mathcal{Q} = \langle 0|$, which is equivalent to $\mathcal{Q}^{-1}|0\rangle = |F_0\rangle$ since $\mathcal{Q}$ is diagonal. Using Eq. (31), we find that this relation holds if the initial state is in equilibrium and if the following condition holds

$$\theta_a^- + \theta_b^+ = \theta_a^+ + \theta_b^-. \tag{40}$$

Equation (39) is analogous to the Evans transient time fluctuation theorem [24] and to the Crooks relation [25]. An important point here is that the initial state must be an equilibrium state while the final state at time t does not have to be (and in general is not) an equilibrium state. Crooks relation can be derived using a path representation of the ratio of forward to backward probabilities according to a specific protocol, assuming a Markov process and using a general-

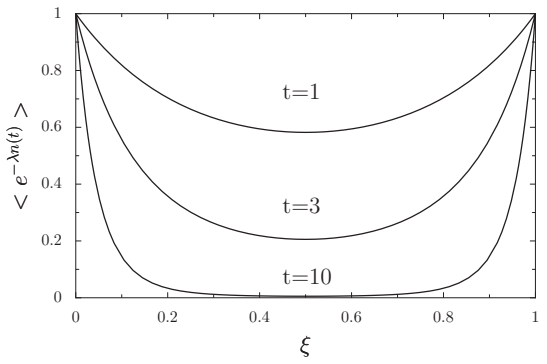

FIG. 7. Graphical illustration of the symmetry of the finite-time fluctuation theorem for a simplified model without chemical variable. The left hand side of Eq. (39) is shown as function of $\xi=\lambda/f$ for different times (arbitrary units). The symmetry of the finite time fluctuation theorem amounts to the symmetry of this curve with respect to $\xi=1/2$.

ized detailed balance relation between successive states. In our case, the equivalent of the generalized "local" detailed balance condition needed for the proof is Eq. (38). The symmetry of the transient fluctuation theorem is illustrated graphically in Fig. 7 for a simplified case where the chemical variable is absent (or integrated out).

V. FLUCTUATION THEOREM FOR THE LARGE DEVIATION FUNCTION

A. Explicit calculation of the large deviation function of the current

Here, we again take advantage of our knowledge of the function ϑ, which contains all the information about the long time dynamical properties of the model, to obtain an explicit expression for the large deviation function of the current. To simplify the presentation, we consider the simplified description, given in Eq. (10), in which the chemical variable y is not taken into account. In this case, the generating function is defined by $F_i(\lambda,t)\equiv\Sigma_y\Sigma_n e^{-\lambda n}P_i(n,y,t)$, and the matrix $\mathcal{M}[\lambda]$ becomes

$$\mathcal{M}[\lambda]=\begin{bmatrix} -\overrightarrow{\omega_a}-\overleftarrow{\omega_a} & e^{\lambda}\overleftarrow{\omega_b}+e^{-\lambda}\overrightarrow{\omega_b} \\ e^{\lambda}\overleftarrow{\omega_a}+e^{-\lambda}\overrightarrow{\omega_a} & -\overleftarrow{\omega_b}-\overrightarrow{\omega_b} \end{bmatrix}. \tag{41}$$

By definition, ϑ is the largest eigenvalue of $\mathcal{M}(\lambda)$, so similarly to Eq. (15) we have

$$\vartheta(\lambda)=\frac{1}{2}\{-\omega_a-\omega_b+[(\omega_a-\omega_b)^2+4(\overleftarrow{\omega_b}e^{\lambda}+\overrightarrow{\omega_b}e^{-\lambda})(\overleftarrow{\omega_a}e^{\lambda}+\overrightarrow{\omega_a}e^{-\lambda})]^{1/2}\}, \tag{42}$$

with the notations $\omega_a=\overrightarrow{\omega_a}+\overleftarrow{\omega_a}$ and $\omega_b=\overrightarrow{\omega_b}+\overleftarrow{\omega_b}$.

We have already seen that $\vartheta(\lambda)$ has the property that $\langle e^{-\lambda n}\rangle\sim e^{\vartheta(\lambda)t}$ for large t. On the other hand, the large deviation function $G(v)$ is defined for large time t by

$$\mathcal{P}\left(\frac{n}{t}=v\right)\sim e^{-G(v)t}, \tag{43}$$

in terms of $\mathcal{P}(n/t=v)$ the probability to observe a current v after the motor has gone a distance n from the origin in a time t. The relation between $\vartheta(\lambda)$ and $G(v)$ is

$$\langle e^{-\lambda n}\rangle=\int e^{-\lambda n}dn\mathcal{P}(n), \tag{44}$$

$$=\int tdv\mathcal{P}\left(\frac{n}{t}=v\right)e^{-\lambda vt}, \tag{45}$$

$$\sim\int dve^{[-G(v)-\lambda v]t}. \tag{46}$$

Using the saddle point method, we find that $\vartheta(\lambda)=\max_v[-G(v)-\lambda v]$ and thus $\vartheta(\lambda)$ and $G(v)$ are Legendre transform of each other. We have also $-G(v)=\max[\vartheta(\lambda)+\lambda v]$, which can be written in parametric form

$$\frac{\partial\vartheta}{\partial\lambda}[\lambda=\lambda^*]+v=0, \tag{47}$$

$$\vartheta(\lambda^*)+\lambda^* v=-G(v). \tag{48}$$

Using Eqs. (42)–(48), we find the following expressions for $G(v)$ (see the Appendix for details of the derivation): for $v>0$

$$G(v)=\frac{\omega_a+\omega_b}{2}+\frac{\sqrt{\Omega}}{2v}\left(Y^-(v)-\frac{1}{Y^-(v)}\right)-v\lambda^-(v) \tag{49}$$

and for $v<0$,

$$G(v)=\frac{\omega_a+\omega_b}{2}+\frac{\sqrt{\Omega}}{2v}\left(Y^+(v)-\frac{1}{Y^+(v)}\right)-v\lambda^+(v), \tag{50}$$

where

$$Y^{\pm}(v)=\frac{1}{2}(Z(v)\pm\sqrt{Z(v)^2-4}),$$
$$\lambda^{\pm}(v)=-\frac{\Psi}{2}+\frac{1}{2}\ln\left(\frac{Z(v)\pm\sqrt{Z(v)^2-4}}{2}\right), \tag{51}$$

and

$$Z(v)=\frac{v^2}{\sqrt{\Omega}}+\left(\frac{v^4}{\Omega}+4+\frac{v^2\Sigma^2}{\Omega}\right)^{1/2}, \tag{52}$$

with the following parameters:

$$\Omega=4\overrightarrow{\omega_a}\overrightarrow{\omega_b}\overleftarrow{\omega_a}\overleftarrow{\omega_b}, \tag{53}$$

$$\Sigma^2=(\omega_a+\omega_b)^2-4(\overleftarrow{\omega_a}\overleftarrow{\omega_b}+\overrightarrow{\omega_a}\overrightarrow{\omega_b}), \tag{54}$$

and Ψ is the effective potential defined in Eq. (11). As shown in Fig. 8, the function $G(v)$ has a single minimum at the average velocity $v=\bar{v}$, which was defined in Eq. (18), and at

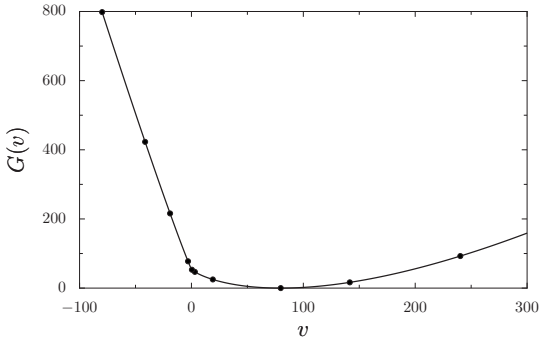

FIG. 8. Large deviation function $G(v)$, the solid line is the exact expression using Eqs. (49) and (50) and the points are the numerical evaluation of the Legendre transform using Eq. (48). For the values of the rates used here, the average velocity, as given by Eq. (18), is $\bar{v} \simeq 80$: thus, the system is far from equilibrium. Note that $G(v)$ is minimum at $\bar{v}$ and that $G(\bar{v})=0$.

this point $G(v=\bar{v})=0$, which can be deduced from Eq. (48). Remarkably, although $G(v)$ is a complicated nonlinear function of v, the difference $G(v)-G(-v)$ is a simple linear function of v as required by the fluctuation theorem. Using the expressions (48) and (49), it is straightforward to verify that

$$G(v) - G(-v) = \Psi v, \tag{55}$$

which in turns implies that the ratio of the probabilities to observe v or $-v$ for large t must obey

$$\frac{\mathcal{P}\left(\frac{n}{t}=v\right)}{\mathcal{P}\left(\frac{n}{t}=-v\right)} = e^{-\Psi v t}. \tag{56}$$

From Eq. (55), and the fact that $G(v)$ and $\vartheta(\lambda)$ are related by a Legendre transform, we obtain a third formulation of the fluctuation theorem

$$\vartheta(\lambda) = \vartheta(-\Psi - \lambda). \tag{57}$$

Near equilibrium, the large deviation function is well approximated by a half parabola when both v when $\bar{v}$ are either positive or negative. For $\bar{v}>0$, this part of the large deviation function becomes flatter and flatter, when going away from equilibrium (i.e., for increasing entropy production). As a result, the remaining part of the large deviation function for $v<0$ must be linear $G(v<0) \simeq -\Psi v$, so that Eq. (55) is obeyed. This linear part for $v<0$ and the half parabola for $v>0$ can be seen in Fig. 8.

It is interesting to note the central role played by the quantity Ψ defined initially as an effective potential, and which now enters the three formulations of the fluctuation theorem in Eqs. (55)–(57). Note that these equations were obtained for arbitrary forms of the rates $\overrightarrow{\omega_a}$, $\overrightarrow{\omega_b}$, $\overleftarrow{\omega_a}$, and $\overleftarrow{\omega_b}$. If we make a specific choice for these rates as in Eq. (8), with no chemistry, i.e., for $\Delta\mu=0$, we recover $\Psi=-f$, and then Eq. (57) reduces to $\vartheta(f-\lambda)=\vartheta(\lambda)$, which is indeed compatible with Eq. (32) when there is no chemical variable and no dependence on the rates on chemistry. If the rates are those of Eq. (8) for $\Delta\mu \neq 0$, we obtain using Eq. (12), the expression

$$\frac{\mathcal{P}\left(\frac{n}{t}=v\right)}{\mathcal{P}\left(\frac{n}{t}=-v\right)} = e^{[f-f_{\rm st}(\Delta\mu)]vt} \quad (\text{for } t\to\infty) \tag{58}$$

with the stalling force defined in Eq. (21), and related to Ψ by $\Psi=-f+f_{\rm st}(\Delta\mu)$.

Note that an Einstein relation can be obtained near stalling, by performing a Taylor expansion of the right-hand side of Eq. (57) with respect to $-\Psi$, in a way similar to what was done in Eqs. (35) and (36) for the derivation of the Einstein and Onsager relations. This procedure means that for $f \simeq f_{\rm st}(\Delta\mu)$,

$$\bar{v} \simeq \frac{1}{2}[f - f_{\rm st}(\Delta\mu)] \left.\frac{\partial^2\vartheta}{\partial^2\lambda}\right|_0, \tag{59}$$

which shows that near the stalling force, the Einstein relation holds in this description where the chemical variable is absent [30].

B. Discussion

Note that Eq. (58) puts a constraint on the ratio of the probabilities of observing a velocity v to the probability of observing a velocity $-v$. These velocities should be estimated from the ratio n/t based on an observation of the motor running a distance n (or a distance $-n$), after a time t. This relation has been proven here in the limit of long time t, but we expect that such a relation will also hold at finite time t under some conditions, as suggested by our derivation of the transient FT of Eq. (39). Such a relation at finite time was also investigated in Ref. [28].

Single molecule experiments on kinesin in which backward steps were studied were performed in Refs. [19,40]. In particular, it was shown in these references that ATP binding was necessary for backward steps, and that the ratio of the overall probability of making one forward step (whatever the time) to the overall probability of making one backward step (whatever the time) is an exponential function of the load, which approaches one near the stalling force. It is important to point out that this ratio which was measured experimentally is not the same quantity as the left-hand side of Eq. (58) although both quantities should be related. In view of this, Eq. (58) should be considered as a prediction for the behavior of single motors like kinesin, which to our knowledge has not yet been tested experimentally. This suggests that it would be very interesting to probe Eq. (58) experimentally, by trying to compute directly the distributions $\mathcal{P}(\frac{n}{t}=\pm v)$ for various times. At the same time, it would be also useful to study more extensively the behavior of motors of various types near stalling as function of the ATP concentration. No notable difference could be measured in the stalling force at an ATP concentration 1 mM or 10 μM in the experiments of Ref. [19] on kinesin, although in principle according to general grounds [16,38] one should expect that the behavior of motors near stalling (and in particular the stalling force of the motor itself) should depend on the ATP concentration and more generally on the details of the chemical cycle of ATP hydrolysis.

C. Other forms of FT relations

We have seen that the form of the FT relation depends on the state variables of the system, or in other words, it depends on the level of coarse-graining of the description. We consider in this paper the following levels of description. (I) The mechanical displacement n is the only state variable. (II) The chemical variable y is the only state variable. (III) Both variables n and y are taken into account. For case (I), the dynamics is described by the simplified master equation (10) and Eqs. (55)–(57) are the appropriate forms of FT. For case (II), we find that FT can be written in the following forms [we shall omit the large deviation function form of FT for cases (II) and (III)]:

$$\frac{\mathcal{P}\left(\frac{y}{t}=r\right)}{\mathcal{P}\left(\frac{y}{t}=-r\right)}=e^{-\chi rt}, \tag{60}$$

which also holds generally for $t\to\infty$ and

$$\vartheta(\gamma)=\vartheta(-\chi-\gamma). \tag{61}$$

In the above two equations, $-\chi$ can be interpreted as the affinity [32] associated with a chemical cycle (see the representation of the chemical cycle in Fig. 2, and the next section for a discussion on the notion of affinity). We find that χ is given by

$$\chi=\ln\left(\frac{\omega_b^{-1}\omega_a^0}{\omega_a^1\omega_b^0}\right), \tag{62}$$

where $\omega_a^l=\vec{\omega}_a^l+\overleftarrow{\omega}_a^l$ and $\omega_b^l=\vec{\omega}_b^l+\overleftarrow{\omega}_b^l$ for $l=-1,0$ or 1. The physical interpretation of χ can be clarified by using a method similar to [14]: after integrating out the position variable n from Eq. (1), and decimating over the odd or even sites, one can derive an effective evolution equation for the occupation probabilities of the remaining sites. In this equation, χ plays the role of a effective potential for the chemical variable. When the rates of Eq. (8) are used, we find that this quantity is given by

$$\chi=-\Delta\mu+\Delta\mu_{\mathrm{st}}(f). \tag{63}$$

As expected, the conditions for which χ vanishes are the same as those for which the chemical current r, given in Eq. (19), vanishes.

For case (III), the FT can be written as follows:

$$\frac{\mathcal{P}\left(\frac{n}{t}=v,\frac{y}{t}=r\right)}{\mathcal{P}\left(\frac{n}{t}=-v,\frac{y}{t}=-r\right)}=e^{-(\tilde{\Psi}v+\tilde{\chi}r)t} \tag{64}$$

for $t\to\infty$ and

$$\vartheta(\lambda,\gamma)=\vartheta(-\tilde{\Psi}-\lambda,-\tilde{\chi}-\gamma). \tag{65}$$

Here, the affinities associated with the mechanical and chemical variables are given, respectively, by $-\tilde{\Psi}$ and $-\tilde{\chi}$. Note that these quantities are in general not the same as the ones calculated above in cases (I) and (II) (i.e., $\tilde{\Psi}\neq\Psi$ and $\tilde{\chi}\neq\chi$). When the rates of Eq. (8) are used, $\tilde{\Psi}=-f$ and $\tilde{\chi}=-\Delta\mu$, so that Eq. (32) is recovered from Eq. (65).

VI. FLUCTUATION THEOREM AND ENTROPY PRODUCTION

In this section, we discuss the connections between the fluctuation theorem described in the last section and the entropy production [23]. In particular, we show by an explicit calculation, that the parameters Ψ, χ, f, and $\Delta\mu$ that appear in the symmetry relations Eqs. (55)–(58) are identical to the affinities associated with the various macroscopic currents (mechanical and chemical) flowing in the system [28]. Affinities, introduced a long time ago in chemical thermodynamics [32], represent intrinsic quantities that depend only on the microscopic transition rates of the system. Thus, the fact that these quantities also appear in the fluctuations theorems, valid far from equilibrium, shows a remarkable connection between classical thermodynamics and nonequilibrium statistical mechanics.

We shall first discuss the simplified model, in which the chemical variable y is not taken into account in the description as a state variable [case (I)]. The mechanical entropy $S_M(t)$ then only contains contribution from the disorder in the distribution of the mechanical variable n and is defined as

$$S_M(t)=-\sum_{i=a,b}\sum_n P_i(n,t)\ln P_i(n,t) \tag{66}$$

in units where $k_B=1$. Using the master equation (10), one can calculate the variation of $S_M(t)$ with time

$$\frac{dS_M}{dt}=\sum_{i\neq j}\sum_n[\vec{\omega}_iP_i(n,t)-\overleftarrow{\omega}_jP_j(n+1,t)]\ln\frac{P_i(n,t)}{P_j(n+1,t)}, \tag{67}$$

where i,j take the two possible values a and b but are different from each other. By transforming the last term in this equation as follows:

$$\ln\frac{P_i(n,t)}{P_j(n+1,t)}=\ln\frac{\vec{\omega}_iP_i(n,t)}{\overleftarrow{\omega}_jP_j(n+1,t)}-\ln\frac{\vec{\omega}_i}{\overleftarrow{\omega}_j},$$

the time derivative of the entropy can be rewritten as the difference of an entropy production (which is always positive) and an entropy flux. Since we are interested in a stationary state where $dS/dt=0$, both contributions must be equal. From such a calculation, one finds that the entropy production and the entropy flux in the long time limit are given by

$$\Pi_{\mathrm{M}}=\frac{\vec{\omega}_a\vec{\omega}_b-\overleftarrow{\omega}_a\overleftarrow{\omega}_b}{\vec{\omega}_a+\vec{\omega}_b+\overleftarrow{\omega}_a+\overleftarrow{\omega}_b}\ln\left(\frac{\vec{\omega}_a\vec{\omega}_b}{\overleftarrow{\omega}_a\overleftarrow{\omega}_b}\right)=-\Psi\bar{v}, \tag{68}$$

where Ψ is the effective potential defined in Eq. (11), and $\bar{v}$ is defined in Eq. (18). According to the general definition [28], we deduce from Eq. (68) that the mechanical affinity of the displacement variable is $-\Psi$.

It is interesting to recall that this result can also be derived in a different way: in Ref. [23], it was proven that the entropy flux can be calculated by using a fluctuating quantity $W(t)$, called the action functional, which can be seen as a local measure of the lack of detailed balance on a given path at time t. The matrix $\mathcal{N}(\nu)$ that describes the evolution of the

generating function of $\langle \exp[-\nu W(t)] \rangle$ is given by

$$\mathcal{N} = \begin{bmatrix} -\overrightarrow{\omega}_a - \overleftarrow{\omega}_a & \overleftarrow{\omega}_a^{(1-\nu)} \overrightarrow{\omega}_b^{\nu} + \overleftarrow{\omega}_b^{\nu} \overrightarrow{\omega}_a^{(1-\nu)} \\ \overleftarrow{\omega}_b^{(1-\nu)} \overrightarrow{\omega}_a^{\nu} + \overleftarrow{\omega}_a^{\nu} \overrightarrow{\omega}_b^{(1-\nu)} & -\overleftarrow{\omega}_b - \overrightarrow{\omega}_b \end{bmatrix}.$$

This matrix is obtained by deforming the original Markov matrix by a parameter ν. We emphasize that this deformation is not the same as that used in Eq. (41) to calculate the large deviation of the currents. The time derivative of $W(t)$ is precisely the entropy flux. Therefore, we have, in agreement with Eq. (68),

$$\Pi_M = -\frac{\partial q}{\partial \nu}(0) = -\bar{v}\Psi, \tag{69}$$

where $q(\nu)$ is the largest eigenvalue of $\mathcal{N}(\nu)$. Since the matrix $\mathcal{N}$ has the property $\mathcal{N}^{\dagger}(\nu) = \mathcal{N}(1-\nu)$, its largest eigenvalue $q(\nu)$ satisfies a fluctuation theorem

$$q(1-\nu) = q(\nu). \tag{70}$$

Note that Eq. (68) is valid for arbitrary transition rates; if we make a specific choice for the rates such as that of Eq. (8), we find that $\Pi = [-f + f_{\mathrm{st}}(\Delta\mu)]\bar{v}$ when $\Delta\mu \neq 0$. When $\Delta\mu = 0$, we recover $\Pi = -f\bar{v}$, a well-known result [11], but our more general expression for $\Delta\mu \neq 0$ shows explicitly the dependence of the entropy production on a measurable quantity $\Delta\mu$ and its connection to the FT which we saw in Eq. (58).

If we now use a description of the model where only the chemical variable y is taken into account [case (II)] and the total displacement n is integrated out, we can define a "chemical entropy" $S_{\mathrm{C}}(t)$ as follows:

$$S_{\mathrm{C}}(t) = -\sum_{i=a,b} \sum_{y} P_i(y,t) \ln P_i(y,t). \tag{71}$$

Calculations similar to the ones described above allow us to derive the purely chemical entropy production in the stationary state

$$\Pi_{\mathrm{C}} = \frac{\omega_a^1 \omega_b^0 - \omega_a^0 \omega_b^{-1}}{\omega_a + \omega_b} \ln\left(\frac{\omega_a^1 \omega_b^0}{\omega_b^{-1} \omega_a^0} \right) = -r\chi; \tag{72}$$

the chemical current r and the chemical affinity χ were defined in Eq. (19) and Eq. (62), respectively. We also note that the entropy production in Eq. (73) can be calculated using an action functional whose generating function is the largest eigenvalue of the Markov matrix suitably deformed [23].

Finally, we can use the complete description of Eq. (1), in which both the displacement n and the chemical variable y are taken into account [case (III)]. In this case, the entropy is given by

$$S(t) = -\sum_{i=a,b} \sum_{n} \sum_{y} P_i(n,y,t) \ln P_i(n,y,t). \tag{73}$$

Again, if we make the specific choice for the rates of Eq. (8), we find that the following well-known result [11] is recovered for the entropy production:

$$\Pi = f\bar{v} + r\Delta\mu. \tag{74}$$

This relation makes explicit the fact that f is the affinity of the mechanical position variable with the current $\bar{v}$, and that $\Delta\mu$ is the affinity of the chemical variable with the current r. We note that these affinities are different from those found above in the purely mechanical and in the purely chemical models, which correspond respectively to Eqs. (11) and (63). The fact that the expression of the entropy (and hence that of the affinity) strongly depends on the level of coarse-graining used in a given description should not come as a surprise. The two affinities f and $\Delta\mu$ appear in the Gallavotti-Cohen relation (32). This suggests that one should be able to construct an effective potential describing the evolution of the motor in a two-dimensional phase space of n and y, and that this potential should be equivalent to the potential of mean force discussed in Ref. [41].

We have seen here that the FT for the currents and the FT for the entropy are closely related; this fact is true for a large class of models as explained in Ref. [23]. However, although the FT for the entropy holds generally for any Markovian dynamics as shown in Ref. [23], a FT for the currents exists only if the dynamics can be decomposed into cycles with well defined affinities [28]. This is why the periodicity of the motion of the motor along track and of the evolution of the chemical variable was a crucial assumption in our derivation of the FT for the currents but was not used when deriving the FT for the entropy.

VII. CONCLUSION

We have studied a discrete stochastic model of a molecular motor, which is a minimal ratchet model. We made contact in this paper between various formulations of FT. Through a detailed analysis of a simple model, we have brought out some physical implications of FT for molecular motors in general and for kinesin in particular. One important message is that FT puts constraints on the operation of a molecular motor or nanomachines far from equilibrium. Further experimental work and theoretical modeling is necessary to check more precisely the implications of FT for molecular motors. For instance, it would be interesting to study a molecular motor in which both the velocity and the average ATP consumption rate could be measured simultaneously, or if this is too difficult study more extensively the behavior of motors near the stalling force as function of ATP concentration. This would allow a study of the violations of the fluctuation-dissipation at the level of a single motor, which would lead to much deeper insights into the mechanotransduction mechanism of molecular motors.

Due to the broad applicability of the ratchet concept in biological systems, we believe that the results of this paper should be of general applicability: the model could describe processive molecular motors of various types, nanomachines similar to enzymes performing chemical cycles or polymers which are translocated through a pore under the action of a force (for instance, the force created by an electric field applied to a charged polymer). More generally, we hope that the present work illustrates the usefulness of statistical physics of nonequilibrium systems for the understanding of active systems, and in particular biological systems.

ACKNOWLEDGMENTS

We acknowledge stimulating discussions with A. Ajdari, M. Schindler, J.F. Joanny, F. Jülicher, and J. Prost. We thank C. Schmidt for pointing out to us Ref. [19]. A.W.C.L. acknowledges support from the ESPCI (Chaire Joliot) and from NSF Grant No. DMR-0701610 (for A.W.C.L.). D.L. acknowledges support from the Indo-French Center for Grant No. 3504-2.

APPENDIX: CALCULATION OF THE LARGE DEVIATION FUNCTION $G(v)$

To obtain an explicit form for $G(v)$, we take the square of Eq. (47),

$$\left(\frac{\partial \vartheta}{\partial \lambda}[\lambda = \lambda^*]\right)^2 = v^2. \tag{A1}$$

Using Eq. (42) the derivative on the left-hand side can be written as

$$\frac{\partial \vartheta}{\partial \lambda} = \frac{1}{4}\frac{U'(\lambda)}{\sqrt{U(\lambda)}}, \tag{A2}$$

with $U(\lambda)=(\omega_a-\omega_b)^2+4(\overleftarrow{\omega_b}e^{\lambda}+\overrightarrow{\omega_b}e^{-\lambda})(\overleftarrow{\omega_a}e^{\lambda}+\overrightarrow{\omega_a}e^{-\lambda})$. After performing the change of variable

$$Y = e^{2\lambda}\sqrt{\frac{\overleftarrow{\omega_a}\overleftarrow{\omega_b}}{\overrightarrow{\omega_a}\overrightarrow{\omega_b}}}, \tag{A3}$$

and using the parameters Ω and Σ introduced in Eqs. (53) and (54), we can write

$$U'(\lambda) = 4\sqrt{\Omega}\left(Y - \frac{1}{Y}\right), \tag{A4}$$

and Eq. (A1) becomes

$$16\Omega\left(Y - \frac{1}{Y}\right)^2 = 16v^2\left[\Sigma^2 + 2\sqrt{\Omega}\left(Y + \frac{1}{Y}\right)\right]. \tag{A5}$$

We deduce that $Z=Y+1/Y$ satisfies

$$Z^2 - \frac{2v^2}{\sqrt{\Omega}}Z - 4 - \frac{v^2\Sigma^2}{\Omega} = 0. \tag{A6}$$

There are two solutions to this equation but since $Z>0$, only the positive solution must be retained which is Eq. (52). To obtain Y in terms of $Z(v)$, one must solve another second order equation $Y^2-ZY+1=0$. This equation has two positive acceptable solutions, which are the two solutions $Y^{\pm}(v)$ of Eq. (51). We have $Y^+(v)>Y^-(v)=1/Y^+(v)$. Using Eqs. (47) and (A2), we see that $Y^+(v)$ corresponds to $v<0$. Similarly, $Y^-(v)$ corresponds to $v<0$. Once the relation $Y=Y(v)$ is determined, it is easily inverted using Eq. (A3) to yield $\lambda^*(v)$, which is precisely $\lambda^{\pm}(v)$ in the second equation of Eq. (51). The final expression of $G(v)$ is obtained by substituting this result into Eq. (48).

[1] P. Martin, A. J. Hudspeth, and F. Jülicher, Proc. Natl. Acad. Sci. U.S.A. **98**, 14380 (2001).
[2] S. Camalet, T. Duke, F. Jülicher, and J. Prost, Proc. Natl. Acad. Sci. U.S.A. **97**, 3183 (2000).
[3] J. B. Manneville, P. Bassereau, S. Ramaswamy, and J. Prost, Phys. Rev. E **64**, 021908 (2001).
[4] K. Kruse, J. Joanny, F. Jülicher, J. Prost, and K. Sekimoto, Eur. Phys. J. E **91**, 198101 (2003).
[5] D. Mizuno, C. Tarding, C. F. Schmidt, and F. C. MacKintosh, Science **315**, 370 (2007).
[6] S. Mayor and M. Rao, Traffic **5**, 231 (2004).
[7] A. W. C. Lau, B. D. Hoffmann, A. Davies, J. C. Crocker, and T. C. Lubensky, Phys. Rev. Lett. **91**, 198101 (2003).
[8] J. Howard, *Mechanics of Motor Proteins and the Cytoskeleton* (Sinauer Associates, Sunderland, MA, 2001).
[9] C. Asbury, Curr. Opin. Cell Biol. **17**, 89 (2005).
[10] F. Jülicher, A. Ajdari, and J. Prost, Rev. Mod. Phys. **69**, 1269 (1997).
[11] A. Parmeggiani, F. Jülicher, A. Ajdari, and J. Prost, Phys. Rev. E **60**, 2127 (1999).
[12] A. Kolomeisky and B. Widom, J. Stat. Phys. **93**, 633 (1998).
[13] M. Fisher and A. Kolomeisky, Proc. Natl. Acad. Sci. U.S.A. **96**, 6597 (1999); **98**, 7748 (2001).
[14] Y. Kafri *et al.*, Biophys. J. **86**, 3373 (2004).
[15] C. Jarzynski and O. Mazonka, Phys. Rev. E **59**, 6448 (1999).
[16] R. Lipowsky, Phys. Rev. Lett. **85**, 4401 (2000); G. Lattanzi and A. Maritan, *ibid.* **86**, 1134 (2001).
[17] M. Schnitzer and S. Block, Nature (London) **388**, 386 (1997); K. Visscher *et al.*, *ibid.* **400**, 184 (1999).
[18] C. Coppin *et al.*, Proc. Natl. Acad. Sci. U.S.A. **94**, 8539 (1997); M. Nishiyama *et al.*, Nat. Cell Biol. **4**, 790 (2002); C. L. Asbury *et al.*, Science **302**, 2130 (2003).
[19] N. Carter and R. Cross, Nature (London) **435**, 308 (2005).
[20] J. Shaevitz *et al.*, Biophys. J. **89**, 2277 (2005).
[21] D. J. Evans, E. G. D. Cohen, and G. P. Morriss, Phys. Rev. Lett. **71**, 2401 (1993); G. Gallavotti and E. G. D. Cohen, *ibid.* **74**, 2694 (1995); C. Jarzynski, *ibid.* **78**, 2690 (1997); J. Kurchan, J. Phys. A **31**, 3719 (1998); C. Maes, J. Stat. Phys. **95**, 367 (1999).
[22] G. Gallavotti, Phys. Rev. Lett. **77**, 4334 (1996).
[23] J. L. Lebowitz and H. Spohn, J. Stat. Phys. **95**, 333 (1999).
[24] D. Evans and D. Searles, Adv. Phys. **51**, 1529 (2002); D. J. Evans and D. J. Searles, Phys. Rev. E **50**, 1645 (1994).
[25] G. E. Crooks, Phys. Rev. E **61**, 2361 (2000).
[26] J. Liphardt *et al.*, Science **296**, 1832 (2002); D. Collin *et al.*, Nature (London) **437**, 231 (2005); V. Blickle, T. Speck, L. Helden, U. Seifert, and C. Bechinger, Phys. Rev. Lett. **96**, 070603 (2006).
[27] H. Qian, J. Phys.: Condens. Matter **17**, S3783 (2005).
[28] P. Gaspard and E. Gerritsma, J. Theor. Biol. **247**, 672 (2007); D. Andrieux and P. Gaspard, Phys. Rev. E **74**, 011906 (2006); P. Gaspard, J. Chem. Phys. **120**, 8898 (2004).

[29] U. Seifert, Europhys. Lett. **70**, 36 (2005).
[30] A. W. C. Lau, D. Lacoste, and K. Mallick, Phys. Rev. Lett. **99**, 158102 (2007).
[31] T. L. Hill, *Linear Aggregation Theory in Cell Biology* (Springer, New York, 1987).
[32] T. De Donder, *L'Affinité* (Gauthiers-Villars, Paris, 1927).
[33] Note that this expression of $\Delta\mu$ requires that the solution be ideal. With the concentrations of ATP used in the experiments with molecular motors (at most a few mM), the solutions are sufficiently dilute that they can be considered ideal. Another assumption implicit in the use of transition state theory is that there is a barrier height associated with the transition (which does not have to be of order ϵ) which is larger than k_BT.
[34] This change of sign is only due to a different convention for the orientation of the force: F_e must be changed into $-F_e$ in all of the rates to recover the rates used in Ref. [14]. In our convention, a positive force corresponds to the direction of average motion of the motor.
[35] B. Derrida, J. Stat. Phys. **31**, 433 (1983).
[36] K. Sekimoto, J. Phys. Soc. Jpn. **66**, 1234 (1997); Phys. Rev. E **76**, 060103(R) (2007).
[37] J. M. R. Parrondo and P. Español, Am. J. Phys. **64**, 1125 (1996).
[38] S. Liepelt and R. Lipowsky, Europhys. Lett. **77**, 50002 (2007); J. Stat. Phys. **130**, 39 (2008).
[39] T. Schmiedl, T. Speck, and U. Seifert, J. Stat. Phys. **128**, 77 (2007).
[40] M. Nishiyama, H. Higuchi, and T. Yanagida, Nat. Cell Biol. **4**, 790 (2002).
[41] D. Keller and C. Bustamante, Biophys. J. **78**, 541 (2000).

Fluctuation theorem for the flashing ratchet model of molecular motors

D. Lacoste[1] and K. Mallick[2]
[1]*Laboratoire de Physico-Chimie Théorique, UMR 7083, ESPCI, 10 rue Vauquelin, 75231 Paris Cedex 05, France*
[2]*Institut de Physique Théorique, CEA Saclay, 91191 Gif, France*
(Received 5 March 2009; published 20 August 2009)

Molecular motors convert chemical energy derived from the hydrolysis of adenosine triphosphate (ATP) into mechanical energy. A well-studied model of a molecular motor is the flashing ratchet model. We show that this model exhibits a fluctuation relation known as the Gallavotti-Cohen symmetry. Our study highlights the fact that the symmetry is present only if the chemical and mechanical degrees of freedom are both included in the description.

DOI: 10.1103/PhysRevE.80.021923 PACS number(s): 87.16.Nn, 05.40.−a, 05.70.Ln

Molecular motors are subject to intense study both from biological and technological point of view [1,2]. These remarkable nanomachines are enzymes capable of converting chemical energy derived from ATP hydrolysis into mechanical work. They typically operate far from equilibrium, in a regime where the usual thermodynamical laws do not apply. Generically such motors are modeled either in terms of continuous flashing ratchets [3,4] or by a master equation on a discrete space [5,6]. Recently, a general organizing principle for nonequilibrium systems has emerged which is known under the name of fluctuation relations [7,8]. These relations, which hold for nonequilibrium steady states, can be seen as macroscopic consequences of generalized detailed balance conditions, which themselves arise due to the invariance under time reversal of the dynamics at the microscopic scale [9].

An interesting ground to apply these concepts is the field of molecular motors [10–16]. The fluctuation relations impose thermodynamic constraints on the operation of these machines, particularly in regimes arbitrary far from equilibrium. Near equilibrium, they lead to Einstein and Onsager relations. For nonequilibrium steady states, they can be used to quantify deviations from Einstein and Onsager relations as we have shown in Refs. [13,14].

In this paper, we investigate fluctuation relations for continuous ratchet models. We first study a purely mechanical ratchet (model I), which applies to the translocation of a polymer through a pore [17]. We then consider a flashing ratchet (model II), which applies to molecular motors [3]. Using a method inspired by Refs. [7,18], we show that the Gallavotti-Cohen symmetry is always present in model I, but we emphasize that in model II the symmetry exists only if the chemical and mechanical degrees of freedom of the motor are both included in the description.

Let us first consider a random walker in a periodic potential subject to an external force F (model I) [2,19]. The corresponding Fokker-Planck equation is

$$\frac{\partial P}{\partial t} = D_0 \frac{\partial}{\partial x}\left[\frac{\partial P}{\partial x} + \frac{U'(x) - F}{k_B T} P\right], \tag{1}$$

where $U(x)$ is a periodic potential $U(x+a)=U(x)$ and a is the period. This equation describes the stochastic dynamics of a particle in the effective potential $U_{eff}(x)=U(x)-Fx$. By solving Eq. (1) with periodic boundary conditions [17,19], it can be readily proven that the system reaches a stationary state with a uniform current J in the long-time limit. This current is nonvanishing if a nonzero force is applied. When $F=0$, there is no tilt in the potential, $J=0$ and the stationary probability is given by the equilibrium Boltzmann-Gibbs factor.

We call $x(t)$ the position of the ratchet at time t knowing that the ratchet was located at $x(0)=0$ at time $t=0$, which we decompose as $x=(n+\zeta)a$ where n is an integer and $0\leq\zeta<1$. The stationary current J is related to the average position $x(t)$ by $J=\lim_{t\to\infty}\frac{\langle x(t)\rangle}{t}$, i.e., J is the mean speed of the ratchet in the long-time limit. More generally we are interested in the higher cumulants of $x(t)$ when $t\to\infty$. It is useful to define the generating function

$$F_\lambda(\zeta,t) = \sum_n \exp[\lambda(\zeta+n)]P[(n+\zeta)a,t]. \tag{2}$$

The time evolution of this generating function F_λ is obtained by summing over Eq. (1). This leads to the following equation:

$$\frac{\partial F_\lambda(\zeta,t)}{\partial t} = \mathcal{L}(\lambda)F_\lambda(\zeta,t), \tag{3}$$

where the deformed differential operator $\mathcal{L}(\lambda)$ acts on a periodic function $\Phi(\zeta,t)$ of period 1 as follows:

$$\frac{a^2}{D_0}\mathcal{L}(\lambda)\Phi = \frac{\partial^2\Phi}{\partial\zeta^2} + \frac{\partial}{\partial\zeta}(\tilde{U}'_{eff}\Phi) - 2\lambda\frac{\partial\Phi}{\partial\zeta} - \lambda\tilde{U}'_{eff}\Phi + \lambda^2\Phi, \tag{4}$$

where $\tilde{U}'_{eff}=a\partial_x U_{eff}/k_BT$ and the left-hand side of Eq. (4) is proportional to the inverse of the characteristic time $\tau=a^2/D_0$. A similar procedure exists in solid-state physics, where periodic functions are expanded in eigenfunctions of Bloch form, which are eigenfunctions of an operator similar to $\mathcal{L}(\lambda)$ [17].

The operator $\mathcal{L}(\lambda)$ has the following fundamental conjugation property:

$$e^{U(x)/k_BT}\mathcal{L}(\lambda)(e^{-U(x)/k_BT}\Phi) = \mathcal{L}^\dagger(-f-\lambda)\Phi, \tag{5}$$

with $f=Fa/k_BT$ the normalized force. This property implies that operators $\mathcal{L}(\lambda)$ and $\mathcal{L}^\dagger(-f-\lambda)$ are adjoint to each other, and thus have the same spectrum. If we call $\Theta(\lambda)$ the largest

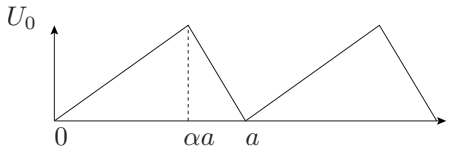

FIG. 1. Sketch of the sawtooth potential $U(x)$. The potential has period a, αa is the distance from a minimum to the next maximum on the right, and U_0 is the maximum of the potential.

eigenvalue of $\mathcal{L}(\lambda)$, we obtain from Eq. (5) that $\Theta(\lambda)$ satisfies the Gallavotti-Cohen symmetry

$$\Theta(\lambda) = \Theta(-f-\lambda). \tag{6}$$

In fact, this symmetry holds for all eigenvalues. For the special case $f=0$, the conjugation relation (5) reduces to the *detailed balance* property [18]. Finally, it is important to note that $\Theta(\lambda)$ is the generating function for the cumulants of $x(t)$.

We have calculated numerically the function $\Theta(\lambda)$ for the case of the sawtooth potential shown in Fig. 1, with a barrier height U_0 on order of several k_BT [17]. This function was obtained by first discretizing the operator $\mathcal{L}(\lambda)$ and then calculating its largest eigenvalue using the Ritz variational method. This method does not require finding a basis specific to the chosen potential, in contrast to what was done in Ref. [20]. for the cosine potential. Our numerical method can handle any shape of the potential.

The form of $\Theta(f\eta)$ with $\eta=\lambda/f$ is shown in Fig. 2 for different values of the normalized force f. The symmetry of all the curves with respect to $\eta=1/2$ corresponds to the symmetry of Eq. (6). At weak force, $\Theta(f\eta)$ has a parabolic shape associated with Gaussian fluctuations, whereas at higher forces a flattening occurs associated with non-Gaussian fluctuations [10,14,20]. By numerically taking derivatives of $\Theta(\lambda)$ with respect to λ near $\lambda=0$, we recover the velocity obtained by directly solving Eq. (1) [17,19].

We now come to the derivation of the Gallavotti-Cohen symmetry for the flashing ratchet model (model II). In this model [3,21,22], the motor has two internal states $i=1,2$, which are described by two time-independent potentials $U_i(x)$. We assume that these potentials are periodic with a common period a. The probability density for the motor to

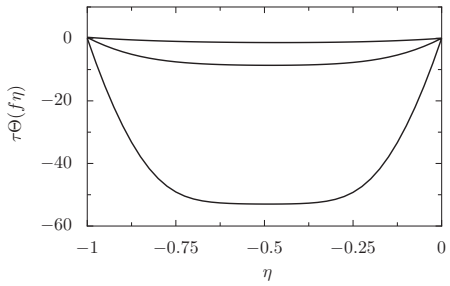

FIG. 2. Normalized eigenvalue $\tau\Theta(f\eta)$ (with $\tau=a^2/D_0$) as function of η for different values of the normalized force f; from top to bottom, $f=5$, $f=10$, and $f=20$. The parameters of the potential are $\alpha=0.7$, $U_0/k_BT=5$. The symmetry of all the curves with respect to $\eta=-1/2$ is Gallavotti-Cohen symmetry expected for model I.

be at position x at time t and in state i is $P_i(x,t)$. The dynamics of the model is described by

$$\frac{\partial P_1}{\partial t} + \frac{\partial J_1}{\partial x} = -\omega_1(x)P_1 + \omega_2(x)P_2$$

$$\frac{\partial P_2}{\partial t} + \frac{\partial J_2}{\partial x} = \omega_1(x)P_1 - \omega_2(x)P_2, \tag{7}$$

where $\omega_1(x)$ and $\omega_2(x)$ are space dependent transition rates, and the local currents J_i are defined by

$$J_i = -D_0\left[\frac{\partial P_i}{\partial x} + \frac{1}{k_BT}\left(\frac{\partial U_i}{\partial x} - F\right)P_i\right], \tag{8}$$

with D_0 the diffusion coefficient of the motor and F a nonconservative force acting on the motor. The transition rates can be modeled using standard kinetics for the different chemical pathways between the two states of the motor [21]

$$\omega_1(x) = [\omega(x) + \psi(x)e^{\Delta\mu}]e^{(U_1(x)-fx)/k_BT},$$

$$\omega_2(x) = [\omega(x) + \psi(x)]e^{(U_2(x)-fx)/k_BT}, \tag{9}$$

where $\Delta\mu=\Delta\tilde{\mu}/k_BT$ is the normalized chemical potential and $\Delta\tilde{\mu}$ the chemical potential associated with ATP hydrolysis. Terms proportional to $\omega(x)$ are associated with thermal transitions, while terms proportional to $\psi(x)$ correspond to transitions induced by ATP hydrolysis. One could easily introduce more chemical pathways than the ones considered here [21] but this extension is not essential for the present argument. Note that the way the force enters the rates is unambiguous in such a continuous model [5,14].

Note that Eq. (7) can be rewritten as a matrix $\mathcal{L}$ of operators

$$\frac{\partial}{\partial t}\begin{pmatrix} P_1 \\ P_2 \end{pmatrix} = \mathcal{L}\begin{pmatrix} P_1 \\ P_2 \end{pmatrix} = \begin{pmatrix} \mathcal{L}_1 - \omega_1 & \omega_2 \\ \omega_1 & \mathcal{L}_2 - \omega_2 \end{pmatrix}\begin{pmatrix} P_1 \\ P_2 \end{pmatrix}, \tag{10}$$

where the action of the operator $\mathcal{L}_i$ on a function $\Phi(x,t)$ is given by

$$\mathcal{L}_i\Phi = D_0\frac{\partial^2\Phi}{\partial x^2} + D_0\frac{\partial}{\partial x}\left(\frac{U_i' - F}{k_BT}\Phi\right). \tag{11}$$

When $F=0$ and $\Delta\mu=0$, the system is at equilibrium and

$$\frac{\omega_2(x)}{\omega_1(x)} = \exp\left(\frac{U_2 - U_1}{k_BT}\right). \tag{12}$$

In this case, the stationary solution of the system (7) is the Boltzmann distribution for P_1 and P_2, the currents J_1 and J_2 vanish and there is no global displacement of the motor. If both F and $\Delta\mu$ do not vanish, then the system is out of equilibrium and nonvanishing currents can appear.

If the switching between the two potentials occurs only by thermal transitions, i.e., when $\Delta\mu=0$, the rates satisfy the detailed balance condition of Eq. (12), even in the presence of a nonzero force F. The Gallavotti-Cohen symmetry follows by considering a 2×2 diagonal matrix of operators $\mathcal{L}_i(\lambda)$ of the form (4). The symmetry is indeed present as shown in the solid curves of Fig. 3. In the general case how-

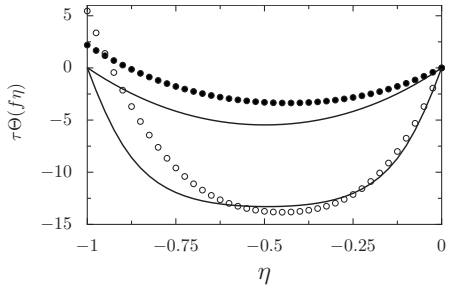

FIG. 3. Normalized eigenvalue $\tau\Theta(f\eta)$ as function of η for a normalized force $f=5$ (top two curves) and $f=10$ (bottom two curves) for the flashing ratchet (model II). The solid curves correspond to the case where the switching rates satisfy detailed balance which leads to the Gallavotti-Cohen symmetry. The curves with filled symbols ($f=5$) and empty symbols ($f=10$) correspond to cases where detailed balance is broken with constant switching rates $\omega_1(x)=\omega_2(x)=10\tau^{-1}$ and with the same potentials. The lack of symmetry in these curves with respect to $\eta=-1/2$ is apparent especially near $\eta=-1$.

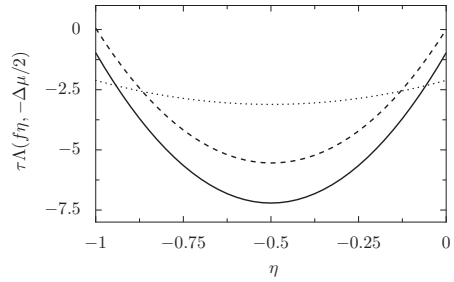

FIG. 4. For model II, the normalized eigenvalue $\tau\Lambda(f\eta,-\Delta\mu/2)$ is shown as function of η. The dashed curve corresponds to $f=5$ and $\Delta\mu=0$, the solid curve corresponds to $f=5$ and $\Delta\mu=10$, and the dotted curve corresponds to $f=2$ and $\Delta\mu=10$. The symmetry is recovered in all cases in this description which includes both the mechanical and chemical degrees of freedom.

ever, where the normalized force f and chemical-potential $\Delta\mu$ are both nonzero, the relation (12) is no more satisfied and the Gallavotti-Cohen relation (6) is not valid. This is shown in the curves with symbols in Fig. 3 where for simplicity we took constant switching rates $\omega_1=\omega_2=10\tau^{-1}$. For all the curves of this figure, we took a sawtooth potential U_1 with the same parameters as in Fig. 2, and a potential U_2 constant in space. The breaking of the symmetry of Eq. (6) can be interpreted as a result of the existence of internal degrees of freedom, similarly to the violations discussed in Ref. [23].

To establish a fluctuation relation for the flashing ratchet model, one must consider both the mechanical and chemical currents present [13,16].

Let us introduce the probability density $P_i(x,q;t)$ associated with the probability that at time t the ratchet is in the internal state i, at position x and that q chemical units of ATP have been consumed. The evolution equations for this probability density is obtained by modifying Eq. (7) after taking into account the dynamics of the discrete variable q. We have

$$\frac{\partial P_1(x,q,t)}{\partial t} = [\mathcal{L}_1 - \omega_1(x)]P_1(x,q,t) + \omega_2^{-1}(x)P_2(x,q+1,t) + \omega_2^0(x)P_2(x,q,t) \tag{13}$$

$$\frac{\partial P_2(x,q,t)}{\partial t} = [\mathcal{L}_2 - \omega_2(x)]P_2(x,q,t) + \omega_1^0(x)P_1(x,q,t) + \omega_1^1(x)P_1(x,q-1,t). \tag{14}$$

We use a notation similar to that of Ref. [14], where $\omega_i^l(x)$ denotes the transition rate at position x from the internal state i with $l=-1,0,1$ ATP molecules consumed. This leads to $\omega_1^0=\omega e^{(U_1-fx)/k_BT}$, $\omega_2^0=\omega e^{(U_2-fx)/k_BT}$, $\omega_1^1=\psi e^{(U_1-fx)/k_BT+\Delta\mu}$, and $\omega_2^{-1}=\psi e^{(U_2-fx)/k_BT}$, with $\omega_1(x)=\omega_1^0(x)+\omega_1^1(x)$ and $\omega_2(x)=\omega_2^0(x)+\omega_2^{-1}(x)$.

As above we introduce two generating functions $F_{1,\lambda,\gamma}$ and $F_{2,\lambda,\gamma}$, depending on two parameters λ and γ which are conjugate variables to the position of the ratchet and to the ATP counter q. We have for $i=1,2$,

$$F_{i,\lambda,\gamma}(\zeta,t) = \sum_q e^{\gamma q}\sum_n e^{\lambda(\zeta+n)}P_i[a(\zeta+n),q;t]. \tag{15}$$

The evolution equation for these generating functions is obtained from Eq. (15) as

$$\frac{\partial}{\partial t}\begin{pmatrix} F_{1,\lambda,\gamma} \\ F_{2,\lambda,\gamma} \end{pmatrix} = \mathcal{L}(\lambda,\gamma)\begin{pmatrix} F_{1,\lambda,\gamma} \\ F_{2,\lambda,\gamma} \end{pmatrix}, \tag{16}$$

with the operator $\mathcal{L}(\lambda,\gamma)$ decomposed as

$$\mathcal{L}(\lambda,\gamma) = \mathcal{D}(\lambda) + \mathcal{N}(\gamma), \tag{17}$$

with $\mathcal{D}(\lambda)$ the diagonal matrix $\mathrm{diag}[\mathcal{L}_1(\lambda)-\omega_1, \mathcal{L}_2(\lambda)-\omega_2]$, and

$$\mathcal{N}(\gamma) = \begin{pmatrix} 0 & \omega_2^0 + \omega_2^{-1}e^{-\gamma} \\ \omega_1^0 + \omega_1^1 e^{\gamma} & 0 \end{pmatrix}. \tag{18}$$

Consider now the diagonal matrix Q defined by $\mathrm{diag}(e^{-U_1/k_BT}, e^{-U_2/k_BT})$. By direct calculation, one can check that $Q^{-1}\mathcal{N}(\gamma)Q=\mathcal{N}^\dagger(-\Delta\mu-\gamma)$. From Eq. (5), one obtains $Q^{-1}\mathcal{D}(\gamma)Q=\mathcal{D}^\dagger(-\Delta\mu-\gamma)$. By combining these two equations, we conclude that

$$Q^{-1}\mathcal{L}(\lambda,\gamma)Q = \mathcal{L}^\dagger(-f-\lambda,-\Delta\mu-\gamma), \tag{19}$$

which leads to the Gallavotti-Cohen symmetry

$$\Lambda(\lambda,\gamma) = \Lambda(-f-\lambda,-\Delta\mu-\gamma), \tag{20}$$

where $\Lambda(\lambda,\gamma)$ is the largest eigenvalue of $\mathcal{L}(\lambda,\gamma)$. If we consider only the mechanical displacement of the ratchet, the relevant eigenvalue $\Theta(\lambda)$ is given by $\Theta(\lambda)=\Lambda(\lambda,0)$, which clearly does not satisfy the fluctuation relation as shown in Fig. 3. In Fig. 4, we have computed $\Lambda(f\eta,-\Delta\mu/2)$ for the same potentials and with rates $\omega_i^l(x)$ of the form given above with $\omega(x)=5\tau^{-1}$ and $\phi(x)=10\tau^{-1}$. We have verified that in all cases the symmetry of Eq. (20) holds.

In this paper, we have shown that the large deviation function of the mechano-chemical currents obeys the Gallavotti-Cohen relation. Another related but different symmetry relation for the entropy production exists under more general conditions [7,10,15,18,20]. We have shown here that

the symmetry for the currents is valid for the flashing ratchet model when internal degrees of freedom are taken into account. This raises a fundamental question concerning the validity of fluctuations relations and their applicability to other types of ratchet models [2,4]. Other mechanisms exist which are known to produce deviations from fluctuations relations [23], and it would be interesting to investigate whether fluctuations relations can always be restored by a suitable modification of the dynamics.

On the experimental side, it would be very interesting to investigate fluctuations relations for molecular motors using single molecule experiments, in a way similar to what was achieved in colloidal beads or biopolymers experiments [8]. Using fluorescently labeled ATP molecules, recent experiments with myosin 5*a* and with the F_0-F_1 rotary motor, aim at simultaneous recording of the turnover of single fluorescent ATP molecules and the resulting mechanical steps of the molecular motor [24]. These exciting results indicate that a simultaneous measurement of the values of the mechanical and chemical variable of the motor is achievable, and therefore from the statistics of such measurements it is possible to construct $P(x,q,t)$. With enough statistics of such data, one could thus in principle verify Eq. (20). Such a verification would confirm that the Gallavotti-Cohen symmetry is a thermodynamic constraint that plays an essential role in the mechano-chemical coupling of molecular motors.

We acknowledge fruitful discussions with A. W. C. Lau and J. Prost. D.L. also acknowledges support from the Indo-French Center CEFIPRA (Grant No. 3504-2).

[1] J. Howard, *Mechanics of Motor Proteins and the Cytoskeleton* (Sinauer Associates, Sunderland, MA, 2001).
[2] P. Hänggi and F. Marchesoni, Rev. Mod. Phys. **81**, 387 (2009).
[3] F. Jülicher, A. Ajdari, and J. Prost, Rev. Mod. Phys. **69**, 1269 (1997).
[4] P. Reimann, Phys. Rep. **361**, 57 (2002).
[5] A. Kolomeisky and M. Fisher, Annu. Rev. Phys. Chem. **58**, 675 (2007).
[6] R. Lipowsky, Phys. Rev. Lett. **85**, 4401 (2000).
[7] J. Kurchan, J. Phys. A **31**, 3719 (1998); e-print arXiv:0901.1271.
[8] D. Collin *et al.*, Nature **437**, 231 (2005); V. Blickle, T. Speck, L. Helden, U. Seifert, and C. Bechinger, Phys. Rev. Lett. **96**, 070603 (2006).
[9] B. Derrida, J. Stat. Mech.: Theory Exp. **2007**, P07023 (2007).
[10] P. Gaspard, J. Chem. Phys. **120**, 8898 (2004); D. Andrieux and P. Gaspard, Phys. Rev. E **74**, 011906 (2006).
[11] U. Seifert, EPL **70**, 36 (2005).
[12] R. Lipowsky and S. Liepelt, J. Stat. Phys. **130**, 39 (2008); **135**, 777 (2009).
[13] A. W. C. Lau, D. Lacoste, and K. Mallick, Phys. Rev. Lett. **99**, 158102 (2007).
[14] D. Lacoste, A. W. C. Lau, and K. Mallick, Phys. Rev. E **78**, 011915 (2008).
[15] W. De Roeck and C. Maes, Phys. Rev. E **76**, 051117 (2007).
[16] T. Schmiedl, T. Speck, and U. Seifert, J. Stat. Phys. **128**, 77 (2007).
[17] D. K. Lubensky and D. R. Nelson, Biophys. J. **77**, 1824 (1999).
[18] J. L. Lebowitz and H. Spohn, J. Stat. Phys. **95**, 333 (1999).
[19] H. Risken, *The Fokker-Planck Equation* (Springer, Berlin, 1989).
[20] J. Mehl, T. Speck, and U. Seifert, Phys. Rev. E **78**, 011123 (2008).
[21] A. Parmeggiani, F. Julicher, A. Ajdari, and J. Prost, Phys. Rev. E **60**, 2127 (1999).
[22] H. Wang, C. S. Peskin, and T. C. Elston, J. Theor. Biol. **221**, 491 (2003).
[23] S. Rahav and C. Jarzynski, J. Stat. Mech.: Theory Exp. **2007**, P09012 (2007).
[24] Y. Ishii and T. Yanagida, HFSP J. **1**, 15 (2007); E. M. De la Cruz and A. O. Olivares, HSFP J. **3**, 67 (2009).

Membrane Tension Lowering Induced by Protein Activity

M. D. El Alaoui Faris,[1] D. Lacoste,[2] J. Pécréaux,[1,*] J.-F. Joanny,[1] J. Prost,[1,3] and P. Bassereau[1]

[1]*Institut Curie, Centre de Recherche; CNRS, UMR 168; Université Pierre et Marie Curie, Paris, F-75248 France*

[2]*ESPCI, Laboratoire de Physico-Chimie Théorique; CNRS, UMR 7083, 75231 Paris Cedex 05, France*

[3]*ESPCI; ParisTech, 10 rue Vauquelin, 75231 Paris Cedex 05, France*

(Received 20 June 2008; published 21 January 2009)

Using videomicroscopy we present measurements of the fluctuation spectrum of giant vesicles containing bacteriorhodopsin pumps. When the pumps are activated, we observe a significant increase of the fluctuations in the low wave vector region, which we interpret as due to a lowering of the effective tension of the membrane.

DOI: 10.1103/PhysRevLett.102.038102 PACS numbers: 87.16.dj, 05.40.−a, 05.70.Ln

Membranes are self-assembled bilayers of surfactants or phospholipids, which form flexible surfaces. The mechanical properties of membranes are essentially controlled by parameters, such as the membrane tension, bending modulus, and spontaneous curvature [1]. These parameters completely characterize the membrane fluctuation spectrum at thermal equilibrium, but they are not sufficient to characterize real biological membranes, such as cell plasma membranes, which are nonequilibrium systems [2,3]. Biological membranes are in general active in the sense that they are constantly maintained out of equilibrium either by active proteins inside the membrane that are often ATP-consuming enzymes or by an energy flow, for example, a lipid flux. Because of the complexity of active biological systems *in vivo*, recent studies have focused on *in vitro* biomimetic systems. An example of an active system is a giant unilamellar vesicle (GUV) which is rendered active by the inclusion of light-activated bacteriorhodopsin (BR) pumps. The bacteriorhodopsin pumps transfer protons unidirectionally across the membrane as a consequence of their conformational changes, when they are excited by the light of a specific wavelength. Experiments on giant unilamellar vesicles containing bacteriorhodopsin pumps or Ca^{2+} ATPase pumps have shown that the nonequilibrium forces arising from ion pumps embedded in the membrane are able to significantly enhance the membrane fluctuations [4–7]. In these experiments, the membrane tension has been fixed by means of micropipet aspiration and the corresponding excess area measured. The slope of such a curve defines an effective temperature, measuring the enhancement of the membrane fluctuations by the protein activity. The amplification of the fluctuations due to activity was originally predicted in Ref. [8].

In this Letter, we report the first experimental measurements, using videomicroscopy, of an active fluctuation spectrum of GUVs containing bacteriorhodopsin pumps. The details of the technique and of the analysis are given in Ref. [9]. These measurements are complementary to previous experiments using micropipets since they probe a range of wave vectors not accessible otherwise. Micropipet experiments provide information on the active fluctuations integrated over all wave vectors which require an independent calibration of the membrane tension. On the contrary, videomicroscopy gives a direct measurement of the fluctuation spectrum from which the membrane tension can be extracted [9]. In this Letter, we analyze theoretically the active fluctuation spectrum using the model of Ref. [10], which is an extension of the hydrodynamic model of Ref. [5], to quasispherical vesicles, taking into account the active noise of the pumps and localized active forces.

Let us first discuss the passive behavior of giant vesicles. For the sake of simplicity we use notations appropriate to quasiplanar membranes. We consider a quasiplanar membrane surface in the Monge gauge, in which it is defined by its height $u(\mathbf{x})$ at position $\mathbf{x}$. Two density fields are defined on the surface, $\psi^{\uparrow}$ and $\psi^{\downarrow}$, corresponding to the surface densities of proteins oriented with the two possible orientations [5]. The membrane free energy is a function of the height field $u(\mathbf{x})$ and of the imbalance of protein densities $\psi(\mathbf{x}) = \psi^{\uparrow}(\mathbf{x}) - \psi^{\downarrow}(\mathbf{x})$. We expand the free energy to quadratic order in these variables:

$$F[u, \psi] = \frac{1}{2} \int d^2\mathbf{x}[\kappa(\nabla^2 u)^2 + \sigma(\nabla u)^2 + \chi\psi^2 - 2\Xi\psi\nabla^2 u], \quad (1)$$

where κ is the bending modulus, σ the surface tension, χ a susceptibility coefficient, and Ξ a coefficient characterizing the coupling between the membrane curvature and the average orientation of the proteins. In the following, we neglect the curvature induced coupling; this is justified for bacteriorhodopsin pumps since the incorporation of proteins does not lead to any measurable renormalization of the bending modulus [5]. Note that for dilute proteins in the membrane, $\chi = k_B T/n_0$, where n_0 is the average density of proteins, of the order of 10^{16} m^{-2}. In our experiments, only the vesicle contour at the equator corresponding to a slice of the vesicle in the plane $y = 0$ is recorded and is used to calculate the fluctuation spectrum. The measured quantity is

$$\langle |u(q_x, y=0)|^2 \rangle = \frac{1}{2\pi} \int_{-\infty}^{+\infty} \langle |u(q_x, q_y)|^2 \rangle dq_y. \quad (2)$$

The passive equilibrium value of this fluctuation spectrum is calculated using the equipartition theorem from Eqs. (1) and (2):

$$\langle |u(q_x, y=0)|^2 \rangle = \frac{k_B T}{2\sigma} \left[\frac{1}{q_x} - \frac{1}{\sqrt{\frac{\sigma}{\kappa} + q_x^2}} \right] = g(q_x, \sigma, \kappa). \quad (3)$$

Fluctuation spectra are often analyzed in terms of power laws defined by $g(q_x, \sigma, \kappa) \sim q_x^{\nu}$. Two regimes can be distinguished depending on the position of the wave vector q_x compared to the crossover wave vector $q_c = \sqrt{\sigma/\kappa}$. For $q \ll q_c$, membrane tension dominates and $\nu = -1$, whereas for $q \gg q_c$ bending elasticity dominates and $\nu = -3$. Our experiments lead to $\nu \simeq -2$, in the crossover region between these two regimes.

We now discuss active membrane fluctuations. In Ref. [5], a hydrodynamic theory was developed to calculate the nonequilibrium fluctuations of an active membrane containing ion pumps. This work has stimulated substantial theoretical interest, focused mainly on the general question of the proper description of nonequilibrium effects associated to protein conformation changes [11,12]. More recent developments of a similar hydrodynamic approach have led to a general theoretical description of active gels [13–15]. In Ref. [10], the active force distribution is modeled as a superposition of dipoles located along the membrane normal $\mathbf{n}$ (and not along z as in previous models), which generalizes Ref. [5]. Experiments do not probe this force distribution directly but rather its first two moments. The first moment represents the active contribution to the membrane tension and is denoted by σ_{dip} and the second moment Q represents the modification of the membrane bending moments by the activity of the force dipoles [10]. Both active contributions to the tension and to the membrane curvature are also present in Ref. [16] where the activity is due the myosin molecular motors in the cortical layer bound to the cell membrane.

The fluctuation spectrum of an active membrane in a quasispherical geometry can be calculated using an expansion around a spherical shape with radius R_0 to first order in the deviations from the sphere using spherical harmonics, with $\mathbf{R} = \mathbf{R_0} + \mathbf{n} R_0 \sum_{l,m} u_{lm} Y_{lm}$. The fluctuation spectrum of a quasispherical vesicle is characterized by the amplitude of the spherical modes $\langle |u_{lm}|^2 \rangle$ which are function of l only for symmetry reasons. In Ref. [9], the fluctuation spectrum of a quasispherical vesicle is compared to the corresponding spectrum for a planar membrane, and this comparison showed that for modes $l > 5$, the fluctuation spectrum of a quasispherical vesicle is very well approximated by that of a planar membrane at a wave vector q, $\langle |u(q)|^2 \rangle$; at a wave vector $q = l/R_0$, the two spectra are related by $\langle |u(q)|^2 \rangle = R_0^4 \langle |u_{lm}|^2 \rangle$. For the sake of simplicity, we discuss in the following the effect of the activity on the fluctuation spectrum only at the level of planar membranes. We have also simplified the calculation of Ref. [10], by neglecting the shot noise, which is the intrinsic noise of the pumps [8]. This approximation is reasonable because the main effect of the shot noise is to modify the fluctuation spectrum in the high wave vector region [10] which is not the region where we observe a large modification of the spectrum due to activity in our experiments. We denote here F_2 as the constant entering in $Q = F_2 \psi$ [10]. This generalizes the notation of Ref. [5], where this quantity represented the quadrupole moment of the force dipole. With these three approximations, we obtain the following spectrum

$$\langle |u(q_x, q_y)|^2 \rangle = \frac{k_B T}{\kappa q^4 + \tilde{\sigma} q^2} \left\{ 1 + \frac{F_2^2}{4\chi} \frac{q^2}{\kappa q^2 + 4\eta D q + \tilde{\sigma}} \right\}, \quad (4)$$

where D is the diffusion coefficient of the proteins which is of the order of 10^{-12} m^2 s^{-1} [17] and η is the viscosity of water. Since the tension of the vesicles is at least of the order of 10^{-8} N/m, we find that the term $4\eta D q$ can be neglected with respect to $\tilde{\sigma}$ in the range of wave vectors relevant to the experiments. The effective tension $\tilde{\sigma}$ is defined as $\tilde{\sigma} = \sigma + \sigma_{\mathrm{dip}}$, where σ is the passive contribution to the tension and σ_{dip} the active part due to BR proteins. After integration as in Eq. (3), we find

$$\langle |u(q_x, y=0)|^2 \rangle = g(q_x, \tilde{\sigma}, \kappa) + \frac{F_2^2 n_0}{16\kappa^2} \frac{1}{(q_x^2 + \frac{\tilde{\sigma}}{\kappa})^{3/2}}, \quad (5)$$

in which both terms on the right-hand side contain active contributions when σ_{dip} or F_2 do not vanish. Note that Eq. (4) is very similar to the active spectrum given in Ref. [5] with the correspondence $F_2 = 2w\mathcal{P}_a$ except for one important difference: the tension contains an active contribution but not the bending modulus, whereas in

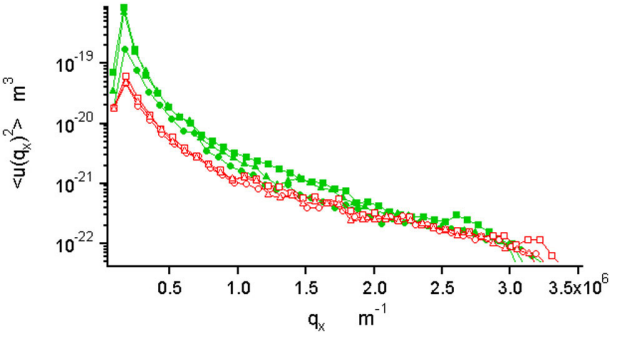

FIG. 1 (color online). Fluctuation spectrum of a single GUV containing BR in a buffer with 1 mM sodium azide. The red (empty) symbols correspond to three consecutive recorded passive spectra, and the green (filled) ones to three consecutive active spectra.

Ref. [5] it is the opposite. Because of this difference the active spectrum of Ref. [5] does not fit our experiments (it would predict a large effect of activity at high wave vectors, whereas the effect is observed here mainly at small wave vectors). Another consequence of this difference is that the active spectrum of Eq. (5) cannot in general be described in terms of an active temperature even in the low wave vector limit [18].

Experiments have been performed with GUVs made of egg phosphatidylcholine at a molar fraction of 240 lipids per protein, using the BR reconstitution protocol developed in Ref. [19]. We have used a polyethylene glycol passivated substrate and checked that vesicles fluctuate without adhering [9]. In Fig. 1, we show the measured fluctuation spectrum for the same GUV containing BR in active and passive states. To ensure reproducibility of the data, three consecutive passive and then three active spectra were recorded. This figure confirms that activity leads to an enhancement of the fluctuations as expected from previous experimental studies [5,6]. It is important to point out that to observe this effect 1 mM of azide must be present in the solution. In the absence of this compound no enhancement of the fluctuation spectrum was observed [20]. This observation is consistent with several studies which suggest that azide enhances the proton transfer in BR [21]. A large enhancement of the active as compared to passive fluctuations is observed at low wave vectors, which we attribute to a lowering of the membrane tension due to the activity.

We first fit the passive spectrum using Eq. (3). This leads to $\sigma = 3.9 \times 10^{-7} \pm 3 \times 10^{-8}$ N/m and an apparent bending modulus $\kappa = 5.6 \times 10^{-19} \pm 4.4 \times 10^{-20}$ J. The value of the bending modulus deduced from such a fit is overestimated. Several artifacts perturb the measurements at high wave vectors: the pixel noise due to the discrete detection of the images, the integration time of the camera, and the effect of gravity [9]. Taking into account these corrections at high q becomes very difficult in the active case; we thus have chosen a simple fitting procedure, in which the corrections due to the integration time and to the gravity are neglected for both passive and active spectra. This procedure is justified by the observation that both spectra are superimposed at high q. The determination of the bending modulus κ is therefore delicate with our video-microscopy technique, while the measurement of the tension is reliable. With the value of the bending modulus kept fixed, we fit the three active spectra of Fig. 1 using Eq. (5). One fit which is shown in Fig. 2 leads to $\tilde{\sigma} = 5.3 \times 10^{-8}$ N/m and $F_2 = 3.9 \times 10^{-28}$ J m. Thus the active contribution to the tension $\sigma_{\mathrm{dip}} = \tilde{\sigma} - \sigma$ is negative and of the order of -3.3×10^{-7} N/m for this particular vesicle (see Table I for a summary of the results of the fits for the GUV of Fig. 1). The lowering of the tension is systematic in all our experiments. The fact that $\sigma_{\mathrm{dip}} \simeq -3.3 \times 10^{-7}$ N/m is very different from the estimate of 1.6×10^{-3} N/m based on Refs. [5,10] suggests that the modeling of the force distribution of these references is not appropriate to our experiments. In Table I, we have also shown the exponent ν, which is the apparent power law exponent of the spectrum. When the vesicle is active, the exponent gets closer to -3, which is the expected value in the bending dominated regime. This is consistent with a lowering of the crossover wave vector $q_c = \sqrt{\tilde{\sigma}/\kappa}$, and thus with a lowering of the tension since in this model κ is not affected by activity. We have ignored any dependence of the protein activity on the local membrane curvature, an assumption justified by the observation that the main effect is a correction to the tension and not to the bending modulus. The value of the parameter F_2 deduced from our fit is of the same order of magnitude as that estimated in Ref. [5] based on micropipet experiments since the factor 2–3 increase in effective temperature measured in this reference leads to $F_2 \simeq 9 \times 10^{-28}$ J m. To summarize, Eq. (4) successfully describes both the micropipet and the fluctuation spectrum measurements.

We now discuss in more detail the lowering of the membrane tension due to activity. We have checked that this effect is compatible with the constraints of constant surface and volume of the vesicle, which must be imposed if permeation is negligible [5]. To do so, we estimate the excess area $\alpha = \int q^3 dq \langle |u(q)|^2 \rangle / 4/\pi$ for passive and active vesicles based on the above fluctuation spectra, by

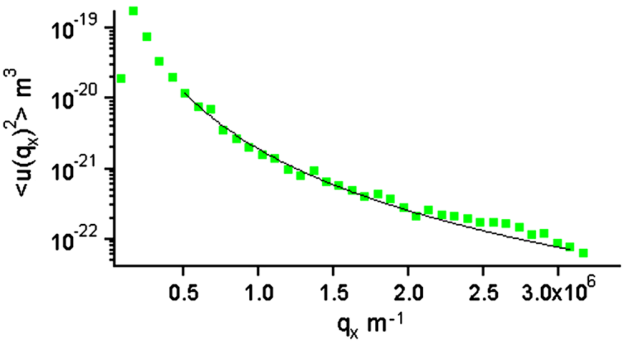

FIG. 2 (color online). Fit of one active spectra of Fig. 1 using Eq. (5). The parameter apparent κ was fixed to 5.6×10^{-19} J obtained by fitting the passive spectrum. This fit gives $\tilde{\sigma} = 5.3 \times 10^{-8}$ N/m and $F_2 = 3.9 \times 10^{-28}$ J m.

TABLE I. Fitting parameters using the fluctuation spectrum of Eq. (5). The passive spectrum is fitted with the condition $F_2 = 0$. Then three consecutive active spectra are fitted with the same vesicle using the value of $\kappa_{ap} = 5.6 \times 10^{-19} \pm 4.4 \times 10^{-20}$ J determined from the fit of the passive spectrum. From this, the membrane tension σ, F_2 and the exponent ν are deduced.

Spectrum	σ ($\times 10^{-7}$ N/m)	F_2 ($\times 10^{-28}$ J m)	ν
Passive	3.9 ± 0.3	0 (imposed)	-2.15 ± 0.04
Active 1	0.53 ± 0.2	3.9 ± 1.1	-2.7 ± 0.04
Active 2	0.79 ± 0.06	9.6 ± 1.1	-2.78 ± 0.06
Active 3	0.35 ± 0.1	7.2 ± 0.6	-2.87 ± 0.07

taking the lower bound of integration to be $q_{\min} = 2\pi/R_0$, with $R_0 = 10$ μm the radius of the vesicles; this lower bound corresponds roughly to the lowest measured value in Fig. 1. In the accessible range of q values, the excess area density $q^3\langle|u(q)|^2\rangle/4/\pi$ of the active vesicles is always larger than the excess area density of the passive vesicles. At higher q wave vectors, it should be the opposite, but the q range where this would happen may be outside the accessible range.

Another important question is the sign of the effect, which cannot be fixed by symmetry arguments [4]. Indeed, both orientations of the force dipoles [5,11], inwards or outwards with respect to the membrane surface, are possible. The present experiments suggest that here the force dipoles must have an inward orientation (corresponding to contractile forces [14]) to produce a lowering of the tension. Another possibility would be to consider lateral dipoles. Here, we propose that the lowering of the tension is a consequence of electrostatic effects. This interpretation is not incompatible with the fact that BR conformational changes also play an important role. We have checked experimentally that a pH gradient builds up in our GUVs when they are activated, which suggests that a significant voltage drop exists across the membrane. Furthermore in membranes containing BR, the activity of the BR can be suppressed by applying an external voltage drop across the membrane [22]. In view of these observations, we propose that Maxwell stresses created by ion transport lead to a renormalization of the tension as shown in a simple model developed by two of us [23]. In this model, the electrostatic correction to the tension is proportional to the square of the electric current going across the membrane. Maxwell stresses are large because of the large mismatch in dielectric constants at the membrane, and they tend to reduce the membrane area, thus producing a negative electrostatic contribution to the tension. A lowering of the membrane tension due to the application of normal electric fields very generally leads to instabilities of the membrane [24,25].

To summarize, we have presented what are to our knowledge the first measurements, using videomicroscopy, of active fluctuation spectra of GUVs containing BR proteins. The experiments show that activity enhances the fluctuations. The effect is strong in the low wave vector region, which we interpret as a lowering of the tension due to activity. This effect could not have been detected in micropipet experiments which are done at constant membrane tension. A possible candidate for explaining the lowering of the tension would be that it is caused by Maxwell stresses due to the transport of ions across the membrane. Further experiments (using, for instance, patch-clamp techniques with the same GUV or other GUVs containing ion channels rather than pumps) are required to confirm these suggestions.

We acknowledge many stimulating discussions with J. Tittor, G. Menon, S. Ramaswamy, N. Gov, and M. Lomholt. We thank D. Oesterhelt for kindly providing us with BR. We also acknowledge support from the European Network of Excellence SoftComp (NMP3-CT-2004-502235) and the Indo-French Center CEFIPRA (Grant No. 3504-2).

*Also at MPI for Molecular Cell Biology and Genetics.

[1] U. Seifert, Adv. Phys. **46**, 13 (1997).
[2] B. Alberts, *Molecular Biology of the Cell* (Garland, New York, 2002).
[3] S. Ramaswamy and M. Rao, C. R. Acad. Sci. Paris, t. 2, Ser. IV, 817 (2001).
[4] S. Ramaswamy, J. Toner, and J. Prost, Phys. Rev. Lett. **84**, 3494 (2000).
[5] J. B. Manneville, P. Bassereau, S. Ramaswamy, and J. Prost, Phys. Rev. E **64**, 021908 (2001).
[6] J. B. Manneville, P. Bassereau, D. Lévy, and J. Prost, Phys. Rev. Lett. **82**, 4356 (1999).
[7] P. Girard, J. Prost, and P. Bassereau, Phys. Rev. Lett. **94**, 088102 (2005).
[8] J. Prost and R. Bruinsma, Europhys. Lett. **33**, 321 (1996).
[9] J. Pécréaux, H.-G. Döbereiner, J. Prost, J.-F. Joanny, and P. Bassereau, Eur. Phys. J. E **13**, 277 (2004).
[10] M. A. Lomholt, Phys. Rev. E **73**, 061913 (2006); **73**, 061914 (2006).
[11] S. Sankararaman, G. Menon, and P. B. S. Kumar, Phys. Rev. E **66**, 031914 (2002).
[12] N. Gov, Phys. Rev. Lett. **93**, 268104 (2004); H.-Y. Chen, *ibid.* **92**, 168101 (2004); D. Lacoste and A. W. C. Lau, Europhys. Lett. **70**, 418 (2005).
[13] R. A. Simha and S. Ramaswamy, Phys. Rev. Lett. **89**, 058101 (2002).
[14] S. Ramaswamy and M. Rao, New J. Phys. **9**, 423 (2007).
[15] K. Kruse, J. Joanny, F. Jülicher, J. Prost, and K. Sekimoto, Eur. Phys. J. E **16**, 5 (2005).
[16] G. Salbreux, J. Joanny, J. Prost, and P. Pullarkat, Phys. Biol. **4**, 268 (2007).
[17] N. Kahya, E. Pecheur, W. de Boeij, D. Wiersma, and D. Hoekstra, Biophys. J. **81**, 1464 (2001).
[18] B. Różycki, T. R. Weikl, and R. Lipowsky, Phys. Rev. E **73**, 061908 (2006).
[19] P. Girard, J. Pécréaux, G. Lenoir, P. Falson, J. Rigaud, and P. Bassereau, Biophys. J. **87**, 419 (2004).
[20] A. Giahi, M. E. A. Faris, P. Bassereau, and T. Salditt, Eur. Phys. J. E **23**, 431 (2007).
[21] H. Steinhoff, M. Pfeiffer, T. Rink, O. Burlon, M. Kurz, J. Riesle, E. Heuberger, K. Gerwert, and D. Oesterhelt, Biophys. J. **76**, 2702 (1999).
[22] S. Geibel, T. Friedrich, P. Ormos, P. G. Nagel, and E. Bamberg, Biophys. J. **81**, 2059 (2001).
[23] D. Lacoste, M. C. Lagomarsino, and J. F. Joanny, Europhys. Lett. **77**, 18 006 (2007); D. Lacoste, G. I. Menon, M. Bazant, and J. F. Joanny, arXiv:0806.4321.
[24] R. Dimova, K. A. Riske, S. Aranda, N. Bezlyepkina, R. Knorr, and R. Lipowsky, Soft Matter **3**, 817 (2007).
[25] P. L. H. T. Ambjörnsson and M. A. Lomholt, Phys. Rev. E **75**, 051916 (2007).

Eur. Phys. J. E **28**, 243–264 (2009)
DOI 10.1140/epje/i2008-10433-1

THE EUROPEAN PHYSICAL JOURNAL E

Regular Article

Electrostatic and electrokinetic contributions to the elastic moduli of a driven membrane

D. Lacoste[1,a], G.I. Menon[2], M.Z. Bazant[1,3], and J.F. Joanny[4]

[1] Laboratoire de Physico-Chimie Théorique, UMR 7083, ESPCI, 10 rue Vauquelin, 75231 Paris Cedex 05, France
[2] The Institute of Mathematical Sciences, C.I.T Campus, Taramani, Chennai 600 113, India
[3] Department of Mathematics, Massachusetts Institute of Technology, Cambridge Massachusetts 02139, USA
[4] Institut Curie, UMR 168, 26 rue d'Ulm, 75005 Paris, France

Received 26 June 2008 and Received in final form 27 October 2008
Published online: 28 January 2009 –

Abstract. We discuss the electrostatic contribution to the elastic moduli of a cell or artificial membrane placed in an electrolyte and driven by a DC electric field. The field drives ion currents across the membrane, through specific channels, pumps or natural pores. In steady state, charges accumulate in the Debye layers close to the membrane, modifying the membrane elastic moduli. We first study a model of a membrane of zero thickness, later generalizing this treatment to allow for a finite thickness and finite dielectric constant. Our results clarify and extend the results presented by D. Lacoste, M. Cosentino Lagomarsino, and J.F. Joanny (EPL **77**, 18006 (2007)), by providing a physical explanation for a destabilizing term proportional to $k_\perp^3$ in the fluctuation spectrum, which we relate to a nonlinear (E^2) electrokinetic effect called induced-charge electro-osmosis (ICEO). Recent studies of ICEO have focused on electrodes and polarizable particles, where an applied bulk field is perturbed by capacitive charging of the double layer and drives the flow along the field axis toward surface protrusions; in contrast, we predict "reverse" ICEO flows around driven membranes, due to curvature-induced tangential fields within a nonequilibrium double layer, which hydrodynamically enhance protrusions. We also consider the effect of incorporating the dynamics of a spatially dependent concentration field for the ion channels.

PACS. 87.16.-b Subcellular structure and processes – 82.39.Wj Ion exchange, dialysis, osmosis, electro-osmosis, membrane processes – 05.70.Np Interface and surface thermodynamics

1 Introduction

Phospholipid molecules self-assemble into a variety of structures, including bilayer membranes, when placed in an aqueous environment [1]. The physical properties of such membranes, at thermal equilibrium, are controlled by a small number of parameters, including the surface tension and the curvature moduli. Understanding how these properties are modified when the membrane is driven out of equilibrium either by externally applied or internally generated electric fields, is a problem of considerable importance to the physics of living cells.

Applied electric fields can be used to drive shape changes in lipid membranes [2]. Artificial lipid vesicles can be produced, via a process called electroformation, by applying an AC electric field to a lipid film deposited on an electrode. Applying an electric field to a vesicle can also lead to the formation of pores via electroporation, a technique of relevance to gene or drug delivery. The role of the field in this case is to introduce transient pores, temporarily removing the barrier presented by the cell membrane to transmembrane transport.

Large electric fields are also generated internally in living cells. The transmembrane potential *in vivo* results from the action of a large number of membrane-bound ion pumps and channels. Resting potentials, and their modulation through excitation, are crucial to many cell functions [3]. Changes in the transmembrane potential and in the ion charge distribution close to the membrane accompany shape changes of cell membranes, such as those which occur when a cell divides. They also provide a means of communication between cells, as in the classic example of the action potential of neural cells [4,5].

Many aspects of electroformation, electroporation, and of the collective behavior of ion channels are as yet poorly understood [2,6]. This is because most studies of electrostatic effects in biological membranes have examined fluctuations at and close to thermal equilibrium [7–14]. However, membranes bearing ion pumps or channels which are driven by ATP hydrolysis ("active membranes"), or exposed to electric fields which lead to transmembrane currents in steady state, cannot be described in terms of equi-

[a] e-mail: david@turner.pct.espci.fr

librium physics, in the first case because a nonequilibrium chemical potential for ATP molecules must be maintained externally to produce such driving and in the second because a net current cannot flow in any system constrained by detailed balance.

To proceed beyond an equilibrium description of the membrane, it is necessary to account for forces generated by inclusions such as ion channels, pumps, or artificial pores [15–17]. An example of such an active membrane was discussed in references [18,19]. In the experimental work described in these papers, a giant unilamellar vesicle was rendered active through the inclusion of light-activated bacteriorhodopsin pumps. These pumps transfer protons unidirectionally across the membrane as a consequence of conformational changes, when excited by light of a specific wavelength. In reference [19], a hydrodynamic theory for the non-equilibrium fluctuations of the membrane induced by the activity of the pumps was also developed. This work has stimulated substantial theoretical interest in the general problem of a proper description of non-equilibrium effects associated with protein conformational changes [20–24].

A major limitation of existing active membrane models is that they do not describe electrostatic effects associated with ion transport in detail. These effects are now understood to be very significant in the biological context. A recent paper, authored by two of us [25], addressed this limitation by studying the fluctuations of a membrane containing inclusions such as ion channels or pumps. Our analysis was based on the use of electrokinetic equations [26–28] supplemented by a simple description of ion transport in ion channels.

This paper extends reference [25] by providing details of the calculations and results presented there. It also presents fresh insights into the physical content of some of these results, while incorporating several new features, as detailed below. Our theoretical description of charge fluctuations near the membrane is in the same spirit as earlier work which examined the stability of shape fluctuations of a charged membrane using linear analysis [29]. We provide a simple physical picture for understanding the electrostatically induced part of the surface tension, which corresponds to a term proportional to $k_\perp^2$ in the free energy of the membrane. We do this by relating the surface tension to an integral over components of the electrostatic (Maxwell) stresses acting on the membrane and the fluid in the non-equilibrium steady state.

We also propose a physical interpretation of the term proportional to $k_\perp^3$ in the effective free energy, obtained first in reference [25]. We show that such a term is related to a nonlinear electrokinetic effect called "induced-charge electro-osmosis" (ICEO) [28], first described in the Russian colloids literature [30] and now studied extensively in microfluidics, since the discovery of electro-osmotic flows over electrode arrays applying AC voltages [31,27]. Steady ICEO flows also occur in DC fields around polarizable metallic [32,33] or dielectric [34,35] surfaces, and broken symmetries generally lead to fluid pumping or motion of freely suspended polarizable objects [28,36]. These phenomena are very general and should also be present in the case of a fluctuating membrane containing ion pumps and channels.

We also analyze the relaxation of a concentration field describing a non-uniform, but slowly varying, distribution of pumps and channels. We include the dynamics of the concentration field of the channels as in previous studies of fluctuations of membranes containing active or passive inclusions [20,37]. We first study the case of a membrane of zero thickness. We then generalize the model to the case of a bilayer of finite thickness and a finite dielectric constant, but with a uniform distribution of pumps and channels. This model allows a discussion of capacitive effects.

The results we present confirm the importance of capacitive effects in determining electrostatic and electrokinetic contributions to the elastic moduli of driven membranes [25,38]. They can be compared to results obtained in a recent study of electrostatic contributions to the elastic moduli of an equilibrium membrane of finite thickness [39]. The study of reference [39], which ignores ion transport, predicts a dependence of the bending modulus and tension as a function of the salt concentration which we compare to the one obtained in this paper, in the limiting case where no ion transport occurs in our model.

Our study is limited to the linear response of the ion channels and pumps. Real channels have a nonlinear response which is essential for action potentials. Our study thus excludes these effects as well as other effects such as electro-osmotic instabilities [40], which originate in the nonlinear response of the ion channels.

The outline of this paper is the following. In Section 2, we study a membrane with zero thickness in the linear response regime. We perform a systematic expansion about a flat membrane with a uniform distribution of pumps. We then discuss the charge fluctuations in the Stokes limit. In Section 3, we analyze ICEO flows around the driven membrane, emphasizing the basic physics of this new nonlinear electrokinetic phenomenon. In Section 4, we discuss the extension of the model to the case where the distribution of pumps/channels is nonuniform. In Section 5 we account for the finite thickness of the membrane. Finally, in Section 6 we summarize the results of this paper and indicate possible directions for further research. Appendix A describes a mapping between a driven membrane of finite thickness and an equivalent zero thickness membrane with appropriately modified boundary conditions while Appendix B illustrates the solution of the Stokes equation for the case of the membrane with zero thickness.

2 Electrostatically driven membrane of zero thickness

We begin by deriving the equation of motion of a driven membrane in an electrolyte in the limit in which the membrane has vanishing thickness and zero dielectric constant. We work in a linear regime and consider only steady-state solutions. The quasi-planar membrane is located in the plane $z = 0$. It is embedded in an electrolyte and carries

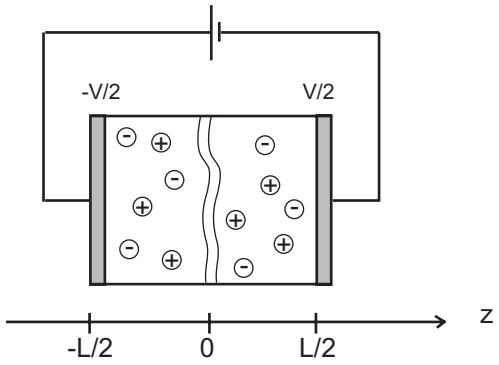

Fig. 1. Schematic of a quasi-planar membrane embedded in a symmetric electrolyte. The (bilayer) membrane is represented by the two wiggly lines near the plane $z = 0$. A voltage V is applied far from the membrane on electrodes separated by a distance L. Note that the electrode at potential $+V/2$ is called the anode and the one at $-V/2$ the cathode.

channels for two species of monovalent ions. The membrane itself is neutral, *i.e.* it bears no fixed charge. There is an imposed potential difference V across the system of length L as shown in Figure 1.

The concentrations of the two ions are denoted by c_k, where the index k is 1 for the positive ion ($z_1 = 1$) and 2 for the negative ion ($z_2 = -1$). A point on the membrane is parameterized, in a Monge representation valid for small undulations, by a height function $h(\mathbf{r}_\perp)$, with $\mathbf{r}_\perp$ a two-dimensional vector.

The calculation proceeds via a perturbation theory about the planar or base state, to first order in the membrane height $h(\mathbf{r}_\perp)$, assuming a uniform concentration field for the channels/pumps. We denote dimensionful variables with a superscript $*$, dropping this superscript for variables which are made dimensionless. A summary of the dimensionful and dimensionless variables used in this paper and the correspondence between them is given in Table 1. To lighten the notation, the inverse Debye length κ, the diffusion coefficients for both species D_k, the electrolyte dielectric constant ϵ, the membrane dielectric constant in the finite thickness case ϵ_m, the charge of the electron e and the thermal energy k_BT, although dimensionful, will not carry a superscript $*$.

The potential obeys the Poisson equation

$$\nabla^{*2}\psi^* = -\left(\frac{ec_1^*}{\epsilon} - \frac{ec_2^*}{\epsilon}\right), \tag{1}$$

which becomes

$$\nabla^2\psi = -\left(\frac{c_1 - c_2}{2}\right), \tag{2}$$

when the following nondimensional variables are introduced: $c_k = c_k^*/n^*$, $\psi = e\psi^*/k_BT$, and $x = \kappa x^*$. Here n^* is the bulk concentration of the electrolyte at large distance from the membrane and κ is the inverse Debye-Hückel length with $\kappa^2 = 2e^2n^*/\epsilon k_BT$.

We assume a symmetric distribution of ion concentrations on both sides of the membrane so that the Debye length is the same on both sides (the asymmetric distribution is discussed in Ref. [25]).

Table 1. Relation between dimensionful variables (column 1) generally denoted with the superscript $*$ and corresponding dimensionless variables (column 2). For notational simplicity, as discussed in the text, the inverse Debye length κ, the diffusion coefficients for both species D_k, the electrolyte dielectric constant ϵ, the membrane dielectric constant in the finite thickness case ϵ_m, the charge of the electron e and the thermal energy k_BT, although dimensionful, will not carry a superscript $*$.

Unit	(1)	(2)	Relation
concentration	c_k^*	c_k	$c_k = c_k^*/n^*$
electrostatic potential	ψ^*	ψ	$\psi = e\psi^*/(k_BT)$
length	x^*	x	$x = \kappa x^*$
particle current	J_k^*	J_k	$J_k = J_k^*/(D_k n^* \kappa)$
chemical potential	μ^*	μ	$\mu = \mu^*/(k_BT)$
ionic current	i_k^*	i_k	$i_k = i_k^*/(D_k n^* \kappa)$
conductance	G_k^*	G_k	$G_k = G_k^* k_BT/(D_k n^* e^2 \kappa)$
charge density (at $z = 0^-$)	σ^*	σ	$\sigma = e\sigma^*/(\kappa\epsilon k_BT)$
pressure	p^*	p	$p = p^*/(2n^* k_BT)$
velocity	v^*	v	$v = v^*\eta^*\kappa/(2n^* k_BT)$

We work with dimensionless currents, obtained by introducing $J_1 = J_1^*/(D_1 n^* \kappa)$ and $J_2 = J_2^*/(D_2 n^* \kappa)$, where D_1 and D_2 are the bulk diffusion coefficient of the positive and negative ions, and n^* is the bulk concentration of the electrolyte at large distance away from the membrane.

We use a Poisson-Nernst-Planck approach [3], in which ion currents are treated as constant. Assuming a steady state for ion concentrations, the equations of charge conservation take the form

$$\nabla \cdot (\nabla c_1 + c_1 \nabla \psi) = 0, \tag{3}$$
$$\nabla \cdot (\nabla c_2 - c_2 \nabla \psi) = 0. \tag{4}$$

The nonlinear coupling between charge densities and potentials implies that the general solutions of equations (2–4) are difficult to obtain analytically. However, as shown in reference [29], a solution can be obtained in terms of a series expansion. In this paper, we retain only the first term in such a series expansion. This is the Debye-Hückel approximation, and corresponds to linearizing equations (3–4). With the definitions $c_1 = 1 + \delta c_1$, $c_2 = 1 + \delta c_2$, we obtain

$$\nabla \cdot (\nabla \delta c_1 + \nabla \psi) = 0, \tag{5}$$
$$\nabla \cdot (\nabla \delta c_2 - \nabla \psi) = 0. \tag{6}$$

2.1 Base state charge distribution

The base state is defined with respect to the flat membrane, for which concentration and potential variations can only occur in the z direction. We denote by δN_1, δN_2 and Ψ, the base state ion concentration profiles and the electrostatic potential, corresponding, respectively, to the

variables δc_1, δc_2 and ψ of the previous section. Since the system is driven by the application of an electric field, this base state is a nonequilibrium steady state. There are constant particle currents for ions 1 and 2, denoted by J_1 and J_2, along the z direction. The equations of charge conservation in the bulk of the electrolyte are

$$\partial_z \delta N_1 + \partial_z \Psi = -J_1, \tag{7}$$
$$\partial_z \delta N_2 - \partial_z \Psi = -J_2. \tag{8}$$

To simplify notation, we introduce

$$Q = \frac{1}{2}(\delta N_1 - \delta N_2). \tag{9}$$

Thus, Q represents half the charge distribution. From equation (2), we have

$$\partial_z^2 \Psi + Q = 0. \tag{10}$$

Equations (7–10) are to be solved with the following boundary conditions:

$$\delta N_1(z \to \pm L/2) = \delta N_2(z \to \pm L/2) = 0, \tag{11}$$
$$\Psi(\pm L/2) = \pm V/2, \tag{12}$$

far from the membrane. At the membrane surface, we enforce continuity of the electric field,

$$\partial_z \Psi_{z=0^+} = \partial_z \Psi_{z=0^-}, \tag{13}$$

since we assume that the membrane has zero fixed charge.

There is, in general, a discontinuity in the potential, due to electrochemical equilibrium across the ion channels. This implies a distribution of surface dipoles on the membrane [41]. In Appendix A, we derive a general Robin-type boundary condition for a thin dielectric membrane of thickness d

$$\delta_m \, \partial_z \Psi_{z=0^\pm} = \Psi(z = 0^+) - \Psi(z = 0^-), \tag{14}$$

where

$$\delta_m = \frac{\epsilon \kappa d^*}{\epsilon_m}, \tag{15}$$

which is also used to describe Stern layers and dielectric coatings on electrodes [42].

The limits of small thickness or small ϵ_m correspond to two distinct regimes with either $\delta_m \gg 1$ or $\delta_m \ll 1$. The regime $\delta_m \gg 1$, for equilibrium membranes, is called the decoupled limit in reference [7], because the electrical coupling between the layers is suppressed at large δ_m. This regime typically corresponds to the physical situation for biological membranes, since $\delta_m \gg 1$ implies that $\kappa d^* \gg 1/40$. Since the thickness of a typical lipid bilayer membrane is around 5 nm, this translates to the requirement that the Debye length $\kappa^{-1} \ll 40 d^* \simeq 200\,\text{nm}$, a condition which is usually satisfied. It is thus tempting to assume that we can take $\delta_m \to \infty$, thus reducing the Robin-type boundary condition to the form

$$\partial_z \Psi_{z=0^\pm} = 0. \tag{16}$$

The boundary condition of equation (16), equivalent to the field vanishing at the surface of the membrane, is simple and convenient to work with for calculational purposes. However, the precise way in which the decoupled limit should be approached is, however, somewhat subtle in the nonequilibrium case.

As we show quantitatively in Appendix A and discuss qualitatively further below, in a calculation in which the zero-thickness case is derived explicitly as a limiting case of the finite thickness problem, the $\delta_m \to \infty$ limit corresponds to unrealistically large values of the ion channel conductance in comparison to the biological situation. This has specific implications for the sign of the diffuse charge at the membrane surface. In the first part of this paper, we will nevertheless assume $\partial_z \Psi_{z=0^\pm} = 0$ for the following reasons: The use of the simpler boundary condition of equation (16) leads to considerable calculational simplification as well as reproduces the profile of the electrostatic potential to reasonable accuracy. Thus, the physical underpinnings of many of our results, including the structure of ICEO flows, can be explained more easily in this limit. Our results in this limit may be more relevant to artificial membrane systems containing pumps and channels or their analogs in which conductances can be tuned to larger values than attainable *in vivo*. The biologically more relevant general case of finite-thickness membranes, for which no such simplifying approximation is made, is analyzed in the last part of the paper. The boundary condition (14) with finite δ_m is discussed in Appendix A.

With the assumptions above, in the limit $L \gg 1$, and for $z > 0$, we obtain

$$Q^+(z) = -\sigma e^{-z}, \tag{17}$$
$$\Psi^+(z) = \sigma \left(z - \frac{L}{2} + e^{-z} \right) + \frac{V}{2}, \tag{18}$$

and for $z < 0$,

$$Q^-(z) = \sigma e^{z}, \tag{19}$$
$$\Psi^-(z) = \sigma \left(z + \frac{L}{2} - e^{z} \right) - \frac{V}{2}, \tag{20}$$

where

$$\sigma = \frac{1}{2}(-J_1 + J_2) \tag{21}$$

is the normalized electrical current, and the superscripts $\pm$ refer to the regions of $z > 0$ and $z < 0$, respectively. The electric-field component along z is $E_z^\pm(z) = -\partial_z \Psi^\pm$. For $z > 0$, we thus have

$$E_z^+(z) = \sigma(e^{-z} - 1), \tag{22}$$

and for $z < 0$

$$E_z^-(z) = \sigma(e^{z} - 1). \tag{23}$$

Note that in our dimensionless formulation $\mp\sigma = Q^+(0^\pm) - Q^-(0^\pm)$ is also the normalized diffuse (ionic) charge density evaluated at the membrane surfaces, $z = 0^\pm$. The potential and the charge distribution calculated here are shown in Figure 2.

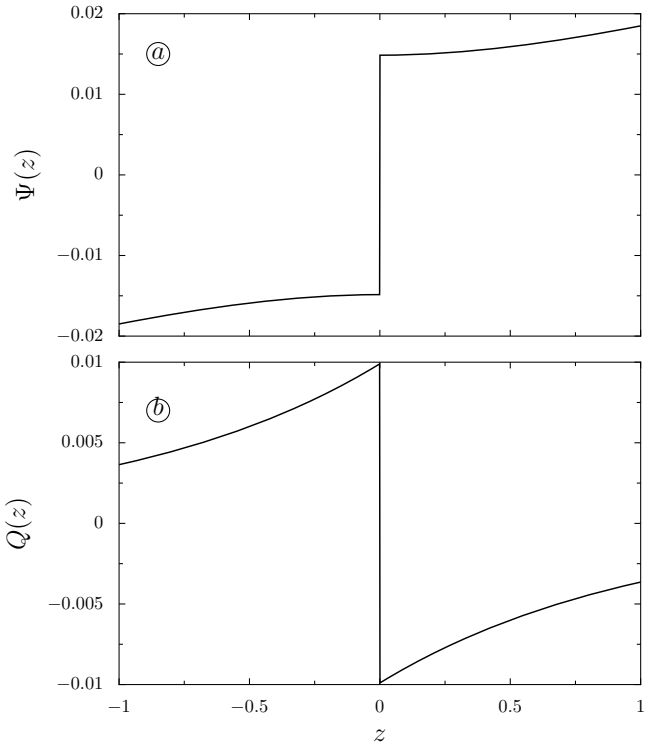

Fig. 2. Solutions of the electrokinetic equations for a membrane of zero thickness and symmetric ions concentrations. The electrostatic potential $\Psi(z)$ is shown in (a) and the quantity $Q(z)$ (which represents half the charge distribution) is shown in (b). We use dimensionless units and the following parameter values $V = 1$, $L = 100$, $G_1 = G_2 = 1$ and $k_\perp = 1$. In these conditions, $\sigma = 0.01$.

In this model, the diffuse layers are intrinsically out of equilibrium and the nonzero DC current influences the distribution of ions through (21). Note that the sign of the non-equilibrium diffuse charge is negative on the positive side of the membrane *i.e.* $z = 0^+$, which we call the cathodic side (although it faces the anode) since positive charge flows towards it. We remind the reader that the cathode is the electrode located at $z = -L/2$ (see Fig. 1), towards which positively charged cations drift, while negatively charged anions drift toward the anode at $z = L/2$.

This sign of the diffuse charge is unexpected —it is opposite to what is found in standard models for electrodes in a Galvanic cell [42] or (potentiostatic) electrodialysis membranes [43] or in other related models of a membrane in an electric field [44], where diffuse charge resides in thin layers in Boltzmann equilibrium (up to the limiting current) and has the opposite sign, positive at the cathodic and negative at the anodic surfaces. Since biological membranes are typically much less conductive than the surrounding electrolyte, it is intuitively reasonable that positive charges should pile up under the action of the electric field directed from the anode to the cathode, near the positive side of the membrane. The "wrong" sign of the charge distribution obtained in equations (17–20) and shown in Figure 2 is thus an artefact of the approximation of zero thickness and zero dielectric constant. Physically, this unusual behavior may be attributed to the following: the positive charges which should pile up near the positive side are overcompensated by a charge of the opposite sign, in order to satisfy the boundary condition equation (16) of a zero electric field on the membrane.

Taking the limit of the general Robin-type boundary condition makes sense if $1/\delta_m$ vanishes. In reality, however, δ_m is finite and although it is larger than one, it is incorrect to assume an infinite δ_m in the calculation of the charge distribution. Using the more general boundary condition (14) with finite δ_m derived in Appendix A, and which is appropriate to describe a membrane of finite thickness and finite dielectric constant, we show in Section 5 of this paper that *both signs of the charge distribution are possible in principle*. Under normal biological conditions, as we demonstrate using numerical estimates at the beginning of Section 5.2, the membrane is much less conductive than the surrounding electrolyte and the diffuse charge distribution has the opposite sign as compared to that of Figure 2.

We now discuss the boundary condition for the ion current at the membrane surface. This is ensured by choosing a specific relation between the current and the voltage at an ion pump or channel. In general such a relation is nonlinear. We assume, for simplicity, a linear relation

$$J_k = -G_k \Delta\mu_k, \tag{24}$$

where $\Delta\mu_k$ is the normalized chemical potential difference of ion k across the membrane, and G_k is a normalized conductance. This (dimensionless) conductance G_k is related to the dimensionful conductance per unit area G_k^* by

$$G_k = \frac{G_k^* k_B T}{D_k^* n^* e^2 \kappa}\,, \tag{25}$$

where the normalizing factor represents the conductance per unit area of a layer of electrolyte of thickness equal to $1/\kappa$ (one Debye layer). The normalized chemical potentials are defined by

$$\mu_1 = \delta N_1 + \Psi, \tag{26}$$

$$\mu_2 = \delta N_2 - \Psi, \tag{27}$$

and

$$\Delta\mu_k = \mu_k(z = 0^+) - \mu_k(z = 0^-). \tag{28}$$

The currents are now determined self-consistently as

$$J_1 = -\frac{G_1 V}{1 + G_1 L}\,, \tag{29}$$

$$J_2 = \frac{G_2 V}{1 + G_2 L}\,. \tag{30}$$

Restoring dimensions, the electrical current is [25]

$$i_k^* = \frac{-G_k^* v_k^*}{1 + \frac{G_k^* L^* k_B T}{D_k n^* e^2}}\,, \tag{31}$$

with $i_k^* = z_k e J_k^*$ the part of the total electric current associated with ion k of charge $z_k = \pm 1$, $v_k^* = V^* - V_{\mathrm{Nernst},k}^*$,

and $V^*_{\mathrm{Nernst},k}$ the Nernst potential of ion k, which is zero here due to our assumption of symmetric concentrations. Note that σ^* has the units of charge per unit surface and is the surface charge of the Debye layers. It is related to σ defined in equation (21) by

$$\sigma^* = \frac{k_B T \kappa \epsilon \sigma}{e}\,. \tag{32}$$

The equivalent of equation (21) in dimensionful form is

$$\sigma^* = -\frac{1}{\kappa^2}\left(\frac{i_1^*}{D_1} + \frac{i_2^*}{D_2}\right). \tag{33}$$

This equation expresses the conservation of charge inside the Debye layers: for each ion k, the contribution in the surface charge of the Debye layer σ^* is the product of the total electric current per unit area i_k^* carried by ion k, with the diffusion time $1/\kappa^2 D_k$ for the ion to diffuse over a length scale equal to the Debye length.

Equation (31) is consistent with the usual electric representation of ion channels in the Ohmic regime in which the contribution of each ion is taken in parallel. There are two conductances for each ion, accounting for the contributions of the electrolyte on both sides, and an electromotive force E_k in series [25]. The form of equations (17–20) is general and holds even when a nonlinear current *versus* chemical potential relation is used in place of equations (24). However, our approach will be restricted to the linear regime for the ion channel response.

We stress that the form of this base state is general in the sense that the precise origin of the ion currents is immaterial because these currents are constant (independent of z). A qualitatively similar base state would describe the situation where such currents are created *internally* by active pumps, in the absence of any externally imposed potential difference or concentration gradients.

To complete the characterization of the base state, we calculate the stresses on the membrane. We define the stress tensor by

$$\tau^*_{ij} = \tau^{H*}_{ij} + \tau^{M*}_{ij}, \tag{34}$$

where τ^{H*}_{ij} and τ^{M*}_{ij} are the hydrodynamic and Maxwell stress tensors, respectively, defined by

$$\tau^{H*}_{ij} = -P^*\delta_{ij} + \eta^*\left(\partial^*_i v^*_j + \partial^*_j v^*_i\right), \tag{35}$$

where η^* is the solvent viscosity and

$$\tau^{M*}_{ij} = \epsilon\left(E^*_i E^*_j - \delta_{ij} E^{*2}/2\right). \tag{36}$$

In dimensionless form these are

$$\tau_{ij} = \tau^H_{ij} + \tau^M_{ij}, \tag{37}$$

with

$$\tau^H_{ij} = -P\delta_{ij} + (\partial_i v_j + \partial_j v_i), \tag{38}$$

and

$$\tau^M_{ij} = E_i E_j - \delta_{ij} E^2/2, \tag{39}$$

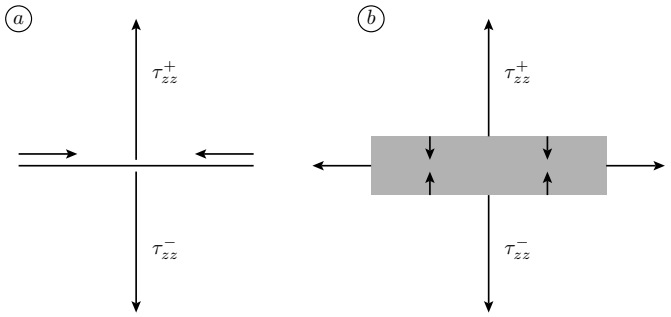

Fig. 3. Electrostatic corrections to the membrane tension for a membrane of zero thickness (a) and finite thickness (b). The Maxwell stresses are represented by vertical arrows while the horizontal arrows represent the resulting tension on the membrane as a consequence of incompressibility.

where E_i is the i-th component of the electric field. The pressure P is the osmotic pressure of the ions in the Debye layers. In the base state, the condition $\nabla \cdot \tau = 0$ is equivalent to $\nabla P = QE$, with Q and E given by equations (17–20).

With the boundary condition $P(z = \infty) = 0$, we obtain

$$P(z) = \sigma^2\left(-e^{-z} + \frac{e^{-2z}}{2}\right), \tag{40}$$

for $z > 0$. Using equations (38, 39), the stress on the positive side is calculated as $\tau^+_{zz}(z = 0) = \sigma^2/2$. It is straightforward to check that the same contribution exists on the negative side. Thus, overall, normal stresses are balanced in the base state, although a pressure gradient is present.

2.2 Interpretation of the electrostatic contribution to the surface tension

The extensive normal stresses discussed in the previous subsection can be argued to result in a positive electrostatic correction to the membrane surface tension (see Fig. 3). This correction to the membrane tension Σ can be obtained from the knowledge of the electric field in the base state $E^{(0)}$ [25]. In our geometry, this correction can be written as

$$\Sigma = \int_{-\infty}^{\infty} [\tau_{xx}(z) - \tau_{zz}(z)]\mathrm{d}z, \tag{41}$$

where τ_{xx} and τ_{zz} are components of the stress tensor. This derivation assumes incompressibility [45].

The electrostatic contribution to the surface tension is obtained from the Maxwell stress by $\Sigma = \Sigma_0 + \Sigma_1$ with

$$\Sigma_0 = -\int_{-L/2}^{L/2} (E^{(0)}_z)^2(z)\mathrm{d}z, \tag{42}$$

and

$$\Sigma_1 = \frac{L}{2}\left[(E^{(0)}_z)^2(z \to \infty) + (E^{(0)}_z)^2(z \to -\infty)\right]. \tag{43}$$

The term in Σ_1 ensures that the stress tensor remains divergence free. Both Σ_0 and Σ_1 contain contributions proportional to L, which originate from the pressure gradient in the fluid. As expected, these terms cancel each other in Σ. Substituting our previous expression for the electrostatic potential into equation (42), we find that $\Sigma = 3\sigma^2$. We will recover this result in the next section using a different method.

We now illustrate our physical picture for the origin of this electrostatic correction to the membrane tension. As shown in Figure 3, for a membrane of zero thickness, only Debye layers above and below the membrane contribute to the electrostatic correction to the membrane tension. The electrostatic force acting on the induced charges in the Debye layers on the positive and negative sides creates extensive stresses $\tau_{zz}^{\pm}$ near the membrane. These stresses, by incompressibility, tend to reduce the membrane area, thus producing an increase in the membrane tension. This can be termed as the "outside" contribution to the surface tension. In the case of a membrane of finite thickness there is, in addition to the "outside" contribution, an "inside" contribution. The "inside" contribution is in general dominant, because the largest voltage drop in this problem occurs across the membrane. This is a consequence of the large mismatch in dielectric constants between the membrane and the electrolyte ($\delta_m \gg 1$).

The "inside" contribution arises from compressive stresses (represented as opposing arrows within the shaded area on the figure on the right), which are generically present in any capacitor. These compressive stresses, directed along the z direction, produce lateral extensional stresses due to the conservation of the inside volume of the membrane. These stresses act to increase the membrane area, thus producing a negative electrostatic correction to the membrane tension. This contribution has been recognized to drive instabilities in membranes when a normal DC electric field is applied [6,39,44].

Recent experimental studies on the fluctuation spectrum of active membranes containing bacteriorhodopsin exhibit a lowering of the membrane tension in active vesicles as compared to passive ones [46]. This observation is consistent with the interpretation suggested above, where the lowering of the tension would be caused by a change in normal Maxwell stresses as a consequence of ion fluxes in or out of the vesicle. Although this interpretation appears plausible, alternate explanations are possible: further experimental work and theoretical modeling are necessary to confirm this proposal.

2.3 Charge fluctuations

In a linear approximation, the electrostatic potential can be written as a superposition of the base state contribution $\psi^{(0)}$ and a contribution linear in the membrane height field $\psi^{(1)}$. We work in the quasi-static approximation, which corresponds to angular frequency ω^*, such that $\omega^* \ll D_k^* \kappa^2$. This approximation means that the membrane fluctuations occur on a time scale which is much slower than the time over which the electrostatic configuration adjust itself. Simple numerical estimates show that there is indeed such a separation of time scales [39]. This approximation allows us to solve the electrostatic problem for a fixed weakly curved geometry of the membrane.

With our previous notation $q^{(0)} = Q$, $c_k^{(0)} = N_k$ and $\psi^{(0)} = \Psi$ in the base state, we now have

$$\begin{aligned} \psi(\mathbf{k}_\perp, z) &= \Psi(z) + \psi^{(1)}(\mathbf{k}_\perp, z), \\ q(\mathbf{k}_\perp, z) &= Q(z) + q^{(1)}(\mathbf{k}_\perp, z), \\ c_1(\mathbf{k}_\perp, z) &= N_1(z) + c_1^{(1)}(\mathbf{k}_\perp, z), \\ c_2(\mathbf{k}_\perp, z) &= N_2(z) + c_2^{(1)}(\mathbf{k}_\perp, z). \end{aligned} \tag{44}$$

We use the following definition of Fourier transforms of an arbitrary function $g(\mathbf{r}_\perp, z)$:

$$g(\mathbf{k}_\perp, k_z) = \int \mathrm{d}\mathbf{r}_\perp \mathrm{d}z e^{-i(\mathbf{k}_\perp \cdot \mathbf{r}_\perp + k_z z)} g(\mathbf{r}_\perp, z), \tag{45}$$

and the inverse Fourier transform,

$$g(\mathbf{r}_\perp, z) = \frac{1}{(2\pi)^3} \int \mathrm{d}\mathbf{k}_\perp \mathrm{d}k_z e^{i(\mathbf{k}_\perp \cdot \mathbf{r}_\perp + k_z z)} g(\mathbf{k}_\perp, k_z). \tag{46}$$

Consider now the contribution linear in the membrane height field $\psi^{(1)}$. The equations for the Fourier transforms of the charge distribution

$$q^{(1)}(\mathbf{k}_\perp, z) = \frac{1}{2}\left(c_1^{(1)}(\mathbf{k}_\perp, z) - c_2^{(1)}(\mathbf{k}_\perp, z)\right) \tag{47}$$

and of the electrostatic potential $\psi(\mathbf{k}_\perp, z)$ follow from equations (2–6),

$$(\partial_z^2 - k_\perp^2)\psi^{(1)}(\mathbf{k}_\perp, z) + q^{(1)}(\mathbf{k}_\perp, z) = 0, \tag{48}$$

$$(\partial_z^2 - k_\perp^2)\left(q^{(1)}(\mathbf{k}_\perp, z) + \psi^{(1)}(\mathbf{k}_\perp, z)\right) = 0. \tag{49}$$

Since L is much larger than a Debye length, we can take the boundary conditions far from the membrane to be $\psi^{(1)}(\mathbf{k}_\perp, \pm\infty) = q^{(1)}(\mathbf{k}_\perp, \pm\infty) = 0$.

The relation between the current and the voltage at the membrane surface incorporating the contribution linear in the membrane height field is then calculated as

$$\begin{aligned} &\partial_z \left(c_1^{(1)}(\mathbf{k}_\perp, z) + \psi^{(1)}(\mathbf{k}_\perp, z)\right)_{z=h(\mathbf{r}_\perp)} = G_1 \\ &\times \big(c_1^{(1)}(\mathbf{k}_\perp, 0^+) - c_1^{(1)}(\mathbf{k}_\perp, 0^-) + \psi^{(1)}(\mathbf{k}_\perp, 0^+) \\ &-\psi^{(1)}(\mathbf{k}_\perp, 0^-)\big), \\ &\partial_z \left(c_2^{(1)}(\mathbf{k}_\perp, z) - \psi^{(1)}(\mathbf{k}_\perp, z)\right)_{z=h(\mathbf{r}_\perp)} = G_2 \\ &\times \big(c_2^{(1)}(\mathbf{k}_\perp, 0^+) - c_2^{(1)}(\mathbf{k}_\perp, 0^-) - \psi^{(1)}(\mathbf{k}_\perp, 0^+) \\ &+\psi^{(1)}(\mathbf{k}_\perp, 0^-)\big). \end{aligned} \tag{50}$$

These relations, the boundary conditions for the potential and the ion concentrations at infinity, as well as equation (48) are all satisfied when $c_1^{(1)}(\mathbf{k}_\perp, z) = -c_2^{(1)}(\mathbf{k}_\perp, z)$ and $q^{(1)}(\mathbf{k}_\perp, z) = -\psi^{(1)}(\mathbf{k}_\perp, z)$. This implies a zero flux

boundary condition for the contribution to first order in the membrane height field

$$\left(\partial_z q^{(1)} + \partial_z \psi^{(1)}\right)_{z=0} = 0. \tag{51}$$

At this order, whether the fluxes are directed along the normal $\hat{\mathbf{n}}$ rather than along $\hat{\mathbf{z}}$ is irrelevant, since the difference between $\hat{\mathbf{n}}$ and $\hat{\mathbf{z}}$ only introduces corrections to equation (51) which are of higher order than linear in h.

As a consequence, $\psi^{(1)}$ only depends on the zeroth-order solution through the boundary conditions for the potential. The boundary condition for the total potential corresponds to a vanishing electric field at the membrane perturbed surface and is thus

$$(\partial_z \psi)_{z=h(\mathbf{r}_\perp)} = \left(h(\mathbf{r}_\perp)\partial_z^2 \Psi + \partial_z \psi^{(1)}\right)_{z=0} = 0. \tag{52}$$

Our final results for the potential thus are, for $z > 0$,

$$\psi^{(1)}(\mathbf{k}_\perp, z) = -q^{(1)}(\mathbf{k}_\perp, z) = \frac{h(\mathbf{k}_\perp)\sigma}{l} e^{-lz}, \tag{53}$$

and for $z < 0$,

$$\psi^{(1)}(\mathbf{k}_\perp, z) = -q^{(1)}(\mathbf{k}_\perp, z) = \frac{h(\mathbf{k}_\perp)\sigma}{l} e^{lz}, \tag{54}$$

where we have introduced

$$l = \sqrt{k_\perp^2 + 1}, \tag{55}$$

the characteristic inverse length of the electrostatic potential. The charge distribution and potential are even functions of z. Figure 2 exhibits the potential $\Psi(z)$ and $\psi^{(1)}(\mathbf{k}_\perp, z)$ in dimensionless units. This illustrates the discontinuity of the potential across the membrane, and the fact that the electric field vanishes at the membrane surface at zeroth order, as imposed by equation (16).

2.4 Membrane elasticity and force balance

In order to describe the coupling between the charge fluctuations in the electrolyte and the membrane, the Stokes equations must be solved with the appropriate boundary conditions, namely, the continuity of the velocity and the tangential stress constraints.

The elastic properties of the membrane are described by an Helfrich free energy

$$F_{mb} = \frac{1}{2} \int \mathrm{d}^2 \mathbf{r}_\perp [\kappa_0 (\nabla^2 h)^2 + \sigma_0 (\nabla h)^2], \tag{56}$$

where κ_0 is the bare bending modulus and σ_0 is the bare surface tension of the membrane.

The components of the stress tensor which act normal to the membrane are discontinuous, and that discontinuity is equal to the restoring force exerted by the membrane on the fluid, which is equal to

$$-\frac{\partial F_{mb}}{\partial h(\mathbf{r}_\perp)} = \sigma_0 \triangle h(\mathbf{r}_\perp) - \kappa_0 \nabla^4 h(\mathbf{r}_\perp). \tag{57}$$

2.5 Linear hydrodynamics of the membrane-fluid system

The equation of motion of the fluid, in the limit of low Reynolds number and slow variation with time, is the Stokes equation supplemented by the condition of incompressibility. The governing equations, in dimensionless form, incorporating an arbitrary force density $\mathbf{f}$, are

$$\nabla \cdot \mathbf{v} = 0, \tag{58}$$

$$-\nabla p + \triangle \mathbf{v} + \mathbf{f} = 0. \tag{59}$$

We have rescaled the velocity by $2n^* k_B T/\eta^* \kappa$, and the pressure by $2n^* k_B T$. The Stokes equation (Eq. (59)) can be written equivalently as $\nabla \cdot \tau = 0$ in terms of the stress tensor of the fluid introduced in equations (38, 39).

In view of the invariance of the problem with respect to translations parallel to the membrane surface, it is helpful to use the 2D Fourier representation introduced in equations (45, 46). As shown in references [1,47], all vector fields in this problem can be decomposed into three components: longitudinal (*i.e.* along $\mathbf{k}_\perp$), transverse or normal (*i.e.* along $\hat{\mathbf{z}}$). These vectors form the triad $(\hat{\mathbf{k}}_\perp, \hat{\mathbf{n}}, \hat{\mathbf{t}})$, where $\hat{\mathbf{k}}_\perp = \mathbf{k}_\perp/k_\perp$, $\hat{\mathbf{n}} = \hat{\mathbf{z}}$ and $\hat{\mathbf{t}} = \hat{\mathbf{k}}_\perp \times \hat{\mathbf{n}}$. In such a coordinate system, the incompressibility condition takes the form

$$\partial_z v_z + i\mathbf{k}_\perp \cdot \mathbf{v}_\perp = 0, \tag{60}$$

and the Stokes equations become

$$-i\mathbf{k}_\perp p - k_\perp^2 \mathbf{v}_\perp + \mathbf{f}_\perp + \partial_z^2 \mathbf{v}_\perp = 0, \tag{61}$$

$$-\partial_z p + \partial_z^2 v_z - k_\perp^2 v_z + f_z = 0, \tag{62}$$

$$\partial_z^2 v_t - k_\perp^2 v_t + f_t = 0. \tag{63}$$

In the bulk of the electrolyte, we know the expression of the force $\mathbf{f}$. It is the electrostatic force acting on the local charge distribution, thus

$$\mathbf{f} = -q\nabla\psi, \tag{64}$$

which, at first order in the perturbation defined in equation (44), is

$$\begin{aligned} \mathbf{f}_\perp(\mathbf{k}_\perp, z) &= -i\mathbf{k}_\perp \psi^{(1)}(\mathbf{k}_\perp, z) Q(z), \\ f_z(\mathbf{k}_\perp, z) &= -\nabla_z \psi^{(1)}(\mathbf{k}_\perp, z) Q(z) \\ &\quad - q^{(1)}(\mathbf{k}_\perp, z) \nabla_z \Psi(z). \end{aligned} \tag{65}$$

Note that the force $\mathbf{f}$ above has no components along the transverse direction, and that the equation for v_t is decoupled from that of the other components of the velocity. In view of the boundary conditions appropriate here, we have $v_t = 0$ everywhere. Thus, we only need to consider the longitudinal and normal components. Although these components appear coupled in equations (61, 62), they can in fact be decoupled and the pressure can be eliminated. Indeed, the pressure can be obtained from equation (61). After using the incompressibility condition, the expression can be written in terms of only v_z and $\mathbf{f}_\perp$

$$p = -\partial_z v_z + \frac{1}{ik_\perp} \mathbf{f}_\perp + \frac{1}{k_\perp^2} \partial_z^3 v_z. \tag{66}$$

After inserting this expression for the pressure in equation (61) and using the incompressibility condition of equation (60), one finds that the normal component of the velocity v_z obeys a single fourth-order differential equation

$$(\partial_z^2 - k_\perp^2)(\partial_z^2 - k_\perp^2)v_z + (q^{(1)}\partial_z\Psi - \partial_z\psi^{(1)}Q) = 0. \quad (67)$$

The boundary conditions are: i) continuity of the velocity, ii) continuity of tangential constraints and iii) discontinuity of the normal-normal component of the stress tensor. The equations of continuity for the velocity field are

$$v_z(z = 0^+) = v_z(z = 0^-) = \frac{\partial h(\mathbf{r}_\perp)}{\partial t}\,, \quad (68)$$

$$\mathbf{v}_\perp(z = 0^+) = \mathbf{v}_\perp(z = 0^-) = 0. \quad (69)$$

We have assumed, in writing equation (68), that there is a negligible amount of permeation of water across the bilayer, an assumption which should be suitable to describe most ion channels [19]. Although the membrane does permit the two-way flow of ions across it, the mechanical response of the membrane is dictated primarily by its relatively low permeability to water. Far from the membrane, we expect that

$$v_z(z \to \pm\infty) = p(z \to \pm\infty) = 0. \quad (70)$$

Interestingly, the boundary conditions for the transverse component of the velocity equation (69) together with the incompressibility condition equation (58) imply another continuity relation for the derivative of v_z [47]

$$\left(\frac{\partial v_z}{\partial z}\right)_{z=0^+} = \left(\frac{\partial v_z}{\partial z}\right)_{z=0^-}. \quad (71)$$

The boundary conditions expressing the continuity of the tangential constraints ii) and the discontinuity of the normal-normal component of the stress tensor iii) are

$$-\tau_{\perp z}(z = 0^+) + \tau_{\perp z}(z = 0^-) = 0, \quad (72)$$

$$-\tau_{zz}(z = 0^+) + \tau_{zz}(z = 0^-) = -\frac{\partial F_{mb}}{\partial h(\mathbf{r}_\perp)}\,. \quad (73)$$

It is important to stress that this problem cannot be formulated only in terms of bulk forces, *i.e.* of the divergence of a stress tensor, because the hydrodynamic and Maxwell stress tensors enter the boundary conditions at the membrane surface explicitly. For this reason, the force of equation (64) only holds in the bulk, but the force localized on the membrane surface is unknown in this problem. It must be determined by enforcing the velocity and the stress boundary conditions.

2.6 Effective elastic moduli of the membrane

In this section, we give the equation of motion of the membrane which is obtained from the solution of the linear hydrodynamic equations. It is convenient to introduce the growth rate s of the height fluctuation defined by $h(\mathbf{r}_\perp, t) = h(\mathbf{k}_\perp)\exp(i\mathbf{k}_\perp \cdot \mathbf{r}_\perp + st)$, so that the continuity equation for the normal component of the fluid velocity equation (68) can be written equivalently as

$$v_z(\mathbf{k}_\perp, z = 0^\pm) = sh(\mathbf{k}_\perp). \quad (74)$$

As shown in Appendix B, the following equation of motion for the membrane results:

$$s = -\frac{1}{4}(3\sigma^2 + \sigma_0)k_\perp + \sigma^2 k_\perp^2 - \left(\frac{3\sigma^2}{16} + \frac{\kappa_0}{4}\right)k_\perp^3. \quad (75)$$

In the particular case where $\sigma = 0$, corresponding to the case where there are no bulk electrostatic forces $\mathbf{f} = 0$, we recover a well-known relation [19], which can be written

$$s = -\frac{1}{4}\sigma_0 k_\perp - \frac{\kappa_0}{4}k_\perp^3, \quad (76)$$

or equivalently

$$\frac{\partial h(\mathbf{k}_\perp)}{\partial t} = -\frac{1}{4k_\perp}\frac{\partial F_{mb}}{\partial h(\mathbf{k}_\perp)}. \quad (77)$$

A convenient way to describe the effect of the additional terms arising in the equation of motion due to the electrostatic force when $\sigma \neq 0$ is to generalize equation (77) to

$$\frac{\partial h(\mathbf{k}_\perp)}{\partial t} = -\frac{1}{4k_\perp}\frac{\partial (F_{mb} + \delta F_{mb})}{\partial h(\mathbf{k}_\perp)}\,, \quad (78)$$

where we have introduced an effective free energy δF_{mb} to account for the contribution of electrostatic stresses on the membrane. We stress that this definition does not imply that this effective free energy is to be understood in thermodynamic terms. It is merely a convenient way of understanding the role of each separate contribution to the stress tensor arising out of membrane fluctuations. Writing this effective free energy as

$$\delta F_{mb} = \frac{1}{2}\int \mathrm{d}^2\mathbf{k}_\perp h(\mathbf{k}_\perp)h(-\mathbf{k}_\perp)[Kk_\perp^4 + \Sigma k_\perp^2 + \Gamma k_\perp^3], \quad (79)$$

we obtain electrostatic corrections to the elastic moduli of the membrane.

Since the second term on the right-hand side of equation (75) is positive (a consequence of the fact that Γ is negative), a finite-wavelength instability of a membrane or vesicle of low tension can occur when σ is sufficiently high [25]. We provide an estimate of the characteristic wave vector k_c below.

When nonthermal noise can be neglected, the fluctuation spectrum of the membrane height field can be obtained from equations (56–79),

$$\langle |h(\mathbf{k}_\perp)|^2 \rangle = \frac{1}{(\sigma_0 + \Sigma)k_\perp^2 + \Gamma k_\perp^3 + (\kappa_0 + K)k_\perp^4}\,. \quad (80)$$

Such a spectrum is shown in Figure 9.

Our results are the following: We find an electrostatic correction to the surface tension $\Sigma = 3\sigma^2$, thus recovering the result obtained in equation (42). There is also

a positive correction to the bending modulus which is $K = 3\sigma^2/4$. Such terms are not surprising because they are present with the same sign in equilibrium charged membranes [7]. What is, however, surprising is the presence of a new purely nonequilibrium term in the factor of $k_\perp^3$ in the free energy, $\Gamma = -4\sigma^2$. We propose a physical interpretation for this term in the section which follows.

In dimensionful form, these moduli are $\Sigma^* = 3(\sigma^*)^2/\kappa$, $K^* = 3(\sigma^*)^2/4\kappa^3$ and $\Gamma^* = -4(\sigma^*)^2/\kappa^2$, in terms of σ^* the dimensionful surface charge, in agreement with reference [25]. For order-of-magnitude estimates, with $V^* = 50\,\mathrm{mV}$, $L^* = 1\,\mu\mathrm{m}$, $G_1^* = G_2^* = 10\,\Omega^{-1}/\mathrm{m}^2$, $D_1 = D_2 = 10^{-5}\,\mathrm{cm}^2/\mathrm{s}$ and $n^* = 16.6\,\mathrm{mM}$, we obtain $\Sigma^* = 3.2 \cdot 10^{-16}\,\mathrm{J\,m}^{-2}$, $\Gamma^* = -10^{-24}\,\mathrm{J\,m}^{-1}$ and $K^* = 10^{-13} k_B T$. Although the ion flux is typical of ion channels, the moduli Σ^*, Γ^* and K^* are very small due to the strong dependence of these moduli on κ^{-1}, which is only 2.3 nm here. As we show below, these low values also reflect the fact that we have, until now, neglected the bilayer character of the membrane and its finite capacitance.

The characteristic wave vector of the finite-wavelength instability discussed in equation (75) is $k_c = -\Gamma/2(K + K_0)$ [25]. With the numerical estimates given above, and a typical value for the bare bending modulus of the membrane $K0$ of 10 kT, one finds that k_c is of the order of $10^{-5}\,\mathrm{m}^{-1}$. This corresponds to a very large length scale, which indicates that this instability is unlikely to be observed in practice. A very different instability arises in a membrane of finite thickness when the tension becomes negative. That instability is a zero-wavelength instability and is a real effect [6,39,44].

3 Electro-osmotic flow induced around the membrane

In this section, we propose an interpretation of the cubic term in $k_\perp$ with coefficient Γ in the effective free energy obtained above. Our arguments are based on the existence of a nonlinear electro-osmotic flow around a curved membrane. This direct electrokinetic effect is present in addition to the usual viscous flow caused by membrane motion [48], shown in Figure 4(a), which couples indirectly to the electric field.

In our geometry, the electric field is directed mainly along the z-direction. Our analysis of charge fluctuations indicated that perturbations in the membrane shape induced a tangential component of the electric field near the membrane. Such a tangential electric field acts on the diffuse charge in the diffuse layers, creating an effective hydrodynamic slip relative to the instantaneous membrane position. This electrokinetic effect creates an array of counter-rotating vortices around the membrane, illustrated in Figure 4(b), which tend to enhance shape perturbations.

The general phenomenon of nonlinear electro-osmotic flow around a polarizable surface has been termed "induced-charge electro-osmosis" (ICEO) [28]. It arises in a variety of situations involving polarizable surfaces, producing circulating flow patterns similar to those in our problem of a fluctuating driven membrane. What we now call ICEO flow was first described by V. Murtsovkin and collaborators in Russia [30] in the case of metallic colloidal spheres. Recent interest in the subject has focused on novel phenomena in microfluidic devices, such as AC electro-osmotic flow around electrode arrays [31, 27], ICEO flow around metal posts [32,33] and dielectric corners [34,35] and induced-charge electrophoresis [28,36]. However, we are not aware of any prior theory or experiment describing ICEO around membranes.

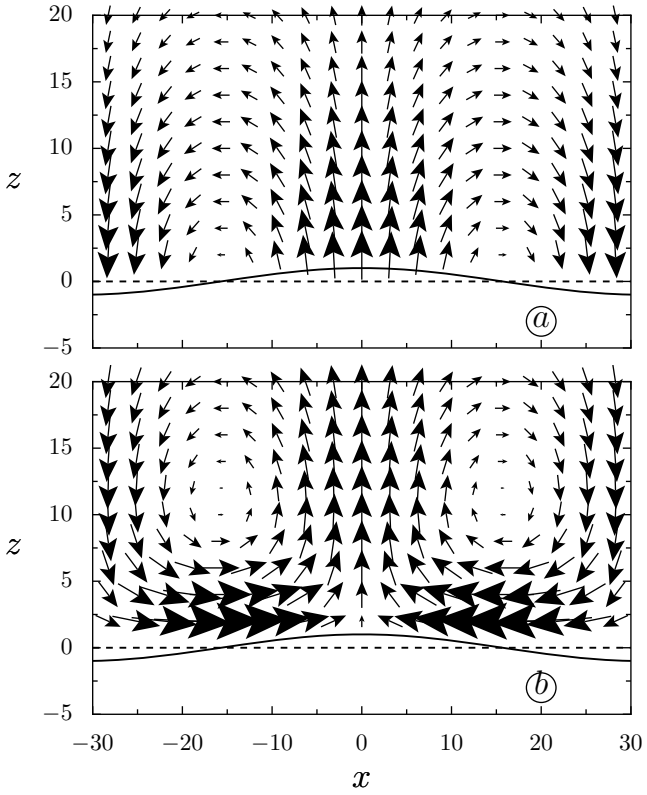

Fig. 4. Two types of fluid flow around a perturbed, driven membrane. (a) The membrane bending mode with associated flow field [48], in the absence of any applied electric field: $\sigma = 0$. In this case, it is the motion of the membrane which drives the flow field by the incompressibility condition. For a growing sinusoidal perturbation, streamlines connect the peaks to the valleys. The membrane seen edge-on as a solid line, undergoes a bending wave of wave vector 0.1 (or of wavelength 20π) and of amplitude 0.1. Note that the height of the membrane has been multiplied by an extra factor 10 for improved visualization. The undeformed membrane is shown edge-on as a dashed line. (b) Vortices of induced-charge electro-osmosis (ICEO) for a nonmoving curved membrane, due to effective slip from the valleys to the peaks, as explained below. Unlike the case (a), here it is the flow field induced by ICEO which determines the modulation of this nonmoving membrane. The applied electric field corresponds to $\sigma = 30$. In this example, as in biological membranes, the double layers are thin compared to the wavelength of the perturbation $k_\perp = k_\perp^*/\kappa \ll 1$. The calculation also assumes linear response to a small amplitude perturbation, $\kappa h^* \ll 1$. In these figures, this condition is satisfied since $h = 0.1$, and the unit length corresponds to one Debye length.

The classical theory of electrokinetic phenomena assumes a constant surface charge, or equivalently, a constant voltage (zeta potential) between the shear plane at the surface and the quasi-neutral bulk electrolyte just outside the diffuse charge layer [26]. In that case, the presence of a tangential component of the electric field (approximately constant across the thickness of the double layer) leads to electro-osmotic flow that is linear in the field. For thin double layers, the effective hydrodynamic slip outside the double layer is given by the Helmholtz-Smoluchowski formula [26]

$$\mathbf{v}_\perp{}^* = -\frac{\epsilon\zeta^*}{\eta^*}\mathbf{E}_\perp{}^*, \tag{81}$$

where ζ^* denotes the zeta potential across the diffuse part. This result holds in the asymptotic limit of thin double layers. It is also valid even if a normal current drives the diffuse charge out of equilibrium —all that is required is for the viscosity and permittivity to be constant within the double layer and for the bulk salt concentration to be uniform (without tangential gradients) [28,43]. At a polarizable surface, the zeta potential and tangential field component vary in response to perturbations of the system. This results in nonlinear ICEO flows which typically vary with the square of the applied voltage.

To understand the appearance of ICEO flow in our system, we begin by considering dominant balances in the dimensionless equations. We first consider the limit of thin double layers compared to the perturbation wavelength, $k_\perp \ll 1$ (or $k_\perp^* \ll \kappa$), which is relevant for biological membranes. In our system of normalized units, the electro-osmotic slip formula (81) predicts the scaling

$$\mathbf{v}_\perp(\mathbf{k}_\perp, z \geq 1) \simeq -\zeta \mathbf{E}_\perp(\mathbf{k}_\perp, z \to 0^+), \tag{82}$$

where the effective slip velocity outside the double layer ($z \geq 1$) is proportional to the typical tangential electric field in the diffuse layer, set by its typical value within the Debye layer at the surface ($z \to 0^+$). Although the scaling is the same, a subtle difference with Helmholz-Smoluchowski theory is that the tangential electric field is confined to the diffuse layer and vanishes in the neutral bulk electrolyte ($z \geq 1$).

The expression (82) can be verified by direct integration of the Stokes equation as follows. After projecting equation (59) in the transverse direction, and retaining only terms of first order, one obtains

$$\triangle \mathbf{v}_\perp + Q(z)\mathbf{E}_\perp{}^{(1)} = 0, \tag{83}$$

which can be simplified using the condition $k_\perp \ll 1$ to give

$$\partial_z^2 \mathbf{v}_\perp(\mathbf{k}_\perp, z) + Q(z)\mathbf{E}_\perp{}^{(1)}(\mathbf{k}_\perp, z) = 0. \tag{84}$$

Now from (53) in the limit $k_\perp \ll 1$,

$$\mathbf{E}_\perp{}^{(1)}(\mathbf{k}_\perp, z) = -i\mathbf{k}_\perp \psi^{(1)}(\mathbf{k}_\perp, z) = -i\mathbf{k}_\perp \sigma h(\mathbf{k}_\perp) e^{-z}. \tag{85}$$

After inserting equation (85) into equation (84), using the no-slip condition $\mathbf{v}_\perp{}^{(1)}(\mathbf{k}_\perp, z = 0^+) = 0$, the transverse first-order velocity profile is found to scale as (dropping a numerical prefactor of $i/4$)

$$\mathbf{v}_\perp{}^{(1)}(\mathbf{k}_\perp, z) \simeq \sigma^2 \mathbf{k}_\perp h(\mathbf{k}_\perp)(1 - e^{-2z}), \tag{86}$$

a scaling which is also confirmed by our solution of the Stokes equation given in the previous section (cf. App. B).

Thus, the scaling of the Helmholz-Smoluchowski relation (Eq. (82)) indeed holds with $\zeta = \zeta^{(0)} = -Q^{(0)}(z = 0^+) = \sigma$. The only difference is the dropped factor of $1/4$, which results from the decay of the tangential electric field within the diffuse layer, in contrast to the Helmholz-Smoluchowski assumption of a uniform field applied in the bulk electrolyte. Note also that the first-order perturbed field due to membrane displacement acts on the leading-order base-state diffuse charge to drive electro-osmotic flow. This thus differs from other examples of ICEO flow [28], where the field acts on the perturbed charge, as discussed below. Taking into account the constant low-voltage capacitance of the diffuse layer $C_D^* = \epsilon\kappa$, the induced zeta potential is related to the total diffuse charge by $\zeta^* = \sigma^*/C_D^*$ [27,49]. In dimensionless units, we recover again $\zeta^{(0)} \simeq \sigma$. Using the incompressibility condition (58), we obtain the scaling $v_z(\mathbf{k}_\perp, z \to 0^+) \simeq k_\perp^2 h(\mathbf{k}_\perp)\sigma^2$. As illustrated in Figure 4(b), the normal velocity is smaller than the tangential velocity by a factor $k_\perp$. Applying the boundary conditions $v_z(\mathbf{k}_\perp, z \to 0^+) = \partial h/\partial t$ together with equations (79–77), we find that the velocity estimated from this ICEO argument indeed corresponds to $\Gamma \simeq \sigma^2$ in the effective free energy of the membrane. Note that the velocity $v_z(\mathbf{k}_\perp, z \to 0^+)$ scales with the square of the applied electric field, so ICEO is relevant for both DC and AC electric fields, as long as the AC period exceeds the charging time (see below).

An equilibrium term in $k_\perp^3$, originating in unscreened dipole-dipole interactions, is also obtained in the calculation of reference [39], but in the high $k_\perp$ limit, in which $k_\perp L \gg 1$. It is absent in the low $k_\perp$ limit. Since the term we derive is obtained after taking $L \to \infty$, it is clear that the origin of this term is very different in both calculations and has an explicitly nonequilibrium origin in our approach.

In the remainder of this section, we give simple scaling arguments (with dimensions, for clarity) to highlight the basic physics of this new phenomenon of ICEO that we predict around driven membranes. For comparison, we first review the canonical example of ICEO flow around an ideally polarizable, uncharged metal post in a suddenly applied DC field E^* [28], illustrated in Figure 5(a-c). We scale the geometry of the metal post to that of our curved membrane with an extent h^* parallel to the field and $k_\perp^{*-1}$ perpendicular to the field. In the base state (a) at $t = 0$, the metal post is an equipotential surface, but this is not a stable situation, since the surface is assumed not to pass any current. Instead, the normal current entering the diffuse layer charges it locally like a capacitor, until all the field lines are expelled (after the "RC" charging time $\tau_c^* \sim (D\kappa k_\perp^*)^{-1}$, where D is a characteristic ionic diffusivity [49]).

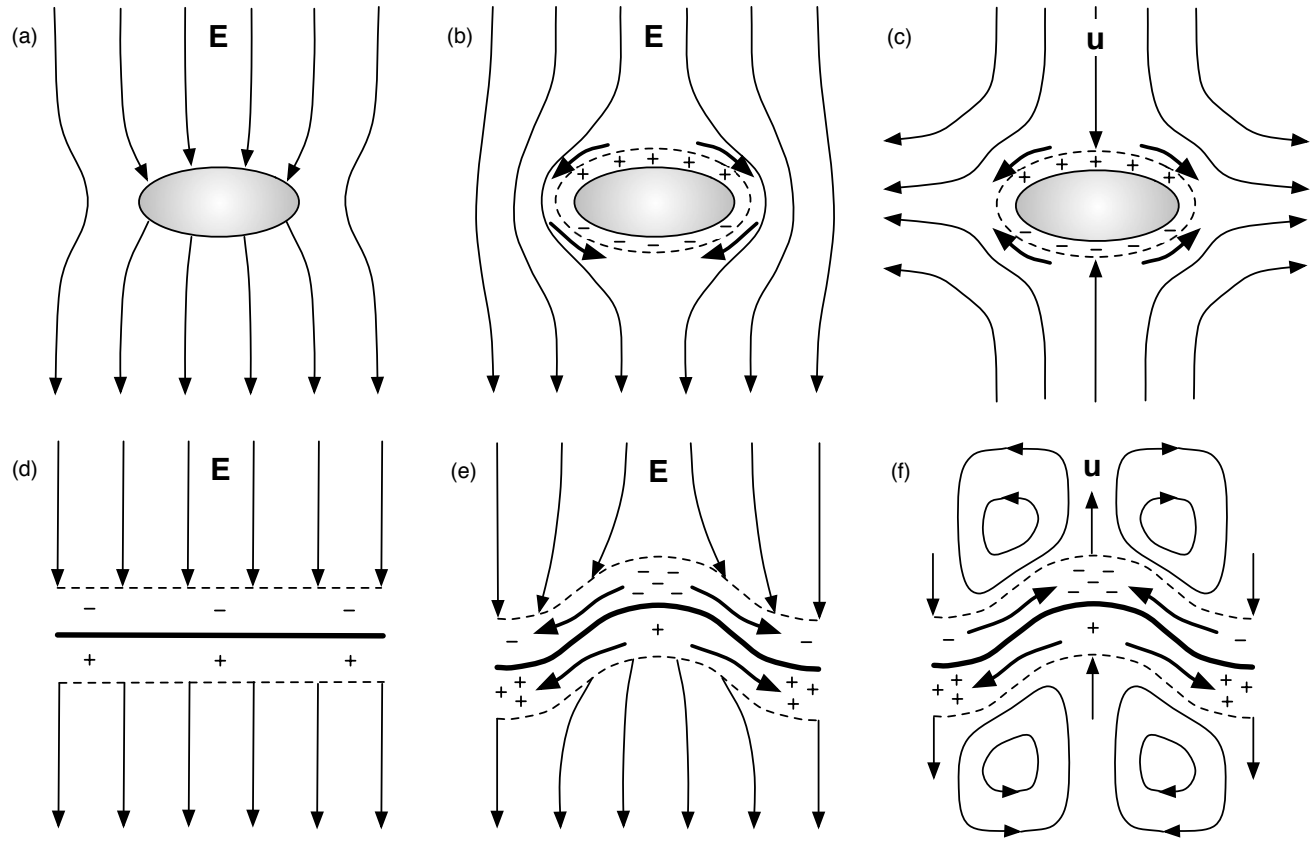

Fig. 5. The basic physics of ICEO around an ideally polarizable metal post [28] in (a-c), contrasted with our new example of a driven membrane in (d-f). (a) The metal post is subjected to an electric field; (b) capacitive charging of the double layers screens the post and thus creates a tangential field (thick arrows); (c) the field acts on the induced diffuse charge to produce electro-osmotic slip (thick arrows) directed from the peak to the sides. (d) The membrane is subjected to an electric field, which drives a current through it, and creates small diffuse charge of the opposite sign (in the case of the first model of this paper, for which the membrane has a zero thickness); (e) the membrane shape fluctuates, inducing a shift in the diffuse charge and a tangential field (thick arrows); (f) the induced field acts on the initial charge to drive ICEO flow (thick arrows) in the reverse direction, from the valleys to the peaks.

The induced voltage across the diffuse layer scales as the background voltage applied across the post, $\zeta^* \sim E^* h^*$. The induced tangential electric field wraps around the post as shown in (b) and scales as ${\mathbf{E}_\perp}^* \sim E^* h^* \mathbf{k}_\perp^*$. Substituting into the slip formula (81) then yields the scaling of the ICEO velocity

$$ {\mathbf{v}_\perp}^*_{\text{metal}} \sim \frac{\epsilon \mathbf{k}_\perp^* h^{*2}}{\eta^*} E^{*2}, \tag{87} $$

which flows in along the field axis toward the peak of the post and outward along its surface, as shown in (c).

In our model membrane, the ICEO flow is different in several important ways, although it shares the same basic principle of an applied field acting on its own induced diffuse charge around a polarizable surface. The physical picture is sketched in Figure 5(d-f). In this paper, we ignore diffuse-charge dynamics and focus on the steady response to shape perturbations. Initially, a normal field $E^* = E_z^{(0)*}$ is applied to the flat membrane to pass a current through it, as shown in (d). This induces a zeta potential scaling as $\zeta^{(0)*} \sim -E^* \kappa^{-1}$ of opposite sign to the ideally polarizable metal post, due to the much lower "inner" capacitance of the membrane compared to the "outer" capacitance diffuse layers ($\delta_m \gg 1$), as explained above.

Now consider a fluctuation in the shape of the membrane, as shown in (e). Since $\delta_m \gg 1$, the membrane carries most of the voltage applied to the total double layer, so the perturbation of the induced zeta potential scales as $\zeta^{(1)*} \sim -E^* h^*$ since there is a transfer of this voltage (or the corresponding diffuse charge $q^{(1)*} \sim -\epsilon\kappa\zeta^{(1)*} = \epsilon E^* \kappa h^*$) from the diffuse layer on the protruding side to that of the other side.

As shown in (e), the induced tangential field, scaling as ${\mathbf{E}_\perp}^{(1)*} \sim \zeta^{(1)*} \mathbf{k}_\perp^*$, is the same on both sides of the membrane (even in z) and directed from the peaks ($h > 0$) to the valleys ($h < 0$) of the shape fluctuation. It may seem surprising that the field is bent away from the extra negative induced charge in the diffuse layer near the peak and toward the extra positive induced charge in the diffuse layer in the valley, but this is due to the large bound positive (negative) charge on the upper (lower) side of the membrane, which greatly exceeds the diffuse charge in the

regime $\delta_m \gg 1$. Ignoring the small diffuse charge, it becomes clear that the field is mainly perturbed to avoid the protrusion of the positively charged membrane.

Substituting these estimates in (81), we obtain the basic scaling of the ICEO velocity

$$\mathbf{v}_{\perp\,\mathrm{membrane}}^{*} \sim -\frac{\epsilon \mathbf{k}_{\perp}^{*} h^{*}}{\eta^{*}\kappa} E^{*2} = -\frac{\mathbf{v}_{\perp\,\mathrm{metal}}^{*}}{\kappa h^{*}} . \qquad (88)$$

As in the example of the metal post, the ICEO flow around the membrane increases with the aspect ratio of the shape perturbation, $k_{\perp}^{*} h^{*}$, since it is associated with protrusions in the field direction. Compared to the ideally polarizable metal post (c), however, the curved membrane (f) exhibits "reverse" ICEO flow, which is directed from the valleys to the peaks. It is also reduced by a factor κh^{*}, which shows that the ICEO flow around a driven membrane is inherently a phenomenon of thick double layers (compared to the shape perturbation amplitude). Although these flows are weak compared to large-scale ICEO flows in microfluidics and colloids in similar geometries, we have seen that they are strong enough to make a significant contribution to the small-scale dynamics of fluctuating biological membranes.

The physical mechanism sketched in Figure 5(d-f) can be seen more clearly in Figure 6, where the electric field and the ICEO flow are shown for a shape perturbation of higher curvature with $k_{\perp}^{*} = h^{*} = \kappa$, where the double-layer thickness is comparable to the perturbation wavelength. In this regime, the ICEO flow can no longer be understood purely as an effective slip given by (81), since normal forces on the fluid in equation (65) also play an important role in the flow. As described above, normal forces contribute to membrane motion and thus viscous flow of the type in Figure 4(a), but they also produce osmotic pressure, which can drive flow relative to the instantaneous membrane position. For a thin quasi-equilibrium double layer, tangential gradients in osmotic pressure are balanced by electrical forces within the double layer and do not contribute to effective slip, as long as the bulk salt concentration is uniform [28,43,26]. For thick double layers, however, normal forces can also contribute to the flow, mainly within a distance of κ^{-1} from the peaks and valleys, and the associated flows have the same scaling as equation (88).

A detailed study of how ICEO around a driven membrane depends on all the dimensionless parameters in our model would be interesting, but here we have focused on the regime $k_{\perp} \ll 1$, $\delta_m \gg 1$, $d \ll 1$ and $\delta_m \gg 1$. This regime corresponds to the first model discussed in this paper of a membrane of zero thickness and zero dielectric constant. As discussed in Section 2, the sign of the charge distribution also depends on how conductive the membrane is as compared to the electrolyte. In real biological membranes the conditions $\delta_m \gg 1$ and $\delta_m \ll 1/G$ both hold simultaneously. In that case, due to the latter condition $\delta_m \ll 1/G$, the sign of zeroth-order charge distribution is reversed as compared to that obtained in the first model of the paper, as shown in Figure 2 and Figure 5(d). To summarize, to adapt these figures to the more biologically relevant case, one should reverse the sign of the charge distribution and that of the first-order correction to the potential. Fortunately, since the ICEO flow velocity scales as the square of the electric field, the direction of the fluid flow shown in Figure 5(f) will always be correct irrespective of the sign of the diffuse charge distribution.

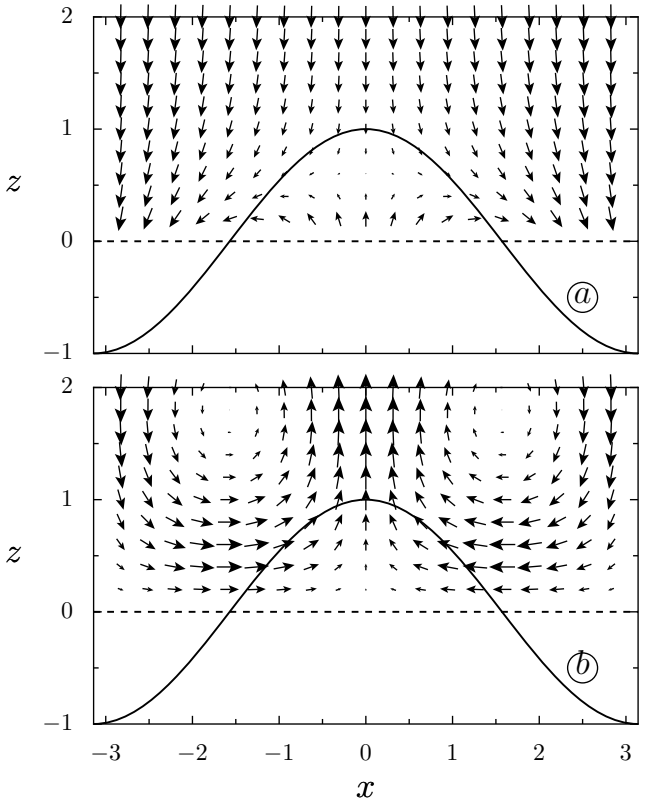

Fig. 6. Induced-charge electro-osmotic (ICEO) flow around a driven membrane in the regime of thick double layers $k_{\perp} = k_{\perp}^{*}/\kappa^{*} \approx 1$, where the thickness of the Debye layer is comparable to the wavelength of the shape perturbation and to the amplitude of modulation of the membrane. Indeed in units of the Debye layer, the amplitude of modulation of the membrane is 1, the wave vector is also 1 and the applied field corresponds to $\sigma = 8$. (a) The total electric field $\mathbf{E}$ avoids the protrusion peak due to the large positive bound charge on the membrane, even though the (much smaller) induced charge in the diffuse layer is negative at the peak and positive in the valley. (b) Vortices of induced-charge electro-osmotic flow, scaling as E^2, and driven from the valleys to the peaks by tangential fluid forces as in the thin double layer case of Figure 4, but with stronger effects of normal forces in the recirculating regions, as explained in the text.

4 Effects due to inhomogeneities in the pumps/channels concentration

We now discuss the effect of including the spatial dependence of the concentration field of the channels or pumps. The membrane free energy is modified by this

concentration field. It is now written as

$$F_{mb} = \frac{1}{2}\int \mathrm{d}^2\mathbf{r}_\perp[\kappa_0(\nabla^2 h)^2 + \sigma_0(\nabla h)^2 - 2\Lambda\phi\nabla^2 h + \beta\phi^2]. \tag{89}$$

The new parameters Λ and β are the curvature-coupling coefficient and the compressibility associated with the channel concentration field, respectively. Note that ϕ represents the deviation of the concentration field with respect to the uniform concentration. For simplicity, terms such as $(\nabla\phi)^2$, describing the energy cost of a nonuniform concentration field, have been ignored.

The equation of motion for the ϕ field follows from the above form of the membrane free energy. Gradients of chemical potential defined as $\mu_{mb} = \partial F_{mb}/\partial\phi$ provide the driving force for the motion of the channels on the membrane. Thus [37],

$$\frac{\partial\phi(\mathbf{k}_\perp)}{\partial t} = -k_\perp^2[\Lambda k_\perp^2 h(\mathbf{k}_\perp) + \beta\phi(\mathbf{k}_\perp)]. \tag{90}$$

In a linear approximation, the electrostatic potential can be written as a superposition of a base state contribution $\psi^{(0,0)}$, a contribution linear in the membrane height field $\psi^{(1,0)}$ and a contribution linear in the channel concentration field $\psi^{(0,1)}$. Augmenting our previous notation, $q^{(0,0)} = Q$, $c_k^{(0,0)} = N_k$ and $\psi^{(0,0)} = \Psi$ in the base state, we now have, instead of equation (44)

$$\begin{aligned}
\psi(\mathbf{k}_\perp, z) &= \Psi(z) + \psi^{(0,1)}(\mathbf{k}_\perp, z) + \psi^{(1,0)}(\mathbf{k}_\perp, z),\\
q(\mathbf{k}_\perp, z) &= Q(z) + q^{(0,1)}(\mathbf{k}_\perp, z) + q^{(1,0)}(\mathbf{k}_\perp, z),\\
c_1(\mathbf{k}_\perp, z) &= N_1(z) + c_1^{(0,1)}(\mathbf{k}_\perp, z) + c_1^{(1,0)}(\mathbf{k}_\perp, z),\\
c_2(\mathbf{k}_\perp, z) &= N_2(z) + c_2^{(0,1)}(\mathbf{k}_\perp, z) + c_2^{(1,0)}(\mathbf{k}_\perp, z).
\end{aligned} \tag{91}$$

The equations obeyed by $\psi^{(1,0)}$ and $q^{(1,0)}$, as well as $\psi^{(0,1)}$ and $q^{(0,1)}$ follow from equation (48).

For the contribution linear in the concentration field $\psi^{(0,1)}$ of the channels, the boundary conditions at the membrane surface impose continuity of the ion fluxes in the channels. Using the linear form for the conductances, we have

$$J_k = G_k\Delta\mu_k = \left(G_k^{(0,0)} + G_k^{(0,1)}\phi\right)\left(\Delta\mu_k^{(0,0)} + \Delta\mu_k^{(0,1)}\phi\right). \tag{92}$$

Collecting terms linear in ϕ, we obtain

$$J_k^{(0,1)} = \alpha_k^{(0,1)}\phi \tag{93}$$

with

$$\alpha_k^{(0,1)} = G_k^{(0,1)}\Delta\mu_k^{(0,0)} + G_k^{(0,0)}\Delta\mu_k^{(0,1)}. \tag{94}$$

We assume $\alpha_k = \alpha$, which represents the pumping rate. This condition only needs to be enforced at the unperturbed interface and along the z direction so that

$$\left(\partial_z q^{(0,1)} + \partial_z\psi^{(0,1)}\right)_{z=0} = \alpha\phi(\mathbf{r}_\perp). \tag{95}$$

We find the following solution for the electrostatic potential with these boundary conditions: for $z > 0$,

$$\psi^{(0,1)}(\mathbf{k}_\perp, z) = -q^{(0,1)}(\mathbf{k}_\perp, z) = \alpha\phi(\mathbf{k}_\perp)\left(\frac{e^{-lz}}{l} - \frac{e^{-k_\perp z}}{k_\perp}\right), \tag{96}$$

and for $z < 0$,

$$\psi^{(0,1)}(\mathbf{k}_\perp, z) = -q^{(0,1)}(\mathbf{k}_\perp, z) = \alpha\phi(\mathbf{k}_\perp)\left(\frac{-e^{lz}}{l} + \frac{e^{k_\perp z}}{k_\perp}\right). \tag{97}$$

Note that the corrections to the charge distribution and potential are odd functions of z in this case. This can be understood from the fact that the ion channels locally create a depletion of ions on one side and an increase of ion concentration on the other side. This depletion can be quantified through the jump in concentration of the charges across the membrane

$$q^{(0,1)}(\mathbf{k}_\perp, 0^+) - q^{(0,1)}(\mathbf{k}_\perp, 0^-) = -\frac{2\alpha\phi(\mathbf{k}_\perp)}{l}. \tag{98}$$

This jump in concentration provides an osmotic pressure difference between the two sides of the membrane, whose effect is irrelevant, however, since we have assumed the absence of permeation in writing the boundary condition of equation (68) [19].

The concentration field ϕ enters the equation of motion of the height field only through the membrane restoring force $\partial F_{mb}/\partial h$. This is because terms proportional to ϕ cancel in the difference of the stress along the z direction between both sides of the membrane in equation (69), due to the fact that $\psi^{(0,1)}(\mathbf{k}_\perp, z)$ is an odd function of z. As a consequence of this simplification, the transport coefficient α introduced in equation (95) does not enter the equation of motion for ϕ or for h. With equation (90), and the equation of motion for h,

$$\begin{aligned}
\frac{\partial h(\mathbf{k}_\perp)}{\partial t} = &-\frac{1}{4k_\perp}[((\sigma_0 + \Sigma)h(\mathbf{k}_\perp) + \Lambda\phi(\mathbf{k}_\perp))k_\perp^2\\
&+h(\mathbf{k}_\perp)(\kappa_0 + K)k_\perp^4 + h(\mathbf{k}_\perp)\Gamma k_\perp^3],
\end{aligned} \tag{99}$$

the condition of stability of the membrane with its inclusions may be obtained, provided the bare elastic moduli of the membrane, and the induced surface charge σ, are known.

5 Electrically driven membrane of finite thickness

In this section, we consider a bilayer of finite thickness d and dielectric constant $\epsilon_m < \epsilon$. There is then an electrical coupling between the membrane and the surrounding electrolyte, with a strength measured by the parameter $t = \epsilon_m/(\kappa d^*\epsilon) = \delta_m^{-1}$ [11,7]. For equilibrium membranes, the importance of this coupling is discussed in references [14,9]. In dimensionless units, this coupling becomes r/d, where $r = \epsilon_m/\epsilon$ and d is the dimensionless membrane thickness.

For nonequilibrium driven membranes, capacitive effects associated with the finite thickness of the membrane dominate electrostatic corrections to the membrane elastic moduli, except at low ionic strength [25]. Further, capacitive effects are essential to explain voltage-induced motion in cell membranes containing ion channels [38] and

shape transitions of giant vesicles in AC electric fields [2]. We ignore variations in the concentration of the channels here [25]. We will also only consider the mode of fluctuation of the membrane in which each layer of the membrane fluctuates in phase with respect to each other, so that the position of each layer is $\pm d/2 + h(\mathbf{r}_\perp)$.

For simplicity, we only discuss the case of symmetric electrolytes: $n^- = n^+$, $D_1 = D_2 = D$, and $G_1 = G_2 = G$. We denote by ψ_m the internal potential for $|z| < d/2$ and ψ the electrolyte potential for $|z| > d/2$. When $t \neq 0$, the boundary conditions at the membrane are modified, becoming

$$\begin{aligned} \partial_z \psi^{(0)}(z \to \pm d/2) &= r \partial_z \psi_m^{(0)}(z \to \pm d/2), \\ \psi^{(0)}(z \to \pm d/2) &= \psi_m^{(0)}(z \to \pm d/2). \end{aligned} \tag{100}$$

The first equation is the continuity condition for the normal electric displacement and the second equation is the continuity condition of the potential.

We solve the analog of equations (5, 6) together with an additional equation describing the region between the bilayer. In this intermediate region, it is assumed that there is no charge density.

We find the following solution for the base state:

$$\begin{aligned} E_z^{(0)}(z) &= -\sigma - \tilde{\sigma} \exp(z + d/2), \quad \text{for } z < -d/2, \\ E_z^{(0)}(z) &= -\sigma - \tilde{\sigma} \exp(-z + d/2), \quad \text{for } z > d/2, \\ E_m^{(0)} &= -\frac{\sigma + \tilde{\sigma}}{r}, \quad \text{for } -d/2 < z < d/2. \end{aligned} \tag{101}$$

Here σ still represents the surface charge of the Debye layers which is defined as in the case of zero thickness in equation (21). The current *versus* voltage relation obtained for zero thickness in equation (29) still holds in the finite thickness case, once L is replaced with $L - d$. Similarly equation (31) holds after replacing L^* with $L^* - d^*$, while equations (33) holds unchanged. In equations (101), we have introduced a new quantity $\tilde{\sigma}$ with the following property

$$\tilde{\sigma} = \int_{d/2}^{\infty} Q^+(z) \mathrm{d}z = -\int_{-\infty}^{-d/2} Q^-(z) \mathrm{d}z. \tag{102}$$

Note that σ and $\tilde{\sigma}$ are related to each other by

$$\tilde{\sigma} = \frac{r(\sigma d - \sigma L + V) - \sigma d}{2r + d}. \tag{103}$$

When dimensions are reinstated, one can see that only the diffusion time of the ions within a Debye layer enters in σ^*, whereas $\tilde{\sigma}^*$ also contains the RC characteristic time of the membrane [25].

The boundary conditions for the first-order correction in the membrane height field to the electrostatic potential and to the charge density are

$$\begin{aligned} \partial_z \psi^{(1)}(\mathbf{k}_\perp, \pm d/2) &= \mp h(\mathbf{k}_\perp) \partial_z^2 \psi^{(0)}(d/2) \\ &\quad + r \partial_z \psi_m^{(1)}(\mathbf{k}_\perp, \pm d/2), \end{aligned} \tag{104}$$

$$\begin{aligned} \psi^{(1)}(\mathbf{k}_\perp, \pm d/2) &= \psi_m^{(1)}(\mathbf{k}_\perp, \pm d/2) \\ &\quad + h(\mathbf{k}_\perp)(\partial_z \psi_m^{(0)} - \partial_z \psi^{(0)})(d/2), \end{aligned} \tag{105}$$

$$\psi^{(1)}(\mathbf{k}_\perp, \pm\infty) = q^{(1)}(\mathbf{k}_\perp, \pm\infty) = 0, \tag{106}$$

$$\partial_z q^{(1)}(\mathbf{k}_\perp, \pm d/2) + \partial_z \psi^{(1)}(\mathbf{k}_\perp, \pm d/2) = 0. \tag{107}$$

The last equation corresponds to the boundary condition of zero flux in the first-order solution. This condition was used in equation (51). The equations to first order in the height in the electrolyte regions $|z| > d/2$ are

$$\left(\partial_z^2 - k_\perp^2\right) \psi^{(1)}(\mathbf{k}_\perp, z) + q^{(1)}(\mathbf{k}_\perp, z) = 0, \tag{108}$$

$$\left(\partial_z^2 - k_\perp^2\right) \left(q^{(1)}(\mathbf{k}_\perp, z) + \psi^{(1)}(\mathbf{k}_\perp, z)\right) = 0, \tag{109}$$

subject to the boundary conditions given above.

The equations in the inside medium for $z < |d/2|$ are $q^{(1)}(\mathbf{k}_\perp, z) = 0$ and

$$\left(\partial_z^2 - k_\perp^2\right) \psi_m^{(1)}(\mathbf{k}_\perp, z) = 0. \tag{110}$$

For $z > d/2$ and $z < -d/2$, $q^{(1)}(\mathbf{k}_\perp, z)$ and $\psi^{(1)}(\mathbf{k}_\perp, z)$ remain of the form $A \exp(\mp z + d/2)$, where A is a complicated function of $k_\perp$, r, d, σ and $\tilde{\sigma}$. The first-order correction to the potential in the inside medium has the form

$$\psi_m^{(1)}(\mathbf{k}_\perp, z) = \psi_m^{(1)}(\mathbf{k}_\perp, d/2) \frac{e^{k_\perp d/2}(e^{k_\perp z} + e^{-k_\perp z})}{e^{k_\perp d} + 1}. \tag{111}$$

In Figure 7, the potential $\Psi(z)$ and the quantity $Q(z)$ (which represents half the charge distribution) are shown in dimensionless units for two choices of parameters. These parameters correspond to a positive and a negative value of $\tilde{\sigma}$. The potential profiles illustrated in Figure 7 show that the sign of the electric field at the membrane surface ($\sim -\nabla\psi$) is controlled by the sign of $\tilde{\sigma}$. As shown in Appendix A, in this case of a symmetric electrolyte and with the approximation $G_1 = G_2 = G$ the sign of $\tilde{\sigma}$ is positive when $\delta_m < 1/G$ and negative otherwise. The condition $\delta_m < 1/G$ is equivalent to $\epsilon_m/\epsilon \gg G^*/G_0^*$, where G^* is the typical conductance of typical ion channels/pumps and G_0^* is the conductance of a layer of electrolyte of thickness d^*. For real biological membranes, the membrane is typically much less conductive than the surrounding medium and thus $\delta_m < 1/G$. So the charge distribution in this case should be as the dashed line of Figure 7b, which as we mentioned earlier, has the opposite sign as compared to the charge distribution shown in Figure 2.

5.1 Electrostatic corrections to elastic moduli

The Stokes equations can be solved as before, although the computations are now more involved. With the potential at zeroth and first order computed above, we first construct $\mathbf{f}(\mathbf{k}_\perp, z)$ using equations (65). After Fourier transforming in z, we insert the result in equations (66, 67).

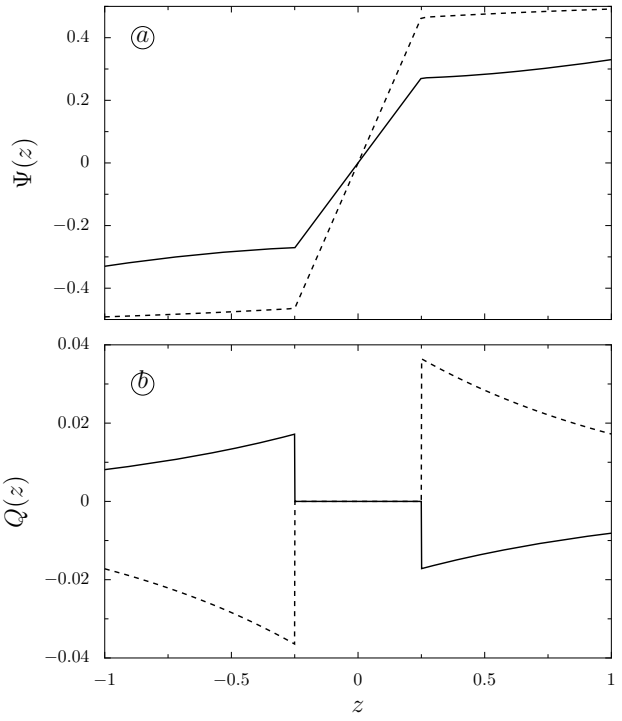

Fig. 7. Solutions of the electrokinetic equations for a membrane of finite thickness and symmetric ion concentrations. The electrostatic potential $\Psi(z)$ is shown in (a) and the quantity $Q(z)$ (which represents half the charge distribution) is shown in (b). We use dimensionless units and the following parameter values $L = 100$, $V = 2$, $G_1 = G_2 = 1$, $d = 0.5$, $r = 1/40$ and $k_\perp = 1$ for the solid line, and the same parameters except for $G_1 = G_2 = 0.01$ for the dashed line. For convenience, the potential represented as the solid line of (a) has been multiplied by an arbitrary factor of 10. For the solid line in (a), the curvature of the potential is positive near $z = d/2$, as in Figure 2a, this corresponds to a negative value of $\tilde{\sigma}$. The charge distribution is as shown in the solid line of (b) and similar to Figure 2b. For the dashed line in (a), the curvature of the potential is negative near $z = d/2$, this corresponds to a positive value of $\tilde{\sigma}$. Note that the sign of the charge distribution (dashed line in (b)) is reversed as compared to the solid line in (b).

From the solution of the Stokes equations, the velocity is obtained everywhere in the domain $|z| > d/2$.

We now have two boundary conditions for the stress tensor $\tau_{zz}^{(1)}$ at $z = \pm d/2$. Solving for the velocity field and extrapolating this velocity to $z = 0$, an effective free energy of the same form as in equation (79) is obtained. The tension obtained from this calculation is the same as the one calculated from equation (42, 43).

Both methods yield the result that the surface tension is the sum of an internal contribution $\Sigma_{\rm in}$, arising from the contribution of the field lines which penetrate within the membrane, and an external contribution $\Sigma_{\rm out}$ associated to the field lines present in the Debye layers. These take the form [25]

$$\Sigma_{\rm in} = -rdE_m^2 = -d\frac{(\sigma+\tilde{\sigma})^2}{r}\,, \tag{112}$$

$$\Sigma_{\rm out} = -\tilde{\sigma}^2 - 4\sigma\tilde{\sigma} + d\sigma^2, \tag{113}$$

or

$$\Sigma_{\rm in}^* = -\frac{(\sigma^*+\tilde{\sigma}^*)^2}{t\kappa\epsilon}\,, \tag{114}$$

and

$$\Sigma_{\rm out}^* = \frac{-(\tilde{\sigma}^*)^2 - 4\sigma^*\tilde{\sigma}^* + \kappa d^*(\sigma^*)^2}{\epsilon\kappa}\,, \tag{115}$$

in terms of dimensionful quantities.

The negative contribution $\Sigma_{\rm in}$ is known as the Lippmann tension [38]. It is usually larger in absolute value than $\Sigma_{\rm out}$. From equation (41), it follows that $\Sigma_{\rm in}$ is the electromagnetic energy of the internal field E_m contained within the space of the membrane. Since $\Sigma_{\rm in}$ is always negative, as illustrated qualitatively in Figure 3, the total membrane tension $\sigma_0 + \Sigma_{\rm in} + \Sigma_{\rm out}$ can become negative at some critical value of the internal field E_m, leading to the instabilities discussed in reference [44]. Note that such an instability is present at zero wavelength, unlike the finite wavelength instability discussed from equation (75). Our calculations also yield the moduli

$$\Gamma = \frac{\sigma\tilde{\sigma}}{2}(8 + d^2 + 4d), \tag{116}$$

and K, which is a complicated quadratic function of σ and $\tilde{\sigma}$.

All these moduli reach simple limiting values when the Debye length goes to zero ($\kappa \to \infty$ or equivalently $n^* \to \infty$). This limit is best understood in dimensionful notation. From equations (31–33), one finds that $i_k^* = -G_k^* V^*$ and $\sigma^* = 0$. From equation (103), we obtain $\tilde{\sigma} = rV/(2r+d)$. Using equation (32) we have

$$\tilde{\sigma}^* = \frac{k_B T\kappa\epsilon r V}{e(2r+d)} = \frac{\kappa\epsilon_m V^*}{2r+\kappa d^*}\,, \tag{117}$$

which in the limit $\kappa \to \infty$ goes to $\epsilon_m V^*/d^*$.

The values of the moduli in this limit are independent of G, a consequence of the fact that electrical currents (i_k^* is nonzero) are not accompanied by charge accumulation in the Debye layers, because $\sigma^* = 0$. From equation (115), we find that $\Sigma_{\rm out}^* = 0$. Using $t = r/\kappa d^*$ in equation (114), we find a nonzero limit for $\Sigma_{\rm in}^* = -\epsilon_m (V^*)^2/d^*$. Thus the limit for the overall tension in the high salt limit is $\Sigma_0^* = -(V^*)^2\epsilon_m/d^*$. This resembles the energy of a plane capacitor with a voltage drop V^* and thickness d^*, although the system is not strictly analogous to a capacitor since electric currents are present (i_k^* is nonzero). For the bending modulus, the limiting value is

$$K_0^* = \frac{5(V^*)^2\epsilon_m d^*}{24}\,, \tag{118}$$

and for Γ the limit is 0. The variation of Σ^*/Σ_0^* and of K^*/K_0^* as a function of the inverse Debye length κ are shown in Figure 8 for the case of zero and nonzero conductance.

Another limit of experimental relevance is that of small conductance $G \to 0$. In this limit, $\sigma = 0$ since there is no ion current in the medium as a consequence of i_k^* being

zero. From equation (103), we obtain $\tilde{\sigma} = rV/(2r + d)$ which means $\tilde{\sigma}^* = V^*\epsilon\kappa t/(1+2t)$ in terms of dimensionful quantities. This shows that the membrane is a capacitor of surface charge $\tilde{\sigma}^* = -\epsilon_m E_m^* = V^*\epsilon\kappa t/(1 + 2t)$, where E_m^* is the internal field [25]. The equivalent circuit for this problem is composed of three planar capacitors in series. One of these is the membrane (of capacitance per unit area ϵ_m/d) while the other two correspond to the Debye layers on each side (of capacitance $\epsilon\kappa$ per unit area), yielding a total capacitance $C^* = \epsilon\kappa t/(2t + 1)$.

Using equations (114, 115), we find $\Sigma_{\rm in}^* = -\tilde{\sigma}^2/t\kappa\epsilon$, $\Sigma_{\rm out}^* = -\tilde{\sigma}^2/\kappa\epsilon$, and $\Gamma = 0$. The same expressions for the surface tension in the $G = 0$ limit were obtained recently using a different method in reference [39]. For comparison, we provide K^* for this case

$$K^* = \frac{1}{24r\epsilon\kappa^3}(\tilde{\sigma}^*)^2(18r + 5(\kappa d^*)^3 + 24\kappa d^* r + 15(\kappa d^*)^2 r). \quad (119)$$

Note that we recover the result of equation (118) when $\kappa \to \infty$.

This expression has some similarities as well as some differences with the expression for the bending modulus given in reference [39]. This discrepancy is likely to originate in the very different starting points for both calculations: the results of reference [39] are obtained from an explicitly equilibrium approach, whose results remain unchanged if hydrodynamic effects are incorporated. On the other hand, we begin with an explicitly nonequilibrium problem incorporating hydrodynamics from the outset.

It is unclear that it should simply suffice to set $G \to 0$ in our results to recover results derived for the equilibrium calculation. However, we note that in any case the predictions for K of both models are numerically very close and there is exact agreement for Σ. We also stress that both models predict that the electrostatic contribution to the bending modulus should increase with the salt concentration, whereas the electrostatic contribution to the surface tension should decrease with the salt concentration as illustrated in the solid lines of Figure 8. Both quantities also reach a well-defined limit in the large salt concentration limit (see similar figure in Ref. [39]).

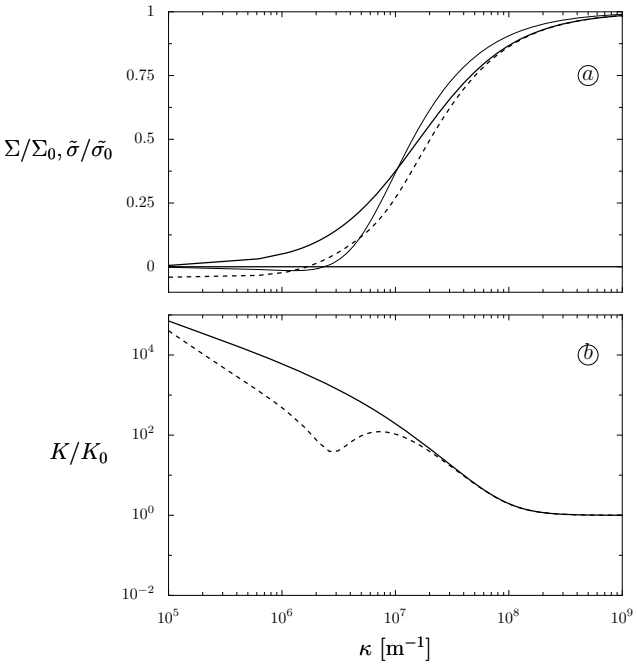

Fig. 8. Electrostatic contribution to the tension Σ and to the bending modulus K as a function of the inverse Debye length κ in the $G^* = 0$ limit (thick solid line) and for $G^* = 10\,\Omega^{-1}/\mathrm{m}^2$ (dashed line). (a) Ratios of normalized electrostatic contribution to the tension Σ/Σ_0 (dashed line for $G^* = 10\,\Omega^{-1}/\mathrm{m}^2$ and solid line for $G^* = 0$) and of $\tilde{\sigma}/\tilde{\sigma}_0$ (thin solid line for $G^* = 10\,\Omega^{-1}/\mathrm{m}^2$) are shown as function of κ. The tension Σ (respectively, the surface charge $\tilde{\sigma}$) are normalized by their value in the infinite κ limit Σ_0 (respectively $\tilde{\sigma}_0$). Below $\kappa = 2 \cdot 10^6\,\mathrm{m}^{-1}$, Σ/Σ_0 and $\tilde{\sigma}/\tilde{\sigma}_0$ both become negative when the membrane is conductive. No such change of sign is present in the tension in the non-conductive *i.e.* capacitor limit when $G = 0$ (thick solid line). For clarity the horizontal solid line represents the point of zero tension or zero of $\tilde{\sigma}$. (b) The ratio of normalized electrostatic contribution to the bending modulus K/K_0 is shown as a function of κ, where similarly K is normalized by its value in the infinite κ limit K_0. The $G^* = 0$ limit is represented as a thick solid line and the $G^* = 10\,\Omega^{-1}/\mathrm{m}^2$ case as a dashed line.

5.2 Numerical estimates, capacitive effects and fluctuation spectra

In the nonconductive limit (capacitor model), we find that $\Gamma = 0$. For $V^* = 50\,\mathrm{mV}$, $L^* = 1\,\mu\mathrm{m}$, $G = 0$, $D = 10^{-5}\,\mathrm{cm}^2/\mathrm{s}$, $n^* = 16.6\,\mathrm{mM}$, $d^* = 5\,\mathrm{nm}$ and $\epsilon_m/\epsilon = 1/40$, we have $\kappa^{-1} = 2.38\,\mathrm{nm}$, $t = 1.2 \cdot 10^{-2}$, $\delta_m = 1/t = 84$ and $d = \kappa d^* = 2.1$, $V = eV^*/k_BT = 1.95$, $L = \kappa L^* = 419.7$. The elastic moduli are $\Sigma_{\rm in}^* = -8.4 \cdot 10^{-6}\,\mathrm{J\,m}^{-2}$, $\Sigma_{\rm out}^* = -1.0 \cdot 10^{-7}\,\mathrm{J\,m}^{-2}$, $\Gamma = 0$ and $K^* = 0.011k_BT$. Let us now consider instead the case of a conductive membrane, with $G^* = 10\,\Omega^{-1}/\mathrm{m}^2$, a value typical for ion channels [3]. This corresponds to a density of the potassium channels of $0.5\,\mu\mathrm{m}^{-2}$ and for $V^* = 50\,\mathrm{mV}$, the electrical current going through the membrane is about $0.5\,\mathrm{A/m}^2$, which corresponds to about $3{\cdot}10^6$ ions going through a patch of $1\,\mu\mathrm{m}^2$. The dimensionless channel conductance is $G = 3.8 \cdot 10^{-7}$. This very small value indicates that the membrane is significantly much less conductive than the electrolyte, and thus we are typically always in the regime $\delta_m \ll 1/G$ for biological membranes. We also find that the order of magnitude of the tension and bending modulus are unchanged and a small value of $\Gamma^* = 8.2 \cdot 10^{-20}\,\mathrm{J\,m}^{-1}$ is found [25]. This indicates that the capacitor model with $G = 0$ is a good starting point for the calculation of the moduli in this case.

The importance of capacitive effects is confirmed by the observation that the values of the moduli obtained here are much larger than the corresponding estimates for the zero-thickness case. This can be understood using an equivalent zero-thickness model discussed in Appendix A. Also, by varying the ionic strength in the case where ion transport is present ($G \neq 0$), we find that the capacitor

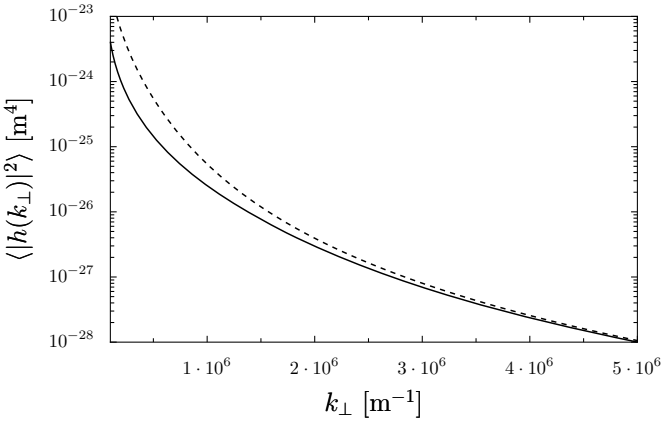

Fig. 9. Fluctuation spectrum of membrane fluctuations for the numerical values of the parameters discussed in the text. The solid line corresponds to the spectrum of a membrane of bare tension $\sigma_0^* = 10^{-7}\,\mathrm{J\,m^{-2}}$ and bare bending modulus $\kappa_0^* = 15k_BT$, while the dashed line corresponds to the fluctuation spectrum of a driven membrane in an electric field, which we describe with equation (80). The parameters are the same as discussed in the text except that here the potential drop which is applied is only of $V^* = 5\,\mathrm{mV}$, so that $\Sigma^* = -8.5{\cdot}10^{-8}\,\mathrm{J\,m^{-2}}$, $\Gamma^* = 8.1 \cdot 10^{-22}\,\mathrm{J\,m^{-1}}$ and $K^* = 0.0011k_BT$.

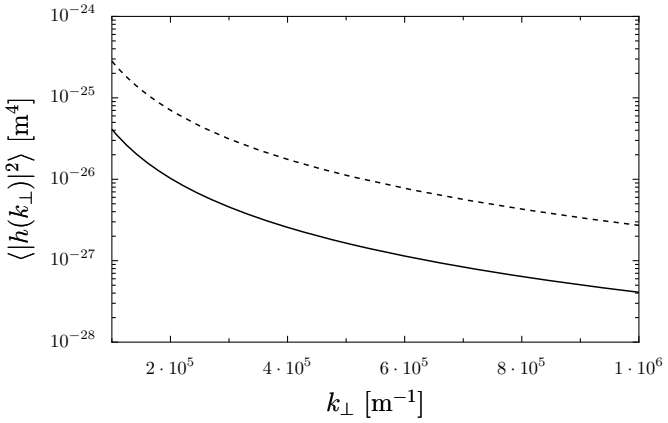

Fig. 10. Fluctuation spectrum of membrane fluctuations in the same conditions as in Figure 9 except for the potential $V^* = 50\,\mathrm{mV}$ and for the bare tension $\sigma_0^* = 10^{-5}\,\mathrm{J\,m^{-2}}$.

model holds at high ionic strength but becomes invalid at low ionic strength, where ion transport has a stronger impact on the moduli.

This point is illustrated in Figure 8, where the electrostatic contribution to the tension Σ and the bending modulus K, as a function of the inverse Debye length κ in the $G = 0$ limit (solid line) and for $G^* = 10\,\Omega^{-1}/\mathrm{m}^2$ (dashed line), are shown. The solid and dashed lines only deviate at small values of κ. The decrease of K/K_0 with salt concentration is also obtained in reference [40]. We have no simple explanation for the nonmonotonicity of K/K_0 which is observed near $\kappa = 2{\cdot}10^6\,\mathrm{m}^{-1}$, but note that a qualitatively similar nonmonotonicity —in the spontaneous curvature modulus, however— is seen in reference [40].

We find a reversal of the sign of Σ in the conductive case at small values of κ. The sign reversal is absent in the nonconductive case. This remarkable feature is shown in Figure 8(a). This mechanism of sign reversal may provide an explanation of some recent experiments, such as the study of cell movement of reference [38], where a reversal of movement/tension was observed in response to a change of ionic strength. This change of sign of the tension is clearly due to a change of sign of $\tilde{\sigma}$ as shown in Figure 3 (see also appendix for the condition of the change of sign of $\tilde{\sigma}$). One can see there that a change of sign of $\tilde{\sigma}$ occurs when the conductance G or the parameter δ_m are varied away from the point where $\tilde{\sigma} = 0$, which occurs when $\delta_m \simeq 1/G$.

Figures 9 and 10 show fluctuation spectra corresponding to the parameter values as indicated in the figure caption. The range of wave vectors indicated corresponds roughly to experimentally accessible values in video microscopy. Note the substantial increase of fluctuation amplitudes at low wave vectors in Figure 9, which arises from the lowering of the surface tension. Such a lowering is similar to the one observed in reference [46]. For the parameters used in Figure 10, corresponding to a larger bare tension σ_0^*, we see a significant increase of fluctuations over the full range of wave vectors.

6 Conclusion

In conclusion, we have analyzed the steady-state fluctuations of a membrane driven by an applied DC electric field. Our analysis is valid in the linear regime for the response of the ion channels and for the description of the electrostatic effects. We have confirmed the main results of reference [25], including the presence of a term proportional to $k_\perp^3$ in the fluctuation spectrum. We have provided a simple physical argument for the physics underlying this term, relating it to a nonlinear electrokinetic effect termed induced-charge electro-osmosis (ICEO). The predicted flow around a curved driven membrane is in the reverse direction from typical ICEO flows around blocking metal surfaces [28] and has different dependence on the geometry, in the limit we describe for the zero-thickness case. We stress, more generally, the importance of electrokinetic effects such as the one described here for descriptions of the dynamic properties of the soft, non-equilibrium membranes found in living cells.

Although our calculations addressed the case of a membrane driven out of equilibrium through the combined action of an external potential and ion channels or pumps which transferred ions across the surface, most of our results should translate directly to the cell, where the potential difference across the membrane is maintained solely through active pumps and channels. This is a consequence of the observation that once steady currents are established which drive the system out of equilibrium, the precise way in which such transmembrane currents are maintained should be irrelevant to the description of membrane properties, which are dominated by effects at the much smaller scales of the bilayer thickness and the Debye screening length.

We have also confirmed the importance of capacitive effects, which are responsible for a negative contribution to the membrane tension and can lead to membrane instabilities. In agreement with the recent results of reference [24], we find that the electrostatic and electrokinetic contribution to the bending modulus increases with the salt concentration, whereas the electrostatic contribution to the surface tension decreases with the salt concentration. We have also found a reversal of sign of the tension and of the surface charge in the Debye layer $\tilde{\sigma}$ in the low salt limit (as compared to the situation at high salt).

We have extended the calculations of reference [25] by including a channel concentration field in the description. This did not lead to qualitatively new effects within our perturbative treatment with our assumptions that the response of the channels to positive and negative ions is identical.

Extensions of the work described here include the description of non-equilibrium effects in membranes bearing a fixed charge which could be distributed asymmetrically across the two layers. The modulation of this fixed charge through remodeling of plasma membrane lipids is now understood to play an important role in cell division and phagocytosis. The cytoskeleton of the cell couples to the membrane, lending the coupled cytoskeleton-membrane system a shear modulus. In addition, cytoskeletal proteins are typically charged. Understanding how such effects modify the elastic properties of the coupled membrane-cytoskeleton system out of equilibrium is an area which is largely unexplored.

The clarification of the mechanical properties and fluctuation spectrum of lipid vesicles containing active pumps and channels is another possible application of the ideas presented here. Incorporating a biologically more reasonable model for the nonlinear current voltage relation associated with ion pumps into the calculation would provide a useful extension of this work. Finally, achieving a more detailed understanding of the role of nonlinear electrokinetic effects, such as ICEO, in modulating the dynamic properties of membranes driven out of equilibrium, appears to be an important new direction for further research.

We thank Patricia Bassereau, Madan Rao, Sriram Ramaswamy, Jacques Prost, V. Kumaran, Pierre Sens and Armand Ajdari for useful discussions. MZB thanks the National Science Foundation, under Contract DMS-070764 for support. MZB also acknowledges the hospitality of ESPCI and support from the Paris Sciences Chair. DL and GIM acknowledge support from the Indo-French Center for the Promotion of Advanced Research under Grant No. 3502, the DBT (India) and the DST (India).

Appendix A. Mapping the finite membrane thickness model to zero thickness

The calculation of the electrostatic corrections in the case of a membrane of finite thickness is complex, leading to expressions which are often hard to interpret. It is thus useful to consider simpler, alternative formulations of the physics which could be used to gain physical insight. We describe one such approach briefly below, based on the "Stern boundary condition" for thin dielectric layers [42], and use it to calculate the internal and external contributions to the surface tension.

The idea is to map the finite-thickness problem into an equivalent zero-thickness one, but with boundary conditions which are different from the ones we considered in the body of the paper. Beginning with the definition

$$Q = \frac{1}{2}(\delta N_1 - \delta N_2), \tag{A.1}$$

following equations (8) we obtain

$$\partial_z^2 \Psi = -Q. \tag{A.2}$$

We can write the solutions to the problem for the $z > 0$ case as

$$\Psi(z) = \sigma\left(z - \frac{L}{2}\right) - Ae^{-z} + \frac{V}{2}, \tag{A.3}$$

and for the $z < 0$ case

$$\Psi(z) = \sigma\left(z + \frac{L}{2}\right) - A'e^{z} - \frac{V}{2}. \tag{A.4}$$

Applying the electrostatic boundary condition

$$r\partial_z \Psi_m\left(\pm\frac{d}{2}\right) = \partial_z \Psi\left(z = \pm\frac{d}{2}\right), \tag{A.5}$$

where the internal electric field is

$$E_m = -\partial_z \Psi_m(z). \tag{A.6}$$

The internal field is a constant which we can calculate from

$$\int_{-d/2}^{d/2} E_m(z)\mathrm{d}z = \mathrm{d}E_m = \Psi\left(-\frac{d}{2}\right) - \Psi\left(\frac{d}{2}\right). \tag{A.7}$$

This leads to the boundary condition

$$-\partial_z \Psi\left(z = \pm\frac{d}{2}\right) = \frac{r}{d}\left[\Psi\left(-\frac{d}{2}\right) - \Psi\left(\frac{d}{2}\right)\right]. \tag{A.8}$$

We will now treat this as an equivalent zero-thickness problem with the constraint that

$$\delta_m \partial_z \Psi(z = 0^{\pm}) = \Psi(0^+) - \Psi(0^-), \tag{A.9}$$

where

$$\delta_m = \frac{d}{r} = \frac{\epsilon d}{\epsilon_m} \tag{A.10}$$

is an effective length scale characterizing the membrane (scaled to κ^{-1}), over which the potential in the electrolyte extrapolates linearly to its value on the other side of the membrane. Note that equation (A.9) is a mixed Robin-type boundary condition, involving both the field Ψ and its derivative at the boundaries $z = 0^{\pm}$. In order to pass to the limit of zero membrane thickness, $d = d^*\kappa \to 0$,

we take the joint limit $r = \epsilon_m/\epsilon \to 0$, keeping δ_m fixed. The boundary condition (A.9) also explicitly shows the importance of the coupling parameter $t = \delta_m^{-1}$, which has been discussed for finite-thickness membranes [11,7,14,9].

The boundary condition equation (A.9) is now widely used to describe thin dielectric layers on metal surfaces and electrodes [49,42], although we are not aware of any prior application to ion-permeable membranes. It was perhaps first used to describe the compact Stern layer at the electrode/electrolyte interface [50] and recently extended to nonlinear surface capacitance [42]. In this context, it has been postulated that the field-dependent voltage drop, $\Delta\psi = \delta\,\partial_z\psi$, drives Faradaic electrochemical reactions [51, 42]. In our case, the same voltage drop contributes to electrochemical potential differences across the membrane, which set the ionic currents. In modeling ICEO flows around metal surfaces, the same boundary condition is also used to describe thin dielectric coatings, such as oxide layers [27,28,32], which is again similar to our modeling of the ICEO flow around a driven membrane. The same type of Robin-type boundary condition has also been derived under more general conditions for the interface between a dielectric body (not necessarily a thin layer) and an electrolyte and used to model ICEO flows around dielectric microchannel corners and dielectric particles [35].

The physical interpretation of the parameter δ_m becomes clearer when written in terms of dimensional variables,

$$\delta_m = \frac{\epsilon\kappa}{\epsilon_m/d^*} = \frac{C_D}{C_m}\,, \tag{A.11}$$

as the ratio of the low-voltage capacitance of the diffuse part of the double layer, $C_D = \epsilon\kappa$, to that of the compact part, $C_m = \epsilon_m/d^*$, which in our case is the membrane (but could also be a surface coating or Stern layer). In the linear regime of low voltages ($< kT/e$) and for thin double layers ($\kappa L \gg 1$, $d = d^*\kappa \gg 1$), these are constant capacitances, effectively in series [49], where $\delta_m(1+\delta_m)^{-1}$ is the fraction of the total double-layer voltage across the membrane, while $(1+\delta_m)^{-1}$ is the fraction across the diffuse layers.

There are two limiting cases of (A.9) which are commonly assumed in the literature [42]. In the "Gouy-Chapman limit" $\delta_m \ll 1$, most of the voltage drop occurs in the diffuse layer. In the "Helmholtz limit" $\delta_m \gg 1$, the compact layer —or in our case, the membrane— carries most of the voltage. We make the latter assumption in the main text to reduce equation (A.9) to the simpler boundary condition of equation (16).

Here, we briefly consider the general case $0 < \delta_m < \infty$. Using the above equations,

$$\begin{aligned}\partial_z\Psi(z=0^+) &= \sigma + A,\\ \partial_z\Psi(z=0^-) &= \sigma - A',\end{aligned} \tag{A.12}$$

we have thus

$$\partial_z\Psi(z=0^+) = \partial_z\Psi(z=0^-) \implies A = -A' \tag{A.13}$$

We can fix A, using the result for $\Psi(z)$, yielding

$$A = \frac{V + \sigma(-\delta_m - L)}{2+\delta_m}\,. \tag{A.14}$$

Comparing equations (A.12) with equation (101), we see that $A = \tilde{\sigma}$ and equation (A.14) are equivalent to equation (103) in the limit $r \to 0$, $d \to 0$, keeping δ_m fixed.

We now illustrate the calculation of the tension, using our earlier result

$$\begin{aligned}\Sigma^{\rm out} = &-\int_{-L/2}^{L/2}(E_z^{(0)})^2(z)\mathrm{d}z\\ &+\frac{L}{2}\Big[(E_z^{(0)})^2(z\to\infty)+(E_z^{(0)})^2(z\to-\infty)\Big]\,,\end{aligned} \tag{A.15}$$

which yields

$$\begin{aligned}\Sigma^{\rm out} &= -2\int_0^{L/2} E^2(z)\mathrm{d}z + LE^2(z\to\infty)\\ &= -2\int_0^{L/2}(\sigma + Ae^{-z})^2\mathrm{d}z + L\sigma^2\\ &= -2\int_0^{L/2}(\sigma^2 + A^2e^{-2z} + 2\sigma Ae^{-z})\mathrm{d}z + L\sigma^2\\ &= -2\left[\frac{A^2}{2} + 2\sigma A\right],\end{aligned} \tag{A.16}$$

which goes to $3\sigma^2$ in the limit of $\delta_m \to 0$ for the zero thickness limit, where $A = -\sigma = \tilde{\sigma}$. We can also obtain

$$\Sigma^{\rm in} = -rE_m^2 = \frac{-r}{d^2}\left[\Psi(0^+) - \Psi(0^-)\right]^2 = -\frac{d}{r}(\sigma + A)^2, \tag{A.17}$$

which coincides with equation (112) given in the main text.

Using the definition of σ of equation (21), and the expression of the ion fluxes of equations (29, 30), we have that $\sigma \simeq GV/(1+GL)$. From equation (A.14), one obtains

$$A \simeq \frac{V}{(1+GL)(2+\delta_m)}(1 - G\delta_m), \tag{A.18}$$

which shows that $A > 0$ when $\delta_m < 1/G$ and $A < 0$ when $\delta_m > 1/G$. The condition $\delta_m < 1/G$ is equivalent to $\epsilon_m/\epsilon \gg G^*/G_0^*$, where G^* is the typical conductance of typical ion channels/pumps defined in equation (25) and $G_0^* = Dn^*e^2/d^*k_BT$ is the conductance of a layer of electrolyte of thickness d^*.

Appendix B. Solution of the Stokes equations for the first model of a membrane of zero thickness and zero dielectric constant

We recall that the normal component of the velocity satisfies a single fourth-order differential equation, equation (67). With the expressions for the charge and the potential at zeroth and first order given in the previous sections, the flow can be solved on each side separately as

$$\begin{aligned}v_z(\mathbf{k}_\perp, z) &= (A_1 + B_1 z)e^{-k_\perp z} + C_1 e^{-lz}, \quad \text{for } 0 < z,\\ v_z(\mathbf{k}_\perp, z) &= (A_2 + B_2 z)e^{k_\perp z} + C_2 e^{lz}, \quad \text{for } z < 0,\end{aligned}$$

where the integration constants must be determined by proper matching boundary conditions. Note that the boundary conditions on the membrane are enforced at $z = 0^{\pm}$ rather than at the actual position $h(\mathbf{r})$ of the interface because of our assumption of small deformations limited to first order in the membrane height.

Imposing the boundary conditions for the velocity of equations (68–71), the flow on the positive side $z > 0$ is explicitly calculated to be

$$\begin{aligned} v_z(\mathbf{k}_\perp, z) = \sigma^2 k_\perp^2 \left(z - \frac{1}{l} - \frac{z k_\perp}{l} \right) e^{-k_\perp z} h(\mathbf{k}_\perp) \\ + s(1 + z k_\perp) e^{-k_\perp z} h(\mathbf{k}_\perp) \\ + \frac{\sigma^2 k_\perp^2}{l} e^{-l z} h(\mathbf{k}_\perp), \end{aligned} \tag{B.1}$$

and

$$\begin{aligned} \mathbf{v}_\perp(\mathbf{k}_\perp, z) = -i\mathbf{k}_\perp \sigma^2 \left(-1 + k_\perp z - \frac{k_\perp^2 z}{l} \right) \\ \times e^{-k_\perp z} h(\mathbf{k}_\perp) - z s i \mathbf{k}_\perp h(\mathbf{k}_\perp) e^{-k_\perp z} \\ - i\sigma^2 \mathbf{k}_\perp h(\mathbf{k}_\perp) e^{-l z}. \end{aligned} \tag{B.2}$$

Note that, at this point, the stress boundary conditions have not been used yet. In the particular case where no electrostatic force is present (for $\sigma = 0$), one recovers the fluid flow created with a membrane bending mode [48], which is represented in Figure 4a.

$$v_z(\mathbf{k}_\perp, z) = s(1 + z k_\perp) e^{-k_\perp z} h(\mathbf{k}_\perp), \tag{B.3}$$

$$\mathbf{v}_\perp(\mathbf{k}_\perp, z) = -i\mathbf{k}_\perp z s e^{-k_\perp z} h(\mathbf{k}_\perp). \tag{B.4}$$

In the general case where $\sigma \neq 0$, we are interested in the solution of the Stokes equation where the growth rate s is determined from the stress boundary conditions. For Figure 4b and Figure 6, we have assumed that $s = 0$, which corresponds to a quasi-stationary membrane, whose shape is determined by the flow field.

The stress component along z, obtained to first order in the membrane height field and evaluated at the membrane surface, is

$$\tau_{zz}^{(1)} = -p + 2\partial_z v_z + \partial_z \psi^{(1)} \partial_z \Psi + h(\mathbf{r}_\perp) \partial_z [-P + (\partial_z \Psi)^2/2]. \tag{B.5}$$

As follows from equations (22, 23), and (40), the stress is balanced in the base state. Thus, the last term drops out and

$$\tau_{zz}^{(1)} = \left(-p + 2\partial_z v_z + \partial_z \psi^{(1)} \partial_z \Psi \right)_{z=0}. \tag{B.6}$$

Similarly the transverse stress is

$$\tau_{\perp z}^{(1)} = \left(\partial_\perp v_z + \partial_\perp \psi^{(1)} \partial_z \Psi \right)_{z=0}. \tag{B.7}$$

In fact, because of our use of the boundary condition of a vanishing electric field on the membrane, these expressions further simplify to $\tau_{zz}^{(1)} = (-p + 2\partial_z v_z)_{z=0}$ and $\tau_{\perp z}^{(1)} = (\partial_\perp v_z)_{z=0}$. These stresses can be evaluated using the expression of the pressure in terms of v_z and $\mathbf{f}_\perp$, while v_z itself can be obtained by solving equation (67).

With the expressions of the velocity given in equations (B.1, B.2), the discontinuity in the normal-normal stress equation (73) component fixes the value of the growth rate s. After expanding the obtained expression in powers of $k_\perp$, one obtains the growth rate equation given in equation (77).

After inserting the expression of the growth rate s into the equations for the flow field given in equations (B.1, B.2) and Taylor expanding with respect to $k_\perp$, one finds that (at lowest order in $k_\perp$)

$$\mathbf{v}_\perp(\mathbf{k}_\perp, z) \simeq i\mathbf{k}_\perp h(\mathbf{k}_\perp) \sigma^2 (1 - e^{-z}), \tag{B.8}$$

which is essentially the result of equation (86). This result confirms that the tangential velocity $\mathbf{v}_\perp$, which is strictly zero at $z = 0$ according to the non-slip boundary condition, has a significant (non-zero) value at a distance z of the order of one Debye length away from the interface, as predicted from the Helmholz-Smoluchowski formula of equation (81).

References

1. For an extensive review, see U. Seifert, Adv. Phys. **46**, 13 (1997).
2. R. Dimova, K.A. Riske, S. Aranda, N. Bezlyepkina, R. Knorr, R. Lipowsky, Soft Matter **3**, 817 (2007).
3. B. Hille, *Ion Channels of Excitable Membranes* (Sinauer Press, Sunderland, MA, 2001).
4. E. Kandel, J. Schwartz, T. Jessel, *Principles of Neural Science* (MacGraw-Hill, New York, 2000).
5. T. Yeung, M. Terebiznik, L. Yu, J. Silvius, W.M. Abidi, M. Philips, T. Levine, A. Kapus, S. Grinstein, Science **313**, 347 (2006).
6. S. Lecuyer, G. Fragneto, T. Charitat, Eur. Phys. J. E **21**, 153 (2006).
7. D. Andelman, in *Handbook of Biological Physics*, edited by R. Lipowsky, E. Sackmann (Elsevier, Amsterdam, 1995).
8. P. Pincus, J.-F. Joanny, D. Andelman, Europhys. Lett. **11**, 763 (1990).
9. T. Chou, M.V. Jaric, E. Siggia, Biophys. J. **72**, 2042 (1997).
10. B. Duplantier, R.E. Goldstein, V. Romero-Rochin, A.I. Pesci, Phys. Rev. Lett. **65**, 508 (1990); R.E. Goldstein, A.I. Pesci, V. Romero-Rochin, Phys. Rev. A **41**, 5504 (1990).
11. M. Winterhalter, W. Helfrich, J. Phys. Chem. **92**, 6865 (1988); **96**, 327 (1992).
12. H.N.W. Lekkerkerker, Physica A **159**, 319 (1989).
13. S.T. Milner, J.-F. Joanny, P. Pincus, Europhys. Lett. **9**, 495 (1989).
14. M. Kiometzis, H. Kleinert, Phys. Lett. A **140**, 520 (1989).
15. J. Prost, R. Bruinsma, Europhys. Lett. **33**, 321 (1996).
16. S. Ramaswamy, J. Toner, J. Prost, Phys. Rev. Lett. **84**, 3494 (2000).
17. S. Ramaswamy, M. Rao, C. R. Acad. Sci. Paris. **2**, Série IV, 817 (2001).
18. J.-B. Manneville, P. Bassereau, D. Lévy, J. Prost, Phys. Rev. Lett. **82**, 4356 (1999).

19. J.-B. Manneville, P. Bassereau, S. Ramaswamy, J. Prost, Phys. Rev. E **64**, 021908 (2001).
20. S. Sankararaman, G.I. Menon, P.B.S. Kumar, Phys. Rev. E **66**, 031914 (2002).
21. D. Lacoste, A.W.C. Lau, Europhys. Lett. **70**, 418 (2005).
22. H.-Y. Chen, Phys. Rev. Lett. **92**, 168101 (2004).
23. M.C. Sabra, O.G. Mouritsen, Biophys. J. **74**, 745 (1998).
24. M.A. Lomholt, Phys. Rev. E **73**, 061913; 061914 (2006).
25. D. Lacoste, M. Cosentino Lagomarsino, J.F. Joanny, EPL **77**, 18006 (2007).
26. W.B. Russel, D. Saville, W.R. Schowalter, *Colloidal Dispersions* (Cambridge University Press, Cambridge, UK, 1989); R.J. Hunter, *Foundations of Colloid Science* (Oxford University Press, 2001).
27. A. Ajdari, Phys. Rev. E **61**, R45 (2000); A. González, A. Ramos, N.G. Green, A. Castellanos, H. Morgan, Phys. Rev. E **61**, 4019 (2000).
28. M.Z. Bazant, T.M. Squires, Phys. Rev. Lett. **92**, 066101 (2004); T.M. Squires, M.Z. Bazant, J. Fluid Mech. **509**, 217 (2004); **560**, 65 (2006).
29. V. Kumaran, Phys. Rev. E **64**, 011911 (2001); R. Thaokar, V. Kumaran, Phys. Rev. E **66**, 051913 (2002); V. Kumaran, Phys. Rev. Lett. **85**, 4996 (2000).
30. V.A. Murtsovkin, Kolloidn. Zh. **58**, 358 (1996).
31. A. Ramos, H. Morgan, N.G. Green, A. Castellanos, J. Colloid Interface Sci. **217**, 420 (1999); N.G. Green, A. Ramos, A. Gonzalez, H. Morgan, A. Castellanos, Phys. Rev. E **61**, 4011 (2000).
32. J.A. Levitan, S. Devasenathipathy, V. Studer, Y. Ben, T. Thorsen, T.M. Squires, M.Z. Bazant, Colloids Surf. A **267**, 122 (2005).
33. C.K. Harnett, J. Templeton, K.A. Dunphy-Guzman, Y.M. Senousy, M.P. Kanouff, Lab on a Chip **8**, 565 (2008).
34. S.K. Thamida, H.C. Chang, Phys. Fluids **14**, 4315 (2002).
35. G. Yossifon, I. Frankel, T. Miloh, Phys. Fluids **18**, 117108 (2006); **19**, 068105 (2007).
36. S. Gangwal, O.J. Cayre, M.Z. Bazant, O.D. Velev, Phys. Rev. Lett. **100**, 058302 (2008).
37. F. Divet, G. Danker, C. Misbah, Phys. Rev. E **72**, 041901 (2005).
38. P.-C. Zhang, A.M. Keleshian, F. Sachs, Nature **413**, 428 (2001).
39. T. Ambjörnsson, M.A. Lomholt, P.L. Hansen, Phys. Rev. E **75**, 051916 (2007).
40. S. Chatkaew, M. Leonetti, Eur. Phys. J. E **17**, 203 (2005); M. Leonetti, E. Dubois-Violette, F. Homblé, Proc. Natl. Acad. Sci. U.S.A. **101**, 10243 (2004); M. Leonetti, E. Dubois-Violette, Phys. Rev. Lett. **81**, 1977 (1998).
41. J.D. Jackson, *Classical Electrodynamics*, 3rd edition (Wiley, 1999).
42. M.Z. Bazant, K.T. Chu, B.J. Bayly, SIAM J. Appl. Math. **65**, 1463 (2005); K.T. Chu, M.Z. Bazant, SIAM J. Appl. Math. **65**, 1485 (2005).
43. B. Zaltzman, I. Rubinstein, J. Fluid Mech. **579**, 173 (2007).
44. P. Sens, H. Isambert, Phys. Rev. Lett. **88**, 128102 (2002).
45. J.S. Rowlinson, B. Widom, *Molecular Theory of Capillarity* (Oxford University Press, Oxford, 1982).
46. M.D. El Alaoui Faris, D. Lacoste, J. Pécréaux, J.-F. Joanny, J. Prost, P. Bassereau, Phys. Rev. Lett. **102**, 038102 (2009).
47. T. Bickel, Phys. Rev. E **75**, 041403 (2007).
48. A. Levine, F.C. MacKintosh, Phys. Rev. E **66**, 061606 (2002).
49. M.Z. Bazant, K. Thornton, A. Ajdari, Phys. Rev. E **70**, 021506 (2004).
50. E.M. Itskovich, A.A. Kornyshev, M.A. Vorotyntsev, Phys. Status Solidi A **39**, 229 (1977).
51. A. Bonnefont, F. Argoul, M.Z. Bazant, J. Electroanal. Chem. **500**, 52 (2001).

Nonequilibrium Self-Assembly of a Filament Coupled to ATP/GTP Hydrolysis

Padinhateeri Ranjith,[†*] David Lacoste,[‡] Kirone Mallick,[§] and Jean-François Joanny[†]
[†]Physico-Chimie UMR 168, Institut Curie, Paris, France; [‡]Laboratoire de Physico-Chimie Théorique, Ecole Supérieure de Physique et de Chemie Industrielles, Paris, France; and [§]Service de Physique Théorique, Commissariat à lÉnergie Atomique-Saclay, Gif, France

ABSTRACT We study the stochastic dynamics of growth and shrinkage of single actin filaments or microtubules taking into account insertion, removal, and ATP/GTP hydrolysis of subunits. The resulting phase diagram contains three different phases: two phases of unbounded growth: a rapidly growing phase and an intermediate phase, and one bounded growth phase. We analyze all these phases, with an emphasis on the bounded growth phase. We also discuss how hydrolysis affects force-velocity curves. The bounded growth phase shows features of dynamic instability, which we characterize in terms of the time needed for the ATP/GTP cap to disappear as well as the time needed for the filament to reach a length of zero (i.e., to collapse) for the first time. We obtain exact expressions for all these quantities, which we test using Monte Carlo simulations.

INTRODUCTION

A large number of structural elements of cells are made of fibers. Well-studied examples of these fibers are microtubules and actin filaments. Microtubules are able to undergo rapid dynamic transitions between growth (polymerization) and decay (depolymerization) in a process called dynamic instability (1). Actin filaments are able to undergo treadmilling-like motion. These dynamic features of microtubules and actin filaments play an essential role in cellular biology (2). For instance, the treadmilling of actin filaments occurs in filopodia, lamellipodia, flagella, and stereocilia (3–5). Actin growth dynamics is also important in acrosome reactions, where sperm fuses with egg (6–8). During cell division, the movements of chromosomes are coupled to the elongation and shortening of the microtubules to which they bind (2,9). Recently, it has been discovered that ParM, a prokaryotic actin homolog, also displays dynamic instability (10).

Energy dissipation is critical for these dynamic nonequilibrium features of microtubules and actin. Energy is dissipated when ATP (respectively, GTP) associated to actin monomers (respectively, tubulin dimers) is irreversibly hydrolyzed into ADP (respectively, GDP). Since this hydrolysis process typically lags behind the assembly process, a cap of consecutive ATP/GTP subunits can form at the end of the filament (11,12).

Let us first consider studies of the dynamic instability of microtubules. The notion of dynamic instability as a switch between growing and shrinking phases was put forward in early studies of Hill (13) and was reanalyzed a decade later in a simple and pedagogical model proposed by Dogterom and Leibler (14). In the Dogterom and Leibler model, a microtubule exists either in a rescue phase (where a GTP cap exists at the end of the microtubule) or a catastrophe phase (with no GTP cap), with stochastic transitions between the two states. A limitation of such a model is that a switching frequency is built in the model rather than derived from a precise theoretical modeling of the GTP cap. This question was addressed later by Flyvbjerg et al. (15,16), where a theory for the dynamics of the GTP cap was included. At about the same time, a mathematical analysis of the Dogterom-Leibler model using Green functions formalism was carried out in Bicout (17). The study of Flyvbjerg et al. (15,16), was generalized in Zong et al. (18), with the use of a variational method and numerical simulations. This kind of stochastic model for the dynamic instability of microtubules was further studied by Antal et al. (19,20). The model of Antal et al. takes into account the addition and hydrolysis of GTP subunits, and the removal of GDP subunits. Exact calculations are carried out in some particular cases such as when the GDP detachment rate goes to zero or infinity, however, no exact solution of the model is given for arbitrary attachment and detachment rates of both GTP and GDP subunits.

It was thought for a long time that only microtubules were able to undergo dynamic instability. Recent experiments on single actin filaments, however, have shown that an actin filament can also have large length fluctuations slightly above the critical concentration (21,22). A behavior reminiscent of dynamic instability was also observed in experiments where actin polymerization was regulated by binding proteins such as ADF/cofilin (23,24). In this case, however, it is important to keep in mind that the large length fluctuations concern only the pointed end of the filament and are due to the cofilin-actin interaction. Vavylonis et al. (25) have studied theoretically actin polymerization kinetics in the absence of binding proteins. Their model takes into account polymerization, depolymerization, and random ATP hydrolysis. In their work, the ATP hydrolysis was

Submitted September 12, 2008, and accepted for publication December 8, 2008.

*Correspondence: pranjith@curie.fr

Editor: Alexander Mogilner.

0006-3495/09/03/2146/14 $2.00

doi: 10.1016/j.bpj.2008.12.3920

separated into two steps: the formation of ADP-Pi-actin and the formation of ADP-actin by releasing the phosphate Pi. Vavylonis et al. (25) have reported large fluctuations near the critical concentration, where the growth rate of the filament vanishes. More recently, Stukalin et al. (26) have studied another model for actin polymerization, which takes into account ATP hydrolysis in a single step (neglecting the ADP-Pi-actin state) and occurring only at the interface between ATP-actin and ADP-actin (vectorial model) or at a random location (random model). This model too shows large fluctuations near the critical concentration, despite the differences mentioned above. Note that both mechanisms (vectorial or random) are still considered since experiments are presently not able to resolve the cap structure of either microtubule or actin filaments.

In this article, we study the dynamics of a single filament, which can be either an actin filament or a microtubule, using simple rules for the chemical reactions occurring at each site of the filament. The advantage of such a simple coarse-grained nonequilibrium model is that it provides insights into the general phenomenon of self-assembly of linear fibers. Here, we follow the model for the growth of an actin filament developed in Stukalin and Kolomeisky (26). We describe a new dynamical phase of this model, which we call the bounded growth phase in accordance with the terminology used in microtubules where this phase is well known (14). The characterization of this bounded growth phase is particularly important, because this is the phase that should be observable in batch experiments with actin. It may also explain the observation of time-independent filament distribution of actin in Fujiwara et al. (21). In addition, we analyze the dynamic instability with this model. We think that dynamic instability is not a specific feature of microtubules but could also be present in actin filaments. We argue that one reason why dynamic instability is less often observed with actin than with microtubules has to do with the physical values of some parameters that are less favorable for actin than for microtubules. This conclusion is also supported by the work of Hill in his theoretical study of actin polymerization (11,12). In these references, a discrete site-based model for a single actin filament with the vectorial process of hydrolysis is developed, which has many similarities with our model.

In short, the model studied in this article presents three dynamical phases, which are all nonequilibrium steady states: 1) a bounded growth phase (phase I), where the average cap length and the filament length remain constant with time; and two unbounded growth phases, 2), an intermediate phase (phase II), where the average cap length remains constant and the filament grows linearly with time, and 3), a rapidly growing phase (phase III) where the cap and the filament both grow linearly with time. The phases II and III were already present in the study of Stukalin and Kolomeisky (26), but phase I was not analyzed there. Thus, the description of the main features of phase I (such as the average length, the distribution of lengths) is one of main results of this article.

In addition, we discuss how GTP/ATP hydrolysis affects force-velocity curves and we characterize the large fluctuations of the filament, by calculating the time needed for the cap to disappear in phases I and II as well as the time needed for the complete filament to reach a length of zero (i.e., to collapse) for the first time in phase I. Due to the simplicity of the model, we are able to obtain exact expressions for all these quantities. We also test these results using Monte Carlo simulations.

MODEL

We study a model for the dynamics of single actin or microtubule filaments taking into account ATP/GTP hydrolysis. Our model is very much in the same spirit as that of Stukalin and Kolomeisky (26) and has also several common features with the model of Hill et al. (11,12). We assume that polymerization occurs, for actin, via the addition of single ATP subunit (GTP subunit for microtubule), at the barbed end (plus end for microtubule) (2) of the filament. We assume that the other end is attached to a wall and no activity happens there. Let U and W_T be the rates of addition and removal of ATP/GTP subunits, respectively, which can occur only at the filament end. The subunits on the filament can hydrolyze ATP/GTP and become ADP/GDP subunits with a rate R. We assume that this process can occur only at the interface of ATP-ADP or GTP-GDP subunits. This corresponds to the vectorial model of hydrolysis, which is used in the model of Hill et al. (11,12). Once the whole filament is hydrolyzed, the ADP/GDP subunit at the end of the filament can disassociate with a rate W_D. The addition, removal, and hydrolysis events are depicted in Fig. 1. We denote by d the size of a subunit.

This model provides a simple coarse-grained description of the nonequilibrium self-assembly of linear fibers. More sophisticated approaches are possible, which could include in the case of actin, for instance, additional steps in the reaction such as the conversion of ATP into ADP-Pi-actin or the possibility of using more than one rate for the addition of ATP subunits. It is also possible to extend our model to include growth from both ends of the filament rather than from a single end, as discussed in Stukalin and Kolomeisky (26). Another feature of actin or microtubule filaments, which we leave out in our model, is that these fibers are composed of several protofilaments (two for actin and typically 13 for microtubules). In the case of actin, it is reasonable to ignore the existence of the second protofilament due to strong interstrand interactions between the two protofilaments (26). In fact, we argue that the model with a single filament can be mapped to a related model with two protofilaments under conditions that are often met in practice. Indeed the mapping holds provided that the two protofilaments are strongly coupled, grow in parallel to each other, and are initially displaced by half a monomer. The two models can then be mapped to each other provided that d is taken to be half the actin monomer size $d = 5.4$ nm/2 = 2.7 nm. This mapping suggests that many dynamical features of actin should already be present in a model that ignores the second protofilament. Similarly, microtubules may also be modeled using this simple one-filament model, in a coarse-grained way, provided $d = 8$ nm/13 = 0.6 nm is equal to the length of a tubulin monomer divided by 13, which is the average number of protofilaments in a microtubule (2). Keeping in mind the fact that this model is applicable to both actin and microtubules, we use a terminology appropriate to actin to simplify the discussion in the rest of the article.

The actin filament dynamics is studied in terms of two variables n, the number of ADP subunits, and k, the number of ATP subunits, as shown in Fig. 1. The dynamics of this system may be represented as a biased random walk in the upper-quarter two-dimensional plane (n, k). For instance, the addition of one ATP subunit with rate U corresponds to a move in the upward direction. The removal of ATP subunits with W_T corresponds to a move in the downward direction. The hydrolysis of an ATP subunit results in an increase in n and decrease in k, both by one unit, which corresponds to a move in the diagonal direction as shown in the figure. The removal of ADP subunits can happen only when the cap is zero and therefore corresponds to

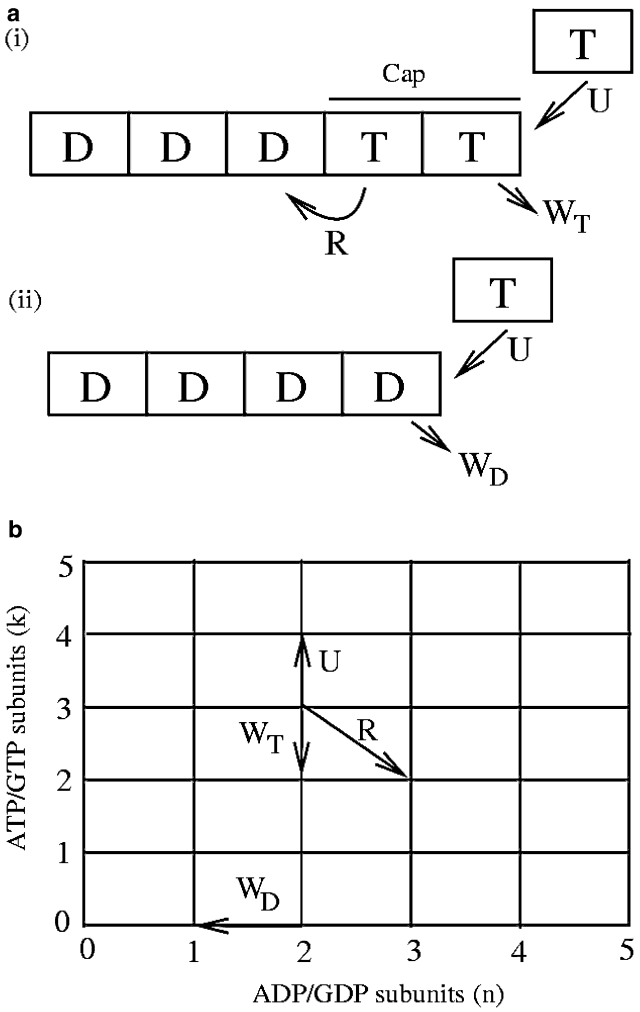

FIGURE 1 (*a*) Schematic diagram showing addition with rate U, removal with rates W_T and W_D, and hydrolysis with rate R: *i* for the case where the cap length is nonzero and *ii* for the case where the cap length is zero. *T* stands for ATP (GTP) bound actin (microtubule) subunits while *D* stands for hydrolyzed ADP(GDP) subunits. At the T-D interface shown in *i*, the hydrolysis occurs with a rate R. (*b*) Equivalent representation of the model as a biased random walk in the upper-quarter two-dimensional plane with rates U to go up(north), W_T to go down (south), R to go south-east, and W_D to go west. The W_D move is only possible along the $k = 0$ (southern boundary) line.

a leftward move along the $k = 0$ line. Let $P(n, k, t)$ be the probability of having n hydrolyzed ADP subunits and k unhydrolyzed ATP subunits at time t, such that $l = (n + k)d$ is the total length of the filament. This probability obeys a set of master equations that are derived and solved using generating functions in Appendix A. From this approach, we obtain various quantities of interest such as the average filament length $\langle l \rangle$, the average velocity of the filament v and that of the cap J, the diffusion coefficient of the filament D and that of the cap D_c.

RESULTS

Phase diagram

Our model for the dynamics of a single filament with ATP hydrolysis leads to the following steady-state phases: a bounded growth phase (phase I), and two phases of unbounded growth: an intermediate phase (phase II) and a rapidly growing phase (phase III). In phase I, the average velocity of the filament v_I and the average velocity of the cap both vanish. Thus, the average filament and cap lengths remain constant in the long time limit. In phase II, the filament is growing linearly in time, with a velocity v_{II}, but the average ATP cap length remains constant as a function of time. In phase III, the filament as well the ATP cap are growing linearly in time with a filament velocity v_{III} and cap velocity J. The boundary between phases I and II is the curve of equation $v_{II} = 0$, and the boundary between phase II and III is the curve of equation $J = 0$.

We have carried out simulations of the dynamics of the length of the filament, using the Gillespie algorithm (27). According to this algorithm, the time to the next on-, off-, or hydrolysis-event is computed stochastically at each step of the simulation. We find that our simulation results agree with the exact calculations.

The bounded growth phase (phase I)

In the representation of the model as a biased random walk shown in Fig. 1, there is a regime of parameters for which the biased random walker converges toward the origin. After some transient time, the random walker enters a steady state, where the motion of the walker is confined to a bounded region containing the origin. In the representation of the model as a filament, the filament length fluctuates as function of time around a time-independent average value $\langle l \rangle$ and at the same time, the cap length also fluctuates as function of time around a different time-independent average value $\langle k \rangle d$. A typical evolution of the total length of the filament $l(t)$, obtained from our Monte Carlo simulations, is shown in Fig. 2.

We first discuss the properties of the cap before considering that of the total length. In the steady state ($t \to \infty$), $F_k(x = 1)$ represents the distribution of cap lengths, as defined in Eq. 41 with

$$F_k(x = 1) = (1 - q)q^k, \tag{1}$$

where

$$q = \frac{U}{W_T + R}. \tag{2}$$

Since $F_0 = 1 - q$, we see that q has the meaning of the probability of finding a nonzero cap in the steady state (26). We consider for the moment only the case $q \leq 1$, which corresponds to phases I and II. From $F_k(x = 1)$, we find that the average number of cap subunits is given by

$$\langle k \rangle = \frac{q}{1 - q} \tag{3}$$

and

$$\langle k^2 \rangle = \frac{q + q^2}{(1 - q)^2}. \tag{4}$$

Note that this expression of $\langle k^2 \rangle$ differs from that found in Stukalin and Kolomeisky (26), which is, we believe, probably due to a misprint in this reference. As expected, these quantities diverge when approaching the transition to phase III when $q \to 1$. The standard deviation of the cap length is

$$\sigma_c^2 = \langle k^2 \rangle - \langle k \rangle^2 = \frac{q}{(1-q)^2}. \quad (5)$$

The relative fluctuations in the cap size are large, since

$$\frac{\sigma_c^2}{\langle k \rangle^2} = \frac{1}{q} > 1. \quad (6)$$

We now investigate the overall length of the filament in the bounded growth phase. This quantity together with the distribution of length in the bounded growth phase can be obtained from the time-independent generating function $G(x, y)$ as shown in Appendix A. We find

$$G(x,y) = \frac{(W_T + Rx)\left(\frac{W_D}{U} - \frac{W_D + R}{W_T + R}\right)(x-1)}{(y - y_+)[W_T(y_- - 1)x + Rx(y_- - x) + W_D y_-(1-x)]}, \quad (7)$$

where $y_\pm$ values are defined by

$$y_\pm = \frac{1}{2U}\left(U + W_T + R \pm \sqrt{(U + W_T + R)^2 - 4U(W_T + Rx)}\right). \quad (8)$$

From the derivatives of $G(x, y)$, we obtain analytically the average length $\langle l \rangle$ using Eq. 47 as

$$\langle l \rangle = \left[\frac{q\left(R^3 + W_D R^2 + 2R^2 W_T + W_T^2 R + 2W_D W_T R + W_D W_T^2\right)}{v_{II}(q-1)(W_T + R)^2}\right] d^2 - \left[\frac{q^2\left(R^2 + 2W_T R + W_D W_T\right)}{v_{II}(q-1)(W_T + R)}\right] d^2, \quad (9)$$

where v_{II} is the shrinking velocity (since $v_{II} < 0$ in this regime) of the filament

$$v_{II} = \left[\frac{U(W_D + R)}{W_T + R} - W_D\right] d. \quad (10)$$

The length $\langle l \rangle$ diverges since $v_{II} \to 0$ when approaching the transition line between phases I and phase II. The length $\langle l \rangle$ as given by Eq. 9 is plotted in Fig. 3 for the parameters of Table 1. We compare this exact expression with the result of our Monte Carlo simulations where the average is computed using 1000 length values taken from different realizations. Excellent agreement is found with the analytical expression of Eq. 9. According to a simple dimensional argument, the average length $\langle l \rangle$ should scale as $-D_{II}/v_{II}$, where D_{II} and v_{II} are the diffusion coefficient and velocity of phase II. We find that this scaling argument actually holds only close to the transition point between phase I and II. On the boundary line between phases I and II, the average filament velocity vanishes, and hence the filament length is effectively undergoing an unbiased random walk. In such a case, we expect that on the boundary line $\langle l^2 \rangle \sim t$. We have also considered the fluctuations of $l(t)$ using the standard deviation σ defined as

$$\sigma^2 = \langle l^2 \rangle - \langle l \rangle^2, \quad (11)$$

for which an explicit expression can be obtained from $G(x, y)$. In Fig. 3, σ is shown as a function of U. Note that σ is larger than $\langle l \rangle$, which corresponds to dynamic-instability-like large length fluctuations.

In the limit $R \to 0$, ATP hydrolysis can be ignored in the assembly process. The model is then equivalent to a simple one-dimensional random walk with rates of growth U and decay W_T. In this case, phases II and III merge into a single growing phase. We find from Eq. 9 that $\langle l \rangle = Ud/(W_T - U)$, which diverges as expected near the transition to the growing phase when $U \simeq W_T$. According to the simple dimensional argument mentioned above, this length must scale as $-D/v$ in terms of the diffusion coefficient and velocity of the growing phase (16). This is the case, since $D = d^2(U + W_T)/2$ and $v = (U - W_T)d < 0$ and thus $\langle l \rangle = Ud/(W_T - U)$ near the transition point.

We have also computed the filament length distribution, $P(l)$, in this phase using Monte Carlo simulations, as shown in Fig. 4. In the inset, we compare the numerically obtained distribution with the following exponential distribution

$$P(l) = P_0 \exp(-l/\langle l \rangle), \quad (12)$$

where $\langle l \rangle$ is given by Eq. 9. In this figure, the distribution appears to be close to this exponential distribution. For any exponential distribution, the standard deviation, σ, should equal the mean $\langle l \rangle$. However as seen in Fig. 3, there is a difference between σ and $\langle l \rangle$. Hence the distribution cannot be a simple exponential, which could also have been guessed from the fact that the expression of $G(x, y)$ is complicated. The exact analytical expression of the distribution could be calculated by performing an inverse Z-transform of the known $G(x, y)$.

In the bounded growth phase, experiments with actin in Fujiwara et al. (21) report an average length in the 5–20-μm

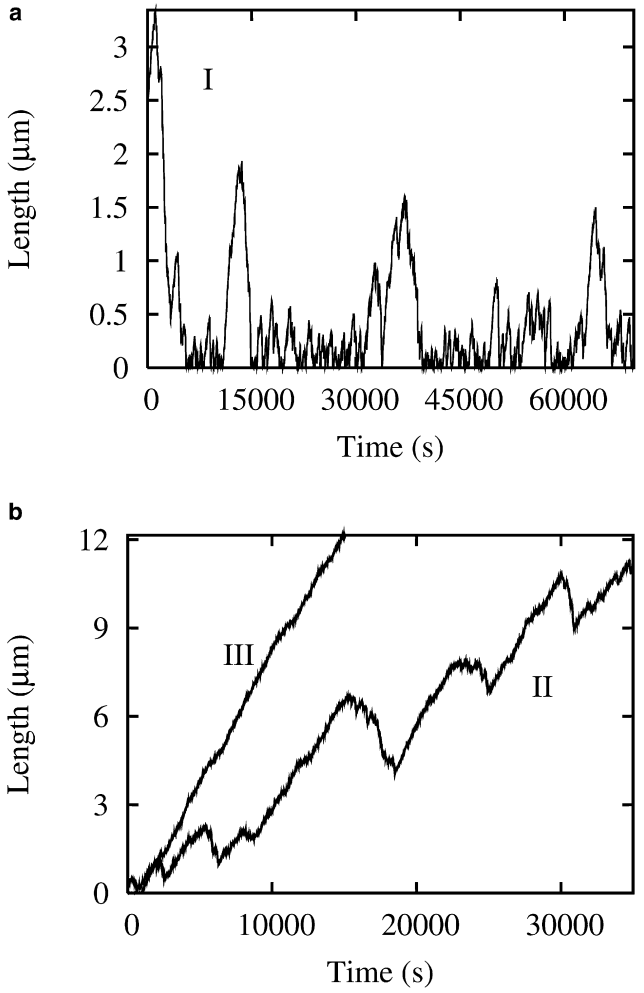

FIGURE 2 Filament length as a function of time for the three different phases of the model, as computed using Monte Carlo simulations. The value of the rates that were used are given in Table 1. Panel *a* represents the bounded growth phase (phase I), where a structure of avalanches in the evolution of the length can be seen. These avalanches correspond to series of sudden depolymerization events (collapse) followed by slow polymerization events (rescue). Panel *b* represents the intermediate phase (phase II) and the rapidly growing phase (phase III). In the intermediate phase (II), the dynamics show large length fluctuations as compared to the rapidly growing phase (III), where the length fluctuations can hardly be resolved.

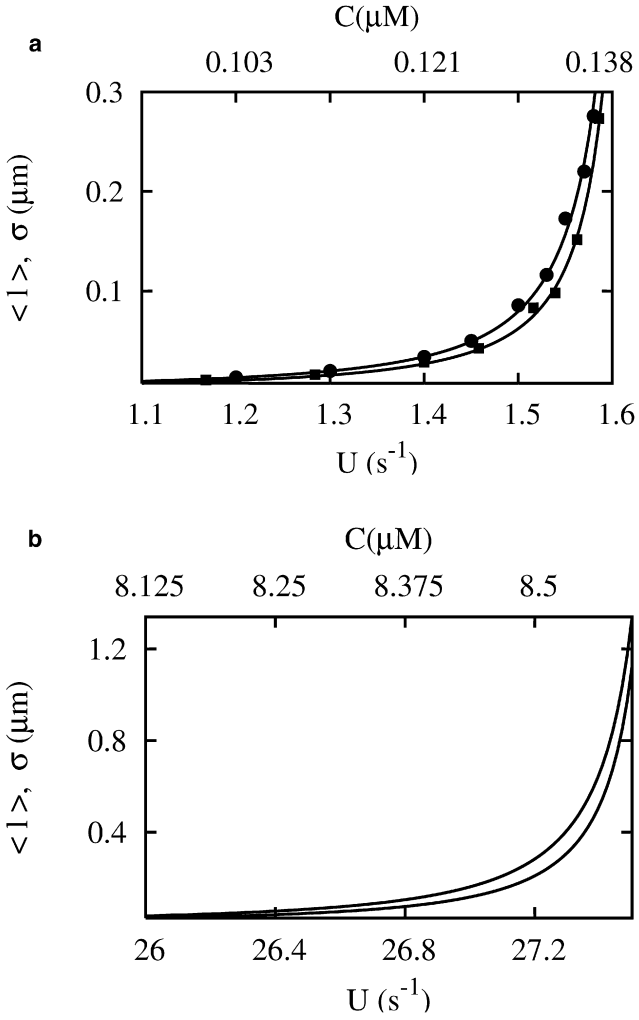

FIGURE 3 Average length $\langle l \rangle$ and its standard deviation σ in the bounded growth phase for (*a*) actin, and (*b*) microtubule as a function of the insertion rate, U (*lower x axis*), and of the concentration of the free ATP/GTP subunits C (*upper x axis*). The solid lines represent analytical expressions of $\langle l \rangle$ (*lower curves*) and σ (*upper curves*). Solid symbols represent values obtained from simulations for these quantities. All the curves and symbols are obtained using values of the rates given in Table 1.

range at different monomer concentrations, and experiments with microtubules of Fygenson et al. (28) report a range 1–20 μm at different temperatures. Neither experiment corresponds precisely to the conditions for which the rates of Table 1 are known. Thus a precise comparison is not possible at the moment, although we can certainly obtain with this approach an average length in the range of microns using the rates of Table 1 as shown in Fig. 3.

Intermediate phase (phase II)

In the intermediate phase (phase II), the average ATP cap length remains constant as a function of time, while the filament grows linearly with time. The presence of this cap leads to interesting dynamics for the filament. A typical time evolution of the filament length is shown in Fig. 2. One can see the filament switching between growth (polymerization) and decay (depolymerization) in a way that is completely analogous to what is observed in the microtubule dynamics (14).

In this phase II, the average velocity of the filament is

$$v_{\mathrm{II}} = [U - W_{\mathrm{T}}q - W_{\mathrm{D}}(1-q)]d. \qquad (13)$$

This expression of v_{II} is the same as Eq. 10 except that now Eq. 13 corresponds to the regime, where $v_{\mathrm{II}} > 0$. The diffusion coefficient in this phase is

TABLE 1 Numerical estimates of the rates W_T, W_D, R, k_0, and subunit length d

	k_0 (μM^{-1} s^{-1})	$W_T(s^{-1})$	$W_D(s^{-1})$	R (s^{-1})	d (nm)
Actin	11.6	1.4	7.2	0.3	2.7
Microtubule	3.2	24	290	4	0.6

The parameters for actin are taken from the literature (2,26) and they characterize the barbed end of an actin filament. The parameters for microtubule hold similarly for the plus end and at 35°C. The rate constant k_0 and rate W_D are taken from Howard (2), while the other two rates, W_T and R, are deduced from fitting the zero-force velocity data of Janson et al. (44) and the critical concentration measurements of Fygenson et al. (28).

$$D_{II} = \frac{d^2}{2}\Big[U + W_T q + W_D(1-q) + \frac{2(W_D - W_T)(U + W_D q)}{W_T + R}\Big]. \quad (14)$$

The expressions of v_{II} and D_{II} are derived in the Appendix A. When d equals to half the size of an actin subunit, we recover exactly the expressions of Stukalin and Kolomeisky (26).

The transition between the bounded growth phase (I) and the intermediate phase (II) is delimited by the $v_{II} = 0$ curve. When going from phase I to II, the average length in Eq. 9 varies as $(U - W_D(W_T + R/W_D + R))^{-1}$, and the variance of the length σ^2 varies as $(U - W_D(W_T + R/W_D + R))^{-2}$. The transition from the intermediate phase II to the rapidly growing phase III is marked by a similar behavior. The cap length diverges as $(U - W_T - R)^{-1}$, and the variance of the fluctuations of the cap length diverges as $(U - W_T - R)^{-2}$.

Rapidly growing phase (phase III)

In phase III, the length of the ATP cap and that of the filament are growing linearly with time. Thus, the probability of finding a cap of zero length is zero in the limit $t \to \infty$, that is $F_0(x = 1) = 0$. This also means that the probability of having a filament of zero length is also zero, i.e., $P(0,0) = 0$.

In this case, Eq. 44 reduces to

$$\frac{dG(x,y,t)}{dt} = \Big[U(y-1) + W_T\Big(\frac{1}{y} - 1\Big) + R\Big(\frac{x}{y} - 1\Big)\Big]G(x,y,t). \quad (15)$$

Using Eqs. 48–51 of Appendix A, one can easily obtain the following quantities

$$v_{III} = [U - W_T]d, \quad (16)$$

$$D_{III} = \frac{d^2}{2}(U + W_T), \quad (17)$$

$$J = [U - (W_T + R)]d, \quad (18)$$

$$D_c = \frac{d^2}{2}(U + W_T + R). \quad (19)$$

Note that these quantities can be obtained from Eqs. 13 and 14 by taking the limit $q \to 1$, which marks the transition between phase III and phase II. In Fig. 2, the filament length is plotted as a function of time. Note that in this phase the velocity and the diffusion coefficient are the same as those of a filament with no ATP hydrolysis. The physical reason is that in phase III, the length of the nonhydrolyzed region (cap) is very large and the region with hydrolyzed subunits is never exposed.

Effect of force and actin concentration on active polymerization

The driving force of self-assembly of the filament is the difference of chemical potential between bound and unbound ATP actin subunits. Since the chemical potential of unbound ATP actin subunits depend on the concentration C of free ATP actin subunits and on the external applied force f, the rates should depend also on these physical parameters. In the biological context, this external force corresponds to the common situation where a filament is pushing against a cell membrane. For the concentration dependence, we assume a simple first-order kinetics for the binding of ATP actin monomers given that the solution is dilute in these monomers. This means that the rate U of binding of ATP actin is proportional to C while W_T, W_D, and R should be independent of C (29–31). For the force dependence of the rates, general thermodynamical arguments only enforce a constraint on the ratio of the rates of binding to that of unbinding (2,32). A simple choice consistent with this and supported by microtubule experiments (33) is to assume that only the binding rate, i.e., U, is force-dependent. A more sophisticated modeling of the force dependence of the rates has been considered for instance for microtubules in Kolomeisky and Fisher (34). All the constraints are then

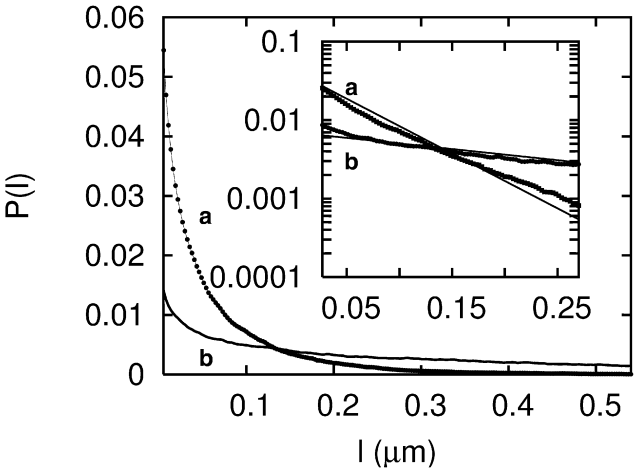

FIGURE 4 Filament length distribution in the bounded growth phase for actin. (*a*) For $U = 1.5$ s^{-1} and (*b*) for $U = 1.6$ s^{-1} with all other parameters taken from Table 1. The inset shows the same quantities (l versus $P(l)$) with $P(l)$ in the log scale. The straight line in the inset is given by Eq. 12.

satisfied by assuming that $U = k_0 C \exp(-fd/k_B T)$, with k_0, W_T, W_D, and R all independent of the force f and of the concentration C. We assume that $f > 0$, so that the on-rate is reduced by the application of the force. The cap velocity in the rapidly growing phase(phase III), given by Eq. 18, can be written in terms of f and C as

$$J(f, C) = \left[k_0 C e^{-fd/k_B T} - (W_T + R)\right] d. \quad (20)$$

The phase boundary between phase II and phase III is defined by the curve $J(C, f = f_c) = 0$. Equating the cap velocity to zero, we obtain the characteristic force,

$$f_c = -\frac{k_B T}{d} \ln\left[\frac{W_T + R}{k_0 C}\right] = -\frac{k_B T}{d} \ln\frac{C_0}{C}, \quad (21)$$

where the concentration C_0 is defined as

$$C_0 = (W_T + R)/k_0. \quad (22)$$

Below f_c, the system is in phase III. This is also the point where $q = 1$.

The force-velocity relation in the intermediate phase is rewritten, using Eq. 13, as

$$v_{II}(f, C) = k_0 C e^{-fd/k_B T} \left[\frac{W_D + R}{W_T + R}\right] d - W_D d. \quad (23)$$

The stall force f_s is, by definition, the force at which $v_{II}(f = f_s, C) = 0$. From Eq. 23, we obtain

$$f_s = -\frac{k_B T}{d} \ln\left[\left(\frac{W_T + R}{W_D + R}\right)\frac{W_D}{k_0 C}\right], \quad (24)$$

which can be written equivalently in terms of the critical concentration of the barbed end C_{crit} as

$$f_s = -\frac{k_B T}{d} \ln\left(\frac{C_{crit}}{C}\right), \quad (25)$$

where

$$C_{crit} = C_0 \left(\frac{W_D}{W_D + R}\right) < C_0. \quad (26)$$

In the absence of hydrolysis, when $R \to 0$, we have $C_{crit} = C_0$ and Eq. 25 gives the usual expression of the stall force given in the literature (2,29,30,35)

The velocity of the filament is shown in Fig. 5 *b*. This figure shows that for $f < f_c$, the filament is in phase III, and that there the velocities of the filament with ATP hydrolysis or without are the same. At $f = f_c$, the force-velocity curve changes its slope, as shown after the vertical line in Fig. 5 (see Fig. 5 *b*). When the concentration rather than the force is varied, a similar change of slope is observed at $C = C_0$, which is accompanied by a discontinuity of the diffusion coefficient slightly above the critical concentration (26).

For $f_c < f < f_s$, the filament is in the intermediate phase, where the velocities in the presence and in the absence of

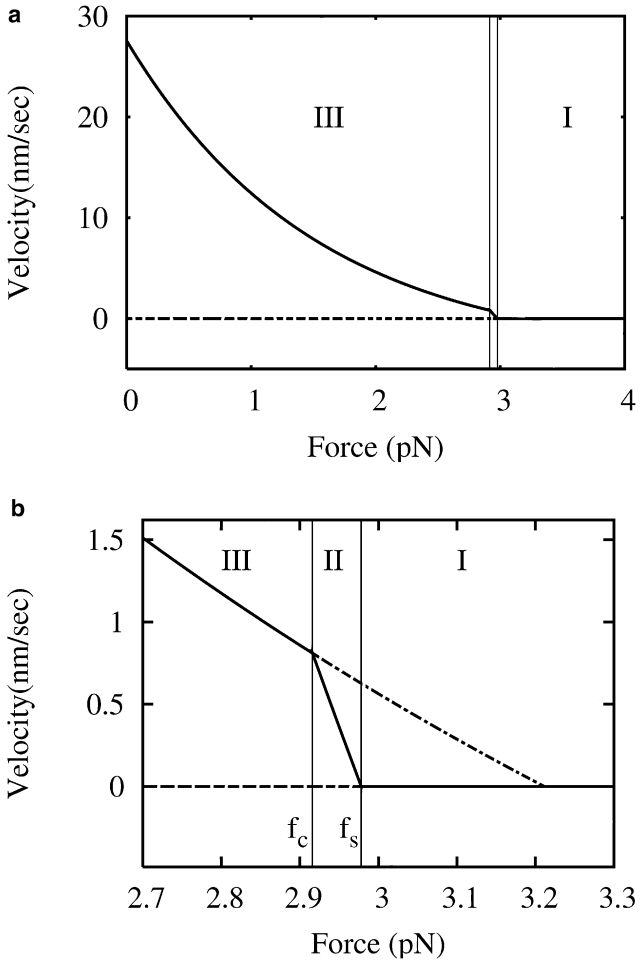

FIGURE 5 (*a*) Steady-state force-velocity relation for a single actin filament shown for $C = 1$ μM (*solid curve*); (*b*) zoom of the force-velocity relation near the stall force. The vertical lines represent f_c and f_s as shown in panel *b*. For $f < f_c$, the filament is in the rapidly growing phase (III) and the velocity is given by Eq. 16. In the bounded growth phase (I) the velocity is zero. In the intermediate phase the velocity is given by Eq. 13. The dash-dotted line (*b*, phases I and II) is given by Eq. 16, showing that the stall force is higher when ATP hydrolysis is neglected.

ATP hydrolysis differ. The stall force with ATP hydrolysis is smaller than that in the absence of ATP hydrolysis. In view of this, a useful conclusion is that it is important to take into account the ATP hydrolysis for estimating the velocity of a filament when the force is close to the stall force. As can easily be shown with the equations above, the stall force is reduced by the ATP hydrolysis only because $W_D > W_T$.

For $f > f_s$, the velocity of the filament vanishes. It must be noted that, in this phase, the instantaneous velocity can be positive or negative, but the average velocity, in the long time limit, is zero. Another important point to note is that when the filament is stalled, ATP is still hydrolyzed. This is analogous with models of molecular motors containing more than one cycle (36–38). Including the chemical cycle of ATP hydrolysis, in addition to the mechanical cycle of

addition/removal of subunits, is, for this reason, important in the context of actin and microtubule models. One could imagine testing these predictions on the effect of ATP hydrolysis on force-velocity relations by carrying out force-velocity measurements near stalling conditions of abundant ATP or when ATP is sequestered by appropriate proteins (39).

All these observations can be summarized in a phase diagram in the coordinates f and C as shown in Fig. 6. As shown in Fig. 6, when $C < C_0$, the filament is either in the intermediate phase (II) or in the bounded growth phase (I). In this region of the phase diagram, the fluctuations of the filament length are large as compared to the very small fluctuations observed in the rapidly growing phase (III). The large fluctuations observed in phase I correspond to the dynamic instability.

In the case of microtubules, we find as shown in Table 2, $C_0 = 8.75\ \mu$M. This value is rather large when compared to typical experimental concentrations $C \simeq 1 - 10\ \mu$M for microtubules. Thus microtubules are usually found in phases I and II where the length fluctuations are large and dynamic instability is commonly observed.

In the case of actin, we find that $C_0 = 0.147\ \mu$M. Typical experimental actin concentrations are above this estimate; therefore, at zero force, actin filaments are usually seen in phase III. This may explain why the dynamic instability is rarely seen in actin experiments with pure actin.

In comparing our model to experiments, it is important to keep in mind that only the dynamics of a single end of the filament is taken into account in the model. If we take into account the dynamics at both ends, we expect the following behavior: above the critical concentration for the pointed end, both ends grow; below the critical concentration of the barbed end, both ends shrink; and between these concentrations, treadmilling occurs. In addition to this, we expect that near the critical concentrations of the pointed and barbed end, two small regions of the phase diagram should exist in which the pointed or barbed end should be in the intermediate phase (phase II) described in this article.

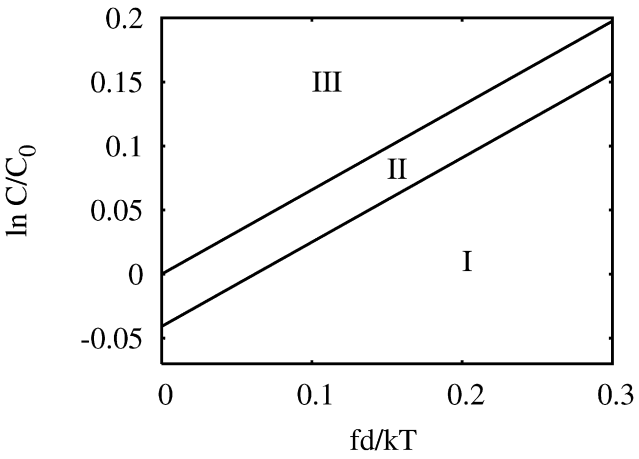

FIGURE 6 Phase diagram as a function of the normalized force fd/k_BT and of the log of the ratio of the ATP subunit concentration C to the characteristic concentration C_0 for actin. The phase diagram shows the bounded growth phase (phase I), the intermediate phase (phase II), and the rapidly growing phase (phase III). The boundary line between phase II and phase III is the curve $J = 0$ and the boundary line between phase I and phase II is the curve $v_{II} = 0$.

TABLE 2 Estimates of the characteristic concentrations C_0 and C_{crit} at zero force, and of the characteristic forces f_c and f_s at a concentration of 1 μM for actin and 20 μM for microtubule using the rates of Table 1

	$C_0(\mu M)$	$C_{crit}(\mu M)$	f_c (pN)	f_s (pN)
Actin	0.147	0.141	2.916 (at 1 μM)	2.978 (at 1 μM)
Microtubule	8.75	8.63	5.65 (at 20 μM)	5.74 (at 20 μM)

When discussing the effect of force on a single actin or microtubule filament, one important issue is the buckling of the filament. Since actin filaments have much smaller persistence length l_p than microtubules, actin filaments buckle easily under external force. Our approach is appropriate to describe experiments like that of Footer et al. (35), where very short actin filaments are used. The length of the filaments must be smaller than the critical length for buckling under a force f. This length can be estimated as $l_b = \pi\sqrt{\kappa/f}$ with a hinged boundary condition, where $\kappa = l_p k_B T$. With $l_p \approx 9\ \mu$m measured in Isambert et al. (40), we estimate $l_b \approx 603$ nm at $f = 1$ pN. Our discussion of the force will be applicable only for filaments shorter than l_b.

Collapse time

In this new section, we shall study experimentally relevant questions such as the mean time required for the ATP cap to disappear or the mean time required for the whole filament (ATP cap and ADP subunits) to collapse to zero length. We are interested in the conditions for which these times are finite. Below we address these questions.

Cap collapse in phases I or II

The dynamics of the cap corresponds to that of a one-dimensional biased random walker with a growth rate U and a decay rate $W_T + R$. Here, we calculate the mean time T_k required for a cap of initial length k_d to reach zero length for the first time. We assume that there is a bias toward the origin so that $W_T + R > U$. This time T_k is nothing but the mean first-passage time for the biased random walker to reach $k = 0$, starting from an arbitrary site k in phases I or II. According to the literature on first passage times, the equation for T_k is (41–43):

$$UT_{k+1} + (W_T + R)T_{k-1} - (U + W_T + R)T_k + 1 = 0. \tag{27}$$

When $W_T + R > U$, this recursion relation can be solved (see Appendix B) with the condition that $T_0 = 0$, and we obtain

$$T_k = \frac{k}{W_T + R - U}. \tag{28}$$

This corresponds to the time the random walker takes to travel a distance k at a constant velocity $-J$. Note that the mean first-passage time T_k becomes infinite in the unbiased case when $J = 0$ or if the bias is not toward the origin, i.e., when $W_T + R \leq U$ (which would correspond to an initial condition in phase III) (41).

One can also define an average of the mean first-passage time with respect to the initial conditions. Averaging over k and using Eq. 3, one obtains

$$\langle T_k \rangle = \frac{U}{(W_T + R - U)^2}. \quad (29)$$

The same time can be recovered by considering the average time associated with the fluctuation of the cap:

$$\langle T_k \rangle = \frac{\langle k^2 \rangle d^2}{2D_c}. \quad (30)$$

This time may be related to the catastrophe rate in the following way. In Flyvbjerg et al. (16), the catastrophe rate is defined as the total number of catastrophes observed in an experiment divided by the total time spent in the growing phase. Since the growing phase ends when the cap disappears for the first time, we interpret similarly $1/\langle T_k \rangle$, as an average collapse frequency of the cap.

Filament collapse in phase I

Now we consider the dynamics of the filament length, which is described similarly by a two-dimensional biased random walk converging toward the origin. Here we investigate the mean time $T_{n,k}$ required for a filament with an initial state of n ADP subunits and k ATP subunits to reach zero length for the first time with an initial condition inside phase I. Again, this is the mean first-passage time now in a two-dimensional domain (in the $n - k$ plane, as shown in Fig. 1) to reach the origin ($n = 0, k = 0$) starting from an arbitrary n and k. This mean first-passage time $T_{n,k}$ obeys the following set of equations (41). When $k > 0$, for all n, the equation is

$$UT_{n,k+1} + W_T T_{n,k-1} + RT_{n+1,\,k-1} - (U + W_T + R)T_{n,k} + 1 = 0. \quad (31)$$

For $k = 0$ and $n > 0$ we have a special equation

$$UT_{n,1} + W_D T_{n-1,0} - (U + W_D)T_{n,0} + 1 = 0, \quad (32)$$

and we also have the condition $T_{00} = 0$.

The simplest way to solve these equations is to guess by analogy with the one-dimensional case that the solution must be a linear function of n and k. This leads to a simple Ansatz of the form $T_{n,k} = An + Bk$, which in fact gives the exact result, as can be shown rigorously. Substituting this in Eq. 31 and Eq. 32, we can solve for unknowns A and B. This leads to

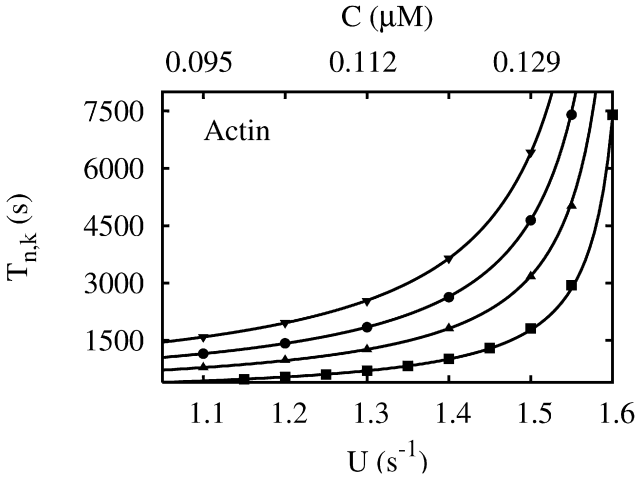

FIGURE 7 Mean time taken by a filament of initial length $(n + k)d$ to collapse to zero length. Curves are given by Eq. 33 and points are obtained from a Monte Carlo simulation for different values of n and k. From bottom to top $(n, k) = (990, 10)$, $(750, 250)$, $(500, 500)$, and $(200, 800)$.

$$T_{n,k} = \frac{nd}{-v_{II}} + \frac{kd}{-v_{II}}\left(\frac{W_D + R}{W_T + R}\right), \quad (33)$$

where v_{II} is the velocity of the intermediate phase given by Eq. 13. Note that $v_{II} < 0$ here, since the initial condition is within phase I.

We first examine some simple particular cases of Eq. 33. As we approach the intermediate phase boundary $v_{II} \to 0$, $T_{n,k} \to \infty$ as expected. When $W_D = \infty$, $T_{n,k} = k/(W_T + R - U) = T_k$, which is the cap collapse time calculated in the one-dimensional case. When $W_D = \infty$, the whole filament collapses immediately after the cap has disappeared for the first time, i.e., after a time T_k. When $R \to \infty$, ATP subunits instantaneously become ADP subunits and we obtain another simple result $T_{n,k} = (n + k)/(W_D - U)$. We have also compared the prediction of Eq. 33 with Monte Carlo simulations in Fig. 7 and we have found an excellent agreement.

We can also define an average of the above mean first-passage time where the average is performed over initial lengths of cap and unhydrolyzed region. Averaging over k and n in Eq. 33 we obtain

$$\langle T_{n,k} \rangle = \frac{U\left(R^2 + W_D R + W_T R + W_D^2\right)}{(UR - W_D W_T - W_D R + UW_D)^2}. \quad (34)$$

The inverse, $1/\langle T_{n,\,k} \rangle$, can be called the collapse frequency of the filament. The filament collapse frequency and the cap collapse frequency are shown in Fig. 8 as a function of U and C for the cases of actin and microtubule using parameters of Table 1. Both frequencies are close to each other because the rate W_D is large compared to other rates (see Table 1). This figure also shows that as the frequency of collapse is increased, the rate U decreases and so the filament length is decreasing, which is expected (16). The behavior of the collapse frequency as function of the growing velocity in

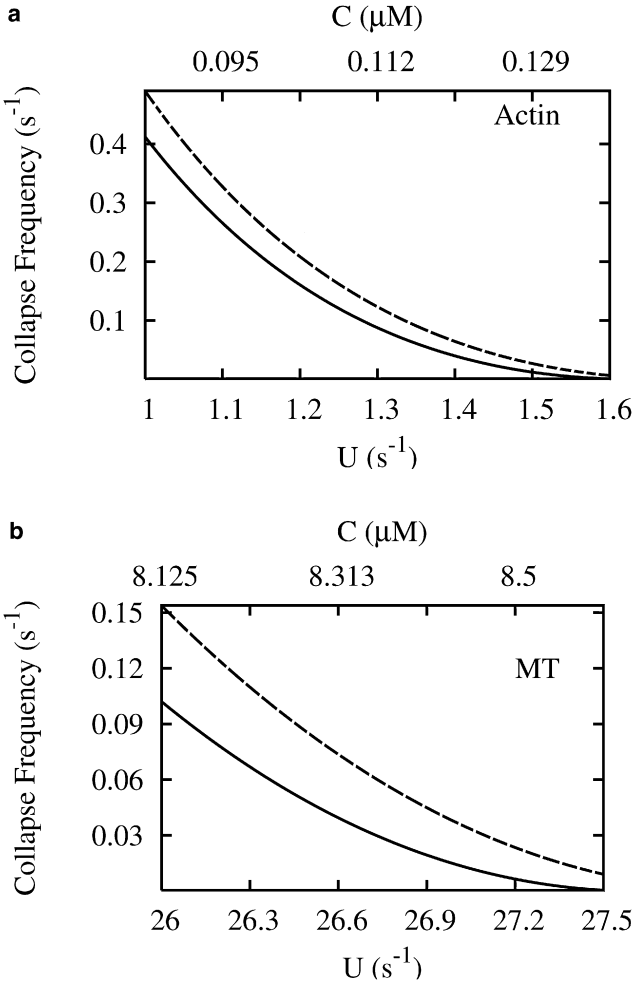

FIGURE 8 Collapse frequencies for actin and microtubule (MT) as function of the rate of addition of monomers U (*lower x axis*) and of the concentration C (*upper x axis*): (*Solid line*) Represents the collapse frequency of the filament given by $1/\langle T_{n,k}\rangle$, the inverse of the time given in Eq. 34. (*Dashed line*) Represents the collapse frequency of the cap given by $1/\langle T_k\rangle$, the inverse of the time given in Eq. 29.

the absence of force agrees with Janson et al. (44). The decrease of the rate of monomer addition is in practice caused by either the application of a force or a lowering of the concentration. Thus the application of force may be seen as a general mechanism to regulate the dynamic instability.

In the opposite limit, when $R/W_D \to 0$, one can also understand the result physically from the following argument. When the filament collapses, the first event is the disappearance of the cap and therefore the first contribution to the collapse time is the mean time required for the cap to disappear, T_k, as obtained from Eq. 28. Once the cap has disappeared, assuming that W_D is very large, ADP subunits start depolymerizing until the next ATP subunit addition takes place. The mean time needed for an ATP subunit addition to take place is $1/U$. Once an ATP subunit is added, one has to wait an average time of T_1 for the cap to disappear again. This cycle of ATP subunit addition and depolymerization repeats many times. The number of times this cycle occurs, starting with a filament of n ADP subunits, is roughly $n/(W_D/U)$. But one also has to take into account the increase in ADP subunits as a result of ATP hydrolysis, which is done by subtracting RT_1 from $n/(W_D/U)$. This leads to the following approximate expression for $T_{n,k}$,

$$T_{n,k} \simeq T_k + \left[\frac{1}{U} + T_1\right]\frac{n}{\left(\frac{W_D}{U} - RT_1\right)}, \tag{35}$$

$$\simeq \frac{nd}{-v_{II}} + \frac{kd}{-J}, \tag{36}$$

where $J = (U - W_T + R)d$ is the cap velocity in the rapidly growing phase. This solves Eqs. 31 and 32 in the limit $R/W_D \to 0$ and agrees reasonably well with the Monte Carlo simulations.

DISCUSSION AND CONCLUSION

In this article, we have studied a model for the dynamics of growth and shrinkage of single actin/microtubule filaments, taking into account the ATP/GTP hydrolysis that occurs in the polymerized filament. We find three dynamical phases with different properties of the ATP/GTP cap and the filament: a bounded growth phase, an intermediate phase, and a rapidly growing phase. For each phase, we have calculated the steady-state properties of the nonhydrolyzed cap and of the filament and we have investigated the role of an external force (f) applied on the filament during polymerization and of the monomer concentration (C), leading to a f-C phase diagram. We have also calculated the collapse time, which is the time needed for the cap or the filament to completely depolymerize.

In batch experiments, the total amount of monomers (free+polymerized) is constant. This constraint leads to a different dynamics than that described in this model, in which the monomer concentration remains constant. Indeed, with a finite amount of monomer present in bulk experiments, the intermediate and rapidly growing phase are not sustainable forever. If only a single filament is present, it would have to eventually settle in the bounded growth phase. For this reason, the bounded growth phase is a very important phase for analyzing batch experiments. It would be interesting to probe experimentally the fluctuations of length at a level of a single filament in the bounded growth phase. Such an experiment could provide insights into the dynamic instability and possibly into the structure of the cap itself, which is very difficult to probe experimentally.

Another important conclusion is the role of ATP/GTP hydrolysis in determining the stall force of the filament: the effect of hydrolysis always reduces the value of the stall force. Dynamic instabilities are in general not observed with actin filaments when no force is applied to the filament. However, in recent experiments (23,24), it has been found that the presence of ADF/cofilin leads to a bounded growth phase even at zero force where actin filaments exhibit large

length fluctuations. In the absence of binding proteins, a natural way to regulate the dynamic instability and the length of the filament is through the application of force.

The intermediate phase is a phase where the filaments grow at a constant velocity with a finite ATP/GTP cap. This is the phase that is, in general, observed in a cell. There are large length fluctuations of the cap in this phase but the length fluctuations are not as large as the average length. Thus, there is no true dynamic instability in this phase but we give predictions for the typical time of the collapse of the cap. Finally, the growth phase corresponds to the case where both the filament and the cap grow at a constant velocity.

One of the limitations of our work is that we considered a single protofilament. This does not seem to be an important issue for actin filaments where the length difference between the two protofilaments is always small and of the order of an actin monomer. For microtubules, the detailed polymerization mechanism seems to be very complex and this certainly plays an important role on the way the force is distributed between protofilaments (45). Recent experiments have also considered the maximum force that can be generated by a bundle of parallel actin filaments (35). Our results raise interesting questions about the role of ATP hydrolysis in this case.

Our work could be extended in several directions. In the biological context, actin or microtubule polymerization is regulated by capping proteins and it would be important to understand quantitatively the regulation mechanism and to incorporate them in our model. This is, for example, the case for motors of the Kin-13 family that have been found to interact with microtubules and induce filament depolymerization (46). So far, we have mainly considered the polymerization kinetics, but in general, there is a complex interplay between the mechanical properties of the filaments and the polymerization kinetics, which we plan to explore in future work.

APPENDIX A: CALCULATIONS USING THE GENERATING FUNCTION APPROACH

Let $P(n, k, t)$ be the probability of having n hydrolyzed ADP subunits and k unhydrolyzed ATP subunits at time t, such that $l = (n + k)d$ is the total length of the filament. It obeys the following master equation: For $k > 0$ and $n \geq 0$ we have

$$\frac{dP(n,k,t)}{dt} = UP(n,k-1,t) + W_{\mathrm{T}}P(n,k+1,t) + RP \times (n-1,k+1,t) - (U + W_{\mathrm{T}} + R)P(n,k,t). \tag{37}$$

When $n = 0$ in Eq. 37, $P(-1, k + 1, t)$ is set equal to zero. For $k = 0$ and $n \geq 1$, we have

$$\frac{dP(n,0,t)}{dt} = W_{\mathrm{D}}P(n+1,0,t) + W_{\mathrm{T}}P(n,1,t) + RP(n-1,1,t) - (U + W_{\mathrm{D}})P(n,0,t). \tag{38}$$

If $k = 0$ and $n = 0$, we have

$$\frac{dP(0,0,t)}{dt} = W_{\mathrm{T}}P(0,1,t) + W_{\mathrm{D}}P(1,0,t) - UP(0,0,t). \tag{39}$$

The time derivative d/dt has the meaning of a partial time derivative at constant n and k. The sum of the probabilities is normalized to 1 such that

$$\sum_{n=0}^{\infty}\sum_{k=0}^{\infty}P(n,k,t) = 1. \tag{40}$$

We define the following generating functions

$$F_k(x,t) = \sum_{n\geq 0}P(n,k,t)x^n, \tag{41}$$

$$H_n(y,t) = \sum_{k\geq 0}P(n,k,t)y^k, \tag{42}$$

$$G(x,y,t) = \sum_{n\geq 0}\sum_{k\geq 0}P(n,k,t)x^n y^k. \tag{43}$$

Summing over n and k in Eq. 37 and using Eqs. 38, 39, and 43, one obtains

$$\frac{dG(x,y,t)}{dt} = \left[U(y-1) + W_{\mathrm{T}}\left(\frac{1}{y}-1\right) + R\left(\frac{x}{y}-1\right)\right]G(x,y,t) - \left[W_{\mathrm{T}}\left(\frac{1}{y}-1\right) + R\left(\frac{x}{y}-1\right) + W_{\mathrm{D}}\left(1-\frac{1}{x}\right)\right]F_0(x,t) + W_{\mathrm{D}}\left(1-\frac{1}{x}\right)P(0,0,t). \tag{44}$$

Similarly one can also write down equations for F_k and H_n. This equation contains F_0, which is coupled to all the F_k. For $k > 0$,

$$\frac{dF_k(x,t)}{dt} = UF_{k-1}(x,t) + (W_{\mathrm{T}} + Rx)F_{k+1}(x,t) - (U + W_{\mathrm{T}} + R)F_k(x,t), \tag{45}$$

and for $k = 0$,

$$\frac{dF_0(x,t)}{dt} = \left(W_{\mathrm{D}}\left(1-\frac{1}{x}\right) - U\right)F_0(x,t) + (W_{\mathrm{T}} + Rx)F_1(x,t) + W_{\mathrm{D}}P(0,0,t)\left(1-\frac{1}{x}\right). \tag{46}$$

Solving this set of equations we shall derive a formula for $G(x, y, t)$. From $G(x, y, t)$, we calculate the following quantities:
The average length

$$\langle l\rangle = [\langle n\rangle + \langle k\rangle]d = d\left(\frac{\partial G(x,1,t)}{\partial x}\right)_{x=1} + d\left(\frac{\partial G(1,y,t)}{\partial y}\right)_{y=1}, \tag{47}$$

the velocity of the filament

$$v = \lim_{t\to\infty}\frac{d\langle l\rangle}{dt} = d\lim_{t\to\infty}\frac{\partial}{\partial x}\left(\frac{dG(x,x,t)}{dt}\right)_{x=1}, \quad (48)$$

and the diffusion coefficient of the filament length

$$\begin{aligned} D &= \lim_{t\to\infty}\frac{1}{2}\frac{d}{dt}\left(\langle l^2\rangle - \langle l\rangle^2\right) \\ &= d^2\lim_{t\to\infty}\left[\frac{1}{2}\frac{\partial^2}{\partial x^2}\left(\frac{dG(x,x,t)}{dt}\right) + \frac{1}{2}\frac{\partial}{\partial x}\left(\frac{dG(x,x,t)}{dt}\right)\right. \\ &\left. -\left(\frac{\partial G(x,x,t)}{\partial x}\right)\frac{\partial}{\partial x}\left(\frac{dG(x,x,t)}{dt}\right)\right]_{x=1} \end{aligned} \quad (49)$$

The average velocity of the cap is

$$J = d\lim_{t\to\infty}\frac{d\langle k\rangle}{dt} = \lim_{t\to\infty}\frac{\partial}{\partial y}\left(\frac{dG(1,y,t)}{dt}\right)_{y=1}, \quad (50)$$

and the diffusion coefficient of the cap is

$$\begin{aligned} D_c &= d^2\lim_{t\to\infty}\frac{1}{2}\frac{d}{dt}\left(\langle k^2\rangle - \langle k\rangle^2\right) \\ &= d^2\lim_{t\to\infty}\left[\frac{1}{2}\frac{\partial^2}{\partial y^2}\left(\frac{dG(1,y,t)}{dt}\right) + \frac{1}{2}\frac{\partial}{\partial y}\left(\frac{dG(1,y,t)}{dt}\right)\right. \\ &\left. -\left(\frac{\partial G(1,y,t)}{\partial y}\right)\frac{\partial}{\partial y}\left(\frac{dG(1,y,t)}{dt}\right)\right]_{y=1} \end{aligned} \quad (51)$$

Calculation of $F(x = 1, t \to \infty)$ in phases I and II

In the steady state, ($t \to \infty$), the cap distribution in phases I and II becomes time-independent and hence $(dF_k/dt)_{x=1} = 0$. In this case, Eqs. 45 and 46 can be written, for $k > 0$, as

$$0 = UF_{k-1} + (W_T + R)F_{k+1} - (U + W_T + R)F_k, \quad (52)$$

and for $k = 0$,

$$0 = (W_T + R)F_1 - UF_0, \quad (53)$$

where we denote for short, $F_k = F_k(x = 1, t \to \infty)$. The solution of Eq. 52 is of the form $F_k = q^kF_0$. If we substitute this back into Eq. 52, we get a quadratic equation in q

$$(W_T + R)q^2 - (U + W_T + R)q + U = 0. \quad (54)$$

The two solutions are $q = U/(W_T + R)$ and $q = 1$, but we can rule out $q = 1$ using the normalization condition $\sum_{k=0}^{\infty} F_k = 1$. In phases I and II, $W_T + R > U$ and therefore $q < 1$. Using the normalization condition, we obtain

$$F_k = (1 - q)q^k, \quad (55)$$

which is Eq. 1.

Calculation of $G(x, y)$ in the bounded growth phase (phase I)

We now explain how to calculate $G(x, y)$ in the bounded growth phase, using a technique of canceling apparent poles (42,43). Since we are interested in the steady-state properties of the bounded growth phase, the time derivative of G on the left-hand side of Eq. 44 is zero, which leads to

$$G(x,y) = \frac{F_0(x)[Rx(y-x) + W_Tx(y-1) - W_Dy(x-1)] - W_DP(0,0)y(1-x)}{x[-Uy^2 + (U + W_T + R)y - Rx - W_T]}, \quad (56)$$

where $F_k(x)$ and $P(0, 0)$ are unknowns. By definition

$$G(x,y) = \sum_{n\geq 0}\sum_{k\geq 0}P(n,k)x^ny^k,$$

since the $P(n, k)$ are bounded numbers, $G(x, y)$ is an analytic function for $0 \leq |x| \leq 1$ and $0 \leq |y| \leq 1$. To guarantee the analyticity of the function $G(x, y)$, the zero of the denominator of Eq. 56,

$$y = y_- = \frac{1}{2U}\left(U + W_T + R - \sqrt{(U + W_T + R)^2 - 4U(W_T + Rx)}\right),$$

must also be a zero of the numerator. This implies that

$$F_0(x) = \frac{W_DP(0,0)y_-(1-x)}{Rx(y_- - x) + W_Tx(y_- - 1) - W_Dy_-(x-1)}. \quad (57)$$

The normalization condition, namely $G(x=1, y=1) = 1$, then fixes the value of $P(0, 0)$ as

$$P(0,0) = 1 - \frac{U}{W_D}\left(\frac{W_D + R}{W_T + R}\right). \quad (58)$$

After substituting Eqs. 57 and 58 into Eq. 56, we obtain the expression of $G(x, y)$ given in Eq. 7.

Velocity and diffusion coefficient in the intermediate phase (phase II)

We recall the definition of $F_k(x, t)$ given in Eq. 43,

$$F_k(x,t) = \sum_{n\geq 0}P(n,k,t)x^n, \quad (59)$$

and we recall that F_k with no argument is a short notation for F_k ($x = 1$, $t \to \infty$). From this, we introduce

$$a_k(t) = \left(\frac{\partial F_k(x,t)}{\partial x}\right)_{x=1} \quad (60)$$

so that $\langle n(t)\rangle = \sum_{k\geq 0}P(n,k,t)n = \sum_{k\geq 0}a_k(t)$.

By taking a derivative with respect to x in Eqs. 45 and 46, one obtains the equations of evolution of $a_k(t)$: for $k > 0$,

$$\frac{da_k(t)}{dt} = Ua_{k-1}(t) + (W_T + R)a_{k+1}(t) - (U + W_T + R)a_k(t) + RF_{k+1}(x = 1,t) \quad (61)$$

and for $k = 0$,

$$\frac{da_0(t)}{dt} = -W_D F_0(x = 1,t) - Ua_0(t) + (W_T + R)a_1(t) + RF_1(x = 1,t). \quad (62)$$

As shown in Stukalin and Kolomeisky (26), there is a solution of these recursion relations in the long time limit in the form of $a_k(t) = M_k t + B_k$, where M_k and B_k are time-independent coefficients. After substituting this equation into Eqs. 61 and 62, and separating terms which are time-dependent from terms that are not time-dependent, one obtains separate recursion relations for M_k and B_k. The recursion relation of M_k is identical to that of F_k obtained in Eqs. 52 and 53. Using Eq. 55, the solution can be written as $M_k = v_{II}(1 - q)q^k/d = v_{II}F_k/d$. The recursion relation of B_k is for $k > 0$,

$$M_k = UB_{k-1} + (W_T + R)B_{k+1} - (U + W_T + R)B_k + RF_{k+1}, \quad (63)$$

and for $k = 0$,

$$M_0 = -W_D F_0 - UB_0 + (W_T + R)B_1 + RF_1. \quad (64)$$

These recursion relations can also be solved with the result

$$B_k = B_0 q^k + \left[\frac{W_D(1-q)}{W_T + R}\right] kq^k. \quad (65)$$

To characterize the intermediate phase, it is convenient to rewrite the evolution equation for the generating function $G(x, y, t)$ of Eq. 44 using the fact that $P(0,0,t \to \infty) = 0$ in this phase, in the form of an evolution equation for $\tilde{G}(x,t) = G(x,x,t)$ as

$$\frac{d\tilde{G}(x,t)}{dt} = \alpha(x)\tilde{G}(x,t) + \beta(x,t), \quad (66)$$

where $\alpha(x) = U(x - 1) + W_T(1/x - 1)$ and $\beta(x, t) = (1 - 1/x)(W_T - W_D)F_0(x, t)$. With this notation, the velocity defined in Eq. 48 is

$$v = d \lim_{t\to\infty} \frac{\partial}{\partial x}\left(\frac{d\tilde{G}(x,t)}{dt}\right)_{x=1} = d[\alpha'(1) + \beta'(1, t\to\infty)], \quad (67)$$

where the prime denotes derivatives with respect to x. Substituting the expressions of $\alpha(x)$ and $\beta(x, t)$ into this equation, it is straightforward to obtain the velocity $v = v_{II}$ characteristic of the intermediate phase which is Eq. 13. Similarly, using Eqs. 49 and 66, the diffusion coefficient can be written as

$$D = \frac{d^2}{2}\lim_{t\to\infty}\left[\alpha''(1) + \beta''(1,t) + \alpha'(1) + \beta'(1,t) - 2\tilde{G}'(1,t)\beta'(1,t)\right], \quad (68)$$

where

$$\tilde{G}'(1,t) = \left(\frac{\partial\tilde{G}(x,t)}{\partial x}\right)_{x=1} = \langle n(t)\rangle + \langle k\rangle, = vt + \frac{1}{1-q}\left[B_0 + \frac{U + W_D q}{W_T + R}\right] \quad (69)$$

After substituting Eq. 69 into Eq. 68 and simplifying, the terms linear in time and the term containing the unknown parameter B_0 cancel out in the expression of the diffusion coefficient, and we finally obtain $D = D_{II}$, which is given in Eq. 49.

APPENDIX B: CAP COLLAPSE TIME T_K

To solve the recursion relation for T_k of Eq. 27, we perform a Z-transformation defined by

$$\tilde{T}(z) = \sum_{k\geq 0} T_k z^{-k}. \quad (70)$$

After using the initial condition $T_0 = 0$, we obtain

$$\tilde{T}(z) = \frac{(1 + UT_1(1-z))z}{U(1-z)^2(q^{-1} - z)} \quad (71)$$

where $q^{-1} = (W_T + R)/U$. By definition, $\tilde{T}(z)$ is analytic for all values of $|z| > 1$. Since we are interested in the case $W_T + R > U$, the numerator in Eq. 71 must vanish to ensure that $\tilde{T}(z)$ is analytic at $z = q^{-1}$. This condition determines the unknown $T_1 = 1/(W_T + R - U)$. Now T_k can be obtained by an inverse Z-transform as

$$T_k = \frac{1}{2\pi i}\oint \tilde{T}(z)z^{k-1}dz = \frac{1}{2\pi i}\oint \frac{z^k dz}{U(1-z)^2(q^{-1}-1)} = \frac{k}{W_T + R - U}. \quad (72)$$

We thank G. I. Menon, J. Baudry, C. Brangbour, C. Godrèche, and M. F. Carlier for useful discussions. We also thank J.-M. Luck for illuminating conversations.

We also acknowledge support from the Indo-French Center CEFIPRA (grant No. 3504-2).

REFERENCES

1. Desai, A., and T. J. Mitchison. 1997. Microtubule polymerization dynamics. *Annu. Rev. Cell Dev. Biol.* 13:83–117.
2. Howard, J. 2001. Mechanics of Motor Proteins and the Cytoskeleton. Sinauer, Sunderland, MA.
3. Schneider, M. E., I. A. Belyantseva, R. B. Azevedo, and B. Kachar. 2002. Rapid renewal of auditory hair bundles. *Nature*. 418:837–838.
4. Rosenbaum, J. L., and G. B. Witman. 2002. Intraflagellar transport. *Nat. Rev. Mol. Cell Biol.* 3:813–825.
5. Prost, J., C. Barbetta, and J. -F. Joanny. 2007. Dynamical control of the shape and size of stereocilia and microvilli. *Biophys. J.* 93: 1124–1133.
6. Liu, D., M. Martic, G. Clarke, M. Dunlop, and H. Baker. 1999. An important role of actin polymerization in the human zona pellucida-induced acrosome reaction. *Mol. Hum. Reprod.* 5:941–949.
7. Shin, J. H., L. Mahadevan, P. T. So, and P. Matsudaira. 2004. Bending stiffness of a crystalline actin bundle. *J. Mol. Biol.* 337:255–261.
8. Breitbart, H., G. Cohen, and S. Rubinstein. 2005. Role of actin cytoskeleton in mammalian sperm capacitation and the acrosome reaction. *Reproduction*. 129:263–268.
9. Hunt, A. J., and J. R. McIntosh. 1998. The dynamic behavior of individual microtubules associated with chromosomes in vitro. *Mol. Biol. Cell*. 9:2857–2871.

10. Garner, E. C., C. S. Campbell, and R. D. Mullins. 2004. Dynamic instability in a DNA-segregating prokaryotic actin homolog. *Science*. 306:1021–1025.

11. Pantaloni, D., T. L. Hill, M. F. Carlier, and E. D. Korn. 1985. A model for actin polymerization and the kinetic effects of ATP hydrolysis. *Proc. Natl. Acad. Sci. USA*. 82:7207–7211.

12. Hill, T. L. 1986. Theoretical study of a model for the ATP cap at the end of an actin filament. *Biophys. J*. 49:981–986.

13. Hill, T. L. 1984. Introductory analysis of the GTP-cap phase-change kinetics at the end of a microtubule. *Proc. Natl. Acad. Sci. USA*. 81:6728–6732.

14. Dogterom, M., and S. Leibler. 1993. Physical aspects of the growth and regulation of microtubule structures. *Phys. Rev. Lett*. 70:1347–1350.

15. Flyvbjerg, H., T. E. Holy, and S. Leibler. 1994. Stochastic dynamics of microtubules: a model for caps and catastrophes. *Phys. Rev. Lett*. 73:2372–2375.

16. Flyvbjerg, H., T. E. Holy, and S. Leibler. 1996. Microtubule dynamics: caps, catastrophes, and coupled hydrolysis. *Phys. Rev. E*. 54:5538–5560.

17. Bicout, D. J. 1997. Green's functions and first passage time distributions for dynamic instability of microtubules. *Phys. Rev. E*. 56:6656–6667.

18. Zong, C., T. Lu, T. Shen, and P. G. Wolynes. 2006. Nonequilibrium self-assembly of linear fibers: microscopic treatment of growth, decay, catastrophe and rescue. *Phys. Biol*. 3:83–92.

19. Antal, T., P. L. Krapivsky, S. Redner, M. Mailman, and B. Chakraborty. 2007. Dynamics of an idealized model of microtubule growth and catastrophe. *Phys. Rev. E*. 76:041907.

20. Antal, T., P. L. Krapivsky, and S. Redner. 2007. Dynamics of microtubule instabilities. *J. Stat. Mech.* Doi:10.1088/1742-5468/2007/05/L05004.

21. Fujiwara, I., S. Takahashi, H. Tadakuma, T. Funatsu, and S. Ishiwata. 2002. Microscopic analysis of polymerization dynamics with individual actin filaments. *Nat. Cell Biol*. 4:666–673.

22. Kuhn, J. R., and T. D. Pollard. 2005. Real-time measurements of actin filament polymerization by total internal reflection fluorescence microscopy. *Biophys. J*. 88:1387–1402.

23. Michelot, A., J. Berro, C. Gurin, R. Boujemaa-Paterski, C. Staiger, et al. 2007. Actin-filament stochastic dynamics mediated by ADF/cofilin. *Curr. Biol*. 17:825–833.

24. Roland, J., J. Berro, A. Michelot, L. Blanchoin, and J. -L. Martiel. 2008. Stochastic severing of actin filaments by actin depolymerizing factor/cofilin controls the emergence of a steady dynamical regime. *Biophys. J*. 94:2082–2094.

25. Vavylonis, D., Q. Yang, and B. O'Shaughnessy. 2005. Actin polymerization kinetics, cap structure, and fluctuations. *Proc. Natl. Acad. Sci. USA*. 102:8543–8548.

26. Stukalin, E. B., and A. B. Kolomeisky. 2006. ATP Hydrolysis stimulates large length fluctuations in single actin filaments. *Biophys. J*. 90:2673–2685.

27. Gillespie, D. T. 1977. Exact stochastic simulation of coupled chemical reactions. *J. Phys. Chem*. 81:23–40.

28. Fygenson, D. K., E. Braun, and A. Libchaber. 1994. Phase diagram of microtubules. *Phys. Rev. E*. 50:1579–1588.

29. Peskin, C. S., G. M. Odell, and G. F. Oster. 1993. Cellular motions and thermal fluctuations: the Brownian ratchet. *Biophys. J*. 65:316–324.

30. Mogilner, A., and G. Oster. 1996. Cell motility driven by actin polymerization. *Biophys. J*. 71:3030–3045.

31. van Doorn, G. S., C. Tanase, B. M. Mulder, and M. Dogterom. 2000. On the stall force for growing microtubules. *Eur. Biophys. J*. 20:2–6.

32. Hill, T. L. 1981. Microfilament or microtubule assembly or disassembly against a force. *Proc. Natl. Acad. Sci. USA*. 78:5613–5617.

33. Dogterom, M., and B. Yurke. 1997. Measurement of the force-velocity relation for growing microtubules. *Science*. 278:856–860.

34. Kolomeisky, A. B., and M. E. Fisher. 2001. Force-velocity relation for growing microtubules. *Biophys. J*. 80:149–154.

35. Footer, M. J., J. W. J. Kerssemakers, J. A. Theriot, and M. Dogterom. 2007. Direct measurement of force generation by actin filament polymerization using an optical trap. *Proc. Natl. Acad. Sci. USA*. 104:2181–2186.

36. Lau, A. W. C., D. Lacoste, and K. Mallick. 2007. Nonequilibrium fluctuations and mechanochemical couplings of a molecular motor. *Phys. Rev. Lett*. 99:158102.

37. Lacoste, D., A. W. Lau, and K. Mallick. 2008. Fluctuation theorem and large deviation function for a solvable model of a molecular motor. *Phys. Rev. E*. 78:011915.

38. Liepelt, S., and R. Lipowsky. 2007. Kinesin's network of chemomechanical motor cycles. *Phys. Rev. Lett*. 98:258102.

39. Romero, S., D. Didry, E. Larquet, N. Boisset, D. Pantaloni, et al. 2007. How ATP hydrolysis controls filament assembly from profilin-actin: implication for formin processivity. *J. Biol. Chem*. 282:8435–8445.

40. Isambert, H., P. Venier, A. Maggs, A. Fattoum, R. Kassab, et al. 1995. Flexibility of actin-filaments derived from thermal fluctuations—effect of bound nucleotide, phalloidin, and muscle regulatory proteins. *J. Biol. Chem*. 270:11437–11444.

41. Redner, S. 2001. A Guide To First-Passage Processes. Cambridge University Press, Cambridge, UK.

42. Saaty, T. L. 1961. Elements of Queuing Theory with Application. McGraw-Hill, Englewood Cliffs, NJ.

43. Karlin, S., and H. M. Taylor. 1975. A First Course in Stochastic Processes. Academic Press, New York, New York.

44. Janson, M. E., M. E. de Dood, and M. Dogterom. 2003. Dynamic instability of microtubules is regulated by force. *J. Cell Biol*. 161:1029–1034.

45. Janosi, I. M., D. Chretien, and H. Flyvbjerg. 2002. Structural microtubule cap: stability, catastrophe, rescue, and third state. *Biophys. J*. 83:1317–1330.

46. Klein, G. A., K. Kruse, G. Cuniberti, and F. Jülicher. 2005. Filament depolymerization by motor molecules. *Phys. Rev. Lett*. 94:108102.

De la matière molle aux milieux biologiques : quelques applications en Physique Statistique

David LACOSTE

Résumé : Ce mémoire présente trois exemples différents d'applications de la Physique Statistique dans le domaine de la matière molle et des milieux biologiques. La première partie porte sur le transport de la lumière dans des milieux complexes comme des milieux biologiques ou des cristaux liquides. La seconde partie porte sur l'élaboration de nouveaux matériaux par auto-assemblage de particules colloïdales, comme des colloïdes magnétiques ou des bâtonnets colloïdaux. La dernière partie porte sur des exemples d'application de la Physique Statistique hors d'équilibre à des systèmes vivants. Nous avons mené des recherches sur les fluctuations hors d'équilibre qui caractérisent certains systèmes biologiques (comme des moteurs moléculaires, des biofilaments ou des membranes contenant des canaux à ions).

From soft matter to biological media : a few applications of Statistical Physics

Abstract : This manuscript is devoted to three different examples of applications of Statistical Physics to soft matter and biological media. The first part contains a study of the transport of light in complex media such as biological media and liquid crystals. The second part is about the elaboration of new materials using the self-assembly of colloidal particles, such as magnetic colloidal particles or colloidal rods. The last part is devoted to applications of non-equilibrium Statistical Physics to living systems. We investigate in this part the proper description of the non-equilibrium fluctuations which characterize biological systems such as molecular motors, biofilaments or membranes containing ions channels..